Scaffold guided 3D brain organoid models

Kaja Ritzau-Reid

A thesis submitted in accordance with the requirements for the degree of Doctor of Philosophy and the Diploma of Imperial College London

The Department of Materials

The Department of Bioengineering

May 2022

Imperial College London

Declaration of Originality

I, Kaja Ritzau-Reid, declare that the original scientific content in this thesis is my own, unless otherwise stated or referenced. Experimental work or data analysis that was done in collaboration with others is acknowledged within the text and figure captions. The work presented in this thesis was performed at Imperial College London and the Institute of Biotechnology (IMBA), Vienna.

Copyright Declaration

The copyright of this thesis rests with the author and is made available under a Creative Commons Attribution Non-Commercial No Derivatives license. Researchers are free to copy, distribute or transmit the thesis on the condition that they attribute it, that they do not use it for commercial purposes and that they do not alter, transform, or build upon it. For any reuse or redistribution, researchers must make clear to others the license terms of this work.

Acknowledgements

I have so many people to thank. My gratitude begins with my supervisor Molly, who has been a wonderful mentor throughout this journey. I am so grateful that Molly trusted me to make choices about the direction of my PhD, giving me autonomy and support in equal measure. It has also been an inspiration for me to see a woman leading and thriving in science, and creating a group that has kindness at its core.

Four years ago, when I changed direction in my PhD from conducting polymers to brain organoid engineering, I asked James Armstrong if he would be my post doc supervisor. It took some convincing (he already had a lot of students!) but asking him was one of the best things I did in my PhD. He has supported, challenged, and encouraged me, and scrupulously edited my work over the last 4 years. I have learnt so much from James and he has undoubtedly made me a better scientist.

There are so many other post docs who have helped me along the way. I would not be where I am today without their support. Chris Spicer was my first post doc supervisor, who was unbelievably kind and patient with me in the early days. Chris Grigsby has been on this journey with me throughout, helping me to develop new ideas and approaches and always willingly, patiently making MORE scaffolds. In the last year, Sebastien Callens and Martina Cihova arrived at the group and helped me to shape and develop the work in Chapter 3 of this thesis. Their enthusiasm was infectious, and I loved our lively scientific discussions. In the microfluidics project, I worked closely with Richard Wang and Ruoxiao Xie, who brought their invaluable expertise to the project. During the writing of this thesis, they graciously took over some of the experiments, allowing the work to continue. I am extremely grateful for their help. Other post docs that have given their support, time and expertise are: Amy Gelmi, Spencer Crowder, Adam Creamer, Daniel Hachim Diaz, Vernon LaLone, Abeni Wickham, Alice Agliano and Paresh Parmar.

I also need to thank Juergen Knoblich, who supervised me at IMBA in Vienna for 10 months. Juergen graciously hosted me in his group, giving me a completely new perspective and

knowledge base, and providing me with the tools to setup the organoid work at Imperial. One of his students, Daniel Reumann taught me all the practical skills in organoid generation, and has become a good friend and collaborator.

The ups and downs of the PhD has been shared with my fellow PhD cohort: Liiliana, Luke, Raya, Maxine, Charlotte, Katya, Dan, Brian, Renee. It has been a wonderfully supportive cohort to share this journey with.

I am extremely lucky to have the most wonderful family. My parents have given me so much love and support, and have reminded me to take time away when I needed it most. When writing this thesis I was reminded of my big sister's English lessons when I was small. As children she always corrected my work, and as a teenager and young adult she edited my essays, teaching me about structure, and writing with simplicity. She is a wonderful writer – far better than anything I could hope to be, but I have no doubt that she gave me the tools to write this. Finally, to my amazing partner Sam, who brings me so much happiness and joy. Alongside this PhD journey, we have had our own journey, and I can't wait to start the next exciting chapter together.

Abstract

The intrinsic self-organisation properties of stem cells provide a unique opportunity to derive 3D *in vitro* models of organs, known as organoids. In recent years brain organoids have emerged as *in vitro* model systems that recapitulate certain functional and organisational properties of embryonic brain development. This nascent technology holds enormous promise to investigate human brain development and disease and has already shown success in modelling certain features of some neurodevelopmental and neurodegenerative brain disorders. Yet, major challenges remain. In particular, the lack of organoid reproducibility, lack of regional patterning, shape heterogeneity and the absence of a proper vasculature system currently hinder the advancement of this technology. Combining expertise from stem cell biology and bioengineering offers a promising approach to address some of these limitations.

Here, a bioengineering platform is developed to guide 3D stem cell and brain organoid growth. This thesis is separated into three sections, exploring: (i) The design and fabrication of biomaterial scaffolds for stem cell culture, where it is shown that scaffold geometry is a key determinant of stem cell self-organisation and collective tissue growth; (ii) The generation of a new method for controlled high-throughput brain organoid formation using the scaffold-culture platform; (iii) Growth factor functionalisation of scaffolds and microfluidic gradients to direct the regional patterning of scaffold-cultured brain organoids.

Taken together, these strategies provide the opportunity to guide brain organoid morphogenesis, utilising scaffold geometry and exploiting the material to incorporate biochemical cues. Importantly, this scaffold mediated process maintains the intrinsic cell autonomous property of self-organisation that is inherent to organoid development. It is hoped that these strategies will be adapted to other organoid systems in the future, allowing for more controlled, complex organoid formation.

Publications

Ritzau-Reid K. I., Spicer C. D., Gelmi A., Grigsby C L., Ponder Jr J F., Bemmer V., Creamer A., Vilar R., Serio A., Stevens M M. "An Electroactive Oligo-EDOT Platform for Neural Tissue Engineering" ***Advanced Functional Materials.*** 30, 2003710 (2020)

Patents

Ritzau-Reid K.I, Wang R, Xie R, Armstrong J, Yeow J, Grigsby L. C., Reumann D, Knoblich A. J., Stevens M. M. Title: Scaffold supported organoid farms for controlled high throughput in vitro organoid aggregation and regional organoid patterning. Filed 9th May 2022. Application number 2206768.0

Table of Contents

LIST OF FIGURES **12**

LIST OF TABLES **15**

LIST OF ABBREVIATIONS **16**

1. INTRODUCTION **20**

1.1. *IN VITRO* BRAIN MODELS: AN OVERVIEW **20**

1.1.1. Overview of mammalian brain development *20*

1.1.2. 2D to 3D in vitro brain models: a historical overview *22*

1.1.3. Clinical need for in vitro brain models *25*

1.2. TOWARDS 3D STEM CELL SELF-ORGANISATION AND ORGANOID FORMATION **28**

1.2.1. Self-organisation and symmetry breaking *28*

1.2.2. Stem cell based lumenogenesis *29*

1.2.3. Mechanical forces direct stem cell behaviour *31*

1.3. BRAIN ORGANOID MODELS **33**

1.3.1. Unguided 3D brain organoid models *33*

1.3.2. Guided 3D brain organoid models *37*

1.4. ENHANCING BRAIN ORGANOID COMPLEXITY **39**

1.4.1. Engineering interregional brain organoid interactions *39*

1.4.2. Brain organoid maturation *43*

1.4.3. Microfluidics and Organ-on-a-chip *44*

1.4.4. Designing scaffolds for brain organoids *46*

1.4.5. Shape guided organoid morphogenesis *50*

1.5. MORAL AND ETHICAL CONSIDERATIONS **52**

1.6. SCOPE OF THIS THESIS **55**

2. MATERIALS AND METHODS **58**

2.1. MELT ELECTROSPINNING WRITING FOR SCAFFOLD FABRICATION **58**

2.2. CELL CULTURE **58**

2.3. SCAFFOLD PREPARATION FOR CELL CULTURE **58**

2.4. CEREBRAL ORGANOID MEDIA FORMULATIONS **59**

2.5. CONVENTIONAL CEREBRAL ORGANOID GENERATION **59**

2.6. CRYOSECTIONING ORGANOIDS 60
2.7. IMMUNOSTAINING ORGANOID SECTIONS 61
2.8. CONFOCAL IMAGING 61
2.9. OPTICAL CLEARING ORGANOID SAMPLES 61
3. SCAFFOLD GUIDED SELF-ORGANISATION OF STEM CELLS 64
3.1. INTRODUCTION 64
3.2. MATERIALS AND METHODS 67
3.2.1. Mechanical testing 67
3.2.2. Scanning Electron Microscopy 67
3.2.3. Scaffold preparation for cell culture 67
3.2.4. Lumen morphogenesis protocol 67
3.2.5. Scanning Electron Microscopy with cells 68
3.2.6. Small molecule inhibitor assays 69
3.2.7. Cerebral organoid formation on scaffolds 69
3.2.8. Wholemount immunostaining hESC scaffold samples 70
3.2.9. Cryosectioning and immunostaining d 20 organoid sections 70
3.2.10. Optical clearing d 15 organoid samples 70
3.2.11. Confocal imaging 71
3.2.12. Time-lapse imaging 72
3.2.13. Mathematical modelling 73
3.3. RESULTS AND DISCUSSION 75
3.3.1. Scaffold fabrication and characterisation 75
3.3.2. hESCs self-organise on MEW PCL scaffolds 77
3.3.3. Scaffold guided lumen formation 83
3.3.4. 3D characterisation of lumen formation on scaffolds 87
3.3.5. Scaffold geometry predictably guides lumen formation and tissue shape 90
3.3.6. Curve-shortening flow predicts tissue growth and evolution on scaffold 93
3.3.7. Rock inhibition increases lumen formation on scaffolds 95
3.3.8. Generating a network of cerebral organoids on scaffolds 97
3.4. CONCLUSION 106
4. SCAFFOLD GUIDED CEREBRAL ORGANOID GENERATION 109
4.1. INTRODUCTION 109
4.2. MATERIALS AND METHODS 112

4.2.1. Cerebral organoid culture on scaffolds 112
4.2.2. Alternative Matrigel embedding protocol 113
4.2.3. Brightfield imaging 113
4.2.4. Cryosectioning and immunostaining organoid sections 114
4.2.5. Confocal imaging 115
4.2.6. Time lapse imaging 115
4.2.7. Optical Clearing 116
4.2.8. Raman spectroscopy imaging 116
4.3. RESULTS AND DISCUSSION 117
4.3.1. Optimising culture conditions for organoids on scaffolds 117
4.3.2. High throughput organoid growth on scaffolds 119
4.3.3. Scaffold guided growth dynamics of early cerebral organoids 123
4.3.4. Scaffold-cultured organoid characterisation 127
4.3.5. Characterisation of long-term scaffold-cultured organoids 131
4.3.6. Advanced organoid characterisation with Raman spectroscopy 135
4.4. CONCLUSION 140
5. SCAFFOLD GUIDED BRAIN ORGANOID PATTERNING 143
5.1. GENERAL INTRODUCTION 143
5.2. MATERIALS AND METHODS 144
5.2.1. Melt electrospinning writing for scaffold fabrication 144
5.2.2. Fabrication of PDMS substrates for elongated organoid culture 144
5.2.3. Scaffold preparation for elongated organoid culture 145
5.2.4. Elongated cerebral organoid culture on scaffolds 145
5.2.5. Generation of ventrally patterned conventionally cultured round organoids with Sonic hedgehog (Shh) morphogen 146
5.2.6. Layer-by-Layer assembly 146
5.2.7. XPS characterisation of Heparin and Chitosan LbL coated scaffolds 147
5.2.8. Sonic hedgehog scaffold functionalisation for organoid culture 147
5.2.9. Sonic hedgehog scaffold immunostaining and imaging 148
5.2.10. Sonic hedgehog release assay 148
5.2.11. Microfluidic chip design 149
5.2.12. 3D printing resin mold 149
5.2.13. PDMS chip fabrication 149

5.2.14. Bonding of chip with glass slide 150
5.2.15. Scaffold holder fabrication 150
5.2.16. Attachment of inlet and outlet valves/tubes 150
5.2.17. Glass plate fabrication 151
5.2.18. Widefield Fluorescence microscopy for gradient detection 151
5.2.19. Computation fluid dynamics (CFD) simulation 151
5.2.20. Generation of ventrally patterned conventionally cultured round organoids with Smoothened agonist (SAG) and iWP2 153
5.2.21. Scaffold preparation for microfluidic organoid culture 153
5.2.22. Microfluidic organoid culture 153
5.2.23. Widefield microscopy 155
5.2.24. Cryosectioning and immunostaining d 20 organoid samples 156
5.2.25. Optical clearing organoid samples 156
5.3. RESULTS AND DISCUSSION I: DIRECTING ELONGATED ORGANOID GROWTH ON SCAFFOLDS 156
5.3.1. Introduction 157
5.3.2. Elongated scaffold design optimisation 158
5.3.3. Elongated organoid characterisation 162
5.3.4. Conclusion 164
5.4. RESULTS AND DISCUSSION II: BIOACTIVE SCAFFOLDS TO DIRECT ELONGATED ORGANOID REGIONALISATION 165
5.4.1. Introduction 165
5.4.2. Shh induced ventralisation of conventionally cultured round organoids 166
5.4.3. LbL functionalisation of scaffolds 167
5.4.4. Material characterisation 171
5.4.5. Organoid characterisation on Shh functionalised scaffolds 173
5.4.6. Conclusion 179
5.5. RESULTS AND DISCUSSION III: MICROFLUIDIC GUIDED ORGANOID POLARISATION 180
5.5.1. Introduction 180
5.5.2. Design principle 182
5.5.3. Microfluidic chip fabrication 183
5.5.4. CFD modelling and Gradient optimisation 186
5.5.5. Organoid growth and characterisation on custom scaffold holder 188
5.5.6. Ventral patterning optimisation 191
5.5.7. Organoids perfused on microfluidic chip without a morphogen gradient 192

5.5.8. Organoids perfused on microfluidic chip with a morphogen gradient 196

5.6. CONCLUSION 201

6. CONCLUSIONS AND FUTURE WORK 204

6.1. MOTIVATION 204

6.2. CONCLUSIONS 205

6.2.1. Scaffold guided self-organisation of stem cells 205

6.2.2. Scaffold guided cerebral organoid generation 206

6.2.3. Scaffold guided brain organoid patterning 207

6.3. PERSPECTIVES 210

6.4. CONCLUDING REMARKS 211

REFERENCES 212

APPENDIX 229

List of Figures

Figure 1.1 Embryonic human brain development 21
Figure 1.2 Timeline overview of CNS in vitro modelling.....25
Figure 1.3 Stem cell self-organisation.....30
Figure 1.4 Mechanical and geometry guided stem cell growth 33
Figure 1.5 Human cerebral organoid generation 34
Figure 1.6 Human cerebral organoid organisation.....36
Figure 1.7 Guided and unguided differentiation of brain organoids 39
Figure 1.8 Engineering interregional brain interactions in brain organoids.....42
Figure 1.9 Microfluidic systems for generating morphogen gradients 46
Figure 3.1 Scaffold fabrication via melt electrospinning writing (MEW). 75
Figure 3.2 Mechanical characterization of MEW scaffolds. 77
Figure 3.3 Schematic illustration of MEW scaffold preparation and stem cell culture.....78
Figure 3.4 SEM images of PCL MEW scaffolds.....79
Figure 3.5 Schematic illustration of hESC seeding on scaffolds 80
Figure 3.6 hESC growth and lumen formation on MEW scaffolds 82
Figure 3.7 Characterisation of lumen formation on scaffolds at d 2 and d 5.....84
Figure 3.8 Cytoskeletal tissue dynamics and onset of lumenogenesis 86
Figure 3.9 Schematic of the mechanistic model describing scaffold guided tissue growth and lumen formation on MEW scaffolds.....87
Figure 3.10 3D characterisation of hESC tissues on MEW.....88
Figure 3.11 3D lumen reconstruction on MEW scaffolds.....89
Figure 3.12 Scaffold geometry guides lumen formation.....91
Figure 3.13 3D characterisation of hESC tissues on triangular scaffolds.....93
Figure 3.14 Curve shortening flow models hESC tissue growth on scaffolds.....94
Figure 3.15 Rock inhibition promotes lumenogenesis on MEW scaffolds 96
Figure 3.16. Characterisation of hESC seeded scaffolds at d 5.....98
Figure 3.17 Cytoskeletal tissue dynamics during cerebral organoid growth on MEW scaffolds 99
Figure 3.18 hESCs form cerebral organoids on MEW scaffolds.....102

Figure 3.19 Image gallery at d 15 showing single slice of cerebral organoids on scaffolds ..103
Figure 3.20 Immunostaining characterisation of d 20 cerebral organoids on MEW scaffolds 105
Figure 4.1 Schematic to show interconnected cerebral organoid tissue on Matrigel coated scaffolds as demonstrated in Chapter 3, and uncoated scaffolds with independently growing cerebral organoids, which is explored in this Chapter. 109
Figure 4.2. Schematic to show protocols for in vitro neural tube or organoid models alongside the adapted scaffold organoid culture platform.....118
Figure 4.3 Stem cell aggregation at scaffold intersections.....120
Figure 4.4 Characterisation of cerebral organoid growth on scaffolds.....122
Figure 4.5 SiR-Actin accumulation and distribution during early cerebral organoid formation 124
Figure 4.6 3D characterisation of the organoid-tissue growth dynamics 126
Figure 4.7 Immunostaining characterisation of d 20 cerebral organoids on scaffolds.....128
Figure 4.8 Immunostaining characterisation of d 40 cerebral organoids on scaffolds.....130
Figure 4.9 Matrigel embedding optimization.....132
Figure 4.10 Tiled overview image of fixed organoids on 1000 µm spaced scaffolds at d 48 133
Figure 4.11 Immunostaining characterisation of d 48 organoids on scaffolds 134
Figure 4.12 Immunostaining characterisation of d 60 organoids on scaffolds 134
Figure 4.13 Schematic overview of Raman spectroscopic imaging of organoids on scaffolds 137
Figure 4.14 Raman spectroscopy imaging of organoids on scaffolds.....138
Figure 5.1. Elongated organoid generation schematic.....158
Figure 5.2 Characterisation of elongated cerebral organoid growth on scaffolds.....161
Figure 5.3 Characterisation of elongated scaffold organoids.....163
Figure 5.4 Conventionally cultured round organoids show ventral tissue identity at d 20 with Shh morphogen treatment 167
Figure 5.5 Scaffold growth factor functionalisation with Layer-by-layer assembly.....168
Figure 5.6. XPS spectra shows presence of heparin and chitosan on scaffolds after LbL assembly with 10 layers.....170
Figure 5.7 Shh functionalisation on scaffolds.....173

Figure 5.8 Elongated organoid growth on Shh functionalised scaffolds 175
Figure 5.9 Characterisation of d 20 elongated organoids grown on Shh functionalised scaffolds 177
Figure 5.10 Characterisation of d 20 elongated organoids grown on Shh functionalised scaffolds 178
Figure 5.11 Design schematic of microfluidic gradient generator for elongated organoid culture 183
Figure 5.12 Microfluidic chip design 184
Figure 5.13 Microfluidic chip fabrication 185
Figure 5.14 Exploded view of the fully assembled microfluidic gradient generator device .186
Figure 5.15 CFD modelling and gradient optimisation 188
Figure 5.16 Schematic illustration of scaffold preparation and cell seeding on custom-built scaffold holders 189
Figure 5.17 Characterisation of elongated scaffold organoids cultured using custom-built scaffold holders 190
Figure 5.18 Conventionally cultured round organoids show ventral tissue identity with morphogen treatment 192
Figure 5.19 Schematic illustration and timeline of elongated organoid perfusion in microfluidic chip without a morphogen gradient 193
Figure 5.20 Characterisation of elongated scaffold organoids perfused in the microfluidic chip without a morphogen gradient 195
Figure 5.21 Schematic illustration and timeline of elongated organoid perfusion in microfluidic chip with a morphogen gradient 196
Figure 5.22 Characterisation of elongated scaffold organoids perfused in the microfluidic chip with a morphogen gradient 199

List of Tables

Table 1 Advantages and disadvantages for different Extracellular Matrix (ECM) biomaterials for organoid engineering 48
Table 2 Proposed research limits on brain organoids 54
Table 3 Antibodies used in Chapter 3. 70
Table 4 Antibodies used in Chapter 4. 114
Table 5 Antibodies used in Chapter 5. 156

List of abbreviations

°C	Degrees Celsius
ALI-COs	Air-liquid interface cerebral organoids
AP	Antero-posterior
aPKCzeta	atypical protein kinase C
BBB	Blood-brain-barrier
BMP	Bone morphogenetic protein
BoC	Brain-on-chip
BSA	Bovine serum albumin
CFD	Computational fluid dynamics
CNS	Central nervous system
CP	Cortical plate
CRISPR	Clustered regularly interspaced short palindromic repeats
CSF	Cerebral spinal fluid
CTIP2	BAF Chromatin Remodeling Complex Subunit BCL11B
d	Days
DAPI	(4',6-Diamidino-2-Phenylindole, Dihydrochloride)
DMEM	Dulbecco's modified eagle's medium
DV	Dorso-ventral
EB	Embryoid body
ECi	Ethyl cinnamate
ECM	Extracellular matrix
ELISA	Enzyme-linked immunosorbent assay
enCOR	Engineered cortical organoid
ESC	Embryonic stem cell
FOXA2	Forkhead Box A2
FOXG1	Forkhead BoxG1
G	Gauge
GAG	Glycosaminoglycans
GSX2	Genetic Screened Homeobox 2
h	Hour
hCS	Human cortical spheroid

hESC	Human embryonic stem cell
Hh	Hedgehog
hMSC	Human mesenchymal stem cell
hPSC	Human pluripotent stem cell
HSPGs	Heparan sulfate proteoglycans
HUVECs	Human umbilical vein endothelial cells
IIT	Integrated information theory
IPs	Intermediate progenitors
iPSC	Induced pluripotent stem cell
iSVZ	Inner subventricular zone
LBL	Layer-by-layer
LGE	Lateral ganglionic eminence
MAP2	Microtubule Associated Protein 2
MDCK	Madine-Darby canine kidney
MEAs	Multi-electrode arrays
MEW	Melt electrospinning writing
MGE	Medial ganglionic eminence
Min	Minutes
MSCs	Mesenchymal stem cells
n	Number of technical replicates
N	Number of independent replicates
N-Cadherin	Neural-Cadherin
NE	Neuroepithelial
ng	Nanograms
NKX2.1	NK2 Homeobox 1
NSC	Neural stem cell
OoC	Organ-on-chip
OPC	Oligodendrocyte precursor cells
oSVZ	Outer subventricular zone
PAX6	Paired Box 6
PCL	Polycaprolactone
PD	Parkinson disease
PDMS	Polydimethylsiloxane
PEG	Polyethylene glycol
PFA	Paraformaldehyde
PFOS	Perfluoroocytyltricholorsilane
PLGA	poly(lactic-*co*-glycolic acid)

PM	Purmorphamine
RG	Radial glial
RI	Rock Inhibitor
Rock	Rho Kinase
ROCK	Rho-associated protein kinase
ROI	Region of interest
SAG	Smoothened agonist
scRNA-seq	Single-cell RNA sequencing
SEM	Scanning electron microscopy
Shh	Sonic hedgehog
SIR	Silicon-Rhodamine
SLA	Stereolithography
SOX2	SRY-Box Transcription Factor 2
SVZ	Subventricular zone
TALENs	Transcription activator-like effector nucleases
TBR1	T-Box Brain Transcription Factor 1
TUJ1	Tubulin Beta 3 class III
UV	Ultraviolet
VZ	Ventricular zone
Wnt	wingless-type mmtv integration site family
XPS	X-ray photoelectron spectroscopy
ZO1	Tight Junction Protein 1
µL	Microlitres
µm	Micrometres
µM	Micromolar

Chapter 1.

Introduction

1. Introduction

1.1. *In vitro* brain models: an overview

1.1.1. Overview of mammalian brain development

The human brain remains one of the most complex and least understood organs in the animal kingdom. Though morphologically unremarkable, it contains billions of neurons and glial cells that organise into complex neural circuits. These mediate the brain's diverse functional capacities, perpetually changing and evolving throughout the span of a lifetime. Compared to other mammals, the human brain is characterised by its large size, cortical folding to increase surface area, and long duration of development.[1] The outer layer of the human brain, the neocortex, comprises 80% brain mass, and is responsible for the exceptional cognitive abilities attributed to humans.

All cells of the neocortex originate from progenitor neuroepithelial (NE) cells, which initially form a monolayer sheet of pseudostratified epithelial cells, constituting the neural plate.[2] During neurulation, which occurs at approximately 16-21 d post conception in humans, the neural plate folds and eventually closes, giving rise to the neural tube: the embryonic precursor to the central nervous system (CNS) **(Figure 1.1a**).[3] Towards the end of neurulation, neural tube closure forms fluid filled cavities, which go on to form the brain ventricles. The posterior region of the neural tube gives rise to the spinal cord, and the anterior portion of the tube expands laterally to form three primary brain vesicles: the prosencephalon (forebrain), mesencephalon (midbrain) and rhombencephalon (hindbrain). These further subdivide, forming five secondary brain vesicles which are aligned along the rostral-caudal (anterior-posterior) axis of the developing embryo (**Figure 1.1b**).[3]

Neural patterning is crucial for establishing the spatial organization of the CNS and occurs through a complex interplay of intrinsic and extrinsic patterning factors.[4] Simultaneous to rostro-caudal axis formation, the neural tube develops a dorso-ventral axis, which is

primarily regulated by three main signalling classes: Wnt, bone morphogenetic protein (BMP) and sonic hedgehog (Shh).[5] Signalling molecules Wnt and BMP are produced in the roof plate of the neural tube and specify a dorsal fate, and Shh is produced in the notochord and specifies a ventral fate (**Figure 1.1b**). The interplay of these instructive cues causes the neural progenitor cells to acquire distinct transcriptional identities at specific positions along the dorso-ventral axis of the neural tube.

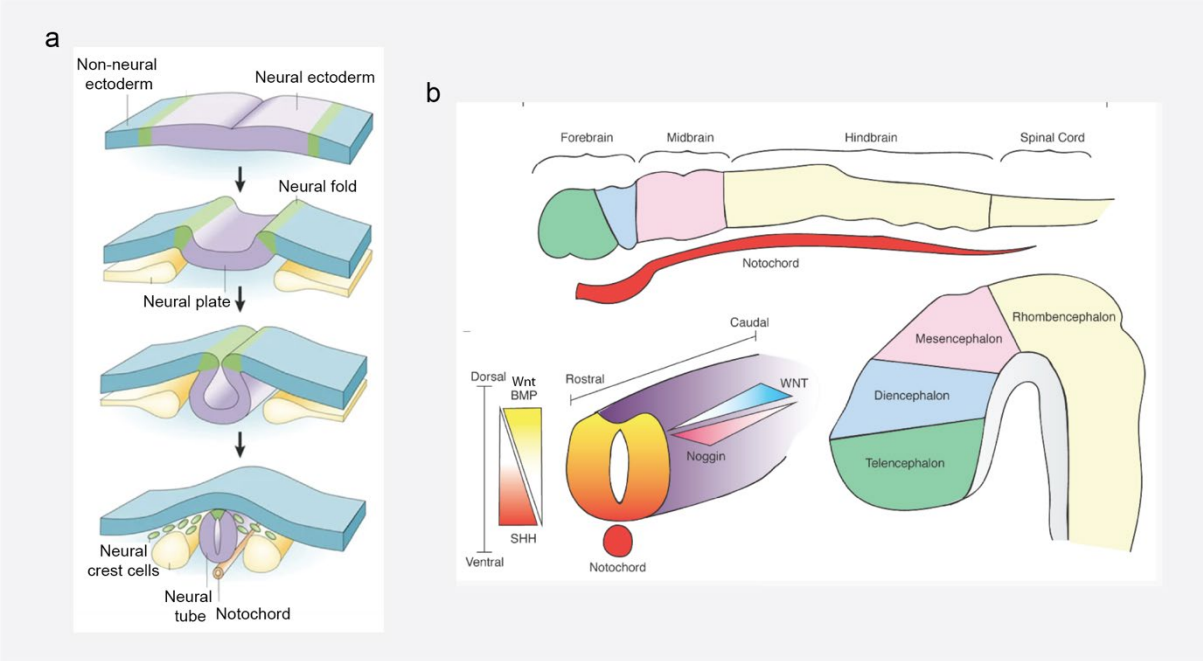


Figure 1.1 Embryonic human brain development. *a) Primary neurulation occurs as the neural plate invaginates, forming a neural tube. Neural crest cells migrate away as the neural tube forms. Image was adapted with permission from Springer Nature.*[6] *b) Regional identity of the developing brain vesicles in early brain and central nervous system (CNS) development (top) and in the mature embryonic brain and CNS structures (bottom, right). Key morphogens involved in the development of the dorso-ventral axes, including BMP, Wnt and Shh, and the rostro-caudal brain axes, including Wnt and Noggin. (bottom, left). Image adapted with permission from MDPI.*[7]

Neurogenesis occurs early in human development, at 5-6 weeks.[8] In the neocortex, neurogenesis occurs in two major proliferative zones: the ventricular zone (VZ) and the subventricular zone (SVZ). Before the onset of neurogenesis, NE cells transform into radial glial (RG) cells. These are bipolar shaped cells, which first undergo a directed movement termed interkinetic nuclear migration.[9] This positions their nuclei at the apical surface in the

VZ, for mitosis to take place, with their basal processes traversing the developing neocortex. After their transition from NE cells, RG cells switch their mode of cell division from symmetrical to asymmetrical, allowing them to generate radial glial progeny as well as neurons or intermediate progenitors (IPs).[8,10] The cell types that are generated from the asymmetric divisions of the RG cells contribute to the formation of a transient population of cells including basal RG or outer RG.[11] These cells migrate towards the basal side of the epithelium to the second proliferative zone, the SVZ. The SVZ is generally thicker and more elaborate in humans, compared to other animals.[12] It is thought that the complexity and neuron production in the SVZ, coupled with the comparatively slow rate of neurogenesis compared to other animals has contributed to the huge expansion of the neocortex in human brain evolution.[13]

In order to orient themselves to their proper location in the developing neocortex, differentiated neurons use the RG processes as a guide, to migrate basally towards the outer cortical plate (CP). Vastly populated by excitatory neurons, there are also several types of inhibitory interneuron types, which have a crucial role in modulating circuity in the adult brain. Interneurons tend to be generated in the ventral forebrain, and migrate long distances to their target location.[14,15] Neurons orient themselves in well-organised layers, in an inside-out manner, with the earlier-born neurons forming the so-called preplate at the deepest layer, finally forming 6 cortical layers in the adult neocortex.[15]

1.1.2. 2D to 3D *in vitro* brain models: a historical overview

The first *in vitro* neural culture system was established over a century ago in 1907. In seminal research considered to be the beginning of the neural tissue engineering era, Ross Harrison generated grafts from frog embryo explants, and observed neurite outgrows of migrating neurons (**Figure 1.2**).[16] Decades later, intact cultures of CNS tissue were isolated from chick embryos and maintained in culture to study early neurodevelopmental events and the formation of retinal tissue *in vitro*.[17] These early studies provided the first insight that neural tissue could be isolated from the body and studied *in vitro* to investigate neural behaviour and mechanisms.

Decades later in the 1960's, cultures of brain slices, called "organotypic" cultures were developed as an important tool to maintain and observe cellular behaviour within an intact tissue, where the main structure of the tissue and cellular organization could be preserved. The first reported organotypic CNS cultures of brain slices were reported by Crain *et al.* (1966), who demonstrated neuronal differentiation and bioelectric properties during maturation of the brain slices (**Figure 1.2)**.[18] This technique has remained popular over the years, and cerebellum organotypic culture slices were used in the first detailed description of brain tissue.[19] Despite some limitations, such as difficult acquisition and handling, researchers continue to use this technique today.[20] Interestingly, several recent studies have reported using cerebral organoid slices to improve neuronal survival and axon outgrowth, demonstrating an adaptation to the classic organotypic slice culture.[21] This is further discussed in **section 1.4.2**.

Since Harrison's seminal work at the beginning of the 20th century, improvements in culture techniques and conditions facilitated the isolation and culture of primary nerve cell cultures, including hippocampal, cortical, cerebellar and midbrain neurons isolated from rat embryos.[22–24] Yet, culturing primary neuronal cells is limited by the finite number of passages of non-proliferative neuronal cells.[25] To overcome this limitation, researchers sought to establish immortalized neuronal cell lines, which have the advantage of being grown easily with minimal variability between cultures. The establishment of one such line, SH-SY5Y was derived from mouse neuroblastoma, and is still widely used today (**Figure 1.2**).[26,27] However, these cultures come with the caveat that they cannot be considered 'normal' neuronal cells, and as such do not accurately model some neurodevelopmental events, such as timed neurogenesis.

In 1989, Temple *et al.* isolated neural stem cells for the first time. Harvested from rat forebrains, these multipotent progenitors differentiated into neurons and glia in culture (**Figure 1.2**).[28] This prompted a surge in research investigating different neural stem cell (NSC) types, and their use in generating *in vitro* models to study basic neuroscience and therapeutic applications.[25] More recent studies have demonstrated limitations in using NSCs

for brain modelling, due to the inability of NSCs to mimic the entire range of neural lineages.[29,30]

The derivation of pluripotent embryonic stem cell (ESC) lines in 1998 heralded a breakthrough for *in vitro* brain modelling, by providing a source of cells capable of differentiating into cell types from all three germ layers, and recapitulate certain neurodevelopmental events (**Figure 1.2**).[31] Another breakthrough took place in 2007, with the discovery of reprogramming factors to covert somatic cells back to a pluripotent state (**Figure 1.2**).[32] This paved the way for induced pluripotent stem cells (iPSCs) to be derived from individuals with specific neurological diseases, to generate neuronal cells directly from the patient and giving an unprecedented opportunity to study patient-specific disease mechanisms. The development of iPSC technology also allowed researchers to circumvent the ethical issues associated with ESCs, which are derived from human embryos. In order to effectively use ES/iPSC technology for *in vitro* brain models, neuralization protocols were developed to enhance differentiation of pluripotent stem cells (PSCs) to neuronal cell types, by using small molecules to inhibit the differentiation of cells into non-neural fates (**Figure 1.2**).[33,34] However, brain development involves a highly complex series of signalling events. Understanding and replicating the same sequence of events to faithfully model neurodevelopment is still an ongoing challenge.

Whilst 2D neuronal cell cultures have contributed hugely to the field of neuroscience and development of neurological disease models, the lack of tissue complexity and cell-cell interactions limit the utility of 2D cultures. 3D culture methods have therefore been a major focus of research for *in vitro* brain modelling platforms, from bioengineered 3D tissue constructs to self-organised cerebral organoids, as further discussed in **section 1.3**.

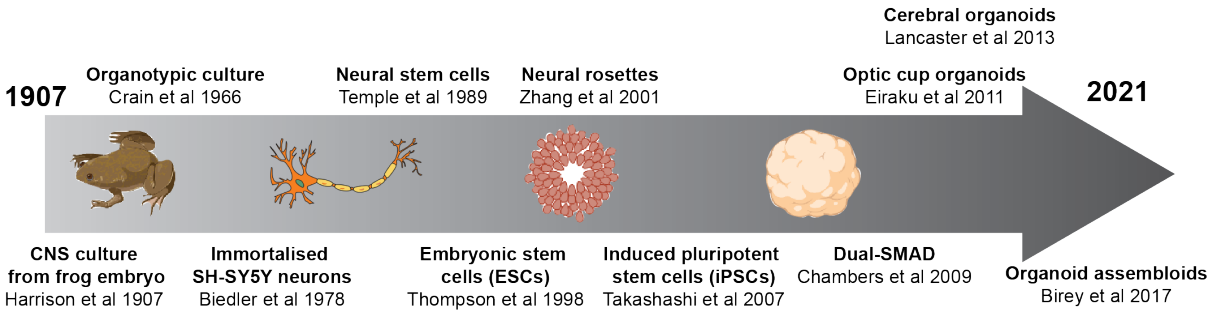


Figure 1.2 Timeline overview of CNS in vitro modelling. *The images were adapted from the Biorender website.*

1.1.3. Clinical need for *in vitro* brain models

Given the highly complex physiology of the human brain, there are a wide range of neurological disorders, which are often accompanied by complex etiologies. According to the U.S. National Library of Medicine, there are currently over 600 diseases known to affect the CNS, yet these are often diagnosed by clinical symptoms, with no clear definition or understanding of the underlying molecular mechanisms or pathology. Current estimates indicate that over 1 billion people are affected by neurological diseases worldwide, placing a significant impact on global health, and calling for new scientific paradigms to address this huge health burden.[35]

As the most complex organ in the human body, the brain is also the most inaccessible, with limited availability and ethical issues surrounding the use of human living tissue for scientific research. The current understanding of mammalian brain development has therefore been elucidated from the study of primates and other animal models. However, fundamental differences in brain development and function between animal models and humans limit the value of this information. This presents a difficult challenge for the study and treatment of neurological disease and has led to high attrition rates in drug trials and failures in targeted therapeutic interventions.[36–38]

Genomic studies including large cohorts of individuals with neurological diseases, such as neuropsychiatric and neurodevelopmental disorders have recently provided a wealth of

genomic information about these complex, idiosyncratic diseases.[39] However, there is still a need to link this data with tractable experimental models of the disease phenotype. The breakthrough in the establishment of ESCs followed by iPSCs provided an essential alternative for studying brain development and disease *in vitro*. In the last decade, there has been a tremendous effort to generate ESC or iPSC derived neurological disease models.[29]

Neuropsychiatric diseases represent a heterogenous subset of neurological diseases that are often characterised by complex genetics and variable symptoms, where diagnosis often relies on subjective, and primarily qualitative data.[40,41] As such, this area of research has seen a very low rate of new therapies in the last 40 years. An example of this is the psychiatric disease schizophrenia. This is characterised by a range of symptoms, such as disorganised thinking and speech, delusions, hallucinations, and catatonic behaviour. Many of these symptoms are impossible to study in animal models due to their uniquely human nature. Patient-derived iPSCs have provided a new approach to model disease mechanisms including those with as yet unidentified genetic defects. Schizophrenia was one of the first neuropsychiatric diseases modelled with patient derived iPSCs in 2D culture, demonstrating gene expression changes associated with key signalling pathways and synaptic transmission, leading to decreased connectivity, synapses and spine density.[42]

In the last decade, a transition from 2D to 3D *in vitro* models has provided a unique opportunity to mimic essential aspects of brain structure and function, and the development of stem cell derived 3D *in vitro* models is discussed in detail in the next **sections 1.2** and **1.3**. Cerebral organoids are 3D self-organizing cultures, displaying tissue architectures and functionalities similar to the developing human brain.[43] As such, they present a powerful *in vitro* model for neurodevelopmental disease. The first study to describe this protocol used patient specific iPSCs to model microcephaly, a disorder characterised by a markedly reduced brain size, which can lead to impaired cognitive development and facial distortions.[44] Genetic mutations in several genes were previously identified, yet previous studies show that mouse models were unable to recapitulate the symptoms seen in humans. The researchers found that cerebral organoid models of

microcephaly were smaller than wild type cerebral organoids, and identified premature neuronal differentiation in patient organoids, which may explain the disease phenotype.[45]

Advancements in genetic engineering techniques have further enhanced the possibilities for *in vitro* modelling with iPSCs. Transcription activator-like effector nucleases (TALENs) and clustered regularly interspaced short palindromic repeats (CRISPR)-Cas9 allow for the possibility to edit living cells by introducing targeted mutations, allowing for more accurate functional analyses of the disease phenotype. Recent studies have combined 3D *in vitro* cerebral organoid models with genome editing techniques to model brain tumor formation, one of the most lethal cancers with limited treatment possibilities. Brain tumorigenesis was modelled by incorporating oncogenic mutations using a combination of CRISPR-Cas9 and transposon mediated mutagenesis.[46] By screening relevant mutations previously identified, the researchers identified combinations of mutations resulting in glioblastoma-like and CNS primitive neuroectodermal-like tumours. The recent emergence of iPSC-based 3D *in vitro* models and genome editing technologies such as CRISPR-Cas9 hold considerable promise for other neurological disease candidates in the future, such as Parkinson's disease, Huntington's disease, Alzheimer's disease and autism spectrum disorder.

1.2. Towards 3D stem cell self-organisation and organoid formation

1.2.1. Self-organisation and symmetry breaking

A central question in developmental and stem cell biology concerns how complex forms are derived from a single cell. During morphogenesis, cells undergo an elaborate developmental choreography, establishing a spatial structure that determines the body axes of the developing organism. The first step to establish this is symmetry breaking, a process in which uniformity is broken and a polarity is established, allowing for spatial reorganisation of the embryo. This process occurs in the absence of any external control and is therefore called self-organisation. Whilst embryonic development is a primary example of self-organisation, this also occurs in other stages of development. For example, in differentiated cellular populations such as tissue patterning of epithelial structures.[47]

The phenomenon of symmetry breaking during embryonic growth has been extensively studied in different model organisms. In *C. elegans*, frogs and sea urchins, pre-patterning events occur at the single cell stage, such that the symmetry is broken before patterning begins. In mammalian embryos, the point at which symmetry breaking and self-organisation first occurs is more complex and still debated.[48,49] There are several different viewpoints in this ongoing argument. The first, long-held view argues that the early embryo is homogenous, and cell specification therefore emerges randomly. The second viewpoint posits that the early embryo is not perfectly homogenous, and that subtle differences result in specified localization of signalling molecules that drive embryonic growth in a non-random way.[48]

To navigate these complex questions, it is possible to look back at the first mathematical model of self-organised pattern formation by Alan Turing in his seminal work describing reaction-diffusion models. In Turing's model, cells interact through diffusing chemicals, and starting from a homogenous, uniform state, a stable pattern can emerge from the

interaction of two diffusing chemicals.[50] This early model of pattern formation has been highly influential in our current understanding of symmetry breaking in embryonic development. Since this seminal work, it has been shown that diffusion is not the only mechanism for cell communication, and other elements including mechanical forces and gene expression play an important role.[47] In Magdalena Zernicka-Goetz's recent publication, the authors bring together new insights to propose an updated model, whereby intracellular reactions lead to 'micro-scale inhomogeneity'.[48] This model combines elements from both viewpoints previously discussed, as the authors propose that these subtle cues in early development are gradually amplified to drive pattern formation. There are still many questions that remain, and further elucidation of these dynamics will continue to push the boundaries in our current understanding of self-organisation in early development.

1.2.2. Stem cell based lumenogenesis

Recently, it has been shown that stem cells cultured *in vitro* also show capacity for self-organisation, by spontaneously breaking their symmetry to undergo *in vivo*-like morphogenesis.[51–53] In 2016, two groups showed for the first time that human blastocysts, formed by *in vitro* fertilisation, show self-organisation properties in the absence of maternal tissues.[54,55] The authors demonstrated that the epiblast cells, which form the embryonic tissue, undergo major reorganisation by forming a polarised lumen. These landmark studies were essential to provide an accurate model to explore the cellular mechanisms of lumenogenesis and remodelling events in the human embryo. However, the availability of human embryos in research are limited, and beset by considerable legal and ethical constraints. To address these challenges, much emphasis has been placed on developing stem-cell-derived models to recapitulate some of these critical developmental steps. Recent studies have demonstrated that dissociated human pluripotent stem cells (hPSCs) show a capacity to self-organise and form polarised lumens, with hallmarks of early embryonic development (**Figure 1.3**). For example, Taniguchi *et al.* (2015) demonstrated that hPSCs form lumens after the first cell division, with an apical domain marked by EZRIN and aPKCzeta (**Figure 1.3c**).[52] In later studies, the same group demonstrated that these hPSC-derived 'cysts' can give rise to amniotic like epiblast cells, as well as post-implantation

apicosome structures, which drive lumen formation.[51,56] Furthermore, using hESCs derived models, Shahbazi *et al*. (2017) explored the mechanistic changes that occur during lumen formation, demonstrating the transitions required in stem cell pluripotency to coordinate lumenogenesis.[53]

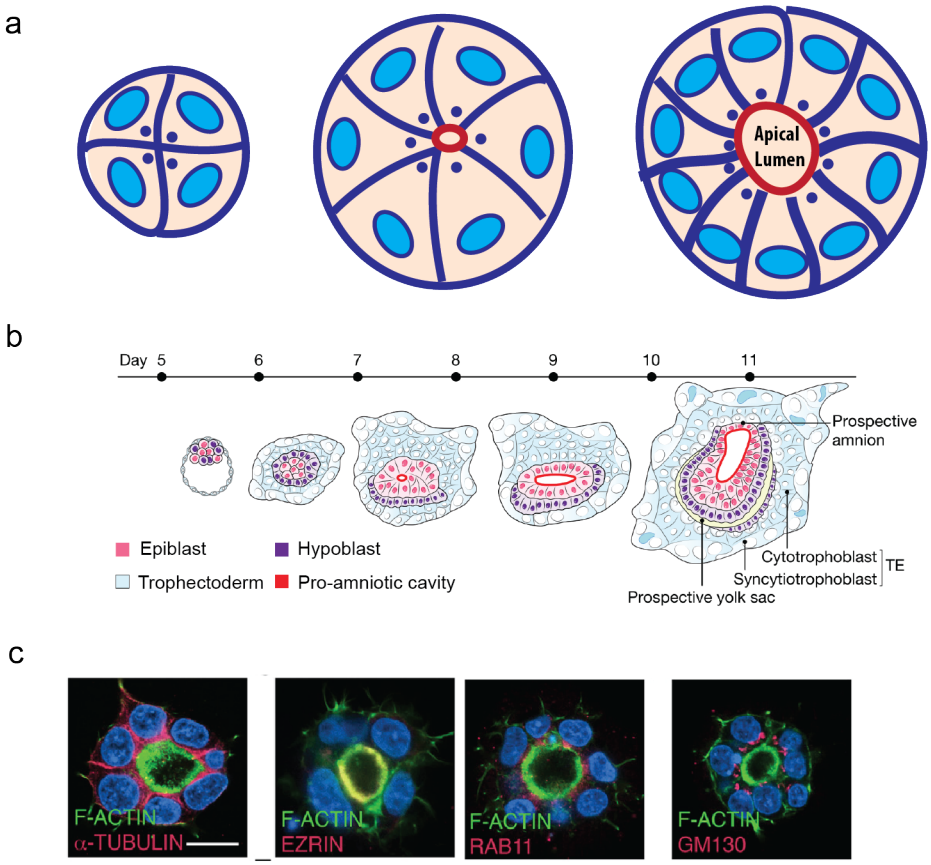


Figure 1.3 Stem cell self-organisation. *a) Schematic of de novo lumen formation. Cells self-organise, forming a central luminal cavity surrounded by pseudostratified cells oriented with an apical-basal polarity. b) Model of self-organizing epiblast cells during embryo implantation, showing the formation of a pro-amniotic cavity in the epiblast. Image adapted with permission from Springer Nature.*[55] *c) iPSCs show an intrinsic ability to self-organise and form lumens in vitro. Scale bar corresponds to 10 µm. Adapted with permission from ISSCR.*[52]

The unique property of self-organisation in stem cells has also facilitated the expansion of stem-cell derived models into 3D organoid models. By directing the stem cells towards a specific cell lineage, the cells and their progeny follow a developmental trajectory that mimics certain architectural and functional aspects of the real tissues and organs. For

example, in seminal work from Yoshiki Sasai's group, hPSCs under direction towards retinal tissue spontaneously formed optic cup like morphology and identity.[57] Since this pioneering work, researchers have harnessed this capacity of self-organisation to develop organoid systems for different organs, including brain,[45] intestine[58], liver,[59] lung,[60] and kidney[61]. Furthermore, 3D expansion of the stem-cell derived models of embryogenesis have been expanded into 3D embryoid models, that include extra-embryonic tissues,[62] and show spontaneous formation of an anteroposterior body axis.[63]

1.2.3. Mechanical forces direct stem cell behaviour

Mechanical forces of the microenvironment are known to play an important role in regulating molecular and cellular processes. In a process known as mechanotransduction, physical cues from the environment are transformed into a biochemical response, altering the intracellular biochemistry.[64–66] The shape and physical stability of the cell is governed by the cytoskeleton, which connects it to the physical microenvironment, bearing the mechanical stresses, and establishing a stabilizing force balance. This process has been likened to tensegrity, a term commonly used in engineering and architecture, where discontinuous compression elements are stabilized by a continuous force.[67] Mechanical forces can be generated across different biological scales, from intracellular actomyosin to forces resulting from muscle contraction.

Surface curvature is a fundamental concept in differential geometry and is used to describe the local geometry of a 3D object.[68] In a useful analogy described by Callens *et al*. (2020), the authors describe curvature in the context of a curved line, whereby curvature can be measured by how much the line diverges from a straight line at any point along that line.[68] Cells respond to surface curvature at the single cell level, for example by cell alignment and migration, and at the collective tissue level. A landmark study by Rumpler *et al.* (2008) showed that the local growth rate of bone tissue is strongly influenced by surface curvature (**Figure 1.4a**).[69] Subsequent studies using pre-osteoblasts consistently demonstrate that the curvature of a pre-defined scaffold affects the proliferation rate and shape of the growing tissue.[70,71] A recent study using human mesenchymal stem cells (hMSCs) demonstrated that

lower surface curvature on convex surfaces lead to nuclear deformation and osteogenic differentiation.[72] In our own group, it has previously been shown that the plasma membrane plays a central role in translating these biophysical changes to cell behaviour in hMSCs.[73]

There is currently limited literature on the role of surface curvature in the self-organisation of hPSCs. However, recent studies have demonstrated that geometric confinement can trigger self-organised patterning in hESCs. By confining hESC colonies in circular micropatterns, cells were able to generate the three germ layers in culture.[74] It has also been shown that the geometric confinement and subsequent exterior border edge of the colony caused specific and reproducible differentiation patterns.[74,75]

Geometric constraints have also been used to direct lumen growth, as 2D micropatterned surfaces were shown to guide lumen shape.[52] As lumen formation occurs in different stages of mammalian development, geometric control provides a powerful tool for different stem cell and organoid models. Using this approach in the formation of human neural tube models, Karzbrun *et al*. (2021) created PDMS molds to generate rectangular micropatterned surfaces for hPSC culture (**Figure 1.4b**).[76] In this way, 2D cell growth was tightly controlled, and the addition of Matrigel triggered a growth transition to create a 3D structure with a continuous elongated lumen, covered by an epithelial monolayer. This provided an experimental system to study neural tube closure, which is essential for the development of drugs targeting neural tube defects. Another mechanical model for neural tube formation was demonstrated by Fattah *et al*. (2021) where the authors showed that mechanical actuation increased growth and enhanced patterning, recapitulating important aspects of neural tube development (**Figure 1.4c**).[77] These recent studies highlight the importance of the external physical environment on morphogenesis, and how this can be harnessed with stem cell and organoid technology to generate more reproducible and programmable organ and tissue models.

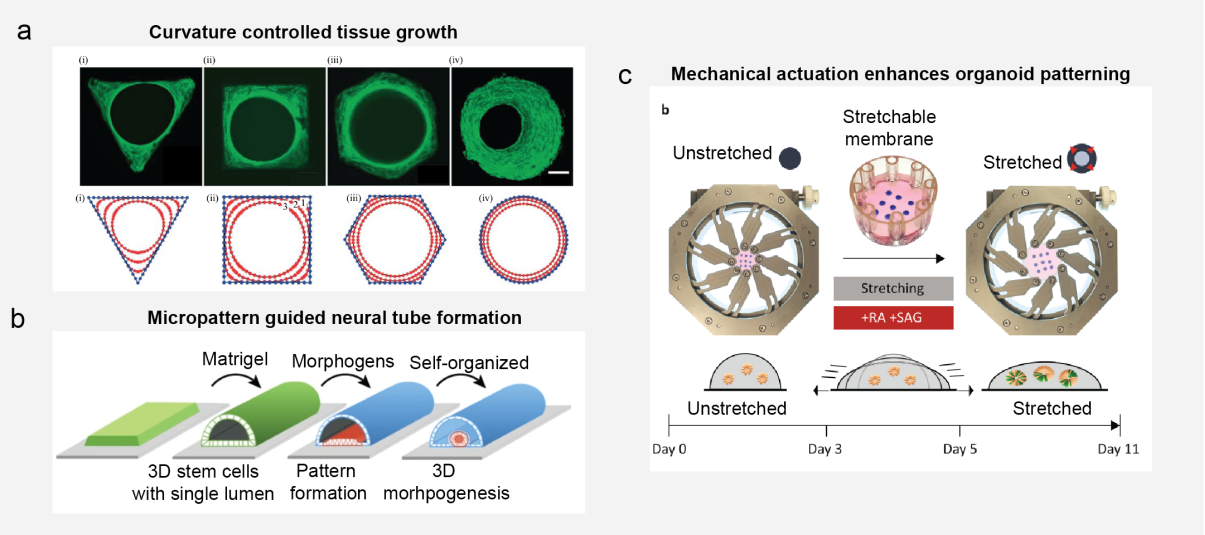


Figure 1.4 Mechanical and geometry guided stem cell growth. *a) Bone-like tissue growth on channels with different shapes and curvatures. Scale bar corresponds to 200 µm. Image adapted with permission from The Royal Society Publishing.*[69] *b) Substrate micropatterning guides stem cell self-organisation and morphogenesis, forming a neural tube like structure with a single elongated lumen. Image adapted with permission from Springer Nature.*[76] *c) Mechanical actuation enhances floor plate patterning in neural tube organoids. Image adapted with permission from Springer Nature.*[77]

1.3. Brain organoid models

1.3.1. Unguided 3D brain organoid models

Cerebral organoids were first demonstrated by the Knoblich group in 2014.[45] A key step in the development of this protocol arose from a seminal study from Hans Clevers group in 2009, where the authors demonstrated that embedding adult intestinal stem cells in a Matrigel matrix could generate self-organised aggregates that resembled the *in vitro* intestinal crypt and epithelium.[78] Using a similar approach, the Knoblich group embedded hPSC derived embryoid bodies (EBs) in a Matrigel matrix, to promote self-organization. Using a protocol adapted from Watanabe *et al.* (2005) EBs were cultured in serum free condition, in the absence of any inductive growth factors.[79] This combination of minimal external signalling factors coupled with Matrigel-embedding gave rise to the first protocol for cerebral organoid generation (**Figure 1.5**). Also known as 'whole-brain organoids', these

organoid structures develop a variety of different subregional identities in the brain, such as forebrain, midbrain, hindbrain, choroid plexus and retinal tissue.[45,80,81] The addition of Matrigel is an essential component for the development of neuroepithelial tissue, resulting in large, fluid filled lobes reminiscent of *in vivo* brain ventricles. It was also discovered that agitation of the organoids in free floating media during later development (> 20 d) promoted the formation of larger tissues by enhancing oxygen and nutrient diffusion. This is typically facilitated by the use of orbital shakers, however, custom made spinning bioreactors have also been used for the same purpose, demonstrating improved efficiency in brain organoid generation.[82]

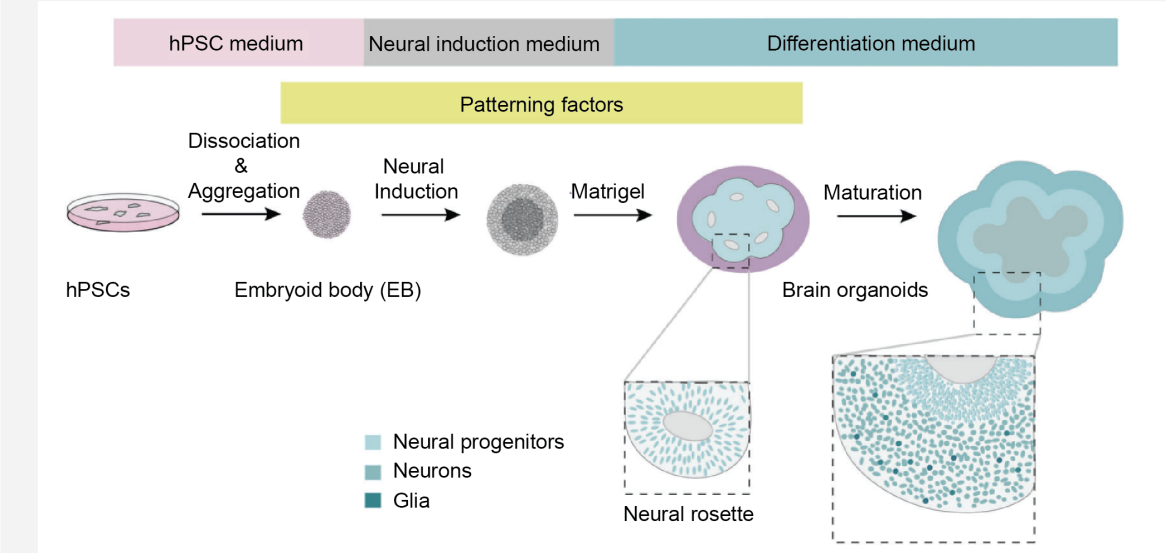


Figure 1.5 Human cerebral organoid generation. *hPSC colonies are dissociated and reaggregated to form embryoid bodies, typically in low attachment 96 well plates, with Rho kinase inhibitor. Transfer to a neural induction medium at d 5 promotes neuroectoderm formation and exposure to Matrigel induces the formation of VZ like lumens. The inset images show different neuronal populations in immature and mature organoids. Image adapted with permission from Springer Nature.*[83]

The self-organised development intrinsic to cerebral organoid growth drives tissue formation that recapitulates aspects of the early embryonic human brain in considerable detail. Within the ventricle like regions, progenitor zones that are highly reminiscent of the VZ and SVZ are present, as shown in **Figure 1.6.** At an even higher level of complexity, the

inner and outer layers of the SVZ (iSVZ and oSVZ), and the CP can also be identified.[45,81] Apical-basal polarity is also evident in the tissue, as neurons show localization to the basal surface. Single-cell transcriptomics also revealed a broad diversity of cells in cerebral organoids, including neural progenitors, excitatory and inhibitory neurons, astrocytes and oligodendrocyte precursor cells (OPCs).[84] As disease models, cerebral organoids have been useful to study phenotypes related to aberrant tissue architecture of the cortex. A recent study used cerebral organoids to model neuronal heterotopia, which is known to cause malformation of the human cortex, leading to serious disability.[85] The researchers demonstrated that cerebral organoids containing gene mutations associated with heterotopia resulted in changes in morphology and migration of neural progenitor cells loss of tissue organisation.

Whilst the generation of cerebral organoids represent a ground-breaking development for in vitro brain models, the lack of inductive signals or microenvironmental cues leads to uncontrolled growth and batch-to-batch differences in cerebral organoids. This presents challenges for high-throughput, systematic study of neurological development and disease.

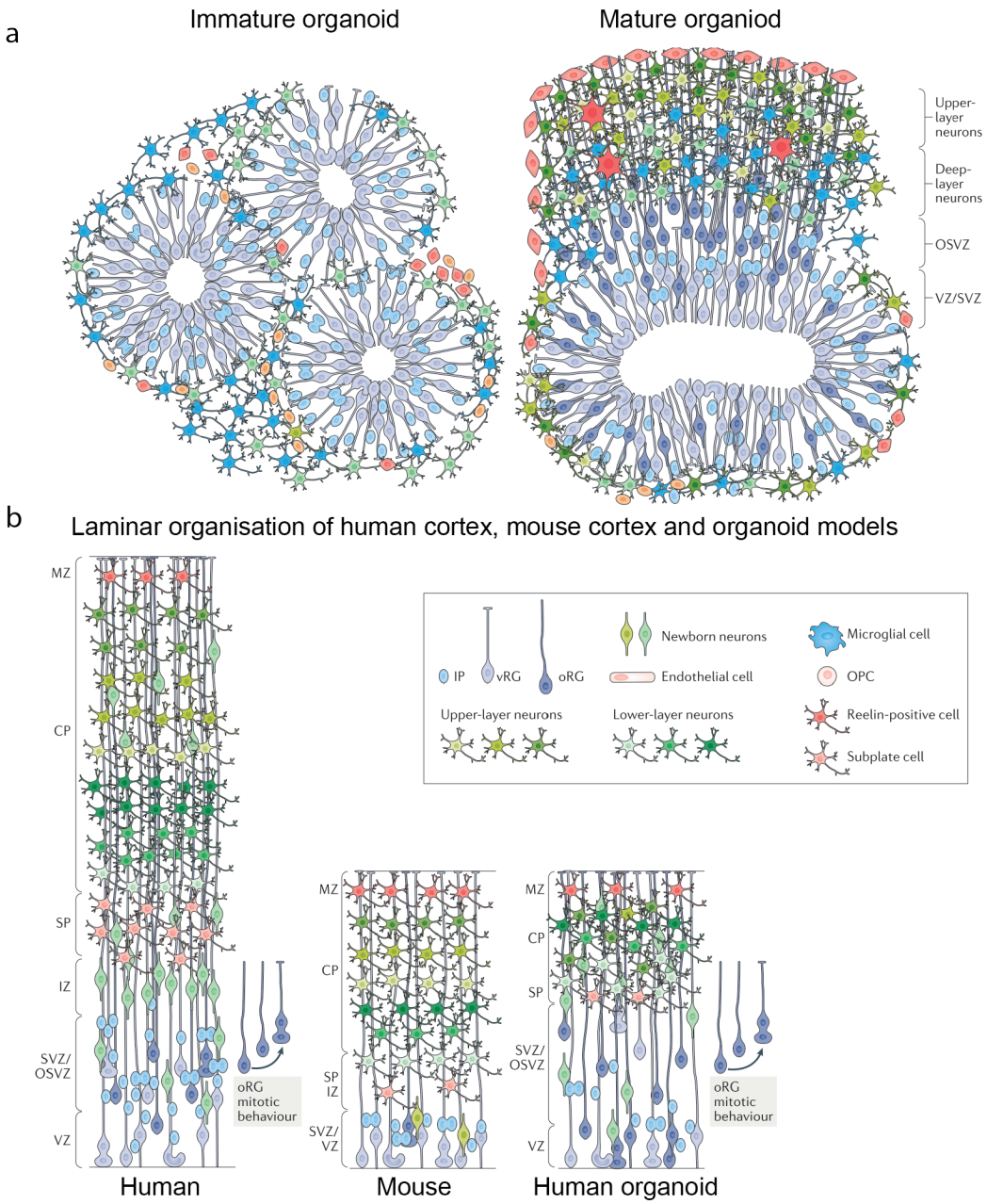


Figure 1.6 Human cerebral organoid organisation. *a) Organoid morphology and organisation in immature and mature cerebral organoids, showing polarised lumen regions with VZ-like characteristics. b) Laminar organization of the human cortex compared to the mouse cortex and organoid models. Image adapted with permission from from Springer, Nature.*[86]

1.3.2. Guided 3D brain organoid models

The use of small molecules and growth factors to direct stem cell differentiation to different multicellular brain regions was first pioneered by the Sasai group, before the first publication of cerebral organoid generation. In a method that has previously been described as: 'existing somewhere in-between 2D and 3D cultures'[29] stem cells were cultured in serum free conditions, with the addition of inductive growth factor signals.[87] This allowed the formation of specific brain regions such as retina,[57] cerebellum,[88] hippocampus[89] and forebrain.[90]

More recently, a similar approach has been applied to the cerebral organoid method, as small molecules and growth factors are used to direct organoid regionalisation and form tissues that are reminiscent of certain brain regions (**Figure 1.7**). Several different groups have designed such protocols based on knowledge from developmental neurobiology and pre-existing 2D differentiation protocols. These are typically based on the morphogen gradients involved in generating the antero-posterior (AP) and dorso-ventral (DV) axes of the developing neural tube. For example, along the AP axis, inhibition of TGF-β and BMP signalling (by the dual-SMAD approach developed by Chambers *et al.*) is known to anteriorize the tissue, forming neuroectoderm tissue.[34] Similarly, TGF-β and WNT inhibition promote anteriorization, resulting in forebrain brain region identity.[87,90] To induce a more posterior (caudal) identity, WNT activation, retinoic acid and insulin have been used to generate thalamic,[91] hypothalamic[82] and midbrain identities.[92] Patterning factors can also be used to induce different identities along the dorso-ventral gradient. Sonic hedgehog (Shh) is one of the primary morphogen gradients involved in the DV axis, forming ventral fates in higher Shh concentrations.[5] *In vivo,* Shh is secreted by the notochord, which acts as a signalling center, driving a ventral fate. Shh activation protocols have been used to derive ventral fates in the telecephalon (forebrain)[93,94] and midbrain.[92] In the opposing direction, a combination of WNT and BMP drive the formation of dorsal brain regions. This patterning regime has previously been used to form dorsomedial telencephalic tissue.[89] In the last 5 years, specific patterning protocols have been developed to generate midbrain,[92] hippocampal,[89] cerebellar,[88] spinal[95] and choroid plexus[96] organoids.

Region specific 'guided' brain organoids have been useful to study the impact of neurological disease on a specific region of the brain. For example, Parkinson's disease (PD) has been modelled in midbrain organoids. PD is the most common neurological disease, and manifests in movement abnormalities such as shaking and tremors, that worsen over time. PD is characterised by the loss of dopaminergic neurons in the substantia nigra, located in the midbrain.[97] Two recent studies generated patient derived hiPSC midbrain organoids to recapitulate the pathological hallmarks associated with the disease.[98,99] These proof of principle studies showed that region specific brain organoids can be used to study PD pathogenesis, as well as patient specific drug screening. In another recent study, choroid plexus specific organoids were generated to demonstrate response to SARS-CoV-2 infection, which is known to cause neurological complications in some cases.[100] Viral expression was found in mature choroid plexus cells in the organoids, which was further shown to cause leakage across the epithelial barrier that normally prevents entry of circulating pathogens into the cerebrospinal fluid and brain.

These examples demonstrate the utility of guided brain organoids, for disease modelling and drug screening purposes. However, this approach limits the investigation of unknown disease phenotypes in other regions of the brain, and interregional interactions. To address this limitation and develop organoids that more accurately recapitulate interacting brain regions, organoid fusion technologies have been developed. This will be further explored in **section 1.4.1**.

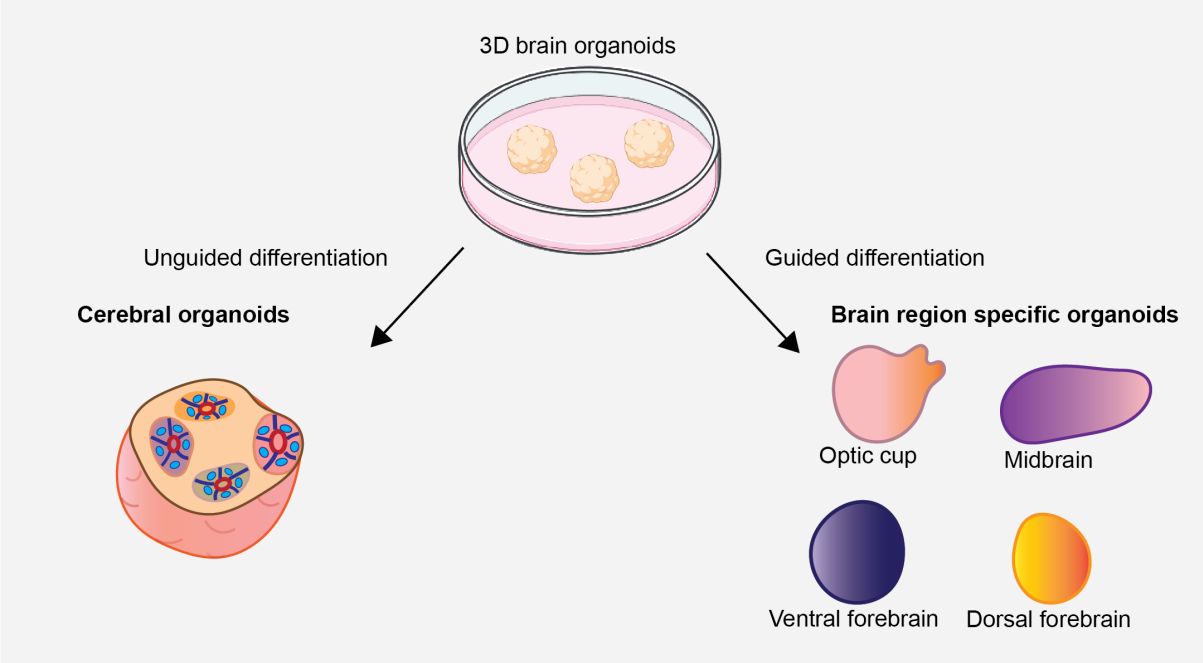


Figure 1.7 Guided and unguided differentiation of brain organoids. *Unguided differentiation harnesses intrinsic self-organisation, forming cerebral organoids that contain heterogenous tissues resembling different brain regions. Guided differentiation uses small molecules and growth factors to generate brain organoids with a specific regional identity.*

1.4. Enhancing brain organoid complexity

Organoids offer a promising platform for studying neurological disease and development. However, critical limitations remain, including lack of regional organisation, maturation, and vascularisation. In recent years, bioengineering has been used to address some of these challenges. Here, the key approaches are described.

1.4.1. Engineering interregional brain organoid interactions

The formation of pre-patterned organoids provided researchers with the building blocks to engineer organoid assembloids. In 2017, three major studies established the organoid assembloid technology, demonstrating that by co-culturing pre-patterned young organoids, and embedding them together in a single drop of Matrigel the organoids fuse together and exhibit cell interactions.[93,94,101] This new paradigm opened up the possibility to study

complex circuity and neuronal migration between different brain regions. Birey *et al*. (2017) reported the first example of modelling interneuron migration using organoid assembloids.[93] The authors pre-patterned the ventral organoids using Wnt inhibitor (for forebrain specification) and a Shh agonist (for ventral specification). Immunostaining and single-cell RNA sequencing (scRNA-seq) revealed that these organoids contained ventral progenitor cells and functionally active inhibitory GABAergic interneurons, demonstrated by patch clamping. Dorsal organoids were generated using a previously reported cortical spheroid (hCS) protocol, that contained cortical excitatory glutamatergic neurons and astrocytes, which typically originate in dorsal forebrain regions. After organoid fusion, GABAergic interneurons from the ventral domain were found to cross the fusion boundary into the dorsal organoid region, eventually forming synapses with the hCS glutamatergic neurons. Furthermore, these organoid assembloids were used as a patient specific disease model of Timothy syndrome, a multi-syndrome disorder that affects the nervous system. Together with a more recent study from the same group, the authors demonstrated aberrant interneuron migration in the disease organoid assembloids, providing insights into the molecular basis of the disease.[93,102]

The functional integration of regionally defined organoids has recently been expanded to combine other pre-patterned organoids, such as the striatum and midbrain.[103,104] The Pasca group first reported the generation of cortical and striatal organoid fusions, to facilitate the study of the cortico-striatal pathway, which is implicated in neuropsychiatric disease (**Figure 1.8a**).[103] Synaptic connections were formed between the organoid regions, as cortical neurons were shown to project axons into the striatal tissue. Furthermore, using fusions derived from patient specific cells with a neurodevelopmental disorder, the authors reported disease specific defects in calcium activity.

The modular assembly and fusion of regionally specific organoids has been further expanded to include three organoid parts. These have been used to study multi-synaptic circuits from the cerebral cortex, through to the hindbrain and spinal cord (**Figure 1.8a**).[105] In a landmark study, Anderson *et al*. (2020) generated 3D cortico-motor assembloids, comprising of hiPSC derived cortical, spinal, and skeletal muscle spheroids with the goal to

model cortical control of muscle contraction *in vitro.*[106] In this three-part assembloid, the authors demonstrated synaptic connection between the cortical and spinal regions by the presence of corticofugal neuron projections, and motor neuron connection between spinal and skeletal muscle regions. Furthermore, stimulation of cortical neurons was shown to trigger contraction of 3D muscle.

During fusion, organoids are randomly oriented. To improve the control of organoid fusion and dictate the orientation of certain organoid structures (e.g. neuroepithelial buds), Ao e*t al*. (2021) developed an acoustofluidic technique, using acoustic assembly to dexterously rotate and fuse the organoids with a high level of control.[104] In a proof-of-concept-model, the authors used this technique to fuse human forebrain and midbrain organoids, aligning the neuroepithelial buds. Post-assembly, midbrain dopaminergic neurons were shown to project from midbrain-to-forebrain, similar to the mesocortical circuit *in vivo*, demonstrating organoid fusion and functionality. This technique may be especially useful in three-part assembloid organoid models in the future.

Despite these exciting advances in brain organoid technology, this modular assembly approach does not recapitulate neural morphogenesis, in which complex morphogen gradients establish the brain axes from a single structure. Fusion or assembloid organoids therefore do not necessarily recapitulate the full complexity of interregional interactions. As previously described, a number of key signalling pathways direct cell fate during early embryogenesis, including Shh, Wnt, TGFβ, and FGF. Another approach to direct regional topography in brain organoids was recently described by Cederquist *et al.* (2017), where the authors supplied a cell cluster that expressed Shh, to act as a signalling centre within the organoid (**Figure 1.8b**).[107] Using a TALEN-mediated genetic engineering approach, hPSCs were programmed to express Shh under the control of the antibiotic, doxycycline. These cells were then embedded at one end of a cortical spheroid, thereby mimicking a signalling centre. The authors demonstrated that this triggered a Shh protein gradient, facilitating the formation of a dorso-ventral positional axis. In the future, genetic engineering approaches may be used to generate other developmental axes, such as the anteroposterior (AP) axis. It is also plausible that multiple signalling cell-clusters could be integrated into growing brain

organoids to more closely mimic the complexity of signalling and morphogen gradients in the early developing brain.

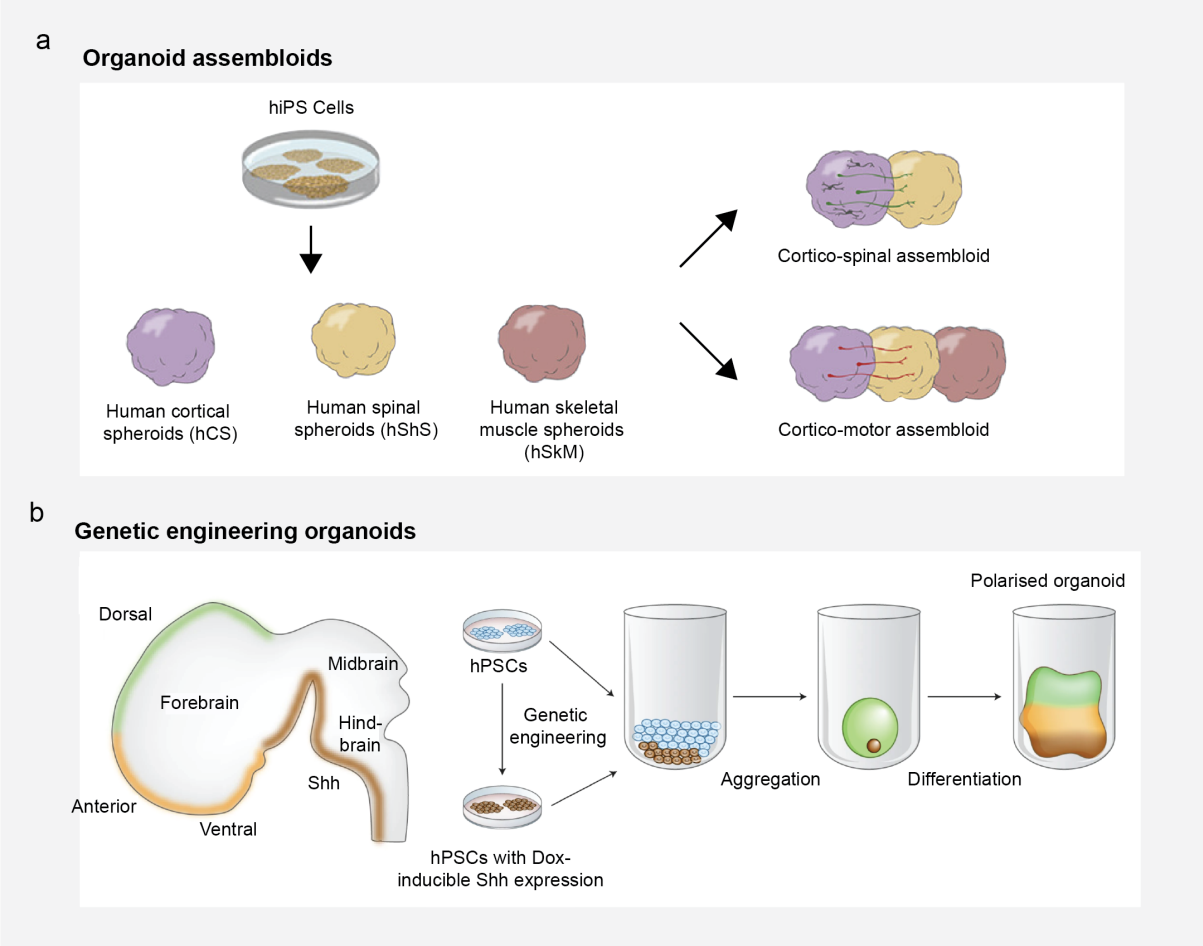


Figure 1.8 Engineering interregional brain interactions in brain organoids. *a) Organoid assembloids are formed by generating brain region specific organoids and fusing organoids in a drop of Matrigel at a specified timepoint. Assembloids containing two brain regions have been generated to model dorso-ventral and cortico-spinal interactions, and assembloids containing three brain regions have been generated to model the cortico-motor network. Image adapted with permission from Springer Nature.*[106] *b) Human brain organoids show dorso-ventral polarisation by genetically engineering cells to conditionally express the signalling molecule Sonic hedgehog (Shh), generating a signalling centre within the growing organoid. Image adapted with permission from Springer Nature.*[108]

1.4.2. Brain organoid maturation

Brain organoid maturation is hindered by limited oxygen, nutrient availability, and waste exchange, due to a lack of blood supply.[109] Blood vessels also act as a microenvironment for neural stem cells (NSCs), maintaining a role in neurogenesis, differentiation, and homeostasis.[110] A lack of blood supply in brain organoids typically induces hypoxia, leading to large areas of necrosis inside the organoid core, hindering neuronal development and migration.[109,111] As such, methods to improve organoid maturation capabilities represents a major current area of study.

In an effort to improve nutrient and oxygen accessibility to the organoid, Lancaster *et al.* (2019) adapted the traditional organotypic slice culture method, and applied this to brain organoids, using a modified slice culture technique.[21] Mature organoids (>55 d) were embedded in agarose and sliced into thick (300 µm) sections, before being placed back in culture medium. These sliced air-liquid interface cerebral organoids (termed ALI-COs) showed improved morphology, and a decrease in necrosis. The authors demonstrated that astrocytes in the ALI-CO cultures showed a healthier morphology compared to conventional whole organoids, that accumulated reactive astrocytes along the organoid surface. ScRNA-seq also revealed a full repertoire of cortical neuronal cell types. Additionally, these slice cultures showed functional neuronal networks, and dynamic axon outgrowth as demonstrated by live imaging studies. Despite the improved maturation capability demonstrated in this study, this was performed using cerebral organoids, that develop in a random and heterogenous way. In the future, the combination of ALI-COs together with regionally defined organoid assembloids may offer a more advanced platform for disease modelling applications.

Other recent studies have addressed the challenges associated with long-term maturation by organoid transplantation. Mansour *et al.* (2018) developed an engraftment model to integrate brain organoids inside a mouse brain.[112] The authors showed that by providing the organoids with a physiological brain tissue environment, the organoids exhibited differentiation of neuronal and glial cells, as well as integration of microglial immune cells from the mouse brain. Furthermore, a microvasculature was formed inside the organoid,

and optogenetics suggested organoid-to-host synaptic connectivity. In another recent study, Cakir *et al.* (2019) formed organoids by mixing hESCs with genetically engineered hESCs that express human ETV2, a reprogramming factor that induces endothelial fates.[113] The resulting organoids were shown to form a vascular like network, and several features of the blood-brain-barrier (BBB), such as increased expression of tight junctions and nutrient transporters. Implantation in a mouse model further supported the formation of functional perfused blood vessels *in vivo*. In another study, co-culture of cortical brain organoids with human umbilical vein endothelial cells (HUVECs) showed typical cortical organoid development with a full repertoire of neuronal cell types, and critically, a vascular structure that was maintained for over 200 d.[114] These latest studies demonstrate that co-culturing techniques may contribute to enhancing the complexity of brain organoid models in the future.

1.4.3. Microfluidics and Organ-on-a-chip

Organ-on-chip (OoC) systems represent a growing trend towards a new technology comprising of miniaturized biological units, integrated by microfluidics.[115–117] These systems offer the advantage of precise control, including analysis of electrical, biochemical, and metabolic processes, as well as high-resolution imaging in real-time. OoC models have already been developed for lung, liver, kidney, intestine, heart, fat, bone marrow, skin and the brain, as well as recently reported human body-on-a-chip microsystems, which cultivate multiple biological units from different organ systems around the human body.[116,117]

In recent years there has been significant momentum to develop microfluidic brain-on-chip (BoC) models as a high-throughput drug screening platform for neurological disease.[118,119] The blood-brain barrier (BBB) is a physiological barrier of endothelial cells around the capillaries of the brain, which acts as a semipermeable border, regulating influx and efflux of nutrients and waste. It is highly selective, preventing the influx of pathogens and neurotoxins. Whilst providing protection for central nervous system (CNS) homeostasis, this also creates an obstacle for drug delivery. BoC models have been developed to address this issue of transport, by employing porous membranes between microchannels to mimic the

BBB structure.[120] However, BoC systems typically host 2D cell culture, and are unable to generate the same biological tissue complexity generated in brain organoid models.[119,121] In an emerging field, BoC and brain organoids have been combined to create a new 'organoid-on-chip' model.[122,123] In one recent study, a microfluidic device was used to culture and periodically perfuse brain organoids, which was found to improve tissue maturation.[124] This was mainly attributed to the enhanced supply of nutrient and removal of waste during culture. Brain organoid-on-chip models have also shown excellent potential to probe the effect of toxic environmental exposure on neurodevelopment. Wang *et al.* (2018) exposed brain organoids to nicotine in a microfluidic chip system, to model prenatal nicotine exposure in a controlled setting.[123] Cortical development and regionalization were impaired, suggesting that nicotine exposure disrupts neurogenesis in early embryonic brain development. Another recent study combined an on-chip microfluidic platform with the recently reported air-liquid interface method (as previously described in **section 1.4.2**) to reduce organoid hypoxia.[125] To simplify the organoid culture procedure, the authors developed a 'one-stop assembly and culture platform' to integrate the organoid culture workflow and avoid moving organoids from one culture dish to another during different stages of growth. Using this platform, the authors exposed the brain organoids to cannabis, to model prenatal cannabis exposure. Under exposure, the organoids showed reduced neuronal maturation impaired neurite outgrowth, and disrupted electrical activity in mature organoids. These studies demonstrate the advantage of brain organoid-on-chip models to provide insights into environmental exposure on neurodevelopment. It is anticipated that this will be applied more broadly in the future, particularly in the context of pharmacologic screening.

Microfluidic systems have also been used to establish gradients of signalling molecules in a cell culture chamber. This is accomplished by diffusive mixing of fluid flow streams, which is controlled by a network of microchannels. In a recent study, Rifes *et al.* (2020) used a microfluidic based gradient generator to expose a 2D monolayer of hiPSCs to an orthogonal WNT-activating gradient (**Figure 1.9a**).[126] After 25 h, the cells exhibited antero-posterior organisation, recapitulating characteristics of neural axis specification in the developing neural tube. A similar approach was also used to generate a dorso-ventral gradient in hESC

2D culture, using overlapping opposing gradients of Shh and BMP4 agonists (**Figure 1.9b**).[127] Despite these advances, there is still limited research on the application of microfluidic based approaches to generate morphogen gradients for brain organoids. In the future, combining the high level of precision and control offered by a microfluidic platform with brain organoids could offer significant advantages for *in vitro* brain modelling.

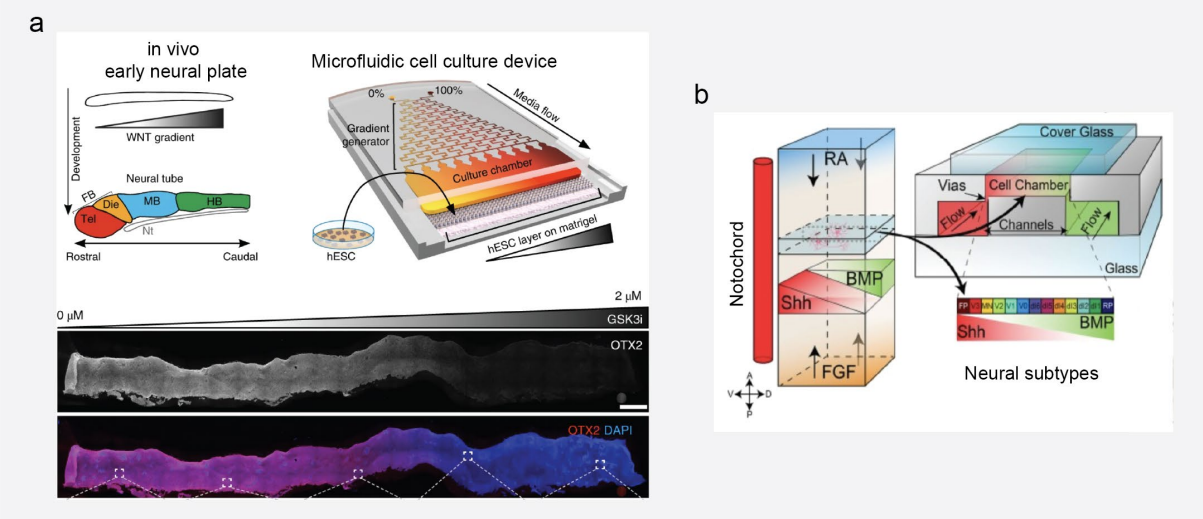


Figure 1.9 Microfluidic systems for generating morphogen gradients. *a) Microfluidic platform exposes 2D culture of hESCs to a WNT-activating gradient and differentiated cells show hallmarks of antero-posterior polarization in a neural tube-like model. Scale bar corresponds to 1 mm. Figure adapted with permission from Springer Nature.*[126] *b) Multiple morphogen gradients in opposing directions are established in a microfluidic chamber for the culture of 2D hESCs to mimic neural tube morphogenesis. Figure adapted with permission from The Company of Biologists.*[127]

1.4.4. Designing scaffolds for brain organoids

Hydrogel matrices

Natural and synthetic hydrogel matrices have been used *in vitro* for 3D neural cultures, because of their ability to mimic the native extracellular matrix (ECM).[128,129] Decellularized animal ECM matrices such as Matrigel offer an abundance of natural protein components that provide important biochemical cues and structural support for cell function (**Table 1**).[130] Matrigel has also been a pivotal component in the development of cerebral organoid

culture, as discussed in **section 1.3.1**. Yet, whilst providing a complex biological environment for cells to grow, Matrigel has a highly heterogenous protein composition and does not offer any direct control over specific protein type or concentration (**Table 1**).[131] This can limit the morphogenetic process, which is governed by spatiotemporal regulation of proteins and other signalling molecules. Batch-to-batch variation can also lead to variability in experimental results. The design toolkit for cell-compatible hydrogel matrices has considerably expanded in the last decade, owing to developments in synthetic ECM matrices, and novel approaches to chemically functionalise and tune biomaterial properties.[132]

Individual components of the ECM, such as collagen, laminin and glycosaminoglycans offer the advantage of being inherently biocompatible and have been successfully used as 3D matrices for *in vitro* neural culture, facilitating the differentiation of stem cells and maturation of functional neuronal networks (**Table 1**).[133–135] However, these often lack the complexity required to facilitate the growth of complex neural tissue constructs. Synthetic matrices can be designed to mimic the ECM and can be engineered with specified stiffness and chemical functionality, offering more control than natural ECM hydrogels (**Table 1**).[136,137] Lutolf *et al.* (2003) pioneered a series of degradable hydrogels, formed via Michael-type addition reactions between multi-arm poly (ethylene glycol) (PEG) macromers and cysteine-containing peptides.[138] These cell-compatible hydrogels could be used to immobilize biomolecules and key ECM components in a controlled way. Using this approach, Ranga *et al*. (2016) generated a synthetic scaffold matrix to support 3D neuroepithelial cysts, differentiated from mouse ESCs to model neural tube morphogenesis *in vitro.*[139] Some studies have also reported use of synthetic or semi-synthetic matrices in intestinal[140] and pancreatic organoids.[141] As yet, these have had limited success in brain organoid cultures and further work is required towards creating an effective alternative to Matrigel. The minimum requirements are to provide the same structural support and biochemical cues as Matrigel, in a more controlled and tuneable way. Synthetically designed hydrogels may also provide the opportunity to deliver signalling molecules or provide biochemical gradients to organoids during development, directing cell differentiation and regional tissue organisation.

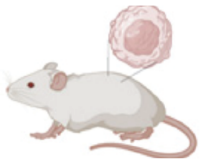
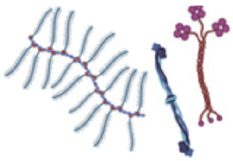
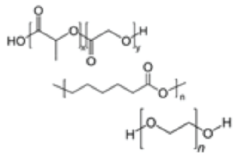
	 Matrigel	 Natural polymers	 dECM	 Synthetic polymers
Advantages	Built-in complex mixture of nutrients and proteins Readily available commercialized product Easy to handle	Inertness Low toxicity Biodegradability	Low toxicity Closely mimics native ECM High bioactivity Biodegradeability	Chemically defined Xenogeneic-free Tunable mechanical and degredation properties
Disadvantages	Not clinically applicaable Poorly defined Low mechanical strength Lot-to-lot variability Lacks tissue-specific ECM compositions	Low mechanical strength Lacks tissue-specific ECM compositions	Poorly defined Low mechanical strength Rapid degredation	Low bioactivity Low cell adhesion Lacks tissue-sepcific ECM compsitions Difficult and expensive synthesis procedure

Table 1 Advantages and disadvantages for different Extracellular Matrix (ECM) biomaterials for organoid engineering. *Table adapted with permission from International Journal of Stem Cells.*[142]

Scaffold biofabrication

Biofabrication techniques have been used to generate biomimetic fibrous scaffolds that mimic characteristics of the native ECM to guide tissue growth. individual PLGA microfilaments of variable size, termed 'floating scaffolds' have been used to guide cerebral organoid growth.[143] Introduced during the cell seeding step, the floating scaffolds provide a material interface for the cells to adhere. The authors found that this facilitated the

generation of elongated organoid structures that formed around the fibres, improving the consistency of neuroectoderm formation. In another recent study, Rothenbucher *et al.* (2021) generated well-defined polycaprolactone (PCL) scaffolds for brain organoid culture, using 3D-filament printing.[144] The scaffold was printed in a honeycomb pattern, which showed good mechanical properties and facilitated the adherence of hESCs, which eventually developed into a large flat organoid. Owing to the shift from a conventional spherical to flat organoid shape, the organoids showed a significant increase in size, as cells attached and grew around the entire scaffold structure. This change in organoid morphology was shown to increase the surface to volume ratio, minimizing necrosis in the organoid core. The authors highlighted that these scaffold guided organoids could enable spatial patterning in future work. This may also be enhanced by incorporation of signalling molecules into the scaffold by chemical functionalization, to synchronously provide biochemical and mechanical guidance. In addition, adapting the scaffold geometry to guide the organoid into a shape that is more morphologically reminiscent of the growing embryonic brain may provide further advantages for driving a more physiologically accurate tissue identity. Shape guided morphogenesis is further explored in the next **section 1.4.4.**

Electrical characterization

Monitoring electrical activity provides important insight into organoid development and functionality. Brain organoids have been shown to generate functional activity by showing spontaneous network activity and can generate action potentials and postsynaptic currents.[145] This is typically measured by calcium imaging, or 2D multi-electrode arrays (MEAs). For example, Fair *et al.* (2020) used 2D MEAs to investigate the maturation of cerebral organoids over a time span of 5 months, demonstrating a developmental trajectory based on changes in electrical synchronization.[146] Whilst MEAs are minimally invasive and can be used for long term measurement, they are rigid, planar structures that are restricted to only record neuronal activity located on the bottom surface of brain organoids.[145] To address this, 3D MEAs have been developed to improve the interface with 3D neural tissue and organoids. Park *et al.* (2021) used reverse engineering to generate a soft, flexible MEA structure, that could buckle into a shape matching cortical organoids.[147] This significantly enhanced the number of contacts for electrophysiological recording, covering much of the

organoid surface area. Despite this progress, long term stable recording of brain organoids with the capability to interrogate neurons inside the organoid core is still an unmet challenge. In a recent report, integration of nanoelectronics inside a cardiac organoid system was reported for the first time, forming so-called 'cyborg organoids'.[148] 3D mesenchymal stem cells (MSCs) were used to derive organoids around soft mesh like nanoelectronics, which were designed to mimic tissue like stiffness and flexibility. The cells migrated into the mesh, forming a 3D tissue structure intimately connected with the microelectrodes. This facilitated systematic recording and stimulation, allowing the authors to closely monitor functional activity across the entire volume of the organoid. Adapting a similar method for brain organoid application in the future will further enhance characterisation of development, maturation, and electrophysiological effects of pharmacologic stimulation.

1.4.5. Shape guided organoid morphogenesis

As previously discussed in the **section 1.2.3** external mechanical cues in the environment are known to influence cell behaviour and fate. Biomaterial scaffolds have been used to facilitate the spatial arrangement of cells in pre-defined geometries. A recent study by the Lutolf group demonstrated that guiding tissue geometry drives intestinal organoid patterning by localized cell differentiation.[149] By mimicking the morphology of the native intestinal epithelium, the organoids adopted more physiologically accurate tissue architecture and identity. In another study, the Lutolf group also used a 3D bioprinting approach, depositing stem cells directly onto permissive ECMs to facilitate self-organisation.[150] Using this methodology, cells, or cellular aggregates could be spatially arranged into constructs or shapes that corresponded to the intestinal epithelia. The ability to combine cells and matrices in defined shapes with high precision highlights a major advantage of 3D bioprinting. However, this technology is still in its infancy for organoid based applications, and several challenges have hindered its advancement in this area, including poor survival of dissociated hPSCs inside the bioprinter, a tendency to spontaneously aggregate in the printing nozzle, and sterility issues.[151]

Physically exerting force on the growing organoid has also been shown to influence organoid fate, affecting regional identity and patterning. As previously described, Fattah *et al.* (2021) developed an instrument with programmable actuated arms, to stretch brain organoids embedded in a crosslinked PEG hydrogel.[152] This mechanoregulated actuation was shown to enhance organoid size and facilitated a more reliable patterning outcome than unstretched controls. As tissue mechanics have been shown to drive rapid changes in cell behaviour in the developing embryonic brain, these results demonstrate that organoid mechanoregulation can similarly modulate organoid fate. Harnessing the effect of mechanical forces on organoid growth will further expand the toolkit available to direct and enhance organoid complexity in the future.

These studies highlight that some of the most complex challenges in the field of brain organoids can be addressed by bioengineering approaches. Whilst it is anticipated that this approach will continue to gain traction in the future, the advancement of brain organoids will also raise serious moral and ethical questions. This will be further discussed in the next **section 1.5**.

1.5. Moral and ethical considerations

The disembodied brain in a dish is a recurring trope in literature. In H. P. Lovecrafts 'The Whisperer in Darkness', a brain cylinder contains a living human brain, removed from its host and preserved in fluid where it can live indefinitely. A similar 'brain in a vat' scenario is well known in philosophy and used in a variety of thought experiments to discuss themes of perception and body reality.

This human fascination with the 'brain in a dish' and the burgeoning field of brain organoids has captivated the imagination of the public, fuelled by sensationalised headlines in the media like 'Brain organoids could spark a Planet of the Apes scenario, scientists warn' and 'Lab-made mini brains grow their own sets of eyes'. But how much of this is true? Are cerebral organoids able to think and feel? Or will they in the future? And if so, does brain organoid research pose a moral and ethical dilemma?

The answer is not straightforward. Currently, brain organoids can be described as aggregates of cells that can recapitulate certain aspects of embryonic brain development such as tissue structure, and some rudimentary circuity, but lack the anatomical structure and mature circuity for higher level sentience. Yet, the last 5 years have shown extraordinary advancements in organoid technology, and the convergence of stem cell biology and bioengineering offers the possibility to overcome major challenges and enhance the complexity of brain organoids in the future. Recent developments in the field have also raised serious questions. In 2019, Muotri's group published a paper reporting spontaneous network formation with complex oscillatory activity, resembling features of brain activity seen in human preterm infants.[153] These findings prompted ethicists and scientists to raise questions about the 'consciousness' of brain organoids, and whether this level of complexity could entitle organoids to some form of moral status in the future.

But this raises an even bigger question: what is consciousness? Physicians, ethicists, and researchers define consciousness in different ways, and for different purposes. For example, according to some theories, such as integrated information theory (IIT), consciousness can

be defined by the ability of a system to integrate information. Neuronal connectivity across the organoid may therefore be sufficient to attribute consciousness.[154] However, according to the standard medical test for consciousness, organoids would not pass as they are unable to respond to a painful stimulus. In a recent interview, Madeline Lancaster, the pioneer in cerebral organoid development suggested that as organoids do not have the same anatomical structure as human brain, it is unlikely that they can become conscious. "Without input and output, the neurons may be talking with each other, but that doesn't necessarily mean anything like human thought."[155] Gaining better anatomical resemblance to a human brain, however, may not be far off. As previously discussed, several recent studies have shown that brain region specific organoids can be fused together, forming 'assembloids' that provide more anatomically relevant organoid systems and form interregional connections and circuitry.

One point that scientists and ethicists unanimously agree so far, is that 'conscious' organoids have not yet been created. Yet, recent advancements in the field highlight that the closer scientists get to the goal of a more physiologically accurate brain model, the more ethical issues arise. In 2018, a group of 17 neuroscientists, biologists, ethicists, lawyers and philosophers wrote in the journal Nature to argue that it was time for guidelines to be established to deal with the advancement of brain organoid research, including issues around consent, establishing appropriate metrics (e.g. for the definition of consciousness in an organoid), data sharing, post-research handling, and the legal definition of death, to name a few.[156] Koplin *et al.* (2019) proposed a framework of research limits, as outlined in **Table 2**.

Equivalent stage of human *in vivo* brain development	**Research restrictions**
Non-conscious brain organoids (e.g., equivalent to fewer than 20 weeks' in vivo brain development)	Research should be regulated according to existing frameworks for stem cell and human biospecimen research

Conscious or potentially conscious brain organoids (e.g., equivalent to 20 weeks' *in vivo* brain development or more)	In addition to the above constraints, research should be subject to the following restrictions: 1. The expected benefits of the research must be sufficiently great to justify the moral costs, including potential harms to brain organoids. 2. Conscious brain organoids should be used only if the goals of the research cannot be met using non-sentient material. 3. The minimum possible number of brain organoids should be used, compatible with achieving the goals of the research. 4. Conscious brain organoids should not have greater potential for suffering than is necessary to achieve the goals of the research. 5. Conscious brain organoids must not experience greater harm than is necessary to achieve the goals of the research. 6. Brain organoids should not be made to experience severe long-term harm unless necessary to achieve some critically important purpose.
Brain organoids with the potential to develop advanced cognitive capacities (e.g., mature brain organoids capable of interacting with outside environment.)	In addition to the above constraints, research should be subject to the following restrictions: 1. Brain organoids should be screened for advanced cognitive capacities they could plausibly develop. In general, such assessments should err on the side of overestimating rather than under-estimating cognitive capacities. 2. Cognitive capacities should not be more sophisticated than is necessary to achieve the goals of the research. 3. Welfare needs associated with advanced cognitive capacities should be met unless failure to do so is necessary to achieve the goals of the research. 4. The expected benefits of the research must be sufficiently great to justify the expected or potential harms. This calculation should take into account the implications of advanced cognitive abilities for brain organoids' welfare and moral status.

Table 2 Proposed research limits on brain organoids. *Table reproduced with permission from Koplin et al. (2019).*[157]

Many would argue that preventing brain organoid research would, in itself, be unethical as neurological disease represents a huge global health problem, and brain organoids provide the only viable means to study the pathogenesis of uniquely human disease, such as schizophrenia, or autism. In these unchartered territories of research, the only certain thing is that attention to creating ethical frameworks is essential while brain organoid research remains in the early phases of development and does not yet pose a serious ethical and moral risk.

1.6. Scope of this thesis

In **Chapter 1,** fundamental concepts about brain organoid research have been introduced. Critically, the emergence of this field has provided a viable model for studying embryonic brain development, neurological disease pathogenesis and to perform drug screening. Yet, despite the rapid progress of brain organoid research in the last decade, this field still faces long-term challenges to overcome, such as lack of organoid reproducibility, lack of regional patterning, shape heterogeneity and the absence of a proper vasculature, as previously discussed. The collaboration between stem cell biology and bioengineering offers the possibility to address some of these issues, to gain more control of organoid morphogenesis by guiding stem cell growth and differentiation in a pre-determined way.

The aim of this thesis is to create a bioengineering platform to generate high-throughput, reproducible organoids and to enhance organoid complexity by using materials to direct regional patterning. To achieve this overall aim, three main research goals were established:

1. To establish a biomaterial scaffold platform to culture stem cells and guide self-organisation.
2. To generate controlled high-throughput brain organoid arrays using the scaffold platform.
3. To guide regional patterning in brain organoids using the scaffold platform.

This thesis is structured into 3 results chapters, corresponding to the research goals outlined above.

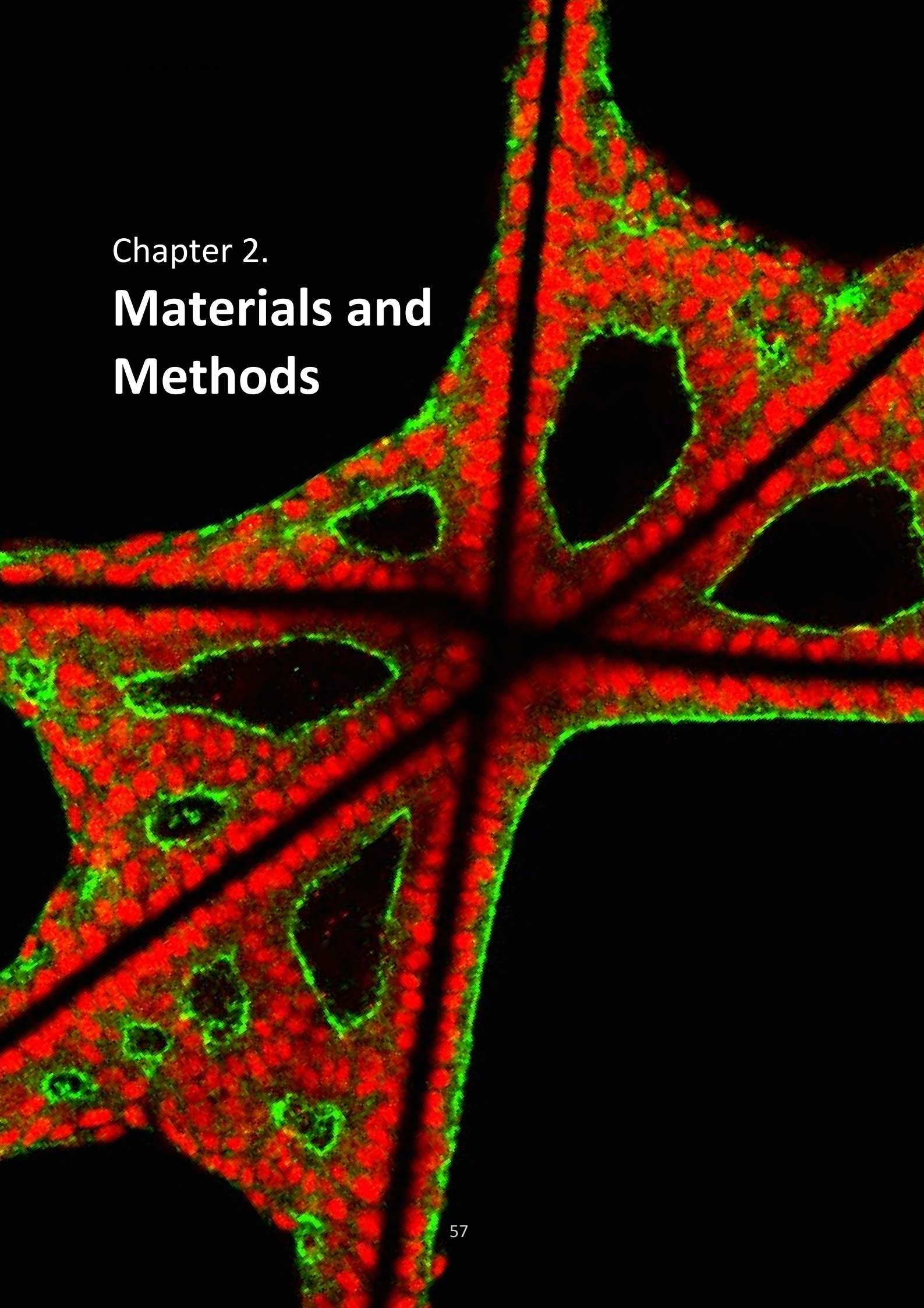
Chapter 3 investigates stem cell self-organisation on scaffolds. PCL macro-scale scaffolds are designed and fabricated using MEW, and a protocol is developed for uniform stem cell attachment and growth on the scaffolds. The effects of scaffold geometry on lumen formation and how this can be harnessed to reproducibly guide the shape and position of emerging lumens are investigated. Moreover, the use of computational models is explored to capture the tissue shape growth on the scaffolds. Finally, this scaffold system is used to generate an interconnected network of brain organoids.

Chapter 4 builds on work in the previous chapter to generate a high-throughput array of scaffold-cultured cerebral organoids, that can scale-up organoid generation, and reduce the labour- and time-intensive steps typically involved in conventional brain organoid culture. The previously established protocol in Chapter 3 is adapted to support the growth of individual (rather than interconnected) organoids, and varying scaffold geometry is explored as a way to support the growth of more mature organoids. Finally, new imaging modalities are investigated for advanced organoid characterisation.

Chapter 5 addresses the uncontrolled morphogenesis and unpredictable anatomies typically seen in conventionally cultured brain organoids. This chapter is subdivided into 3 sections. In part 1, a new scaffold geometry is designed to support the growth of elongated organoids, to facilitate the formation of an axes in the growing organoid. In part 2, scaffold functionalisation with growth factors is explored as a method to specify regional patterning in elongated organoids. Finally, in part 3, a microfluidic gradient generator is designed as an alternative method to establish a controlled morphogen gradient for scaffold-cultured elongated organoids.

Chapter 2.

Materials and Methods



2. Materials and Methods

Chapter specific Materials and Methods are described separately in the individual Chapter sections.

2.1. Melt electrospinning writing for scaffold fabrication

Pure PCL (M_w ~ 75 000 g mol^{-1}) was loaded into a 3cc polypropylene syringe (Nordson #7012074) and heated to 70°C for 30 min. A 23 G needle (Nordson #7018302) was installed, and the syringe was inserted into the spinneret. Scaffolds were printed using a 10 kV accelerating voltage, 10 mm collector distance, axis velocity of 1500 mm/min, feeding air pressure of 1.0 bar, and heating temperatures between 60 and 80°C. Printing was controlled by MACH 3 CNC software (ARTSOFT, Livermore Falls, USA), and dimensions were specified by G-code. Each scaffold consisted of 10 stacked layers. Scaffolds were detached from the collector plate using a drop of ethanol and moved to a petri-dish. For cell culture experiments, scaffolds were sterilized by cell culture-grade UV light irradiation for 30 - 45 min.

2.2. Cell culture

H9 hESCs were obtained from WiCell and maintained in feeder-free culture conditions with verified normal karyotype tested by STR analysis. Cells were cultured on hESC-qualified Matrigel (diluted in DMEM/F12 according to manufacturer's instructions) (Corning, cat. No 354277) coated 6-well culture plates with 2 mL mTESR1 (Stemcell Technologies) media, which was exchanged daily. Cells were passaged every 4 – 5 d at 60 - 70% confluency by EDTA treatment. Cells were maintained in a 5% CO_2 incubator at 37°C and were routinely tested for mycoplasma and confirmed negative.

2.3. Scaffold preparation for cell culture

PCL scaffolds were secured onto a sterile CellCrown holder (Scaffdex CellCrown, Tampere, Finland), followed by sterilization with UV light irradiation for 30 - 45 min. Scaffolds were then stored in a sterile 6-well plate until cell seeding. Immediately before cell seeding, scaffolds were rinsed once in PBS.

2.4. Cerebral organoid media formulations

Neural induction media

DMEM/F12 media (Gibco) is combined with 1% (v/v) N2 supplement, 1% (v/v) GlutaMAX Supplement (Invitrogen), 1% (v/v) MEM-NEAA (Invitrogen), 1% (v/v) Penicillin/Streptomycin, and 1 µg/ml heparin (Sigma, H3149). Sterile filtered before use.

Improved -A media

1:1 mixture of DMEM/F12 (Gibco) and Neurobasal medium (Gibco) containing 1% (v/v) B27 minus vitamin A, 1% (v/v) GlutaMAX supplement (Invitrogen) 0.5% (v/v) N2 supplement (Invitrogen), 0.025% (v/v) Insulin (Sigma, I9278), 1% (v/v) Penicillin/Streptomycin and 1 mg/ml Sodium bicarbonate (cell culture grade). Sterile filtered before use.

Improved +A media

1:1 mixture of DMEM/F12 (Gibco) and Neurobasal medium (Gibco) containing 1% (v/v) B27 plus vitamin A, 1% (v/v) GlutaMAX supplement (Invitrogen) 0.5% (v/v) N2 supplement (Invitrogen), 0.025% (v/v) Insulin (Sigma, I9278), 1% (v/v) Vitamin C solution (from a stock solution of 7mg/mL in DMEM/F12), 1% (v/v) Penicillin/Streptomycin and 1 mg/ml Sodium bicarbonate (cell culture grade). Sterile filtered before use.

2.5. Conventional cerebral organoid generation

At approximately 60% confluency, hESCs were dissociated from the well-plate by adding 1 mL accutase for 3 min at 37°C. The remaining adherent cells were sprayed off with 1 mL mTESR and cells were centrifuged at 200 g for 3 min. The cell pellet was resuspended in mTESR media and a 'Master mix' cell suspension was prepared in mTESR media with 50 µM ROCK inhibitor Y27632 (Selleckchem) and 1% (v/v) Antibiotic-Antimyocytic (ThermoFisher) to ensure a density of 9000 cells/well. 150 µl of the Master mix was pipetted into each well of a 96-well plate using a multichannel pipette. At d 3, media was exchanged with 150 µl mTESR (without Rock inhibitor or Antibiotic/Antimyocytic). At d 5, 7 and 9 media was replaced with a neural induction media (as described in **section 2.4**). When signs of optical clearing on the organoids borders were clearly present (typically d 10-13), organoids were

embedded in Matrigel (Corning, cat. No. 356235). This was done by cutting a piece of parafilm and pressing it down over a pipette holder to make well-like indentations. The parafilm was placed in a 6 cm dish and the cover was peeled off with a pair of forceps. The tip of a P200 was cut off at an acute angle, and the organoids were pipetted up from the 96-well plate and placed in the well-like indentation of the parafilm. Approximately 20 µl of Matrigel was added to each organoid, and a P10 pipette tip was used to move the organoid into the centre of the Matrigel droplet. The dish was then placed in the incubator at 37°C for 30 - 45 min. 10 mL of neural induction media was then added to the dish, flushing the Matrigel embedded organoids off the parafilm. The parafilm was then removed from the dish using forceps. 2 – 3 d after the first addition of Matrigel, media was changed to Improved -A media (as described in **section 2.4**)**.** For 3 d, 3 µM CHIR 99021 (Tocris) was also added. 4 d later, improved +A media was added (as described in **section 2.4**) and media was changed every 2 or 3 d. At d 20, organoids were placed on an orbital shaker, at speed 57 rpm.

2.6. Cryosectioning organoids

Organoids on scaffolds were fixed in 4% (v/v) PFA in PBS overnight at 4°C and washed three times in PBS. To cut samples from the scaffold, the Scaffold-CellCrown assembly was placed on a sterile PDMS cutting mat (with a thickness of approx. 5 mm) and scaffold organoid samples were cut and obtained using a 6 mm biopsy punch. The organoid samples were transferred to a 30% (w/v) sterile filtered sucrose solution in PBS in a 6-well plate, using forceps and left at 4°C overnight. The sucrose solution was removed, and scaffold organoids were equilibrated in OCT embedding matrix (Sakura, cat no. 4583) for 10 min. Using forceps, samples were transferred to a cryomold placed on dry ice, and filled with OCT embedding matrix. Embedded scaffold organoid blocks were then stored at -80°C until cryosectioning. 25 µm tissue slices were obtained using a cryostat (Cryostar NX70 Thermo Cryostat) at -12°C and collected on Superfrost Ultra Plus slides.

2.7. Immunostaining organoid sections

Organoid sections were washed in PBS, then permeabilised and blocked in 0.3% (v/v) Triton X-100 and 5% (w/v) BSA with 0.05% (v/v) sodium azide in PBS for 30 min at room temperature. Primary antibodies were added to the antibody solution (0.1% (v/v) Triton X-100, 5% (w/v) BSA and 0.05% (v/v) sodium azide in PBS) and left in a humidified staining box overnight at 4°C. Slides were rinsed three times in PBS then washed three times in PBS-T (0.01% (v/v) Triton X-100 in PBS), before staining with secondary antibody in the antibody staining solution at a dilution of 1:500 for 2 h in a dark humidified staining box at room temperature, followed by 10 min DAPI staining at 1:1000 dilution in antibody staining solution. Sections were washed twice in PBS-T for 15 min, then washed once in PBS for 15 min. Sections were then mounted with a coverglass using Fluorosave™ (Millipore).

2.8. Confocal imaging

Fluorescence images were acquired using an inverted Leica SP8 confocal microscope (Leica microsystems). Fluorophores were excited with a 405-nm diode laser (DAPI), a 488-nm argon laser (GFP), a 543-nm HeNe laser (Alexa Fluor-543/555) and a 633-nm HeNe laser (Alexa Fluor-633/647). Raw data was processed using open-source image analysis software Fiji ImageJ (version: 2.3.0).

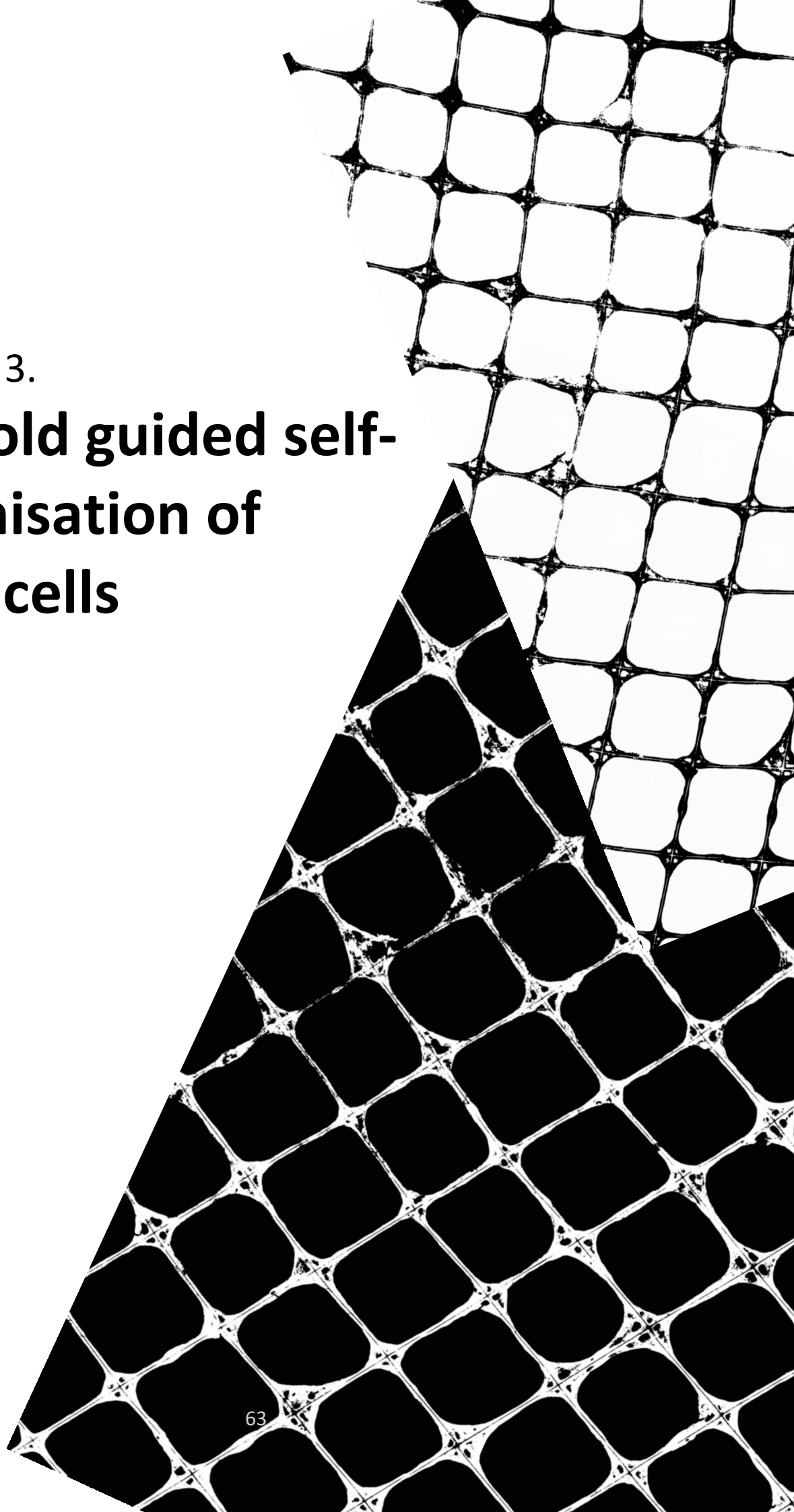
2.9. Optical Clearing organoid samples

For optical clearing, a previously published protocol was adapted.[158] Organoids were fixed in 4% (v/v) PFA in PBS overnight at 4°C and washed three times in PBS. Samples were obtained from the scaffold using a 6 mm biopsy punch, as previously described in **section 2.6**. Before clearing, organoids were immunostained. Organoids were permeabilised and blocked for 24 h at room temperature in a staining solution (PBS-TxDBN) that comprised 2% (v/v) Triton X-100, 20% (v/v) DMSO and 5% (w/v) BSA in PBS. The solution was sterile filtered before use. For staining, antibodies were added to PBS-TxDBN, and left at room temperature for 24 h on a shaker. The samples were washed three times in PBS-TxDBN over 24 h. Alexafluor secondary staining antibody was added to PBS-TxDBN at a dilution of 1:100 and added to the organoid section at room temperature, and left for 24 h. Organoids were

fixed for a second time with 4% (v/v) PFA overnight at 4°C. For clearing, organoids were dehydrated in a series of 30%, 50%, 70% and 100% (v/v) 1-propanol (Sigma Aldrich). The final dehydration was in anhydrous 1-propanol (Sigma Aldrich). The dehydration was performed at 4°C, for at least 4 h per dehydration step, in 3 mm glass bottom well (Ibidi). After dehydration, organoids were transferred to a new 3 mm glass bottom well (Ibidi) and covered with ethyl cinnamate (Sigma Aldrich) and incubated at RT for 1 h before imaging. For storage, samples were light protected, and kept at RT.

Chapter 3.

Scaffold guided self-organisation of stem cells



3. Scaffold guided self-organisation of stem cells

3.1. Introduction

Stem cells are inherently able to self-organise. Starting from fertilization, stem cells undergo a complex choreography of polarisation, symmetry breaking and axis formation, ultimately providing a blueprint for cells to adopt distinct fates during embryogenesis. Recently it has been shown that stem cells cultured *in vitro* also show a remarkable capacity for self-organisation, by spontaneously breaking their symmetry to undergo *in vivo*-like morphogenesis.[51,56,159]

An early emergent process of self-organisation during *in vivo* organogenesis is the formation of lumen: a hollow cavity formed by an asymmetric apical-basal polarisation of cells. A primary example of this is during the first stages of embryogenesis, as epiblasts in the blastocyst self-organise to form a radial alignment, surrounding a central lumen. In later development, lumen formation is the first step of organogenesis in multiple different organ and tissue types, such as intestinal, kidney, blood vessel and lung.[160,161] Recent *in vitro* studies have demonstrated that *ex vivo* pre-implantation blastocysts are able to self-organise as epiblast cells polarise and form a lumen, in a process that mimics post implantation morphogenesis.[54,55,162,163] Furthermore, dissociated hPSCs also show intrinsic self-organisation properties, forming polarised lumens when cultured in 3D culture as aggregates.[52] Yet, it remains a challenge to reproducibly engineer hPSC self-organisation and morphogenesis for more controlled growth of organotypic tissues.

The phenomenon of self-organisation in stem cells has enabled the development of 3D stem-cell-derived models of organ growth and development, termed organoids. Despite considerable success in generating organoids for different physiological systems, some major technical challenges remain. In particular, high variability in the self-organisation and growth of stem cells limits the experimental potential of organoid systems.[164] Furthermore, organoid culture is typically low-throughput, restricting the translatability of organoids.[164] These limitations highlight the currently unmet need for a high-throughput platform to

reproducibly culture and guide stem cells, that can be broadly applied to different organoid systems.

Bioengineering approaches offer an opportunity to create specific physical structures to guide 3D growth and influence the emerging luminal morphologies. In a process commonly known as mechanotransduction, cells convert physical cues in the extracellular environment into biochemical activity, eliciting a cellular response that contributes to the fate of individual cells, as well as the collective growth kinetics.[165,166] In line with this, previous studies have used micropatterning techniques to provide biophysical confinement that can modulate stem cell fate.[52,76] However, a major limitation of these techniques is that geometrical cues are typically constrained to 2D, i.e. as substrates at the bottom of the culture plate.[167] As organoids are highly dynamic 3D cultures, this limits the influence of their guidance.

For 3D tissue engineering, surface curvature, a mathematical concept in differential geometry, has been used to describe the local 3D geometry of the extracellular environment.[68] Previous studies have demonstrated that bone-forming cells in regions of high curvature respond by increasing proliferation rates, demonstrating that local tissue growth is proportional to curvature.[69,71,168] This collective behaviour of cells in response to geometric cues can give rise to measurable physical properties, analogous to a viscous fluid, and computational models have been developed to describe and predict these processes.[70,169]

Motivated by this reported phenomenon of geometry-driven tissue growth, the goal of this Chapter was to: a) guide stem cell self-organisation and lumen formation, and b) generate high-throughput stem cell and organoid growth in a controlled and reproducible way. Using MEW, macro-scale scaffolds were cultured for stem cell culture. It was found that by varying the scaffold geometry, tissue growth can be sculpted on these scaffolds, reproducibly guiding the emergence and morphology of the lumens.
Furthermore, it was demonstrated that the tissue shape evolution on the scaffolds can accurately be captured by a simple geometric model based on curve shortening flow.

Finally, it was shown that these bioengineered stem cell constructs can be differentiated into cerebral organoids and that the curvature-guided lumens further develop into VZ-like zones. This opens opportunities for guiding organoid-forming stem cells, creating new avenues in the field of organoid technology.

3.2. Materials and Methods

3.2.1. Mechanical testing

Scaffold samples were cut to a size of 20 mm x 35 mm. Mechanical testing was performed using a Bose Electroforce 3200 (BOSE, USA) with a 250 g load cell. Samples were clamped into the top grip at the bench, using double sided tape on one side of each clamp. The clamp was screwed into the test frame and bolted to the lower grip. The stage was ramped from 0 mm to maximum stage travel 6.2 mm or failure, at a displacement rate of 0.1 mm/s. The effective modulus was calculated using a custom matlab code. The code finds the cycling region (10 cycles), extracts cycles 5-10 and fits a linear regression to this. All experiments were carried out in triplicate. Mechanical testing and data analysis was carried out by Dr Axel Moore.

3.2.2. Scanning Electron Microscopy

MEW PCL scaffolds were cut with micro scissors and mounted on adhesive carbon tape on a SEM stub, followed by sputter coating with a thin gold layer for electron conductivity. Images were obtained using a JSM 6010LA SEM (JEOL) at 20 kV acceleration voltage.

3.2.3. Scaffold preparation for cell culture

PCL scaffolds were secured onto a sterile CellCrown holder (Scaffdex CellCrown, Tampere, Finland), followed by sterilization by UV irradiation for 30 - 45 min. Scaffold-CellCrown assemblies were then placed in a 6-well plate and coated in 2 mL hESC-qualified Matrigel (diluted in DMEM/F12 according to manufacturer's instructions) (Corning 354277) and left to incubate at 37°C for 1 - 2 h. Immediately before cell seeding, scaffolds were washed once in PBS.

3.2.4. Lumen morphogenesis protocol

<u>D 0</u>

Seeding onto scaffolds

At approximately 60% confluency, hESCs were dissociated from the well-plate by adding 1 mL accutase for 3 min at 37°C. The remaining adherent cells were sprayed off with 1 mL mTESR (Stemcell Technologies) and cells were centrifuged at 200 g for 3 min. The cell pellet was resuspended in mTESR media and a cell suspension was prepared in mTESR media containing 50 µM ROCK inhibitor Y27632 (Selleckchem) and 1% (v/v) Antibiotic-Antimyocytic (ThermoFisher) at a density of 1 x 10^5 cells per scaffold. After Matrigel incubation, scaffolds were washed once in PBS and placed in low attachment 6-well plates, or plates treated with anti-adherence rinsing solution (Stemcell Technologies) for 1 min, followed by washing three times in PBS. Scaffolds were secured at the bottom of the plate by pushing the CellCrown down using forceps. 3 mL of cell suspension was added per well, and the plate gently rocked in a North-South-East-West direction to evenly distribute the cells across the scaffold.

D 1

After 12 - 24 h of culture, CellCrowns were lifted by approximately 5 mm in the well plate to prevent cells from contacting the bottom of the well, while ensuring sufficient media coverage across the scaffold. The cells were left unperturbed on d 2.

D 3

mTESR media was exchanged without ROCK inhibitor or Antibiotic-Antimyocytic.

D 5

For stem cell cultures, cells and scaffolds were fixed for 1 h at room temperature or overnight at 4°C on d 5 with 4% paraformaldehyde (PFA) (v/v) in PBS and washed three times in PBS. For the generation of cerebral organoids on scaffolds, media was exchanged with a neural induction media (**section 2.4**). For subsequent procedure of cerebral organoids see **section 3.2.7**.

3.2.5. Scanning Electron Microscopy with cells

At d 5, samples were fixed in 4% PFA in PBS at 4°C overnight, followed by washing three times in PBS. To cut samples from the scaffold, the Scaffold-CellCrown assembly was placed on a sterile PDMS cutting mat (with a thickness of approx. 5 mm) and scaffold organoid samples were cut and obtained using a 6 mm biopsy punch. Scaffold and tissue biopsy samples were then dehydrated by adding 30, 50, 70 and 80% ethanol in water (v/v) for 30

min each. Then 90 and 100% ethanol (v/v) for 60 min each. Hexamethyldisilazane (HDMS) was added for 30 min, and the sample left to dry overnight. Prior to imaging, samples were sputter coated with a thin layer of gold. Imaging was performed using a JEOL JSM-6400 SEM at 3 kV acceleration voltage in secondary electron (SE) mode. SEM imaging was performed by Dr Martina Cihova.

3.2.6. Small molecule inhibitor assays

For small molecule inhibitor assays, scaffolds were cut into 2 x 2 cm squares and attached to sterile 24 well CellCrowns (Scaffdex CellCrown, Tampere, Finland). These were sterilised by UV irradiation for 30 - 45 min, as previously described. Scaffolds were then placed in a 24-well plate and coated in 500 µl hESC-qualified Matrigel (diluted in DMEM/F12 according to manufacturer's instructions) (Corning 354277) and left to incubate at 37°C for 1 - 2 h. Immediately before cell seeding, scaffolds were washed in PBS. 100,000 cells were seeded in each well and mTESR was supplemented with or without small molecule inhibitors, ROCK inhibitor Y-27632 (Selleckchem) (50 µM) at d 0 as the control condition, and myosin-II inhibitor Blebbistatin (EMD Millipore) (30 µM) at d 0 and d 3. Tissues were stained with 488 or 555 Alexa Fluor phalloidin (ThermoFisher) at d 5.

3.2.7. Cerebral organoid formation on scaffolds

*For Media formulations, see **section 2.4***

PCL scaffolds were prepared and seeded with hESCs as described above in **section 3.2.4.** At d 5, mTESR1 media was replaced with a neural induction media (as described in **section 2.4).** Media was replaced every day until d 10 - 13, when signs of optical clearing on the organoid borders was clearly present. At this stage, 2% (v/v) Matrigel (Corning, Cat. No. 356235) was added to the neural induction media, and at every media change thenceforth. 2 – 3 d after the first addition of Matrigel (usually at d 12), media was changed to improved -A media (as described in **section 2.4**). Additionally, CHIR 99021 (Tocris) at 3 µM was added for the first 3 d of improved -A media. At approximately d 15, the scaffolds were transferred to a 6 cm petri dish to provide a higher volume of media (10 mL) to support organoid

growth. The CellCrown was placed on a sterile plastic ring to prevent the organoids from touching the bottom of the plate. The media was changed every 2 d. At d 18, media was changed to improved +A media (as described in **section 2.4**).

3.2.8. Wholemount immunostaining hESC scaffold samples

At d 5, hESCs on scaffolds were fixed by incubation in 4% (v/v) PFA in PBS overnight at 4°C and washed three times in PBS. Organoid samples were cut from the scaffold, using a PDMS cutting mat and a 6 mm biopsy punch. For wholemount staining, samples were left in a permeabilisation and blocking solution (0.3% Triton X-100 and 5% BSA in PBS) for 2 h at room temperature (RT). Primary antibodies were added to the permeabilisation and blocking solution and left overnight at 4°C. Antibodies are listed in **Table 3.** Samples were rinsed three times in PBS then washed three times in PBS-T (PBS + 0.01% Triton X-100), before staining with secondary antibody or Phalloidin (Alexa Fluor) at a dilution of 1:250 for 2 - 3 h. Sections were washed twice in PBS-T, followed by a final wash in PBS.

3.2.9. Cryosectioning and immunostaining d 20 organoid sections

D 20 organoids on scaffolds were fixed in 4% PFA in PBS overnight at 4°C and washed three times in PBS. Cryosectioning is described in **section 2.6**. Immunofluorescence staining is described in **section 2.7**. Antibodies are listed in **Table 3**.

3.2.10. Optical clearing d 15 organoid samples

D 15 organoids were fixed in 4% (v/v) PFA in PBS overnight at 4°C and washed three times in PBS. Optical clearing is described in **section 2.9**. Antibodies are listed in **Table 3.**

Table 3 Antibodies used in Chapter 3.

Antigen	Host species	Supplier	Cat number	Dilution
SOX2	Rabbit	Abcam	ab97959	1:600

Z01	Mouse	Thermo Scientific	33-9100	1:50
NANOG	Rabbit	Abcam	ab21624	1:100
OCT4	Mouse	Abcam	ab184665	1:100
FOXG1	Rabbit	Abcam	ab18259	1:200
PAX6	Sheep	R&D Systabems	AF8150	1:200
aPKCzeta	Mouse	Santa Cruz	SC-17781	1:200
TUJ1	Mouse	Sigma-Aldrich	T8578	1:500

3.2.11. Confocal imaging

Confocal imaging is described in **section 2.8**.

3D segmentation of lumens: For lumen segmentation SOX2 and Z01 stained tissues were imaged as z-stacks. The Z01 marker was used to segment the lumen, using the Fiji plugin segmentation editor. The lumen were manually segmented using segmentation editor on 4 - 5 slices, including the first and last slice, and the rest were interpolated. The segmented lumens were pseudo-coloured in green and merged with the SOX2 channel, to create confocal cross-sections at the bisector angle. 3D segmentation images were made with 3D script plugin in Fiji.

Lumen volume: Lumen volume was calculated on the segmented lumen regions using the 3D objects counter in Fiji. 9 triangle-shaped scaffold regions were analysed (N = 1, n = 9).

Lumen area and circularity: Lumen area was determined by first generating a maximum intensity z projection, and manually segmenting the lumen. The inbuilt measure function in Fiji was used to calculate area and circularity. Circularity is defined as: *4pi(area/perimeter^2).* 9 triangle-shaped scaffold regions were analysed (N = 1, n = 9).

Total cell count: The central 6 slices of the z stack with the maximum tissue area was summed as a maximum intensity projection. A median smoothing filter was applied with a value of 1, and 0.5 gamma was applied. Images were background subtracted with a rolling ball radius of 5. For cell count, images were thresholded using Auto Huang, and outliers removed. Adjustable watershed was then applied, and regions of interest (ROI's) drawn at 500 µm from the scaffold centre for each angle segment. Cells were counted in each segment using *analyze particles* function. 9 triangle-shaped scaffold regions were analysed (N = 1, n = 9).

Angles between 37° and 54° were grouped as ~45° and all angles between 86° and 93° were grouped as ~90°. Welch's t-test was used for statistical analysis in prism software.

3.2.12. Time-lapse imaging

For time-lapse imaging at d 1 - 5, scaffolds were placed in glass bottom 6 well plates (Ibidi) containing fresh media. The Scaffold-CellCrown assembly was lifted approximately 1 mm from the bottom of the surface. 100 nM SiR-Actin (Cytokeleton, Inc.) was added to the mTESR media approximately 1 h before imaging. A fully automated CellDiscoverer 7 microscope (Zeiss) was used for time-lapse imaging, comprising an environmental chamber (37°C, 5% CO_2). 7 ROIs were imaged every 3 h in brightfield and fluorescence mode. Each position was acquired as a z stack. At d 3, image acquisition was paused for approximately 30 min as the well plate was removed from the microscope for media exchange. Imaging was resumed until d 5. For time-lapse imaging from d 6 – 11, scaffolds were placed in a glass bottom 6 well plate containing neural induction media. At d 9, image acquisition was paused for approximately 30 min as the well plate was removed from the microscope for media exchange containing neural induction media supplemented with 2% (v/v) Matrigel (Corning, cat. no. 356235).

Brightfield images were acquired using the EVOS XL Core imaging system. For tiled images of the entire scaffold, images were acquired using the CellDiscoverer 7 microscope. Z stacks were acquired to account for tilt across the entire scaffold. Tiled images were fused using the Zeiss image processing software.

Growth Curve

Timelapse images were used to determine the growth curve for the scaffold walls and scaffold intersections. 5 ROIs were used of the growing tissue on the scaffold. To measure scaffold wall tissue thickness, 4 measurements were taken for each ROI (n = 20) for each timepoint. To measure scaffold intersection tissue thickness, the maximum thickness of the tissue at the scaffold intersection was measured for each ROI (n = 5). Statistical analysis was determined by Welch's t-test.

Brightfield heatmaps

89 brightfield images of scaffold regions at d 5 from 2 independent experiments were concatenated to create a stack. Images were rotated if required to ensure that the scaffold fibres were aligned throughout the entire stack. A custom Fiji macro was used to overlay the images and create a heatmap, using the 'fire' LUT.

3.2.13. Mathematical modelling

A mathematical model based on discrete curve-shortening flow was implemented in Matlab (Matlab 2020b, Mathworks) to model the shape of the evolving tissue on the square, parallelogram, and triangular-shaped scaffolds. Briefly, the model takes a specific polygon as input (representing the scaffold walls), which is discretised into a user-defined number of points n_p and an equal number of line segments. Subsequently, the algorithm evolves each point in normal direction towards the centre of the original polygon at a speed that is proportional to the local line curvature, and this process is repeated for a number of iterations j_{total}. For every point p_i with neighbouring points p_{i-1} and p_{i+1}, the normal vector $\boldsymbol{n}$ is computed as:

$$\boldsymbol{n} = \|\boldsymbol{u}\| \cdot \boldsymbol{v} + \|\boldsymbol{v}\| \cdot \boldsymbol{u}$$

Where $\boldsymbol{u} = p_{i+1} - p_i$, $\boldsymbol{v} = p_{i-1} - p_i$, and $\| \cdot \|$ represents the vector norm. The local curvature k_i at every point was computed using the *LineCurvature2D* function. For any iteration $j < j_{total}$, the evolution of any point p_i is calculated as:

$$p_i^{j+1} = p_i^j + \delta \boldsymbol{n_i} k_i$$

Where δ is a user-defined control parameter to tune the rate at which the polygon shape evolves inwards so that it can match the experimental observations. After every evolution,

the points along the evolved polygon shape were uniformly remeshed using the *interparc* function. Moreover, to avoid numerical errors, the first and last points along the evolving polygon shape were collapsed when they moved too close to each other, *i.e.* when their distance was within 5% of their original distance. To show the evolution of the initial polygon shape, representing the evolution of the tissue-medium interface, the evolved polygon points were plotted at different iterations j. Moreover, the normalized line curvature $\tilde{k}$ for different iterations was also plotted, with $\tilde{k} = \frac{n \cdot k}{k_{max}^{j=1} - k_{min}^{j=1}}$.

Mathematical modelling was carried out by Dr Sebastien Callens.

3.3. Results and discussion

3.3.1. Scaffold fabrication and characterisation

Tuneable scaffold microstructures were designed and fabricated to guide the growth and self-organisation of hESCs in a highly controlled manner. MEW was selected to fabricate 4 x 4 cm lattice scaffolds, comprising stacked microscale fibres. A schematic of the custom-built MEW device is demonstrated in **Figure 3.1a** and the scaffold fabrication process is described in the materials and methods. Briefly, a thermoplastic polymer is placed in a syringe and heated above its melting temperature. Air pressure is then used to extrude the polymer melt, and a voltage is applied which causes the polymer particles to become charged and protrude from the nozzle, forming a so-called Taylor cone. Above a threshold voltage, a jet is then produced which elongates within the electric field to deposit on a collector. The collector stage has a software-controlled x-y-z stage, which enables polymer fibres to be deposited in a controlled, user-specified geometry (**Figure 3.1b,c**). Scaffold geometries were designed and translated to a G-code print path. For lattice structures, these print paths were written manually, whereas a python script was used to write the G-code for more complex structures.

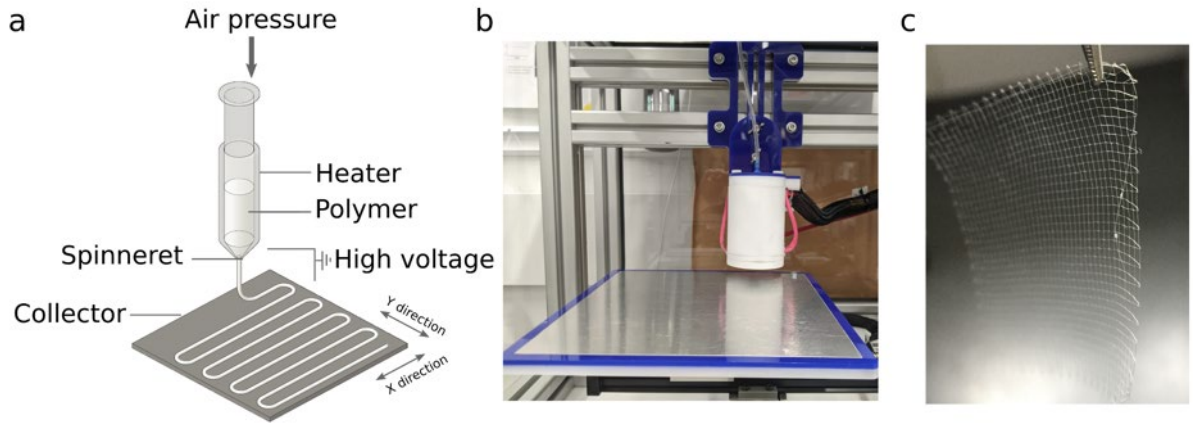


Figure 3.1 Scaffold fabrication via MEW. *a) Schematic of the MEW device. b) Photograph of the MEW device c) photograph of a PCL scaffold fabricated by MEW.*

The polymer PCL was selected as a scaffold material owing to several desirable properties, including biocompatibility, slow biodegradation rate, and stability at ambient temperature.[170] Furthermore, its thermoplastic nature and low melting temperature (~60°C) make it an ideal polymer for MEW, as previously demonstrated.[171,172] Scaffolds were printed using a 10 kV accelerating voltage, 10 mm collector distance, a feeding air pressure of 1.0 bar, and heating temperatures between 60 and 80°C. These printing parameters produced a reproducible fibre diameter of 5 µm (**Appendix A**).

A variety of scaffold geometries were successfully fabricated, including square-shaped geometries with pore sizes of: 250 µm, 500 µm, 800 µm, 1000 µm and 4000 µm, rhombus- and triangle-shaped geometry, showing the versatility of the process (**Figure 3.2a**). Each scaffold consisted of 10 stacked layers of fibres, resulting in a total height of approximately 50 µm. For better structural integrity, fibres at intersections were stacked in alternating order, producing interwoven layers. It was reasoned that using a stacked fibre scaffold could provide a combination of both strength and handleability, as well as the individual thin fibres providing a suitable microenvironment for cell adhesion at the cell scale.

Tensile tests were carried out to characterise the mechanical properties of the scaffolds. Scaffolds were clamped at either end and force was applied at a constant strain rate of 0.1mm/s (0.2 strain/min). The resulting force-displacement curves were used to calculate stress-strain response and evaluate stiffness. Representative force-displacement curves of 500 µm and 1000 µm pore size square-shaped scaffolds are shown in **Figure 3.2b,c**. The 500 µm scaffolds were found to be ~1.5-fold stiffer than the 1000 µm pore size scaffolds (**Figure 3.2d**). Overall, the effective tensile strength fell in the range of values reported in the literature for electrospun PCL, and the tensile properties were tuneable according to scaffold geometry.

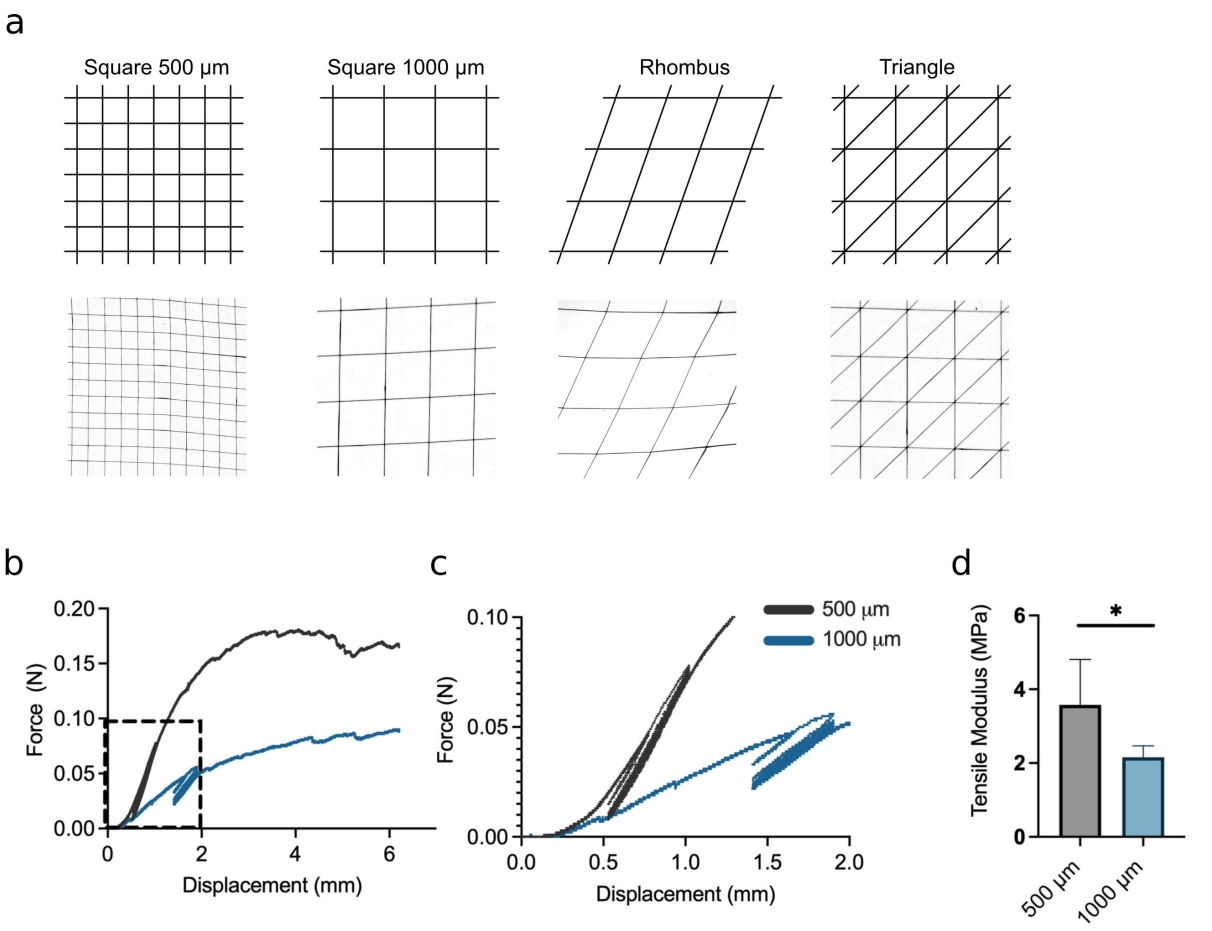


Figure 3.2 Mechanical characterisation of MEW scaffolds. *a) Schematic (top) and brightfield images (bottom) of different scaffold geometries. b) Force-displacement curves of square-shaped PCL scaffolds with 500 µm and 1000 µm pore size. c) inset of Force-displacement curve showing region where modulus analysis is performed. d) Mean effective tensile modulus (MPa) of PCL scaffolds of 500 µm and 1000 µm spacing (N = 3). P values: (*) <0.0370, determined by unpaired t-test. Mechanical testing and data analysis was carried out by Dr Axel Moore.*

3.3.2. hESCs self-organise on MEW PCL scaffolds

Next, MEW scaffolds were used for the culture of hESCs to investigate their ability to guide tissue growth and lumenogenesis. The scaffold preparation for cell culture is demonstrated schematically in **Figure 3.3.** For consistency, scaffolds with square-shaped pores of 1000 µm size were used throughout this study, unless otherwise stated. Scaffolds were fixed onto a cell crown device and sterilised by exposure to UV light for 30 min. To facilitate cell attachment to the PCL fibres, scaffolds were coated with hESC-qualified Matrigel and incubated for 1 h at 37°C, followed by a washing step in PBS to remove excess Matrigel.

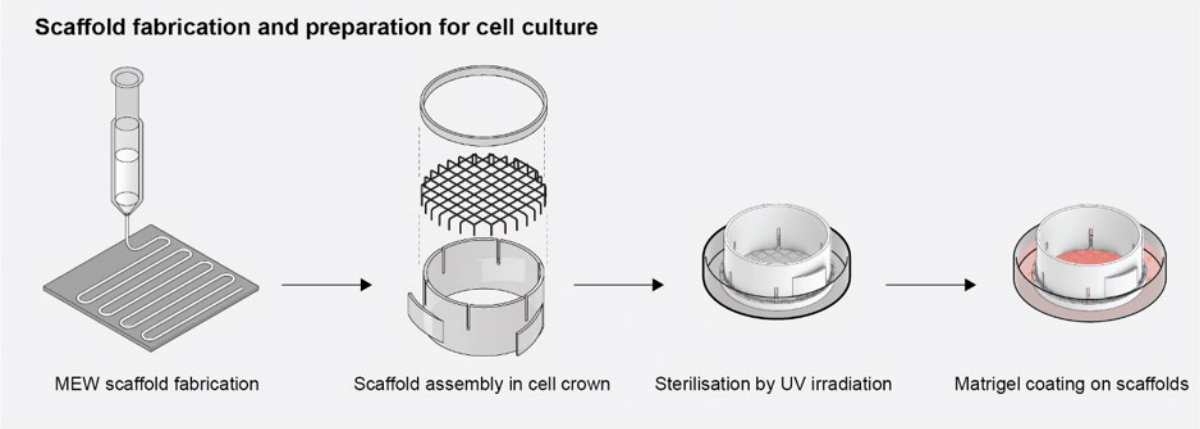


Figure 3.3 Schematic illustration of MEW scaffold preparation and stem cell culture. *PCL scaffolds are fabricated by melt MEW. For cell culture, scaffolds are assembled in a cell crown, then sterilised by UV irradiation. Prior to cell seeding, scaffolds are coated in Matrigel, then incubated for 1 h and washed in PBS.*

Scanning electron microscopy (SEM) images showed the appearance of coated and uncoated MEW PCL scaffolds and confirmed the desired homogenous fibre diameters and high precision architecture in both samples (**Figure 3.4**). Despite the dehydrated nature of the samples inherent to SEM, the coated sample clearly shows a thin layer of Matrigel coating the scaffold.

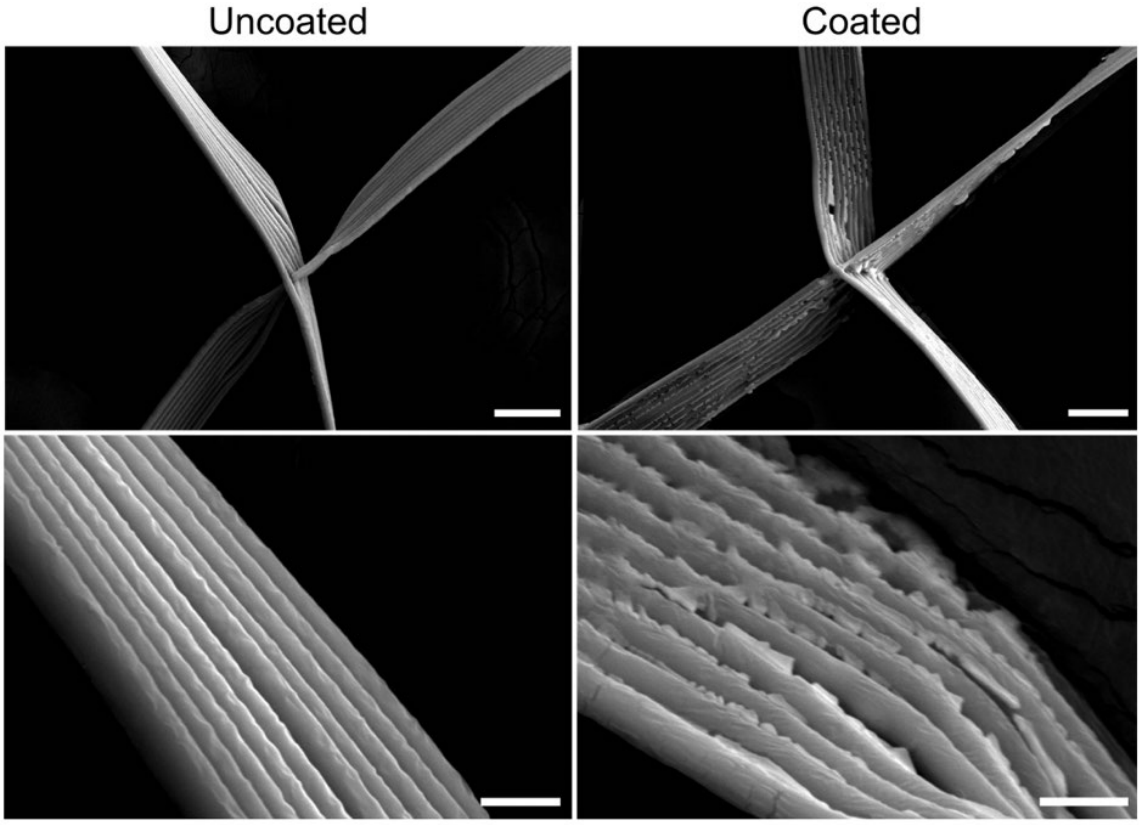


Figure 3.4 SEM images of PCL MEW scaffolds uncoated (left) and coated with Matrigel (right). *Scale bar = top row: 50 µm, bottom row: 10 µm.*

After Matrigel coating, scaffolds were placed in a low attachment well plate, and the supporting cell crowns were pushed down, to ensure that the scaffold was resting on the bottom of the well plate. Next, 100,000 wild-type H9 hESCs suspended in culture media were seeded directly onto the scaffold in a single cell suspension, gently shaking the well plate in a North-South-East-West motion to promote an even distribution of cells across the scaffold (**Figure 3.5**). Importantly, it was necessary to lift the cell crown scaffold assembly approximately 5 mm from the bottom of the plate after 24 h. This prevented cell-material interactions with the bottom of the plate and enabled 3D growth of cells around the scaffold. Notably, failure to do so or lifting at a later timepoint led to a more heterogenous cell coverage on the scaffold and were not considered for further analysis.

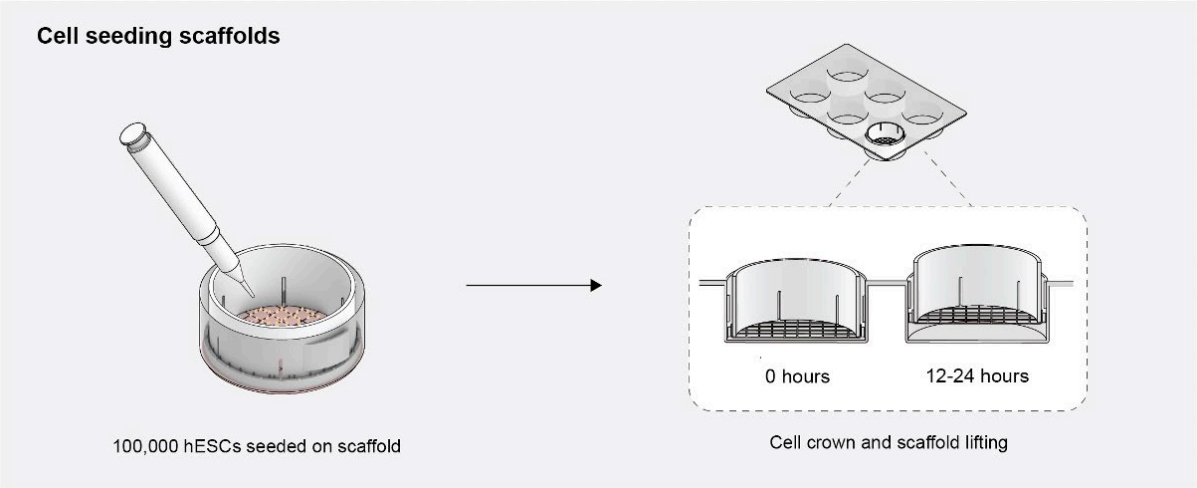


Figure 3.5 Schematic illustration of hESC seeding on scaffolds. *1 x 10^5 hESCs are seeded on scaffolds in stem cell media. CellCrowns are lifted after 12-24 h to prevent cell adhesion to the bottom of the well and promote the growth of 3D stem cell aggregates.*

Tiled overview images of fixed stem cell scaffold constructs allowed us to screen the entire scaffold and revealed a high level of reproducibility in tissue growth across the scaffold (**Figure 3.6a**). hESCs are known to intrinsically self-organise, and form an apical lumen surrounded by a polarised epithelium.[52,160,161,173] Here, it was found that the cells followed this self-organising trajectory, and at d 2, brightfield images showed polarisation of epithelia by radial organisation of cells around a small central lumen within each corner of the scaffold intersection point (**Figure 3.6a**, solid black arrowhead). At d 5, the tissue and lumen had expanded, forming dense tissues at each scaffold intersection points, comprising of lumen oriented in each of the four scaffold corners (**Figure 3.6a**, black line arrowhead). Previous studies have demonstrated that bone-like cells proliferate faster in more concave regions, i.e. at the corner of the scaffolds.[69–71,168] Similarly, the results in this study showed that the hESC tissue was significantly thicker (~3-fold) at the fibre intersection region at d 2 and d 5, compared to that at the fibre walls (see **Figure 3.6a** for schematic of tissue thickness definition), indicating that tissue growth preferentially occurs in the scaffold corners (**Figure 3.6b,c**).

A critical parameter for stem cell and organoid engineering is control and high reproducibility. In the current system, a square-shaped 1000 µm pore size scaffold of 26 mm

total diameter provides approximately 463 scaffold intersections per sample (calculated as an average over 2 independent scaffold samples). At 100% efficiency, this generates 1852 polarised lumens, growing in a highly organised way, thereby providing a high-throughput stem cell platform. The reproducibility of this system was further apparent in the heat map, generated from the digital overlay of 89 images, showing the tissue area at d 5 over 89 individual scaffold intersections (**Figure 3.6d**). The physical structure of the scaffold was also highly stable, with no scaffold rupture observed in any of the experiments.

To study the intrinsic changes in the growing tissue in more detail, tissue time-lapse microscopy was used to track tissue development on the scaffold over the course of 5 d (**Figure 3.6e**). 24 h after plating (d 1), cells were attached to the scaffold, with a noticeably higher density of cells towards the fibre intersections. 48 h after plating (d 2), hESCs started to self-organise around the scaffolds, as small lumen structures were visible in the tissue (**Figure 3.6e**, solid black arrowhead). These lumen structures appeared to gradually expand over the time-course, resulting in large primary lumen formations in each of the scaffold corners by d 5, as shown above (**Figure 3.6e**, black line arrowhead). Over the 5 d time course, the tissue grew uniformly across the scaffold, primarily at the intersections but also along the scaffold fibre walls, eventually creating a connected and polarised tissue network.

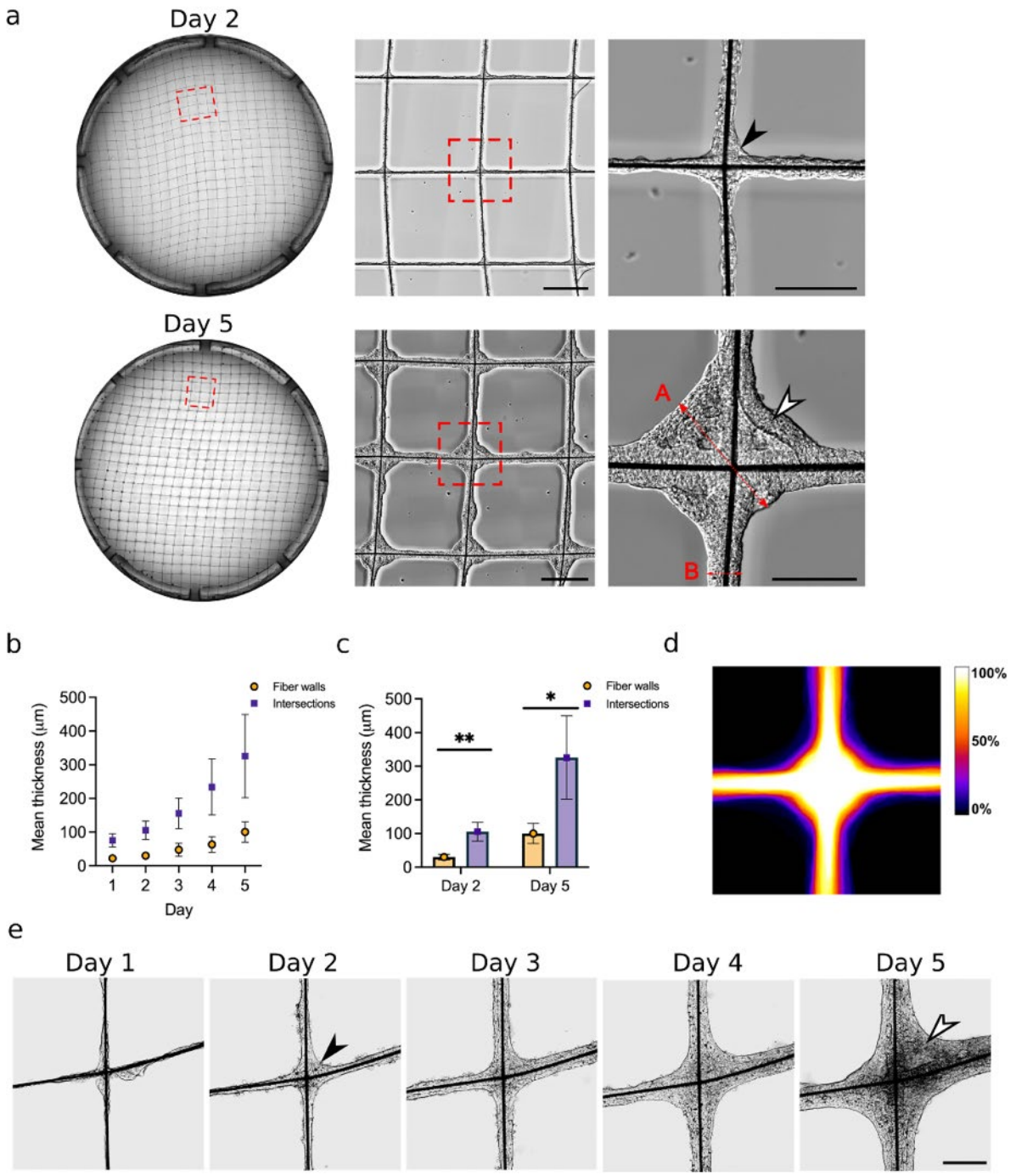


Figure 3.6 hESC growth and lumen formation on MEW scaffolds. *a) Overview images of the entire scaffold (left) and magnified views on the tissues (centre, right) at d 2 and d 5 after hESC seeding. A representative example of lumen emergence is shown at d 2 with solid black arrowhead, and established lumen at d 5 with black line arrowhead. Red dotted lines in the magnified view shows the region of tissue thickness measurement for the Intersection (A) and fibre walls (B) on the scaffolds. b) Mean thickness of tissue on the fibre walls (n = 20, N = 1) and intersections (n = 5, N = 1) at d 1 - 5. Data represent mean ± s.d. c) Comparison of tissue thickness at the walls and intersections at d 2 and d 5. Data represent mean ± s.d. P values:(**) <0.0033 and (*) <0.0147, determined by Welch's t-test. d) Heatmap showing 89*

overlayed brightfield images of individual intersections across the scaffold at d 5 after hESC seeding, from 2 independent experiments (N = 2). Colourbar indicates the percentage of images in which tissue was present in these locations. e) Representative brightfield time-lapse images at d 1 – 5 after hESC seeding on PCL scaffolds (n = 6). Lumen emergence is shown at d 2 with solid black arrowhead, and established lumen at d 5 with black line arrowhead. Scale bar corresponds to 200 µm.

3.3.3. Scaffold guided lumen formation

To characterise the lumen formation on scaffolds, immunostaining was carried out on d 2 and d 5 hESC scaffold samples with apical protein markers, including F-actin (phalloidin) and Z01 (**Figure 3.7**). Results at d 2 showed Z01 and F-actin enriched regions at the scaffold corners, circling a small emerging lumen region (**Figure 3.7**, white line arrowheads). Interestingly, enriched areas of apical markers were also observed at other regions of the tissue along the scaffold walls (**Figure 3.7**, solid white arrowheads). At d 5, Z01 and F-actin staining reveal large primary lumens at the scaffold corners, flanked by smaller lumens along the fibres, with decreasing size the further away from the scaffold corners. This data clearly shows that lumen expansion preferentially occurs at the concave regions of the scaffold.

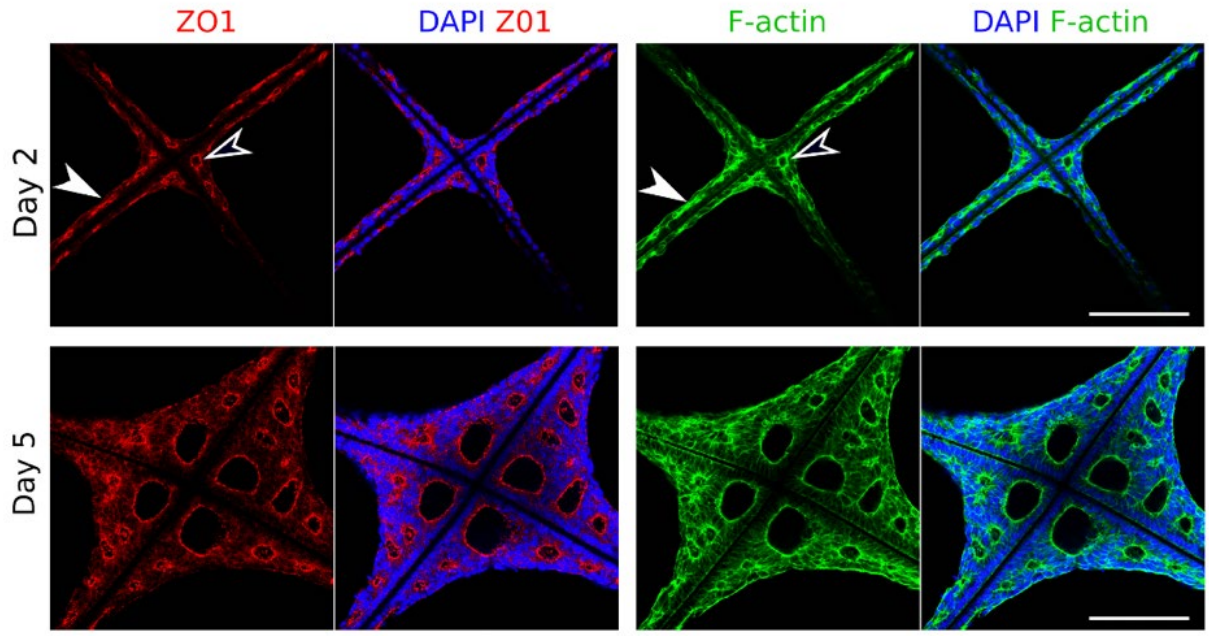


Figure 3.7 Characterisation of lumen formation on scaffolds at d 2 and d 5 by immunostaining with apical protein marker Z01, F-actin (phalloidin) and counterstained with DAPI. *A representative example of lumen emergence at the scaffold corners is shown at d 2 with the white line arrowheads, and at the scaffold walls with the solid white arrowheads. Bottom row shows the matured tissue comprising lumen at d 5. Scale bar corresponds to 200 µm.*

To further explore the tissue growth dynamics on the scaffold and identify the onset of apical polarisation and lumen formation, a live-cell time-lapse experiment was conducted using a cell-permeable F-actin probe, Silicon-Rhodamine (SiR)-actin (**Figure 3.8a**). At 24 h of culture, F-actin expression was low, and non-localised across the tissue. At 48 h, F-actin expression appeared highly localised inside two of the emerging lumens at the scaffold intersections (**Figure 3.8a**, solid white arrowheads), as well as on the scaffold wall (**Figure 3.8a**, white line arrowhead). In brightfield, the cells appeared more uniformly organised around the entire scaffold at this stage, with a higher number of cells at the fibre intersection. From 72 – 96 h, the F-actin expression intensified, overall and particularly within the expanding lumen areas, in all four scaffold corners. Similar to the immunostaining data (**Figure 3.7**), smaller areas of localised F-actin expression were also present along the fibres, away from the scaffold corners. At 120 h (d 5), the distribution of F-actin expression was considerably more homogeneous across the tissues with generally high levels of expression. The F-actin staining at this stage using the SiR-actin probe is less well-defined

than the previous results using phalloidin stain, which may be due to a higher level of background staining. This could also be attributed to the depletion of active lifespan of the SiR-actin probe.

To look more closely at the changes in stress fibres during the onset of lumenogenesis, the time-window between 30 – 51 h was observed more closely (**Figure 3.8b**). Even though the 4 primary lumens initiated at slightly different times (within a 6 h time range), for each lumen, stress fibres first localised at the leading edge of the growing tissue (**Figure 3.8b**, solid white arrowhead), followed by localisation at the expanding lumen area, in the centre of the tissue (**Figure 3.8b**, white line arrowhead). Based on the observations that tissue grows preferentially in the high curvature areas of the scaffold, promoting the formation of large primary lumens, it was hypothesised that lumenogenesis occurs in a curvature dependent manner on these scaffolds. In fact, results show that prior to lumen initiation, the actin fibres follow the curvature of the scaffold corner. It is likely that this generates a force vector, pulling the tissue outwards and promoting lumen formation (**Figure 3.9**).

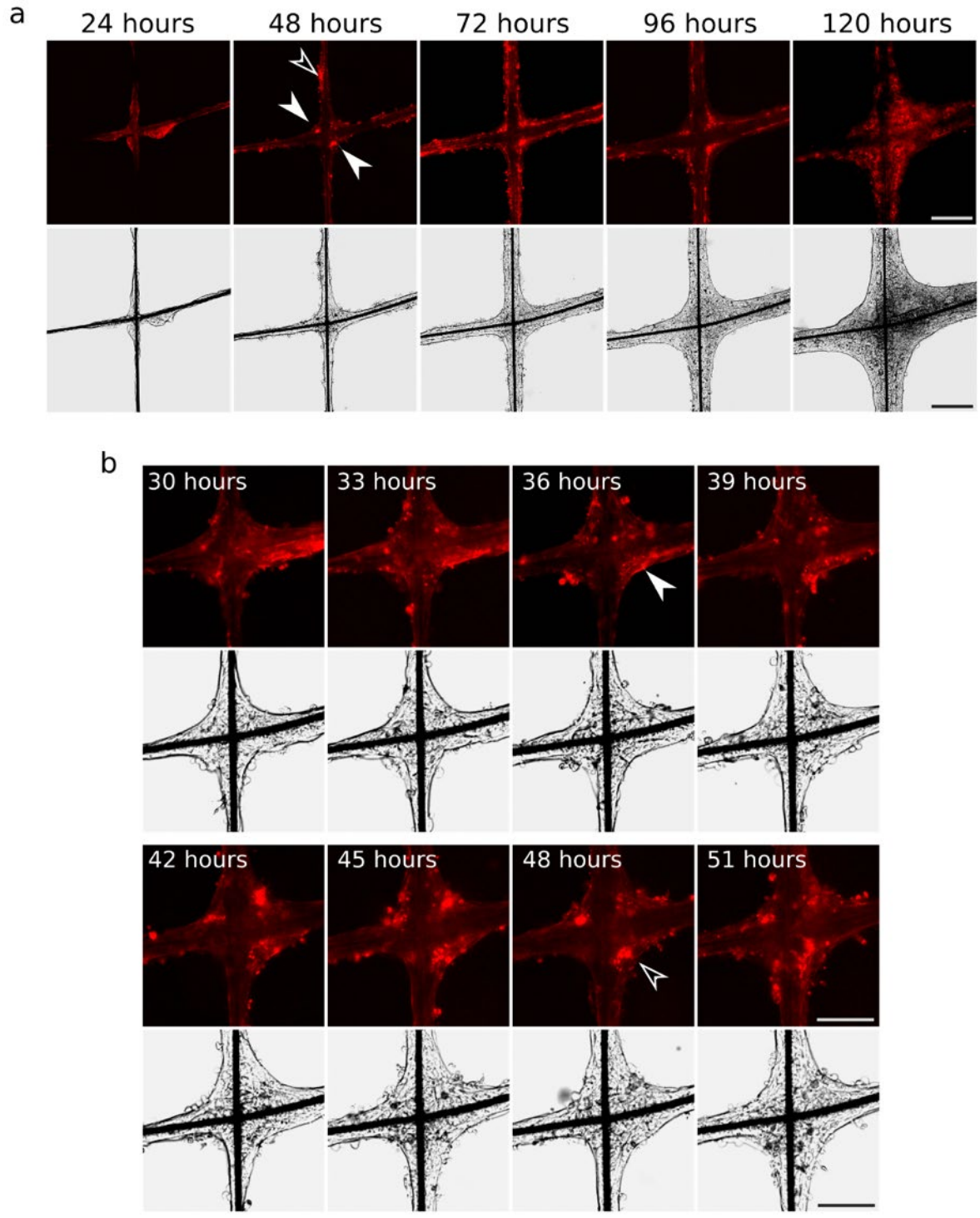


Figure 3.8 Cytoskeletal tissue dynamics and onset of lumenogenesis.*a) Consecutive frames from live imaging of tissues stained with an F-actin probe, SiR-actin, from 24 h to 120 h (d 1-d 5). Top: fluorescent images of F-actin, showing F-actin expression in 2 emerging lumens in the scaffold corners (white solid arrowhead) and on the scaffold wall (white line arrowhead), bottom: brightfield images. Scale bars correspond to 200 µm. b) Consecutive frames from live imaging of tissue stained with F-actin probe, SiR-actin, from 30 h to 51 h. Top: fluorescence images of F-actin during lumenogenesis, displaying actin accumulation at the*

growing edge of the expanding tissue in the corner of the scaffold (white solid arrowhead), followed by accumulation inside the newly formed lumen (white line arrowheads). Bottom: brightfield images. Scale bars correspond to 100 µm.

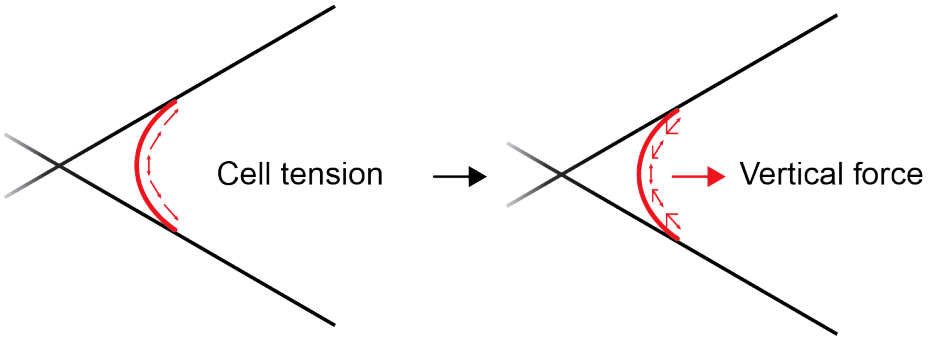


Figure 3.9 Schematic of the mechanistic model describing scaffold guided tissue growth and lumen formation on MEW scaffolds.

3.3.4. 3D characterisation of lumen formation on scaffolds

3D reconstruction from confocal stacks provided valuable information about tissue and lumen structure in relation to the scaffold. 3D projections of phalloidin-stained samples at d 2 and d 5 showed that the hESC tissues encompassed the scaffold completely (**Figure 3.10a,b**). Furthermore, the tissue appeared most dense at the central intersecting point and tissue width tapered out at the edge of the high growth regions in the scaffold corners. This was further validated by SEM imaging of d 5 tissues on scaffolds (**Figure 3.10c**). Despite the dehydrated nature of the samples, high resolution SEM images also showed elongated cells at the growing edge on the corner of the scaffold (**Figure 3.10c**, solid white arrowhead), demonstrating that scaffold geometry promotes cell stretching between the fibre walls at the scaffold corners. This further supported the hypothesis that hESC tissue collectively behaves in a curvature-dependent manner on the scaffolds. SEM images also allowed us to visualise the lumen position and structure. Whilst the lumen is typically enclosed within the tissue by a polarised epithelium, the dehydration procedure caused shrinkage to the cells, thereby revealing a hollow lumen structure within the scaffold corner (**Figure 3.10c**, white line arrowhead).

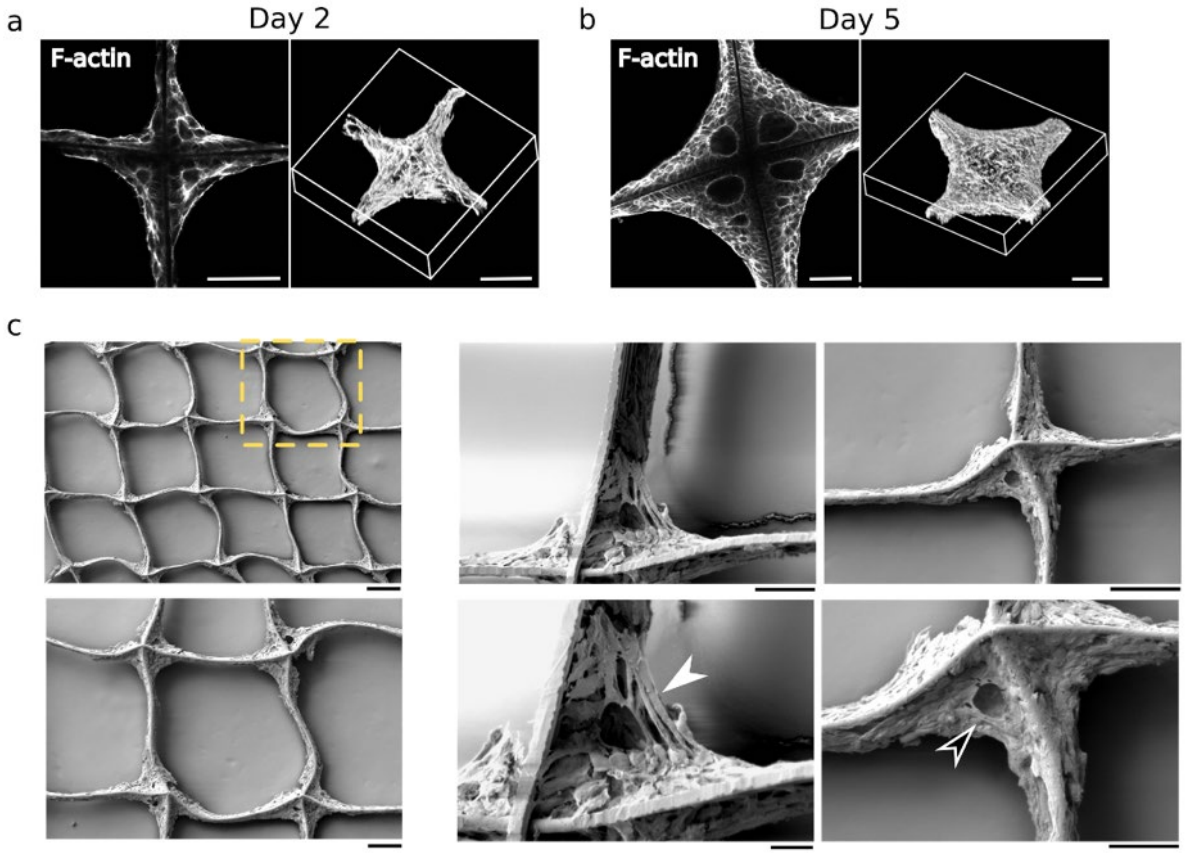


Figure 3.10 3D characterisation of hESC tissues on MEW. *a-b) single slice representation generated from confocal light microscopy (left) and 3D reconstructions (right) of F-actin immunostained samples at (a) d 2 and (b) d 5. c) Representative SEM images of hESCs on PCL scaffolds at d 5. Close up images show elongated cells at the growing edge of the scaffold corner (solid white arrowhead) and the indent in the tissue of the lumen at the corner of the scaffold (empty white arrowhead). SEM imaging carried out by Dr Martina Cihova.*

Lumen structures were well represented in 3D after segmentation, with Z01 apical marker delineating the lumen boundary (**Figure 3.11a**). Digital cross-sections generated from the confocal stacks showed that the large primary lumens were centrally located in the tissue and enclosed by layers of SOX2 positive pluripotent cells. Furthermore, the confocal cross-sections along the perpendicular bisector of the tissue revealed the thickness distribution of the tissues, with increasing tissue thickness at decreasing distance to the scaffold intersections (**Figure 3.11a, right**). The lumen shape followed the overall tissue thickness distribution with larger lumen thickness closer to the scaffold intersections. Segmentation of the lumen also provided an opportunity to quantify lumen size, using the central slice

with maximum area in the z stack to calculate lumen area. The lumen were compared at different days and significantly larger lumen area (~10-fold larger) was identified in d 5 compared to d 2 hESC scaffold samples (**Figure 3.11b**).

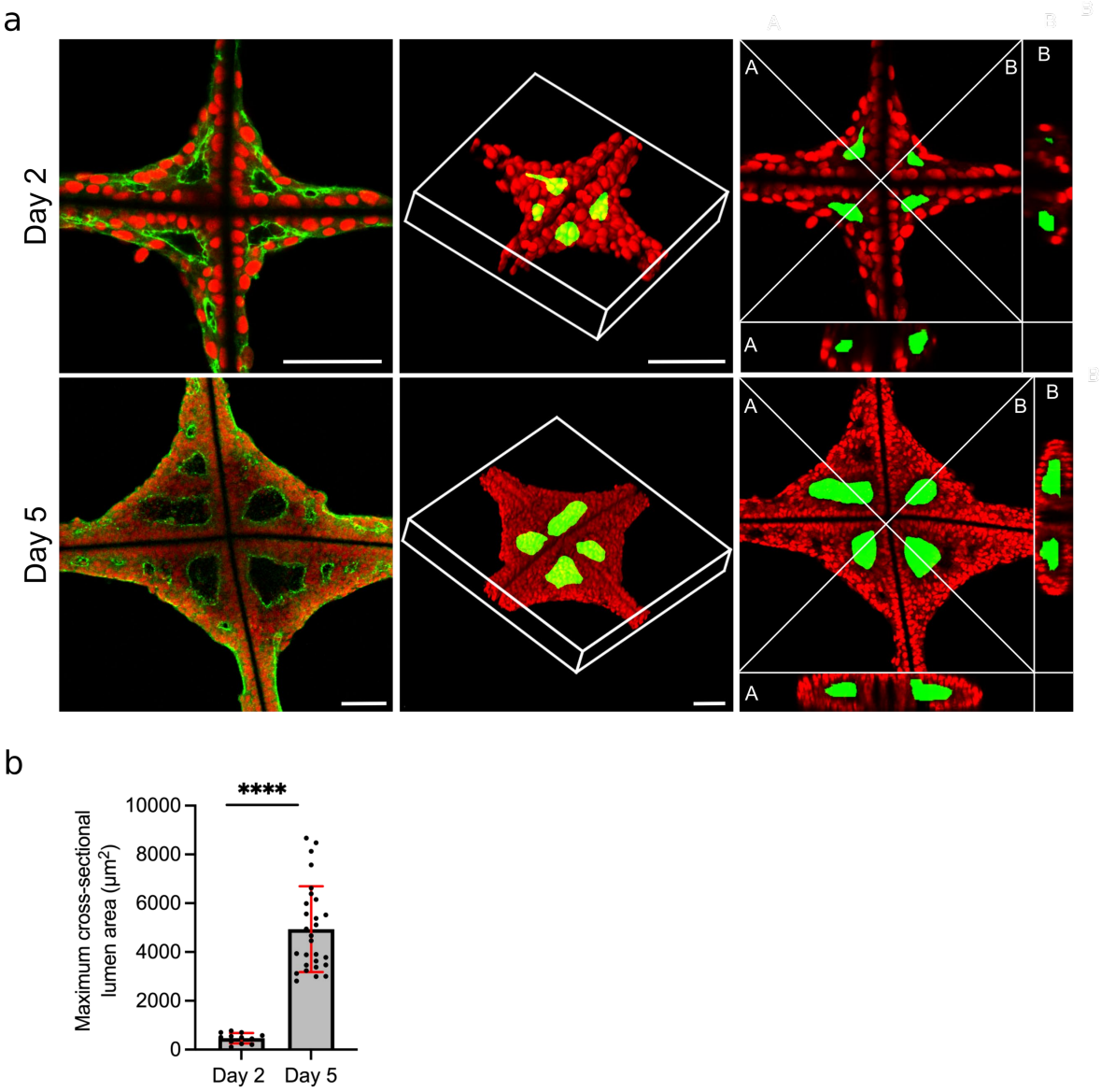


Figure 3.11 3D lumen reconstruction on MEW scaffolds. *a) image gallery at d 2 (top) and d 5 (bottom) showing a single slice of scaffold and hESCs immunostained with SOX2 (red) and Z01 (green) (left), 3D reconstruction from a confocal z stack, with the lumens segmented and pseudo coloured in green (middle), cross-section of the confocal z stack showing a bisector slice through the lumens indicated by the white lines (right). b) Maximum cross-sectional lumen area at d 2 and d 5. Data represent mean ± s.d. P value of (****) <0.0001, determined by Welch's t-test.*

3.3.5. Scaffold geometry predictably guides lumen formation and tissue shape

To address the hypothesis of curvature-driven tissue behaviour, scaffolds were fabricated with varying geometries to compare lumen formation across different curvatures in a highly controlled way. The tissue growth dynamics and lumen formation were tested on square-, rhombus- and triangle-shaped MEW scaffolds (**Figure 3.12a-c**). As expected from our reasoning on curvature-guided tissue behaviour, geometry-dependent tissue growth and lumen formation could be observed via brightfield images and Z01 staining. The triangle and rhombus scaffold geometry created angles that were ~90° or ~45°. Scaffold angles >90° were unable to support tissue growth or lumen formation and resulted in largely underdeveloped tissues (**Figure 3.12b**). For the triangle scaffold, a trapezoid shape was formed in the larger angle regions when the fibres did not precisely overlap at the scaffold intersection. This similarly resulted in underdeveloped tissues with small or absent lumens (**Figure 3.12c**). At ~45° angles, extended tissue growth and lumen formation of primary lumen was observed close to the scaffold intersections. These results support the initial observations that the scaffold angle, which governs the local curvature, plays a role in guiding lumen initiation and lumen size.

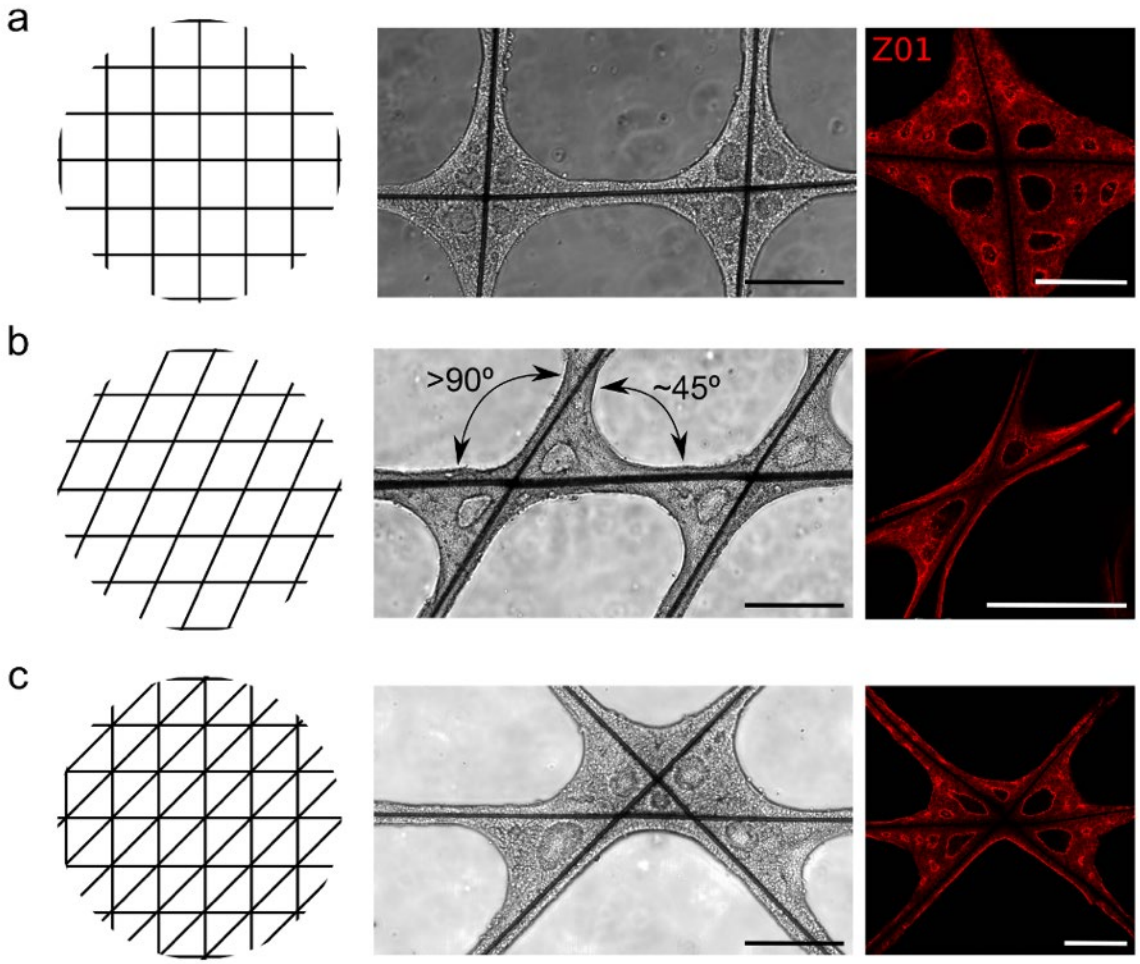


Figure 3.12 Scaffold geometry guides lumen formation. *Graphical illustrations showing the different scaffold geometry designs investigated (left), brightfield images at d 5 showing hESC tissue morphology on the different scaffold geometries (middle), and immunostaining with apical marker Z01 (right) on: a) square-shaped scaffold. b) Rhombus-shaped scaffold that creates two major angles of >90 ° and ~45 ° as labelled in the brightfield image. c) triangle-shaped scaffold. Scale bars correspond to 200 µm.*

To further investigate the relationship of scaffold geometry and lumen characteristics, immunostaining was carried out for the stem cell marker SOX2 and the apical marker Z01. Z stacks were acquired via confocal light microscopy and 3D reconstructions were created of the tissue forming on triangle scaffolds. As previously described in this study, the large primary lumen was segmented to allow for a quantitative description of the lumen shape (**Figure 3.13a**). For its morphometric description lumen volume, cross-sectional area, and cross-sectional circularity were selected. In addition, the total cell count in the tissue was

quantified. All parameters were determined as a function of the angle of the scaffold fibre walls adjacent to the lumen, aiming at investigating a potential correlation between scaffold angle and lumen characteristics. 3D segmentation was facilitated by the Z01 marker that clearly delineated the lumen boundary. However, the top and bottom of the lumen volume (in z-direction) were less clearly defined, and Z01 was found to taper off over several slices. For the 3D lumen reconstruction, the segmentation plugin in Fiji was used. This required certain manual inputs that introduced unavoidable user bias for the start and end slice selection of the individual lumens. Thus, the maximum cross-sectional area of the lumen in 2D was also measured. In both cases (lumen volume and max. lumen area) a similar correlation was found between lumen and angle size, namely significantly ($p < 0.0001$) larger lumen dimensions for the smaller angles with ~2.5 and 3-fold larger area and volume, respectively. These results suggest that scaffold angle size is a clear determinant of lumen size (**Figure 3.13b,c**). Lumen shape was also affected by scaffold angle size, visible from the lumen circularity, which was significantly higher and more consistent in ~90° angles (0.83 ± 0.08), compared to ~45° (0.7 ± 0.12) angles (**Figure 3.13d**).

To further explore the observation that scaffold angle plays a role in determining lumen size, we next sought to establish if cell count varies as a function of scaffold angle. To quantify cell count, the central 6 slices in the z-stack were extracted to generate a z-intensity projection of the SOX2 channel, and the cells were counted using Fiji (see materials and methods, **section 3.2.11**). A significant difference in cell count between the ~90° (121.4 ± 20.8) and ~45° scaffold angles (152 ± 30.1) was observed, whereby the ~45° scaffold angle resulted in a 25% increased cell count (**Figure 3.13e**). Taken together, these results demonstrated a clear correlation between cell count, lumen size and underlying scaffold geometry, whereby higher curvature (prevalent in ~45° scaffold angles) corresponded to increased cell density and greater lumen size.

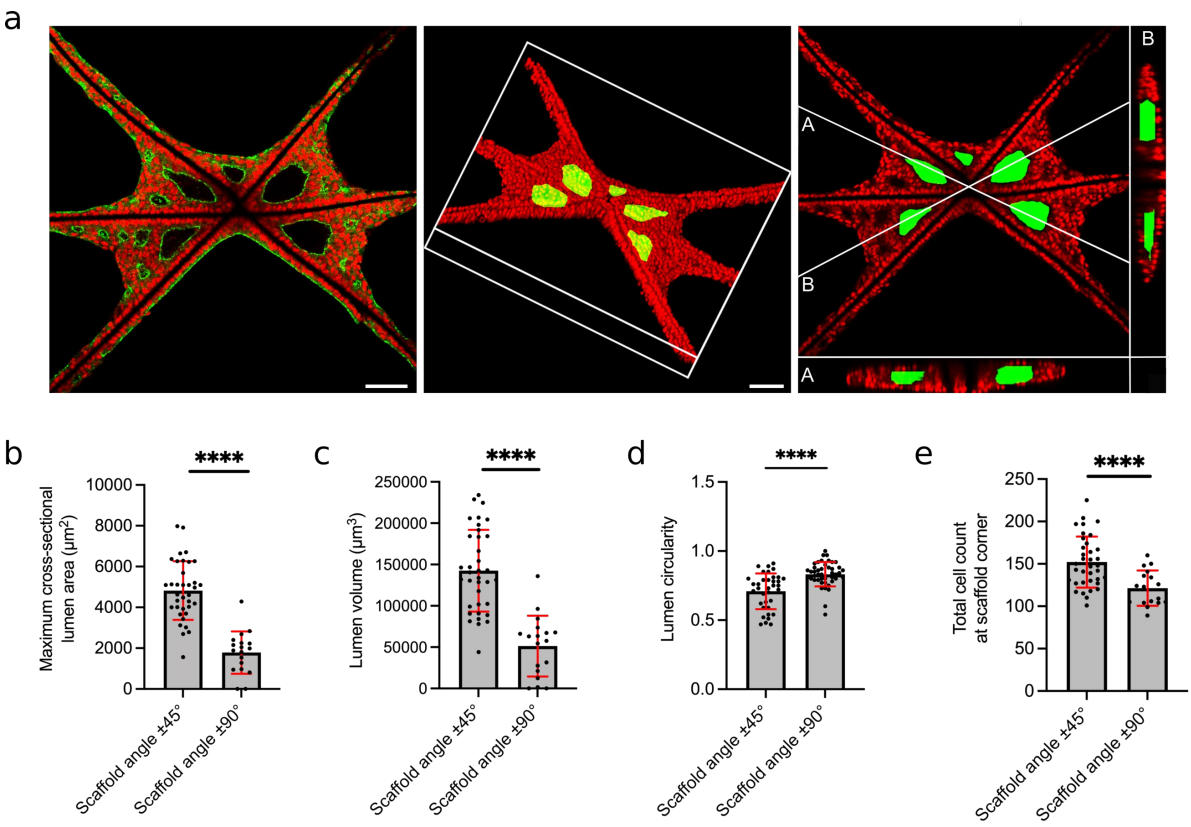


Figure 3.13 3D characterisation of hESC tissues on triangular scaffolds. *a) Image gallery at d 5 showing single slice of scaffold and hESCs immunostained with SOX2 (red) and Z01 (green) (left), 3D reconstruction from a confocal z stack, with the lumens segmented and pseudo coloured in green (middle) cross section of the confocal z stack showing a bisector slice through the lumens indicated by the white lines (right), scale bars correspond to 100 µm. Comparison between ~45° angles (45° ± 9°) and ~90° angles (90° ± 5°) for resulting: b) lumen cross-sectional maximum area, c) lumen volume, d) lumen circularity, and e) total cell count per scaffold corner. Data represent mean ± s.d. P value of (****) <0.0001 as determined by Welch's t-test.*

3.3.6. Curve-shortening flow predicts tissue growth and evolution on scaffold

Curvature-controlled tissue growth has previously been described as a model to predict the collective growth behaviour of cells in concave geometries.[168] This has typically been modelled on the behaviour of bone-like cells, that grow faster in concave regions of higher curvature.[68] The results in this study demonstrate that hESCs behave similarly to the bone-like cells in these studies, by showing preferential growth in the corners of the scaffold on concave geometries, i.e. regions of higher curvature, and increased cell count in scaffolds

with smaller ~45° angles (**Figure 3.12, Figure 3.13e**). To replicate this growth behaviour *in silico*, a simple 2D phenomenological growth model was implemented, largely based on the mathematical concept of curve shortening flow theory.[174] In brief, this model describes the evolution of a closed contour (in this case representing the tissue surface), where all points on the contour move in normal direction at a speed proportional to their curvature. Indeed, this simple model was able to accurately recapitulate the observed evolution of tissue growth that was observed experimentally on the square-, rhombus-, and triangle-shaped scaffolds. **Figure 3.14** demonstrates the curvature-controlled tissue growth for the square-, triangle-, and rhombus-shaped scaffold geometry as modelled by curve shortening flow.

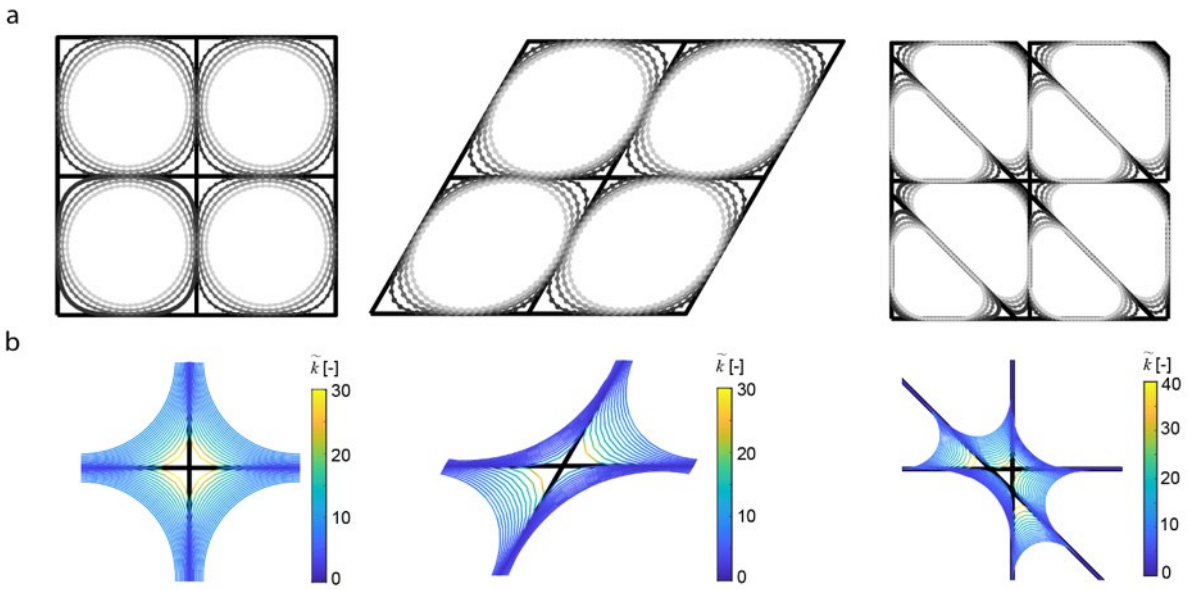


Figure 3.14 Curve shortening flow models hESC tissue growth on scaffolds. *a) tissue growth evolution modelled on a square-, rhombus- and triangular-shaped scaffold, with lighter grey representing later time points; b) evolution of normalised line curvature $\tilde{\boldsymbol{k}}$ of the tissue interface. This modelling was carried out by Dr Sebastien Callens.*

3.3.7. Rock inhibition increases lumen formation on scaffolds

Previous studies have demonstrated that lumen formation in hESCs involves the cytoskeletal contractility machinery.[52,56,173] Rho Kinase (Rock) is a key regulator of this, by mediating reorganisation of the actomysin cytoskeleton and regulating changes in cell shape and movement. Rock inhibitors, that target and inhibit the ROCK pathway and downregulate overall contractility, are commonly used in stem cell culture practices, to limit cell death and apoptosis.[55,173] Rho kinase (Rock) inhibitor was routinely added during the cell seeding step throughout this study, to promote cell survival on the scaffolds.

Interestingly, Rock inhibitor has also been shown to increase lumen formation in MDCK cells and hPSCs.[52,175] It has previously been shown that initial polarity orientation in cells requires Rac1-GTPase signalling, and defects in this signalling cascade can be rescued by ROCK inhibition, highlighting its role in the early stages of lumenogenesis.[176,177] Thus, to investigate the potential role of cytoskeletal contractility in tissue and lumen formation on the scaffold constructs, hESCs were cultured on scaffolds for 5 d in non-treated conditions (i.e. no Rock inhibitor), and compared to the control sample, which was treated with 50 µM Rock inhibitor (Y-27632) at d 0 (**Figure 3.15**). Concurrent with the previous results, the Rock inhibitor treated samples showed cell coverage across the scaffold region, with lumens appearing in the scaffold intersections of the triangle scaffold. In contrast, the non-treated cultures showed reduced cell attachment and proliferation, and no visible lumens.

To further understand whether the increased lumen formation with the addition of Rock inhibitor was due to its role in contractility during lumenogenesis, or due to a reduction in cell death following cell plating, we also looked at the effect of inhibiting another cytoskeletal regulator: myosin-II, that acts as a downstream effector of ROCK.

Myosin-II was inhibited by adding blebbistatin to the culture medium during cell seeding, effectively reducing contractility. Surprisingly, the blebbistatin-treated samples exhibited a similar tissue morphology as seen in the non-treated sample, namely limited cell attachment and minor tissue growth (**Figure 3.15**). A small proportion of lumens were present on the scaffold, however, which were considerably smaller than the samples

treated with Rock inhibitor. In contrast to these results, previous studies have shown that myosin-II inhibition promotes more efficient lumen formation than ROCK inhibition in hESCs.[52] It is plausible that the addition of ROCK inhibitor is a necessary initial step for cell survival on the scaffold, and blebbistatin is unable to act on the cells without this. In future studies it will be essential to test the impact of blebbistatin treatment when administered shortly after Rock inhibitor treatment, to see if lumen formation is further increased when applied in concert.

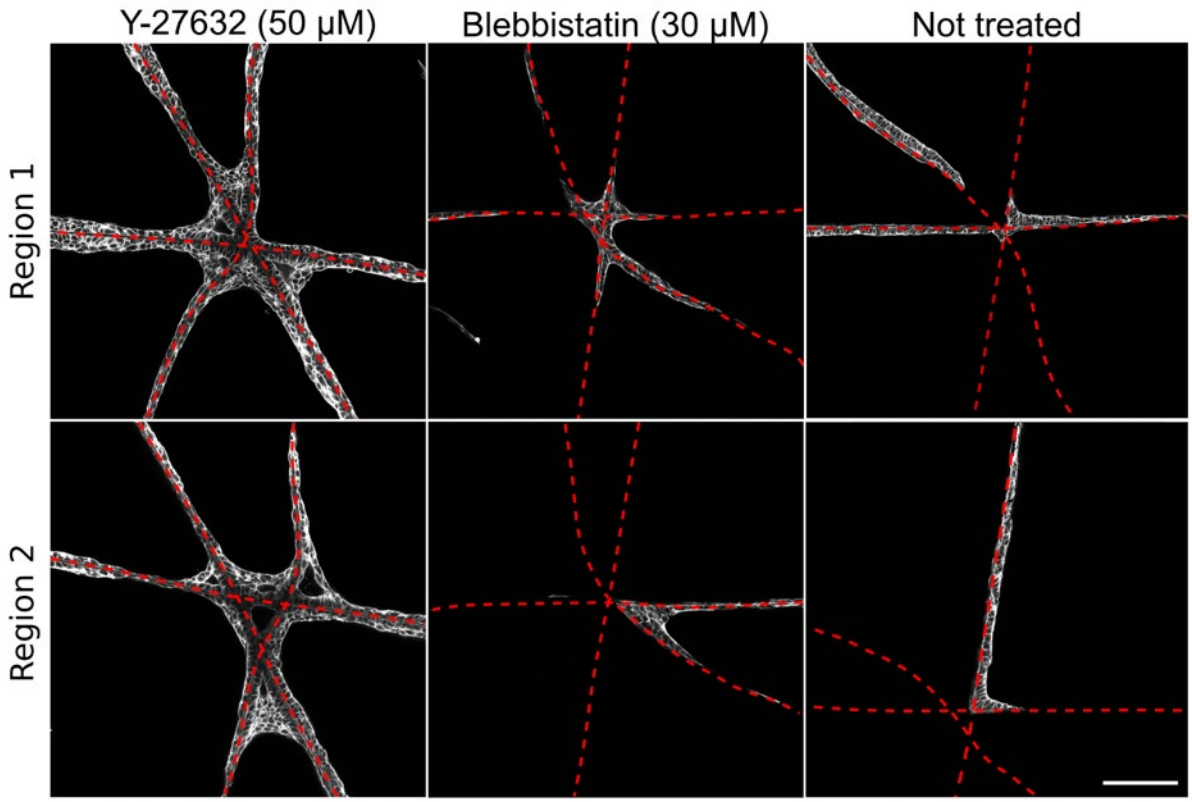


Figure 3.15 Rock inhibition promotes lumenogenesis on MEW scaffolds. *Confocal microscopy images of hESCs on triangle scaffolds stained with F-actin at d 5 with the addition of 50 µM Y-27632 (Rock Inhibitor) (left), with the addition of 30 µM blebbistatin (middle) and not treated (right). The dotted red lines mark the location of the scaffold. Scale bar corresponds to 200 µm.*

These results clearly demonstrate that ROCK inhibitor is necessary for lumen formation on scaffolds. However, it is unclear whether this is solely for cell survival and attachment

following cell plating, or if this plays a larger role in mediating the actomyosin network during lumen formation. It is also plausible that as lumen formation is a highly mechanosensitive process, the physical support provided by the scaffold effects cell and tissue contractility and promotes a different mode of lumen formation to previously reported studies. Further investigation will be essential to further unravel these mechanisms.

3.3.8. Generating a network of cerebral organoids on scaffolds

To determine the pluripotency status after 5 d, i.e., after mature lumens have formed, immunostaining was performed for three pluripotency markers, namely SOX2, NANOG and OCT4 (**Figure 3.16**). The tissues expressed all three markers, demonstrating that the 3D tissues maintained pluripotency during culture. This expression profile is consistent with a pluripotent epiblast identity *in vivo* and could thus give rise to a plethora of different cell types to recapitulate organogenesis in the human body.[32,162] To test if the stem cell scaffold platform was compatible with generating physiologically complex 3D tissue or organoid systems, stem cells were differentiated to cerebral organoids on the scaffolds. It was further investigated whether the lumens established during early growth would transition into the luminal VZ-like regions typically seen in cerebral organoids.[45]

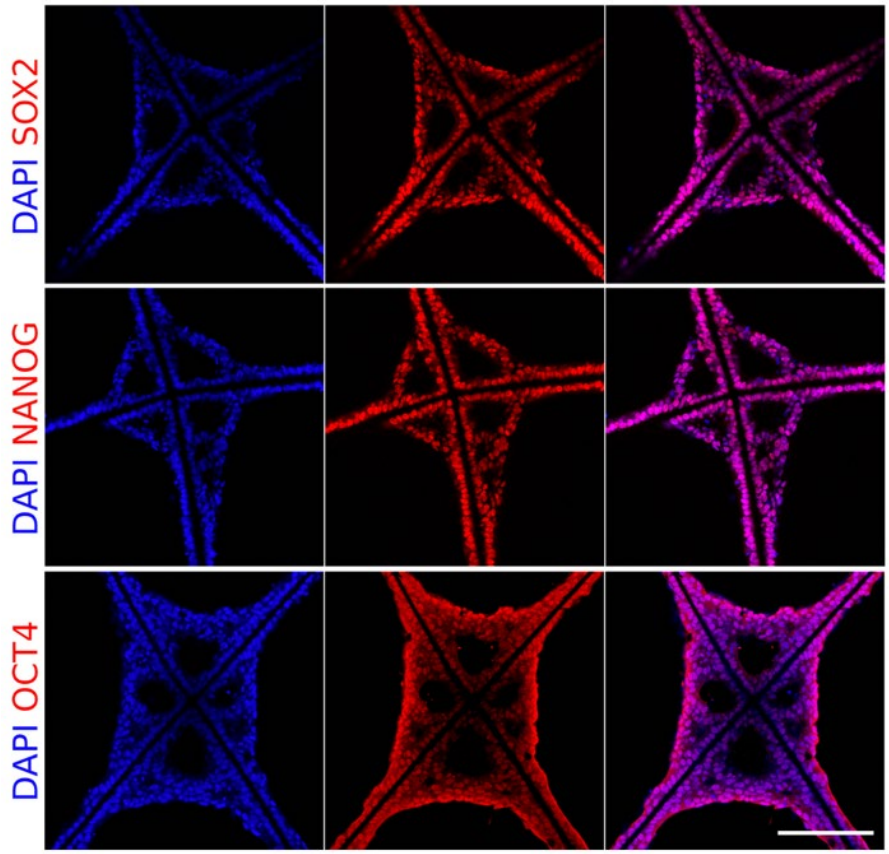


Figure 3.16. Characterisation of hESC seeded scaffolds at d 5. *by immunostaining with pluripotent markers of SOX2, NANOG and OCT4 (middle column) and DAPI counterstaining of the nuclei (left column) and merged images (right column). Scale bar corresponds to 200 µm.*

To first explore the structural changes in the developing organoid tissue from d 5, a time-lapse experiment was conducted using an F-actin probe, SiR-actin (**Figure 3.17**). According to established protocols in the literature, the cells were transferred to a neural induction media following 5 d of culture in mTESR media (as previously described in this Chapter) on square-shaped scaffolds with 500 µm spacing. Brightfield images clearly showed the lumen, whose structure was maintained until d 8. The corresponding fluorescence images showed F-actin strongly expressed at the lumen, similar to d 3 - 5 (**Figure 3.8**). At d 9, the lumens were no longer clearly visible in brightfield, and F-actin expression appeared less localized but increased throughout the entire tissue. Typically, between d 9 - 11, organoids are embedded in Matrigel to promote neuroepithelial expansion.[80] At d 9, the organoids were supplemented with Matrigel (optimised in Chapter 3). Following Matrigel addition, a

significant change was observed in the tissue morphology at d 10, and a total loss of localised F-actin expression at the lumens, indicating a major restructuring of the organoid tissue at this stage.

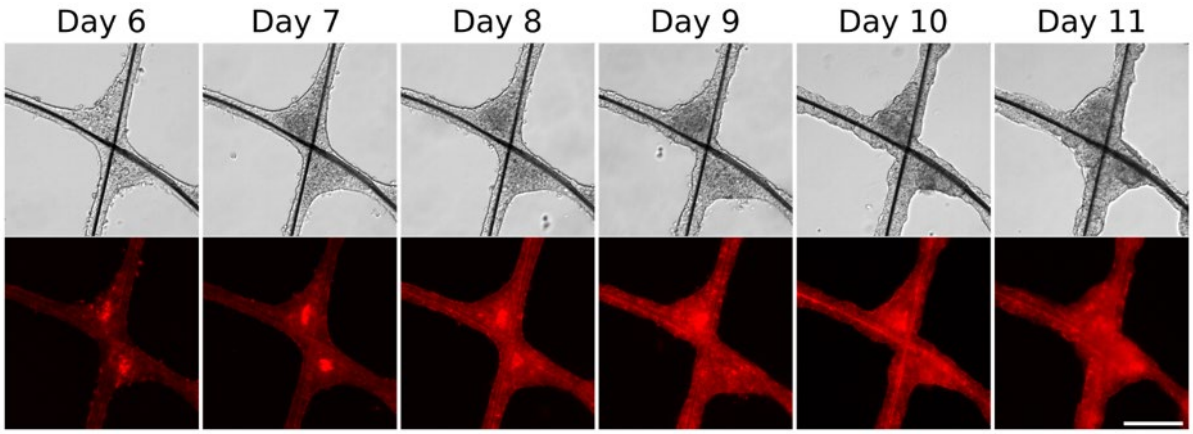


Figure 3.17 Cytoskeletal tissue dynamics during cerebral organoid growth on MEW scaffolds. *Consecutive frames from live imaging with the F-actin probe, SiR-actin, from d 6 (after neural induction) to d 11. Top: brightfield images, bottom: fluorescent images of F-actin. Scale bar corresponds to 200 µm.*

Next, the organoid tissue was cultured up to d 20 on different scaffolds, namely square-shaped scaffolds with 500 µm or 1000 µm spacing, and on triangle-shaped scaffolds. Brightfield images showed that the tissue remained completely interconnected across all scaffolds (**Figure 3.18a**). At d 11, tissue at the scaffold intersections appeared dense in the centre with smooth and optically clear edges, indicating neuroectoderm tissue, similar to the morphology of conventionally cultured cerebral organoids.[45] Interestingly, the scaffold walls were uniformly covered by a less dense, yet optically clear tissue (**Figure 3.18a,b**). According to previous studies, smaller organoids that are generated by lower seeding numbers show more relative clearing with neuroectoderm identity, yet go on to develop smaller neuroepithelial buds.[143] This suggests that the tissues located along the scaffold walls are neuroectoderm, yet less likely to develop large neuroepithlial buds and VZ-like regions than the larger tissues at the scaffold intersections. Unsurprisingly, the tissue thickness and growth characteristics vary between the different scaffolds. On the square-

shaped 500 µm spaced scaffolds, the tissue on the scaffold walls appeared thicker, i.e. the tissue extended further away from the wall, than for the 1000 µm spaced ones at d 11. Recent studies investigating cell bridging kinetics on MEW PCL scaffolds showed that cells proliferated faster in smaller spaced scaffolds compared to larger spaced scaffolds.[70,71] This tissue behaviour was explained by a curvature-driven mechanism that triggers an increase in cell proliferation occurring near the concave intersecting points of the scaffold. Similarly, the smaller scaffold spacing used in this study generates a higher number of geometrically concave regions, leading to a higher density of tissue on the 500 µm scaffold in comparison to the 1000 µm scaffold.

A clear morphological change in the tissues occurred at d 15, following the addition of Matrigel, by reducing the geometry-driven effect observed in previous results. Besides providing important biochemical cues, the addition of Matrigel provided additional mechanical support to the organoid environment, prompting neuroepithelial bud expansion (**Figure 3.18b** black arrowheads) that developed into the VZ-like areas. Additionally, a pulse of the Wnt activator CHIR 99021 (CHIR) was added at d 13 for 3 d. The combination of a polymer microfilament and CHIR pulse has previously been shown to stimulate larger VZ-like areas, with a more consistent formation of dorsal forebrain identity than other brain regions such as midbrain or hindbrain.[143] A greater level of tissue uniformity was also observed across the scaffold at this stage, with less discrepancy between the tissue width on the scaffold walls and intersections.

At d 17, results showed that the organoids on scaffolds displayed less well-defined neuroepithelial buds, and more compact ‘node’ like regions on the scaffold intersections, compared to the scaffold walls. Previous studies have shown that conventionally grown organoids generally expand quickly at d 15 – 20, after Matrigel addition. It was therefore reasoned that the observed morphological change in tissue on the scaffolds at d 17 was due to increased cell proliferation and differentiation, leading to denser organoid tissue at the scaffold intersections, with less visible neuroepithelial buds. It has previously been shown with bone-like cells growing on MEW scaffolds, that once a local cell density threshold is overcome, pore filling occurs and the cells grow inwards, forming a circular pore inside the

square.[71] Owing to the increased cell proliferation in the smaller spaced scaffolds, it was observed that pore filling progressed further by d 17 in the 500 µm scaffold than the 1000 µm scaffold, similar to previous reports. This curvature-controlled growth pattern was also evident in the triangle scaffold, as inward growing cells formed a triangular pore shape.

It should be noted that at this stage the organoids forming on the MEW scaffolds were largely homogeneous across the 4 x 4 cm scaffold in size, morphology, and density. This further demonstrated the suitability of this platform for high throughput screening for organoid culture.

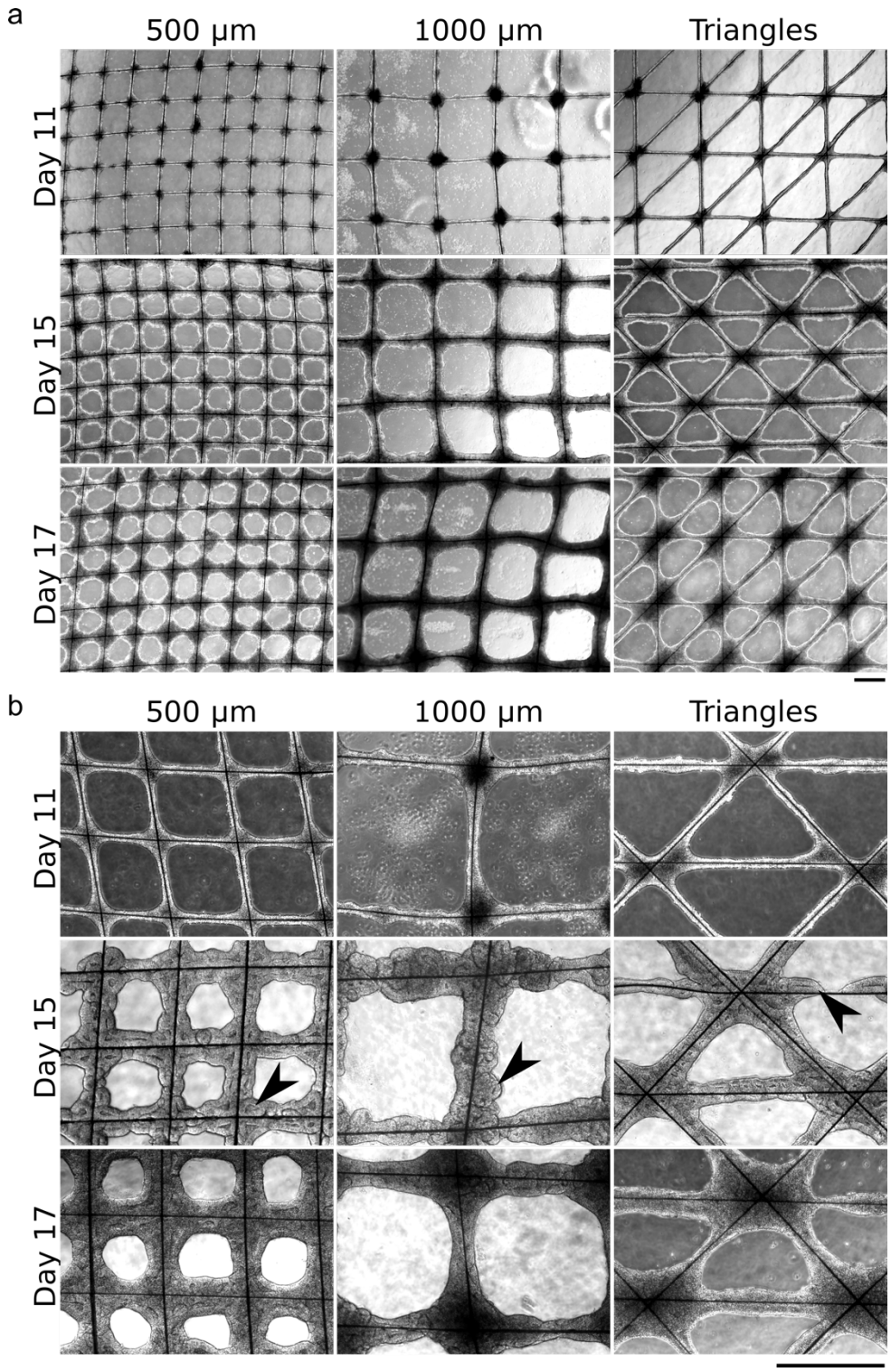


Figure 3.18 hESCs form cerebral organoids on MEW scaffolds. *a) Brightfield images taken at low magnification, showing the development of cerebral organoids on scaffolds at d 11, d 15 and d 17 on square-shaped scaffolds of 500 µm spacing (left), 1000 µm spacing (middle), and on triangle-shaped scaffolds (right). For all geometries, high reproducibility of the forming organoid tissue is apparent across the scaffold. b) Brightfield images taken at high magnification, showing the development of cerebral organoids at d 11, d 15 and d 17. Solid black arrows show neuroepithelial bud expansion. Scale bars corresponds to 500 µm.*

To examine whether the lumens that form during the stem cell culture period (up to d 5) act as precursors to the fluid-filled VZ-like cavities that typically develop in cerebral organoids, fixed samples were immunostained with Z01 marker at d 15. Confocal Z stacks clearly showed large luminal cavities at the scaffold intersections, visualised through 3D segmentation and false colouring (**Figure 3.19** middle and right). The VZ-like luminal cavities were similarly located to the epithelial lumens that were established during the stem cell culture period. This supports the hypothesis that guiding lumen formation using the scaffold structure also guides the formation of more complex organoid structures, such as the VZ-like regions in cerebral organoids.

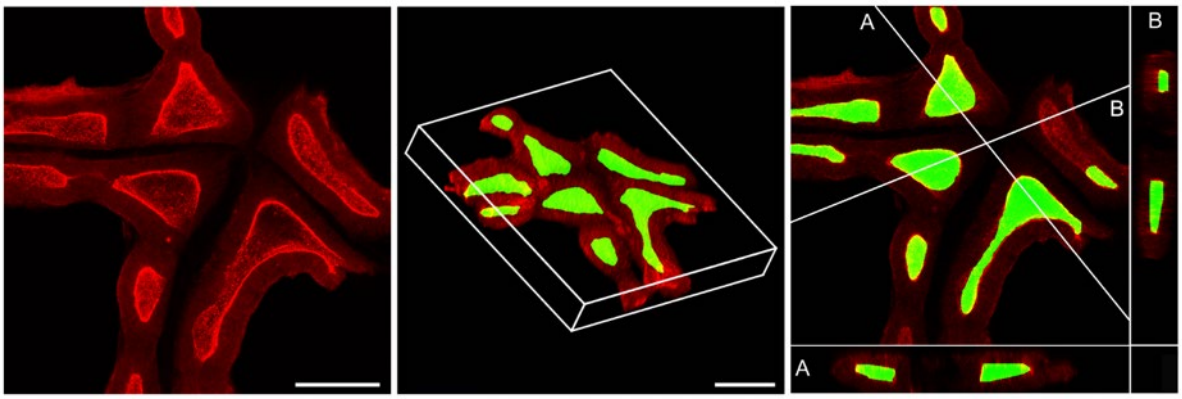


Figure 3.19 Image gallery at d 15 showing single slice of cerebral organoids on scaffolds. *immunostained with Z01 (red) (left), 3D reconstruction from a confocal z stack, with the lumens segmented and pseudo coloured in green (middle), cross section of the confocal z stack showing a bisector slice through the lumens, indicated by the white lines (right). Scale bars correspond to 100 µm.*

To characterise the cellular identity of the scaffold-cultured tissue and establish if they show a similar expression profile to conventionally grown cerebral organoids as reported in the literature, scaffold organoids were immunostained at d 20. Organoid tissue at the scaffold intersections showed the presence of FOXG1 cells, an anterior forebrain marker (**Figure 3.20a**). PAX6, a cortical progenitor marker, is typically expressed in the dorsal forebrain, and areas of co-expression of PAX6 and FOXG1 in the scaffold organoid tissue demonstrated regions of dorsal anterior forebrain identity. It is highly typical of an 'unguided' cerebral

organoid (that has not been subjected to small molecules and growth factors to guide regional patterning) to display a variety of cell lineage identities, such as dorsal forebrain.[45] Furthermore, immunostaining for SOX2, a neural progenitor marker, revealed a thick layer of progenitor cells within the VZ-like region alongside some TUJ1 positive cells, a marker for early neurons (**Figure 3.20b**, solid white arrowhead). This demonstrated the occurrence of neurogenesis and new-born neurons within these scaffold organoids.

Together these results show that the stem cell scaffold platform is compatible with generating interconnected cerebral organoids in a high-throughput way. Immunostaining characterisation further demonstrated a similar expression profile of markers typically present in cerebral organoids at d 20, revealing a highly promising platform for cerebral organoid culture.

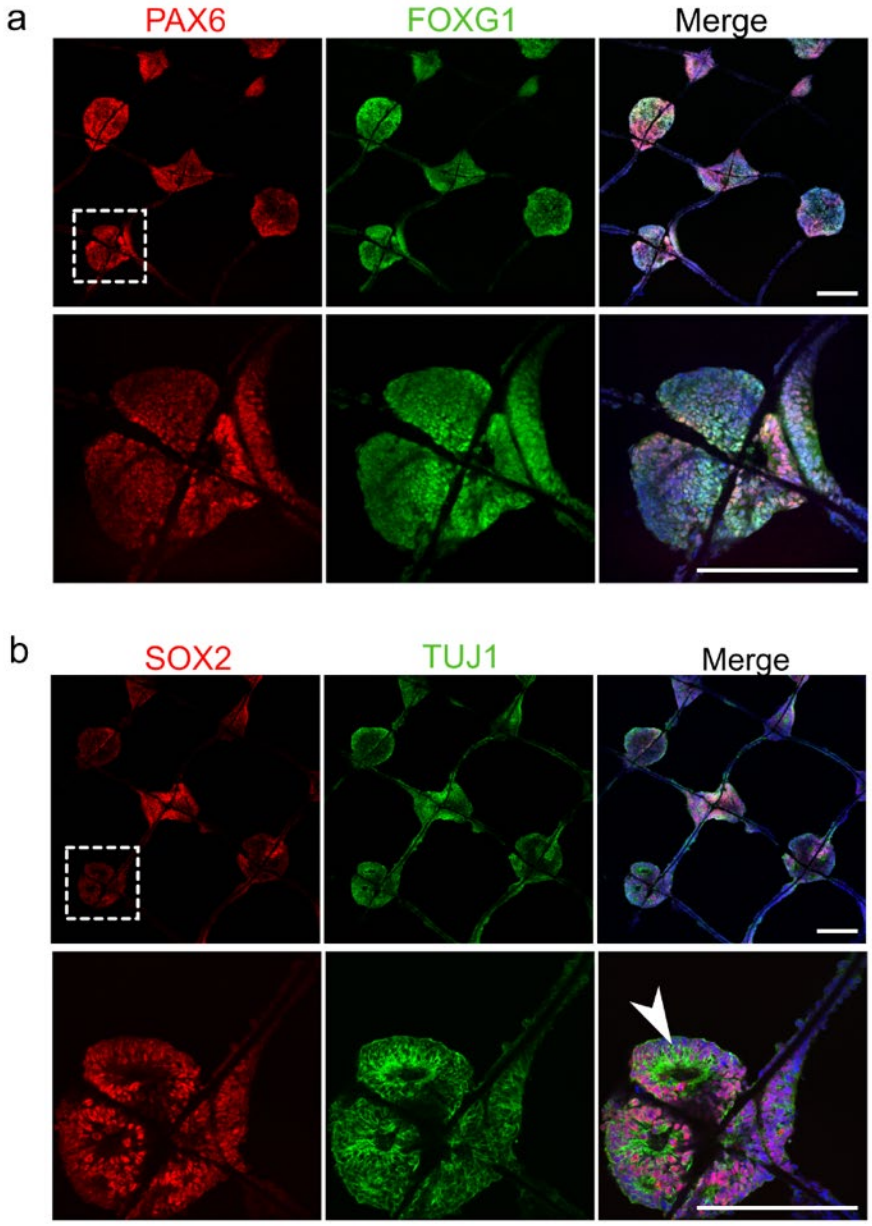


Figure 3.20 Immunostaining characterisation of d 20 cerebral organoids on MEW scaffolds. *Images of histological sections of organoid on scaffolds immunostained with a) dorsal forebrain marker PAX6 (red) and forebrain marker FOXG1 (green), b) with neural progenitor marker SOX2 (red) and neuronal marker TUJ1 (green). a-b) Top rows show overview of multiple organoids, bottom rows show magnified view of the respective region marked with a white dashed line. Scale bars correspond to 500 µm.*

3.4. Conclusion

Here, an *in vitro* stem cell scaffold platform was developed to guide the self-organisation of stem cells in a high-throughput manner. Scaffold geometry was shown to modulate lumen formation in a highly reproducible way, and this technique can be used in the formation of cerebral organoids. While micropatterning techniques used in previous studies were shown to modulate stem cell and organoid fate by providing biophysical confinement, they are typically limited to 2D structures located at the bottom of cell culture plates.[52,76] Thus, after the initial formation of tissue guided by the substrate, there is no further geometrical support provided in 3D.[167] Here, a highly controlled strategy was developed that uses biomaterial scaffolds to grow hESCs, that are suspended in the media during 3D growth. Compared to other platforms, this high-throughput system facilitates the 3D growth of stem cells whilst continuing to exert biophysical support for the duration of the culture period.

Together, these results demonstrate that the primary lumens developed in a highly predictable way on scaffolds and cells maintain pluripotency at d 5, prior to cerebral organoid differentiation. A significant finding of this study is that scaffold geometry and the resulting curvature of the scaffold is a predominant factor in guiding lumenogenesis. Primary lumen consistently grew in the corners of square-shaped scaffolds in the region of high curvature, and further investigation using triangle-shaped scaffolds showed a correlation between lumen size and curvature, with larger lumens preferentially growing in scaffold corners with acute angles. Furthermore, the evolution of tissue growth on the scaffolds was accurately described using a simple 2D curvature driven growth law, largely based on curve shortening flow. In future work it will be important to further explore the cellular mechanisms and signalling networks underlying this mechano-regulated self-organisation, which is expected to provide important insights for future scaffold design.

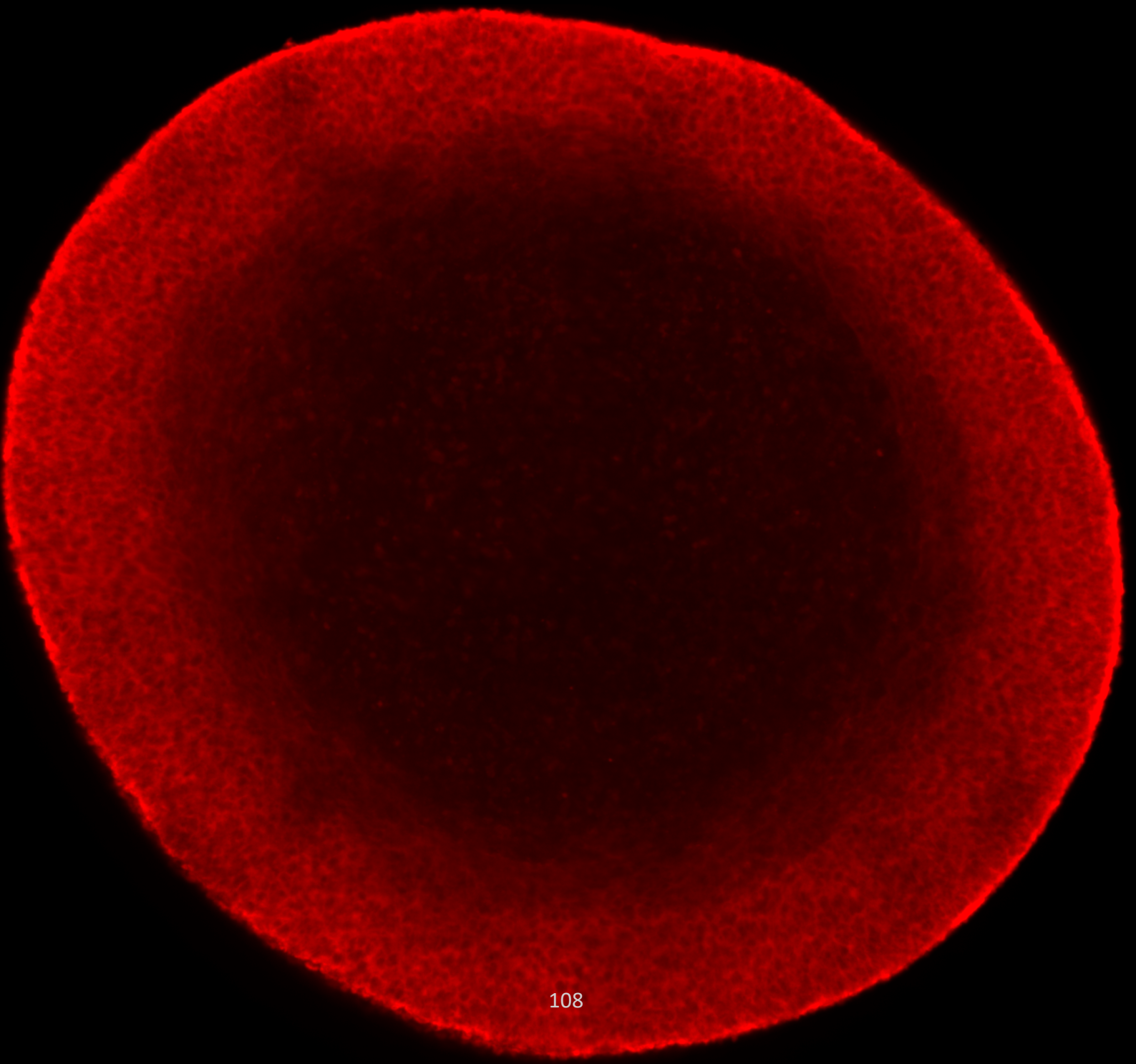
Currently, huge efforts are being made to manipulate and guide organoid models, to recapitulate the corresponding organ system more accurately. These results show that the biomaterial stem cell culture platform can be used in the growth of organoids, generating a large, interconnected network of cerebral organoids. Furthermore, VZ-like cavities were seen in the scaffold corners, demonstrating the continued effects of the biophysical support

during organoid growth. In future work it will be interesting to explore the specific benefits of an interconnected organoid network. This may provide several advantages, such as providing a controlled grid-like structure for electrophysiology studies. As a high-throughput system, this could also be beneficial for drug testing and mechanistic studies. Furthermore, the use of biomaterial scaffolds provides the additional opportunity to functionalise the scaffolds for the controlled delivery of growth factors and morphogens. This is further explored in in Chapter 5.

To unlock the full potential of this platform, it will be important to test the growth of other organoid structures that display prominent luminal features, such as lung, mammary, kidney and gut organoids. Finally, it will be interesting to explore the use of more complex 3D and 4D scaffold structures, potentially supported by parametric modelling approaches and computational design tools.

Chapter 4.

Scaffold guided cerebral organoid generation



4. Scaffold guided cerebral organoid generation

4.1. Introduction

In the previous chapter an *in vitro* scaffold platform was developed to guide stem cell self-organisation and concluded by briefly demonstrating that these scaffolds could be used to direct the culture of interconnected cerebral organoids. In this chapter, the scaffold-cultured organoid method is further explored and optimised, towards the high-throughput growth of spherical, independently growing cerebral organoids on scaffolds, as shown in **Figure 4.1**.

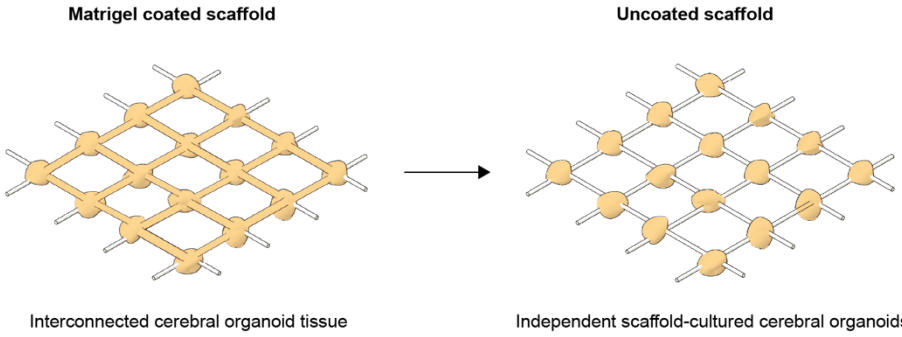


Figure 4.1 Schematic to show interconnected cerebral organoid tissue on Matrigel coated scaffolds as demonstrated in Chapter 3, and uncoated scaffolds with independently growing cerebral organoids, which is explored in this Chapter.

Cerebral organoids were first reported by Lancaster *et al*. in 2013 and have been a valuable tool for investigating developmental neurobiology and neurological disease modelling, as discussed in detail in Chapter 1. However, several major limitations remain which currently hinder the advancement of this *in vitro* model. In particular, the shape heterogeneity, batch-to-batch variability, and lack of a proper vasculature. Another current limitation of brain organoid technologies is the intensive manual manipulation required, limiting their scale-up potential. Overall, improving reproducibility and throughput of cerebral organoid

generation will significantly enhance their application in modelling neurodevelopment and neurological disease.

Bioengineering approaches can have a major contribution to addressing some of these limitations, by steering 3D organisation in a programmable way. During the *in vivo* development of organs, the physical environment plays an essential role in guiding tissue shape and organisation. Some studies have used this principle to develop physical structures to guide organoid morphogenesis *in vitro*. For example, Lutolf's group reported the fabrication of a 3D hydrogel with the characteristic shape of the crypt and villus-like structure typically found in the intestinal epithelium. These scaffolds were used to seed and grow intestinal organoids, that formed perfusable tube shaped epithelia with crypt and villus like domains.[178] However, this technique used microfabrication to form the crypt-like structures, rather than relying on intrinsic self-organisation properties to drive this growth. In more recent work, the same group used bioengineering strategies of photopatterning and microfabrication to guide the intrinsic self-organizing programs, without directing the outcome of the tissue morphology. This allowed the authors to develop macroscopic organoids with physiologically accurate anatomy.[149]

Biomaterials as macro-scale fibrous scaffolds also offer an opportunity to create niche physical structures by guiding 3D growth and influencing the emerging morphologies. Short, individual microfilaments of PLGA have previously been used as 'free-floating' scaffolds to generate engineered cortical organoids (enCORs). Introduced during cell seeding, the free-floating microfilaments provided a material interface for cells to adhere. This led to the formation of elongated organoids, ultimately improving the consistency and size of neuroectoderm by increasing the surface area to volume ratio.[143] While this study clearly demonstrated the potential for fibre-guided organoid formation, it was restricted by the uncontrolled nature of the free-floating microfilaments and variability in the number and size of fibres during the initial cell seeding step. In another recent study, Rothenbucher *et al.* (2021) generated PCL scaffolds for cerebral organoid culture with a well-defined honeycomb geometry, using 3D printing. The scaffold provided a material interface for the cells to adhere, eventually forming a large flat organoid, showing minimal necrosis in the

organoid core.[144] These recent studies demonstrate the advantage of incorporating macro-scale scaffold structures in brain organoid culture. Yet it remains a challenge to generate scaffold-mediated high-throughput organoids in a reproducible and controlled way.

Here, a new methodology that enables the controlled and high-throughput growth of cerebral organoids is described. Using the highly ordered PCL scaffold structures described in Chapter 3, a method was optimised to form spatially separated, spherical scaffold-cultured organoids, utilizing scaffold geometry to guide cell attachment and organoid growth in a controlled way. The scaffold-cultured organoids were benchmarked against conventionally grown cerebral organoids and short- and long-term organoid culture on the scaffolds was demonstrated. This platform can also scale up organoid generation, reducing the time intensive steps typically involved. Finally, scaffold-cultured organoids were used as a platform for advanced characterisation, by optimising a basic workflow for high-content biochemical analysis using Raman spectroscopy. Together, this work offers the advantage of a highly tuneable and controlled system compared to previously reported methods.

4.2. Materials and methods

4.2.1. Cerebral organoid culture on scaffolds

*Media formulations are described in **section 2.4**.*

D 0

At approximately 60% confluency, hESCs were dissociated from the well-plate by adding 1 mL accutase for 3 min at 37°C. The remaining adherent cells were sprayed off with 1 mL mTESR and cells were centrifuged at 200 g for 3 min. The cell pellet was resuspended in mTESR (Stemcell Technologies) stem cell media and a cell suspension was prepared in mTESR media containing 50 µM ROCK inhibitor Y27632 (Selleckchem) and 1% (v/v) Antibiotic-Antimyocytic (ThermoFisher) at a density of 1 x 10^5 cells per scaffold. After washing the scaffolds in PBS, scaffolds were placed in low attachment 6-well plates, or plates treated with 1 mL anti-adherence rinsing solution (Stemcell Technologies) for 1 min followed by washing three times in PBS. Scaffolds were secured at the bottom of the plate by pushing the CellCrown down using forceps. 3 mL of cell suspension was added per well, and the plate gently rocked in a North-South-East-West direction to evenly distribute the cells across the scaffold.

D 1

After 12 - 24 h of culture, CellCrowns were lifted by approximately 5 mm in the well plate to prevent cells from contacting the bottom of the well, while ensuring sufficient media coverage across the scaffold. The cells were left unperturbed on d 2.

D 3

mTESR media was exchanged with media without ROCK inhibitor or Antibiotic-Antimyocytic.

D 5 - 10

mTESR1 media was exchanged with a neural induction media (as described in **section 2.4**). Media was replaced every 2 d until d 10 – 13, when signs of optical clearing on the organoid borders were clearly present, as previously described.[80] Media was replaced every day until d 10 - 13, when signs of optical clearing on the organoid borders was clearly present.

D 10 - 13

When signs of optical clearing on the organoid borders were clearly present, organoids were embedded in Matrigel (Corning, cat. no. 356235). CellCrowns (with scaffolds and organoids attached) were gently lifted from the 6 well plate and placed on parafilm in a 10 cm petri-dish. Matrigel was added to the scaffold, to completely cover the organoids (approximately 1 mL). The organoids were then placed in an incubator for 30 min, to polymerize the Matrigel. The CellCrown was then gently removed from the parafilm (we found that sliding the scaffold off the parafilm rather than lifting minimised any damage to the scaffold or organoids). The CellCrown and scaffold assembly was then placed in a new 6 well plate and filled with 4 mL of neural induction media. 2 – 3 d after the first addition of Matrigel, media was changed to Improved -A media (as described in **section 2.4**). For 3 d, 3 µM CHIR 99021 (Tocris) was also added. 4 d later, improved +A media was added (as described in **section 2.4**), and media was changed every 2 d.

D 15

At approximately d 15, the scaffolds were transferred to a 6 cm petri dish to provide a higher volume of media (10 mL) to support organoid growth. The CellCrown was placed on a sterile plastic ring to prevent the organoids from touching the bottom of the plate.

4.2.2. Alternative Matrigel embedding protocol

When signs of optical clearing on the organoid borders were clearly present, 2% (v/v) Matrigel (Corning, cat. no. 356235) was added to the neural induction media (as described in **section 2.4**), and at every media change until the end of the culture period. The Matrigel solution was prepared by adding Matrigel to cold media. To prevent Matrigel polymerisation the media was warmed at RT prior to feeding, avoiding the use of water baths.

4.2.3. Brightfield imaging

Brightfield images were acquired with using the EVOS XL Core imaging system. For tiled images of the entire scaffold, images were acquired using the CellDiscoverer 7 microscope. Z stacks were acquired to account for tilt across the entire scaffold. Tiled images were fused using the Zeiss image processing software.

Organoid circularity and maximum diameter

Scaffold-cultured organoid diameter and circularity was calculated by creating 5 ROIs for each independent scaffold and using a custom-built macro in Fiji to segment the individual organoids (ROI's are shown in **Appendix B**). The same custom-built macro was used to segment the control organoids. The inbuilt measure function in Fiji was used to calculate area and circularity of the segmented organoid regions. Circularity is defined as: *4pi(area/perimeter^2).*

Scaffold organoid occupancy

Scaffold occupancy was calculated by creating an ROI in the centre of the scaffold, as shown in **Appendix B** and the number of scaffold intersections were counted using the inbuilt Fiji plugin CellCounter. Organoid occupancy was measured by counting the number of occupied intersections in the ROI region on 3 independent scaffolds using the CellCounter plugin.

4.2.4. Cryosectioning and immunostaining organoid sections

D 20 scaffold-cultured cerebral organoids were fixed in 4% (v/v) PFA in PBS overnight at 4°C and washed three times in PBS. Cryosectioning is described in **section 2.6**. Immunofluorescence staining is described in **section 2.7**. Antibodies are listed in **Table 4**.

Table 4 Antibodies used in Chapter 4.

Antigen	Host species	Supplier	Cat number	Dilution
SOX2	Rabbit	Abcam	ab97959	1:600
N-cadherin	Mouse	BD Biosciences	610920	1:500
FOXG1	Rabbit	Abcam	ab18259	1:200
PAX6	Sheep	R&D Systems	AF8150	1:200
TUJ1	Mouse	Sigma-Aldrich	T8578	1:500
GSX2	Rabbit	Sigma-Aldrich	ABN162	1:500
TBR1	Rabbit	Abcam	ab31940	1:300
MAP2	Chicken	Abcam	ab5392	1:500
CTIP2	Rat	Abcam	ab18465	1:300

4.2.5. Confocal imaging

Confocal imaging is described in **section 2.8**. Fluorescence images in this Chapter were also acquired using Visiscope Spinning Disc Confocal (Visitron Systems GmbH) equipped with a Yokogawa W1 spinning disc. Raw data was processed using open-source image analysis software Fiji ImageJ (version: 2.3.0).

4.2.6. Time lapse imaging

For timelapse imaging at d 5 - 9, scaffolds were placed in glass bottom 6 well plates for imaging, containing fresh media. The cell crown was lifted approximately 1 mm from the bottom of the surface. 100 nM SiR-actin (Cytokeleton, Inc.) was added to the neural induction media approximately 1 h before imaging. A fully automated CellDiscoverer 7 microscope (Zeiss) was used for timelapse imaging, comprising an environmental chamber (37°C, 5% CO_2). 7 positions were acquired every 3 h in brightfield and fluorescence mode. Each position was acquired as a z stack. At d 9, image acquisition was paused for approximately 30 min as the well plate was removed from the microscope for fresh media exchange containing neural induction media (as described in **section 2.4**) supplemented with 2% matrigel (Corning cat. no. 356235).

Colour map of organoid growth contours

A custom Fiji macro was used to overlay the images from the time series and create outlines of the growing organoid to generate a colour contour map, using the 'royal' LUT.

Actin intensity and orientation for bi-directionality measurements

Fluorescence images from the time-lapse imaging were analysed using a custom Fiji macro to measure actin intensity and orientation. Briefly, the macro was scripted to assign a value of 1 the angles of the scaffold (0, 90, 180) The points at an angle furthest from the scaffold (45, 135, -45, -135°) were assigned a value of 0. For each timepoint, organoid regions positive for the actin marker were thresholded, then assigned a value between 0 and 1 depending on their location relative to the scaffold (i.e. a value of 1 would be preferentially aligned to the scaffold, whereas a value of 0 would be no particular alignment to the

scaffold). For each timepoint, a mean of these values was taken, generating a bidirectionality measurement. Actin area was also calculated from the thresholded regions.

4.2.7. Optical Clearing

D 11 and 20 organoids were fixed in 4% (v/v) PFA in PBS overnight at 4°C and washed three times in PBS. Optical clearing is described in **section 2.9**.

4.2.8. Raman spectroscopy imaging

Scaffold organoid samples were fixed in 4% (v/v) PFA overnight at 4°C, then washed three times in PBS. The fixed samples were embedded in a 6 cm petri dish in 0.8% (w/v) low melting point agarose. Once the agarose was sufficiently gelled, PBS was added to completely immerse the sample. Organoid samples were imaged using a confocal Raman microscope (alpha300R+, WiTec, GmbH) with a 63x Water immersion objective lens (W Plan-Apochromat, Zeiss) and 532nm excitation laser. For analysis, a reference spectra library of different biomolecules was collected in-house by Xiaoyu Zhao, and compared with the sample spectra to identify the most abundant biomolecules. Raman spectroscopy imaging and analysis was carried out by Dr Vernon Lalone.

4.3. Results and discussion

4.3.1. Optimising culture conditions for organoids on scaffolds

To effectively design a bioengineered platform to generate high-throughput organoids in a controlled way, we started by looking at methods typically used to generate 3D neural cultures in the literature. In 2014, Ranga *et al.* reported 3D differentiation of mouse ESCs into neuroepithelial cysts, with hallmarks of the developing neural tube.[179] The neural cysts were formed by starting with a single cell suspension of mouse ESCs, embedding the single cells in an extracellular matrix, and culturing them under neural induction conditions (**Figure 4.2a).** Whilst culturing single cells promoted the expansion of a single lumen with neuroepithelial identity, the cyst sizes were variable. More recent studies have used geometric confinement to control the size and shape of neuroepithelial cysts to model the neural tube (**Figure 4.2b).**[180] As previously discussed in Chapter 3, one limitation of micropatterning is that the geometrical constraints are provided in 2D, thereby limiting the 3D growth of the tissue.[167] It is also important to note that these studies are limited to neural tube models, with early timepoints (<10 d).

To model more mature stages of embryonic brain development, protocols for the long-term culture of cerebral organoids have been developed (>100 d).[80] As shown by the number of steps illustrated in **Figure 4.2c**, conventional organoid culture is a more labour-intensive process, requiring time consuming maintenance. Typically, hPSCs are dissociated, and plated in low attachment 96 wells. After 3 d of culture in stem cell medium, this is replaced with a neural induction medium to induce neuroepithelial tissue growth. Once the organoids show smooth and optically translucent edges, they are individually selected and embedded in Matrigel, then transferred to a petri dish where the organoids are 'free-floating', and eventually placed on an orbital shaker for long term culture. In more recent studies, it has been shown that incorporation of a PLGA microfilament, combined with a pulse of the Wnt activator CHIR during organoid culture improves the reproducibility of tissue architecture in brain organoids (**Figure 4.2d**).[143]

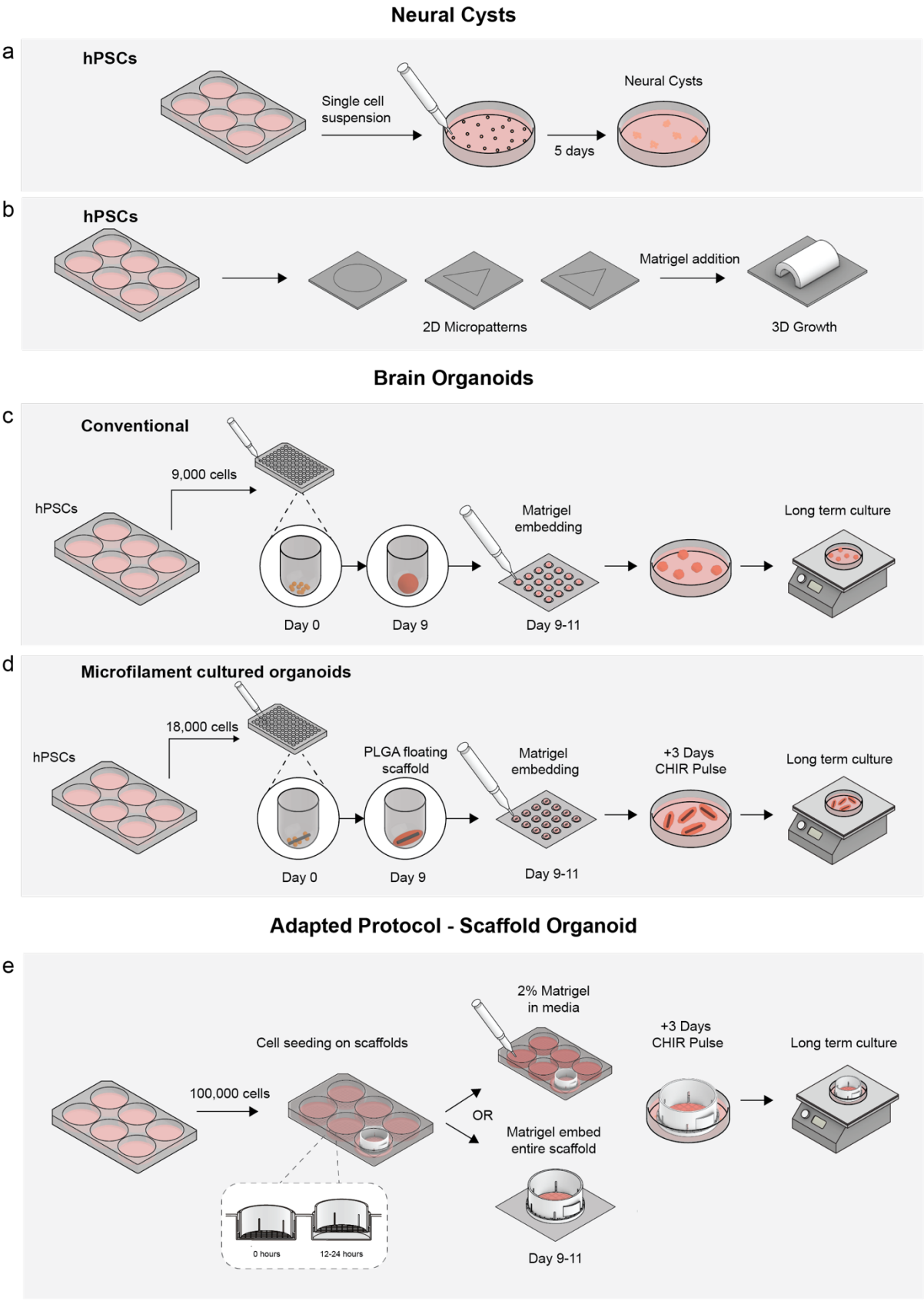


Figure 4.2. Schematic to show protocols for in vitro neural tube or organoid models alongside the adapted scaffold organoid culture platform. *a) Neural cysts with a single lumen are formed by seeding a single cell suspension in neural differentiation medium as*

described by Meinhardt et al. (2014).[179] b) Neural tube formation by seeding on 2D micropatterned substrates as demonstrated by Karzbrun et al. (2021).[76] c) conventional brain organoid culture by seeding cells in 96 well plates, then individually selecting and transferring organoids for Matrigel embedding and long term culture, as shown by Lancaster et al. (2014).[80] d) Microfilament cultured organoids are generated by using PLGA fibres as floating scaffolds during organoid culture, as demonstrated by Lancaster et al. (2017).[143] e) The adapted scaffold organoid culture platform in this study utilizes a PCL scaffold, with a single cell suspension seeded in a 6 well plate for high-throughput organoid generation. Organoids are embedded en masse on the scaffold, or 2% (v/v) Matrigel is added to the media for long term culture.

In preliminary studies before incorporating scaffolds, we first sought to minimise the labour-intensive steps associated with conventional organoid culture, by plating hESCs in a single cell suspension in a low attachment 6 cm plate, similar to previously described methods for neural cyst formation. To encourage the growth of cerebral organoids, media changes described in the conventional cerebral organoid protocol were used (as described in materials and methods). This resulted in a tendency for cells to fuse together in the middle of the well, resulting in highly variable organoid sizes, as further discussed in **section 4.3.2**. However, by incorporating this method together with the PCL scaffolds, it was possible to effectively grow organoids in a controlled, high-throughput manner, minimizing the labour-intensive steps. The scaffold organoid culture platform is schematically illustrated in **Figure 4.2e.**

4.3.2. High throughput organoid growth on scaffolds

For cell seeding, scaffolds with a grid spacing of 500 µm were fixed onto a CellCrown device and placed in a low attachment 6-well plate. Next, 1 x 10^5 wild-type H9 hESCs suspended in culture media were seeded directly onto the scaffold in a single cell suspension, gently shaking the well plate to ensure even distribution of cells across the scaffold. Brightfield microscopy showed that cells started to cluster and aggregate at the lattice intersections at d 2 (**Figure 4.3**). These aggregates continued to grow, forming embryoid body (EB)-like aggregates at d 4.

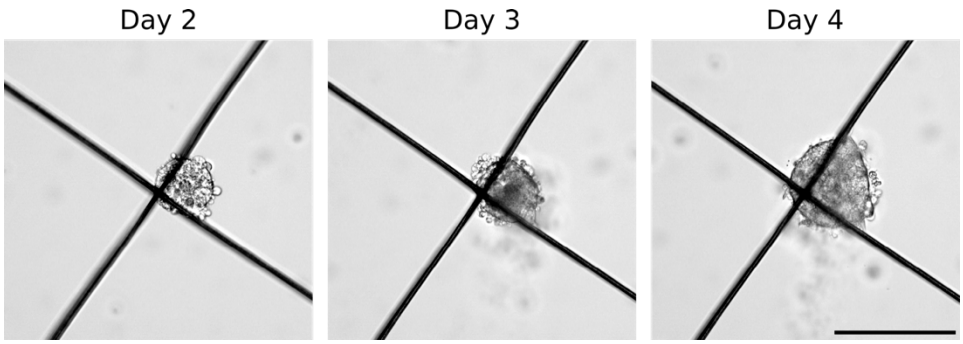


Figure 4.3 Stem cell aggregation at scaffold intersections. *Representative brightfield time-lapse images at D 2-4 show hESCs aggregate and grow at the scaffold intersection (n = 7). Scale bar corresponds to 200 µm.*

At d 5, media was exchanged to a neural induction media, to support the growth of neuroectoderm tissue. At d 9, organoids were visibly fully attached to the scaffold at the intersection points, with smooth edges and optically translucent borders, indicative of neuroectoderm formation (**Figure 4.4a**, solid black arrowhead). Conventionally grown round organoids, and organoids grown from a single-cell suspension in a 6 well plate without a scaffold (hereafter termed 'scaffold-free organoids') showed a similar morphology.

At d 9, scaffold-cultured organoids were embedded in Matrigel to promote the outgrowth of neuroepithelial tissue. In conventional organoid culture, this typically occurs by individually pipetting organoids into drops of Matrigel on dimpled parafilm, and then transferring these to a 60 mm dish in neural induction media after Matrigel polymerisation. Here, an alternative strategy was devised to embed all scaffold attached organoids in Matrigel simultaneously. This was achieved by lifting the entire CellCrown and scaffold onto a sheet of parafilm and adding Matrigel directly to the scaffold. Following Matrigel polymerisation, the parafilm was removed and the CellCrown and scaffold assembly was placed in a 6 well plate with neural induction media. This method evenly coated the organoids across the entire scaffold, which is essential for consistent growth of neuroepithelial tissue. Typically, during conventional organoid culture, organoids are exposed to some shear stress during Matrigel embedding due to the necessity to pipette organoids out of the 96 well plate. Here, the scaffold provided a means to Matrigel embed the organoids without the need for pipetting, causing minimal disturbance to the organoids,

which remained fully attached to the scaffold. The scaffold platform provides a method to simultaneously embed all attached scaffold organoids in a facile, single step process that avoids the time and labour-intensive process of manually pipetting individual organoids.

2 d after Matrigel embedding, organoids were transferred to neural differentiation media, and supplemented with a pulse of Wnt activator CHIR 99021 (CHIR), which has previously been used in combination with PLGA microfilaments for more consistent formation of brain lobules in the growing organoid.[143] At d 17, scaffold organoids clearly displayed neuroepithelial budding, that appeared morphologically similar to conventional and scaffold-free organoids (**Figure 4.4a**, white line arrowhead). Tiled images of the entire scaffold at d 20 demonstrated a highly ordered array of uniform organoids across the entire 4 cm scaffold, that showed progressive increase in maximum organoid diameter over time (**Figure 4.4b,c)**. To assess the efficiency of organoid formation on the scaffolds, the percentage of scaffold intersections occupied by an organoid was measured. Due to some scaffold deformations at the edges, a representative ROI was selected for organoid counting in 3 independent experiments (**Appendix B**). In a typical 500 µm spaced scaffold, the mean organoid occupancy across 3 independent organoid scaffold samples was 35 % ± 14 % with a mean of 402 ± 161 organoids and 1161 scaffold intersections. These results demonstrate that organoid generation on the scaffolds is high-throughput, yet there is significant potential to improve this with further optimisation to increase organoid occupancy in future work.

We next sought to quantitatively characterise the scaffold organoids and compare them to the control systems. Scaffold-cultured organoids were considerably smaller in size at d 20 than conventional or scaffold-free organoids, with a mean maximum diameter of 0.47 ± 0.15 mm compared to 1.95 ± 0.33 mm and 1.53 ± 0.45 mm, respectively (**Figure 4.4d**). The scaffold-cultured organoids were also more consistent in size. In contrast, the scaffold-free organoids showed a larger size distribution. This likely occurs due to uncontrolled fusion of the organoids in the well plate, as previously described. Next, organoid circularity at d 20 was measured, to see if the scaffold influences organoid shape. Scaffold-cultured organoids showed a significantly higher circularity than the organoid controls (**Figure 4.4e)**. Overall,

these results demonstrated that the scaffold platform facilitates controlled growth of organoids, by providing spatial separation on the grids, and promoting a more consistent circular organoid shape.

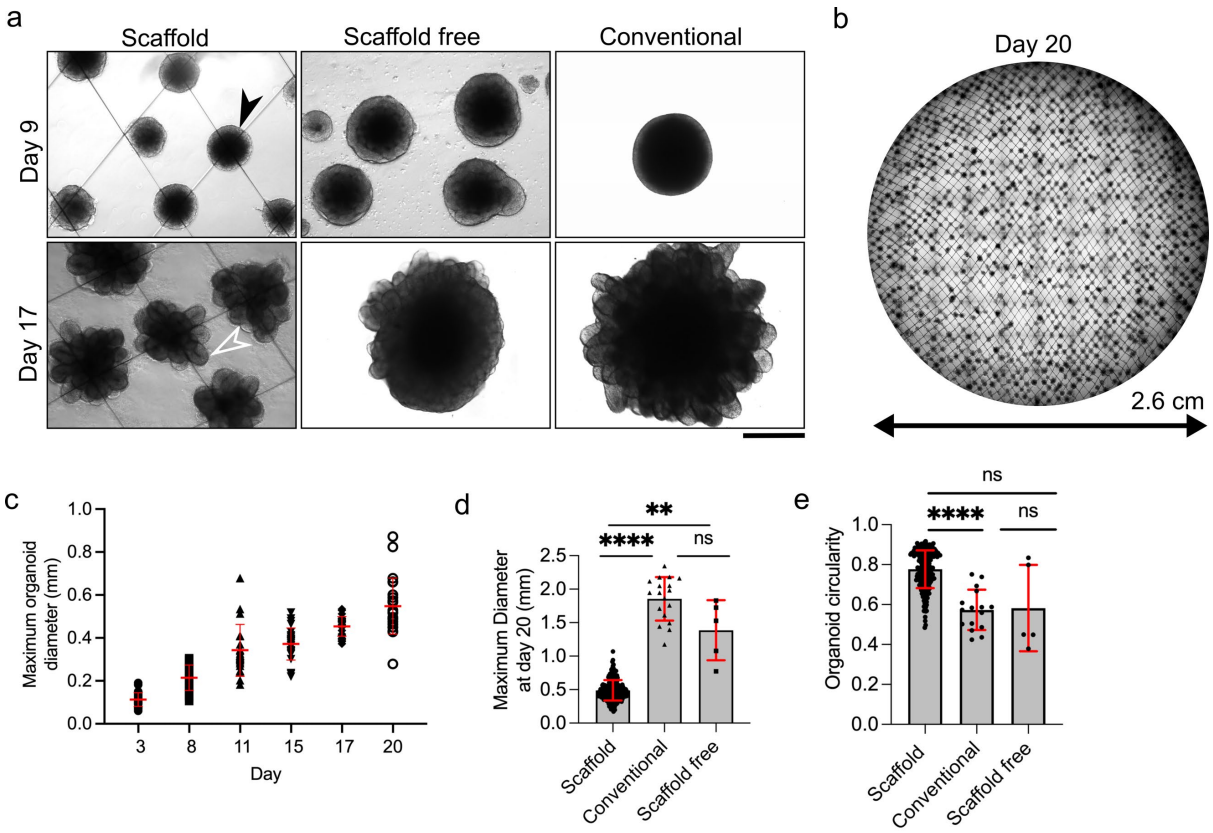


Figure 4.4 Characterisation of cerebral organoid growth on scaffolds*. a) Brightfield images show organoids grown on scaffolds, scaffold-free organoids, and conventionally grown organoids. Top: D 9 before Matrigel embedding. The smooth and optically translucent organoid edges are shown by the solid black arrowhead. Bottom: D 17 after Matrigel embedding and CHIR pulse. Neuroepithelial buds are shown by the white line arrowhead. Scale bar corresponds to 500 µm. b) Tiled overview image of the entire scaffold with organoids at d 20. c) Mean diameter of organoids grown on scaffolds from d 3 to d 20. Analysis was performed on organoids from 1 batch of scaffold-cultured organoids (N = 1) with a minimum of 23 organoids analysed for each time point. Data represent mean ± s.d. d) Maximum diameter of organoids at d 20. Analysis was performed on organoids from 3 independent batches (N = 3) with a minimum of 5 organoids in total using a custom Fiji macro. Data represent mean ± s.d. e) Comparison of organoid circularity at d 20 obtained through image analysis using the inbuilt measure function in Fiji. Analysis was performed on organoids from 3 independent batches (N = 3) with a minimum of 5 organoids in total. Data represent mean ± s.d. P values: (****) <0.0001 and (**) = 0.0011, by determined by Kruskal-Wallis with Dunn's post-test.*

4.3.3. Scaffold guided growth dynamics of early cerebral organoids

To investigate the mechano-biological effects and cytoskeletal response of organoids grown on scaffolds, time-lapse microscopy was carried out with a live F-actin probe, Silicon-Rhodamine (SiR)-actin. This revealed F-actin accumulation on the leading edge of the organoid in contact with the fibre scaffold at d 6 - 9 (white solid arrowhead), and along the entire length of the fibre inside the organoid body from d 8 (white line arrowhead) (**Figure 4.5a,b**). Tracking the organoid contour between d 5 – 9 revealed a dynamic change in the organoid shape, following a growth trajectory aligned with the scaffold structure (**Figure 4.5c**). To quantify the spatial distribution of F-actin and its directionality in the growing organoid, the positive regions of F-actin expression in the organoid was thresholded. Vectors were then assigned to these regions from the centre point of the scaffold, using a custom scripted Fiji macro. This was correlated to the 0 – 90° angle of the scaffold, thereby allowing us to assign a value of bi-directionality. An increase in the directionality of F-actin expression towards the scaffold over time was observed. This was concurrent with an increase in overall F-actin area, calculated through intensity thresholding (**Figure 4.5b,d)**. Taken together, these results demonstrated that the scaffold fibre plays a significant role in guiding organoid morphogenesis on the scaffolds. This was attributed to the mechanical forces of the fibre, which may provide a physical guide for the growing organoid, facilitating the coordinated growth and movement of cells in 3D.

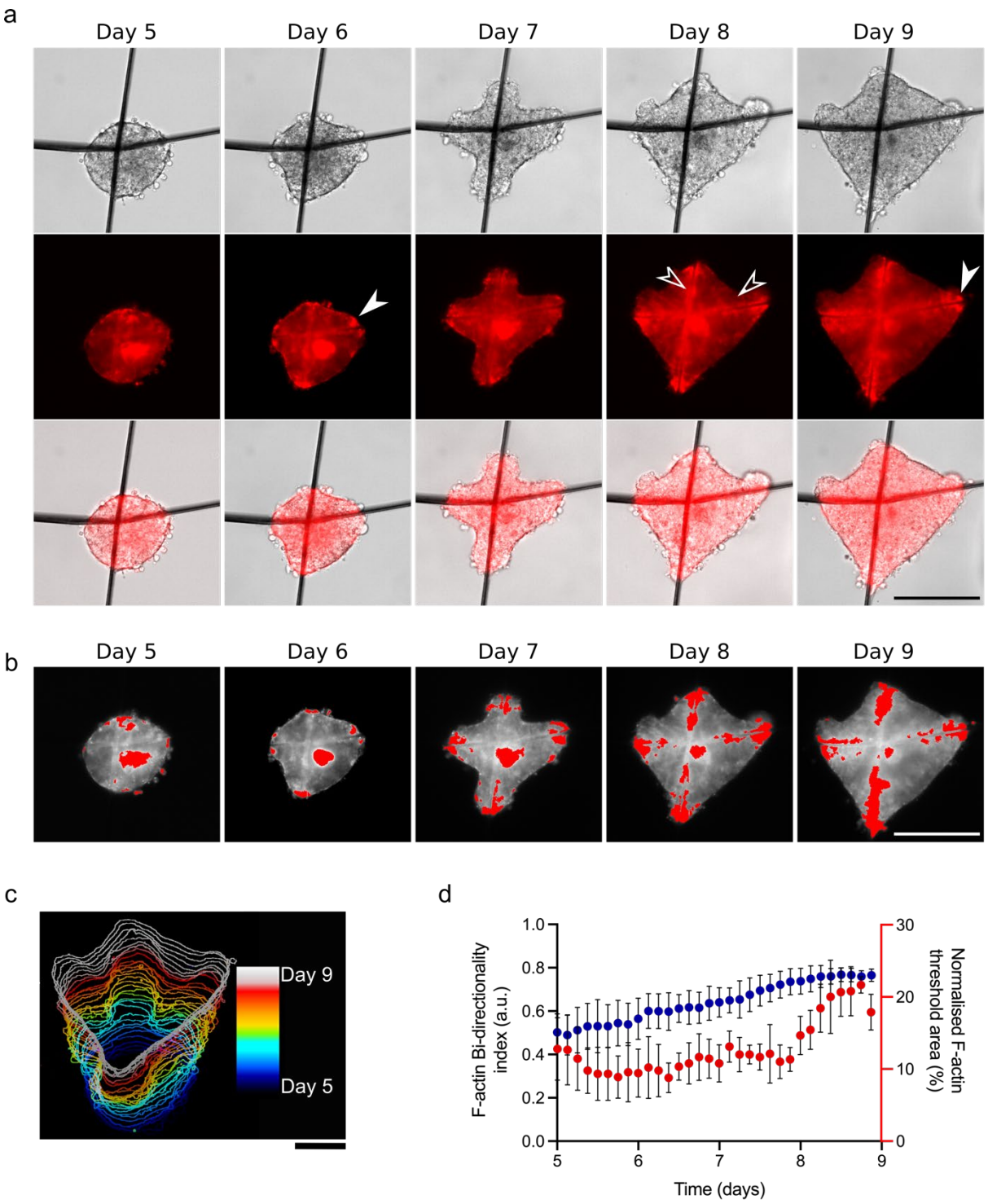


Figure 4.5 SiR-Actin accumulation and distribution during early cerebral organoid formation. *a) Consecutive frames from live imaging of tissues stained with F-Actin from d 5 to d 9 (n = 7). Top: Brightfield images of the growing organoid on the scaffold intersection, middle: fluorescent images showing F-actin expression accumulating in the leading edge of the growing organoid in the direction of the fibre (solid white arrowhead) and along the length of the scaffold fibre at d 8 and 9 (white line arrowhead), bottom: Merged images. Scale bar corresponds to 200 µm. b) Thresholded F-actin signal used to calculate bi-*

directionality value of actin during cerebral organoid growth. Scale bar corresponds to 200 µm. c) Colour map of organoid growth contours from d 5 - 9. Scale bar corresponds to 100 µm. d) Bi-directionality index (calculated as a value of thresholded F-actin expression) increases over time, concurrent with the total percentage of F-actin area in the organoid.

We next performed tissue clearing to visualise the organoids in 3D. Interestingly, at d 11, two separate pseudostratified regions expressing SOX2, demarcated by a concentric ring of N-cadherin were observed in the scaffold-cultured organoid (**Figure 4.6a**, solid white arrowhead). This was morphologically reminiscent of 3D neuroepithelial cysts cultured from a single cell suspension, as previously reported.[139,179,181] The scaffold appeared slightly deformed by the emergence of a rosette structure in the centre. Strikingly, at d 20, the N-cadherin marker showed that the scaffold deformations appeared far more pronounced, as the lumen structures grew around the scaffold, highlighting the interaction between scaffold and tissue (**Figure 4.6b**). Furthermore, brightfield images taken at d 15 and 16 clearly demonstrated the emergence of the VZ-like lumen region which preferentially occurred in the scaffold corners (**Figure 4.6c)**. This was similar to the observation of lumen emergence in the curvature regions on Matrigel coated scaffolds in Chapter 3, demonstrating scaffold guided morphogenesis of the organoids.

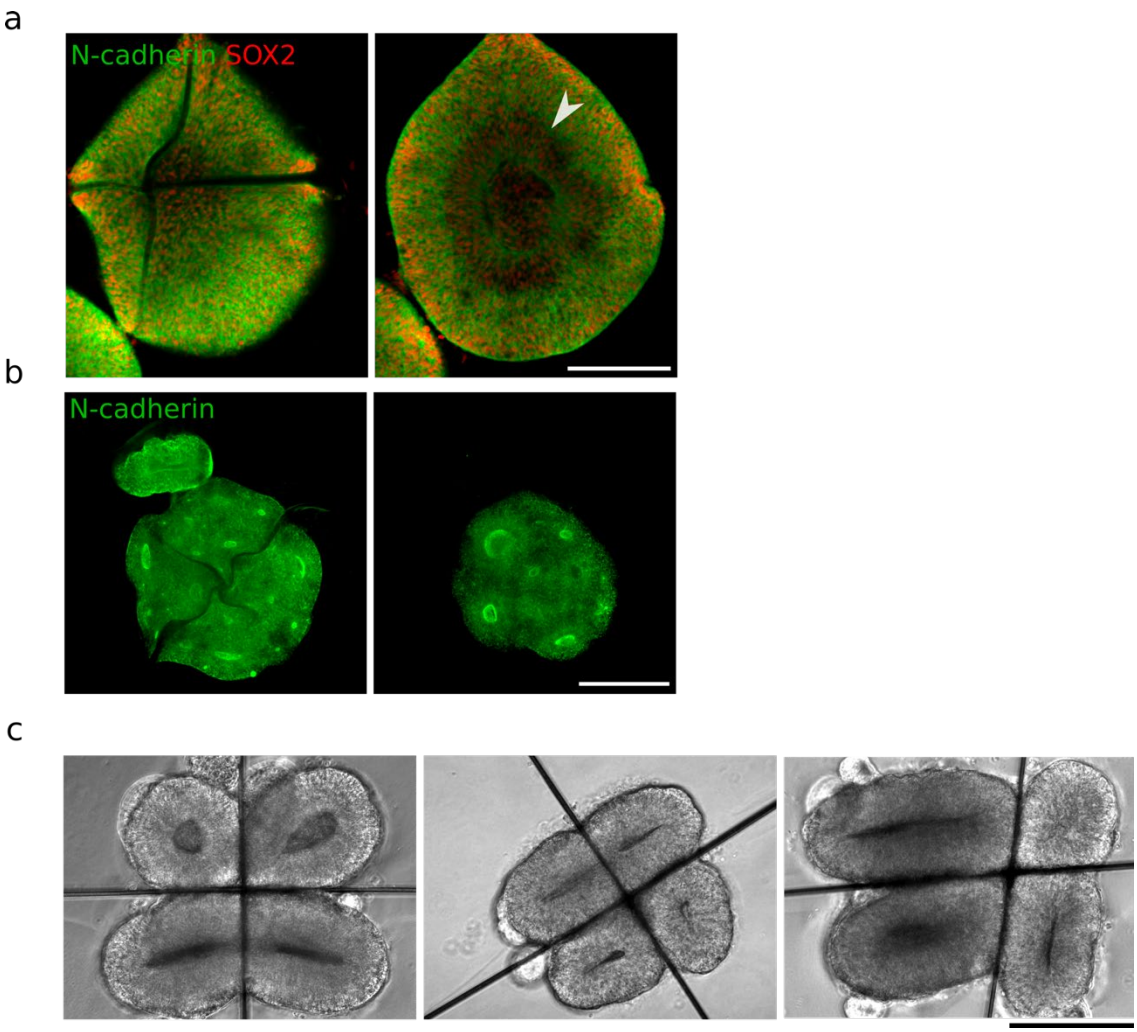


Figure 4.6 3D characterisation of the organoid-tissue growth dynamics. *a) Fluorescent images of a d 11 organoid that has been cleared and immunostained with N-cadherin (green) and SOX2 (red). A single slice from the z stack in the centre of the organoid showing the scaffold outline and organoid tissue (left), and a single slice from the z stack of the organoid showing the central lumen structure surrounded by a pseudostratified ring of SOX2-expressing progenitor cells (solid white arrowhead) (right). Scale bar corresponds to 200 µm. b) Fluorescent images of a d 20 organoid that has been cleared and immunostained with N-cadherin (green). A single slice from the z stack in the centre of the organoid showing the scaffold deformation in response to the organoid growth (left), a single z slice of the organoid showing the lumen near the outer edge of the organoid (right). Scale bar corresponds to 200 µm. c) Brightfield images of d 15 or 16 organoids showing the VZ-like lumen regions growing at the scaffold corners. Scale bar corresponds to 200 µm.*

4.3.4. Scaffold-cultured organoid characterisation

D 20 scaffold-cultured organoids were also sectioned for immunostaining to closely visualize markers at the centre of the organoid. A strategy was devised for sectioning scaffold-cultured organoids to preserve the structural layout of the scaffold and corresponding organoid positions. Briefly, after fixation of the scaffold organoids, the CellCrown and scaffold assembly were lifted out of the well and placed on a PDMS cutting mat, with a width of approximately 5 mm. Using a 6 mm diameter biopsy punch, scaffold samples were cut out and placed in a 35 mm diameter petri dish in PBS, using forceps to gently separate the scaffold sample from the PDMS. PBS was then replaced with 30% (w/v) sucrose and left at 4°C overnight. For OCT embedding, the sucrose solution was replaced with OCT, and the scaffold sample was gently mixed in the OCT using a pipette tip, to remove any remaining streaks from the sucrose. After 5 - 10 min, and scaffold sample was gently moved to a cryomold, positioning the sample in the middle, before filling with OCT and freezing on dry ice, as described in materials and methods.

D 20 organoids showed high expression of neural progenitor marker SOX2 in the VZ-like lumen regions (**Figure 4.7a**). Neuronal marker TUJ1 was sparsely distributed throughout the organoid section, and TUJ1 positive neurons were also observed on the scaffold interface in the centre of the organoid (**Figure 4.7a** solid white arrowhead). Interestingly, forebrain marker FOXG1 showed higher expression in the scaffold-cultured organoids, compared to scaffold free and conventional control organoids (**Figure 4.7b)**. It has previously been reported that the combination of a supporting microfilament and a CHIR pulse results in more consistent formation of VZ-like regions, which show a higher proportion of positive FOXG1 tissue than conventionally grown organoids.[143] This was accounted for in the study, by also treating the control organoids with a 3 d CHIR pulse. Therefore, the observation of increased FOXG1 expression in the scaffold-cultured organoids suggest that the presence of a microfilament (in this case the PCL scaffold) may have a more predominant role than the addition of CHIR in generating organoids with a forebrain identity.

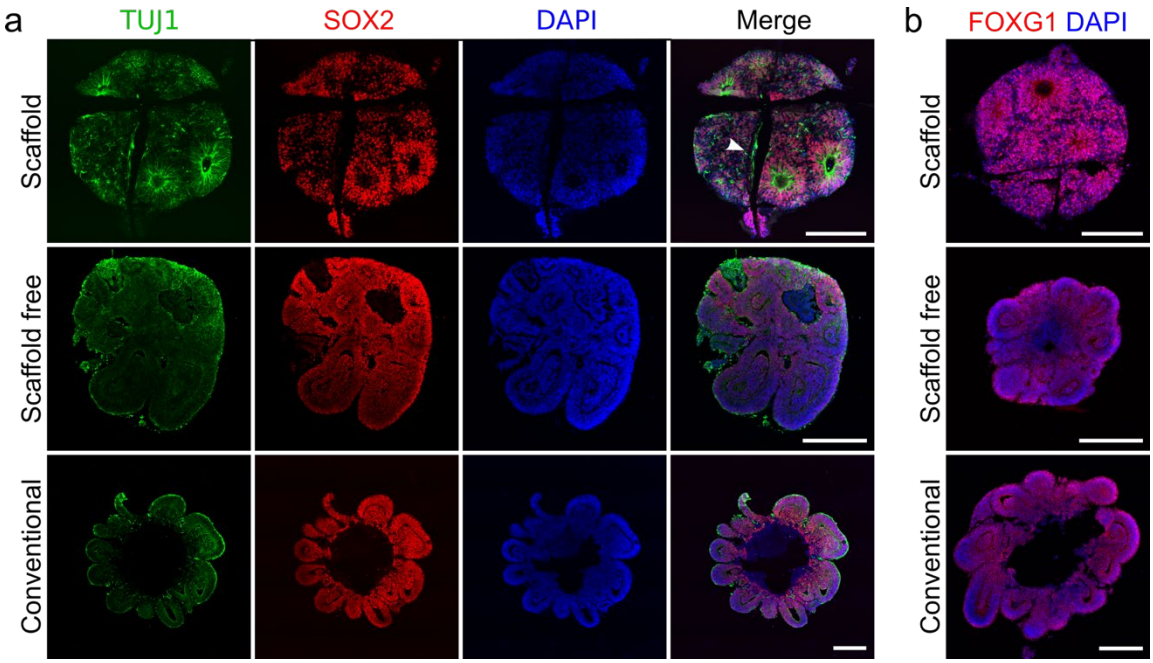


Figure 4.7 Immunostaining characterisation of d 20 cerebral organoids on scaffolds. *a) Image gallery showing histological sections of organoids immunostained with neuronal marker TUJ1 (green), neural progenitor marker SOX2 (red) and nuclear counterstain DAPI (blue). Representative images from three independent experiments (N = 3). Neurons are observed at the interface of the organoid with the scaffold fibres (solid white arrowhead). b) Histological sections of organoids immunostained with forebrain marker FOXG1 (red) and DAPI (blue). Representative images from three independent experiments (N = 3). Scale bars correspond to 200 µm.*

To grow d 40 scaffold-cultured organoids, a larger grid size of 1000 µm was selected to facilitate longer term growth and maintain spatial separation of the organoids. At d 40, TUJ1 positive neurons accumulated on the outer basal layer of the scaffold-cultured organoids, similar to the control organoids. This indicated that the scaffold did not impede the emergence of neuronal layers during organoid growth. Interestingly, at d 40, TUJ1 positive neurons were detected on the scaffold fibres in the organoid core, similar to d 20 organoids (**Figure 4.8b** solid white arrowhead). Previous research has shown that micropatterned scaffolds can provide axonal guidance cues and guide regional cellular identity and migration.[182,183] These results suggest that scaffold fibres provide a structural guidance for neurons, offering the possibility that scaffolds may be harnessed to specifically direct neuronal migration in future work.

To identify specific regional patterning in scaffold-cultured organoids at d 40, we looked at the expression of regional markers that are typically present along the anterior-posterior (AP) and dorsal-ventral (DV) axis *in vivo.* (**Figure 4.8a)**. Regional co-expression of FOXG1 and early dorsal marker PAX6 indicated dorsal identity in the developing forebrain region of the scaffold and control organoids (**Figure 4.8b)**. This was further shown by expression of the deep layer subcortical dorsal marker TBR1 (**Figure 4.8c**). Low expression levels of the ventral forebrain marker GSX2 were also identified in the scaffold and control organoids. Previous studies have similarly shown that CHIR treated organoids are associated with increased dorsal forebrain identity.[143,184] Taken together, these results demonstrate that similar regional growth profiles can be achieved in scaffold-cultured organoids to conventionally cultured organoids, using the adapted protocol.

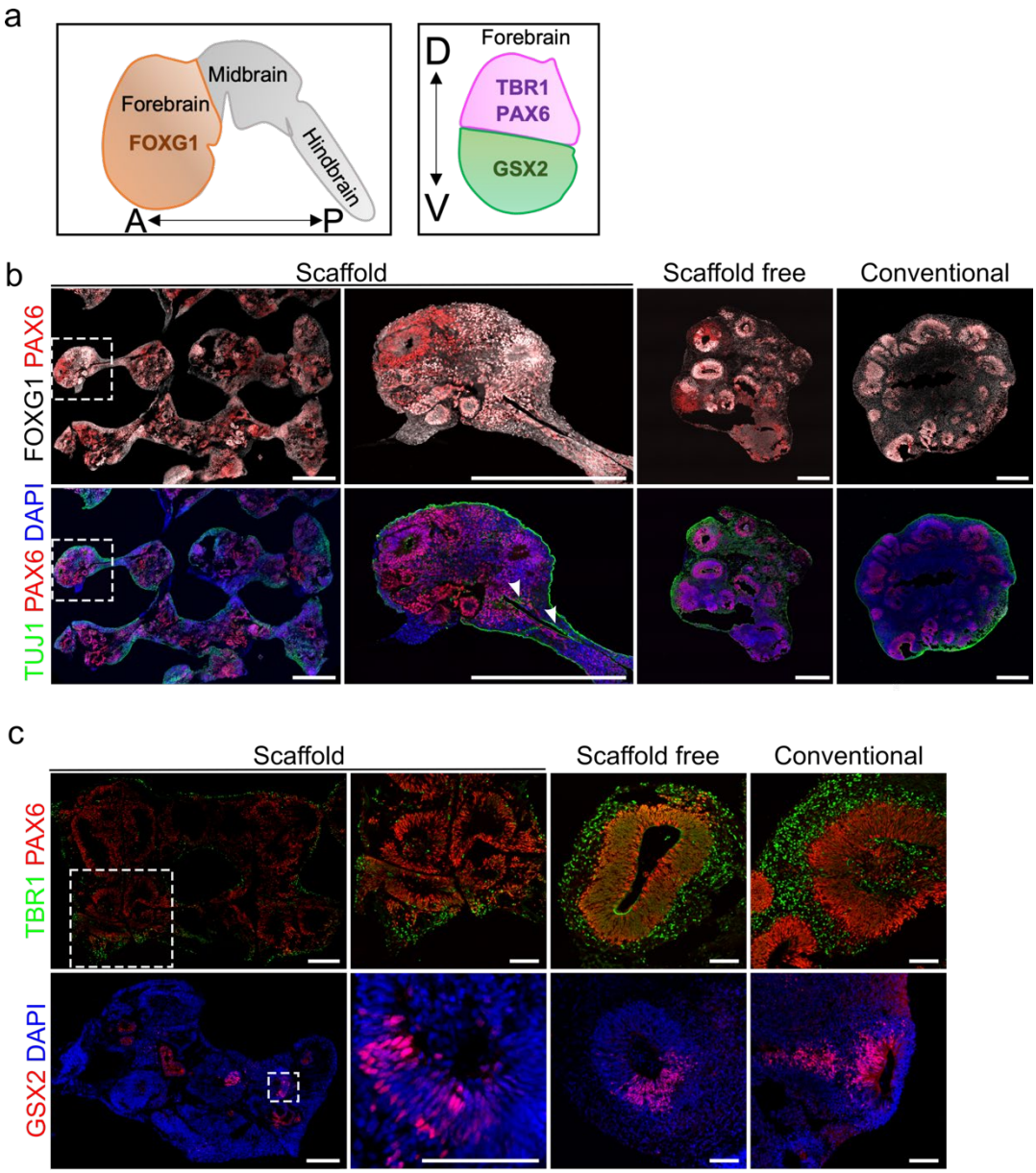


Figure 4.8 Immunostaining characterisation of d 40 cerebral organoids on scaffolds. *a) schematic illustration to show that FOXG1 expression occurs in the forebrain, which is in the anterior region of the developing brain. On the dorsal side of the forebrain, deep cortical marker TBR1 and early dorsal marker PAX6 are expressed. GSX2 is expressed in the ventral side of the forebrain. b) Histological sections of organoids immunostained with dorsal forebrain markers PAX6 (red) and FOXG1 (white), neuronal marker TUJ1 (green) and DAPI (blue). Neurons are seen to grow inside the organoid along the scaffold fibres (white arrowhead). Representative images from three independent experiments (N = 3). Scale bar corresponds to 500 µm. c) Histological sections of organoids immunostained with dorsal markers PAX6 (red) and TBR1 (green), ventral marker GSX2 (red), and DAPI (blue). Magnified regions are marked with a white dashed line. Representative images from three independent experiments (N = 3). Scale bar corresponds to 500 µm.*

b) Histological sections of organoids immunostained with dorsal forebrain markers PAX6 (red) and FOXG1 (white), neuronal marker TUJ1 (green) and DAPI (blue). Neurons are seen to grow inside the organoid along the scaffold fibres (white arrowhead). Representative images from three independent experiments (N = 3). Scale bar corresponds to 500 µm. c) Histological sections of organoids immunostained with dorsal markers PAX6 (red) and TBR1 (green), ventral marker GSX2 (red), and DAPI (blue). Magnified regions are marked with a white dashed line. Representative images from three independent experiments (N = 3). Scale bar corresponds to 500 µm.

4.3.5. Characterisation of long-term scaffold-cultured organoids

An important feature of cerebral organoids is their ability to maintain viability during long-term culture, which allows this model to recapitulate later developmental stages of embryonic brain development. For example, D >60 organoids replicate some features of *in vivo* brain development during the second trimester of gestation, such as similar transcriptional profiles and some features of functional network activity.[82,153] Crucially, the scaffold platform in this study is tuneable, and can be adjusted to accommodate the growth of short- or long-term culture organoids by adjusting the grid sizing. As previously discussed, scaffold grid sizes with 500 µm were used to generate d 20 organoids, and 1000 µm for d 40 organoids. For earlier time points, smaller grid sizes (<500) could be used with more high-throughput capacity in the future.

However, at d 40, some areas of uncontrolled growth were observed between the organoids on scaffolds in some samples, which was attributed to Matrigel attaching to the scaffold fibres at the embedding stage. To address this, the protocol was tweaked by removing the embedding step with 100% Matrigel and instead supplementing the culture media with 1 or 2% Matrigel. These organoids showed less uncontrolled organoid growth on the scaffold fibre walls, whilst maintaining VZ-like regions with expression of FOXG1 forebrain marker, and neuronal marker MAP2 (**Figure 4.9**).

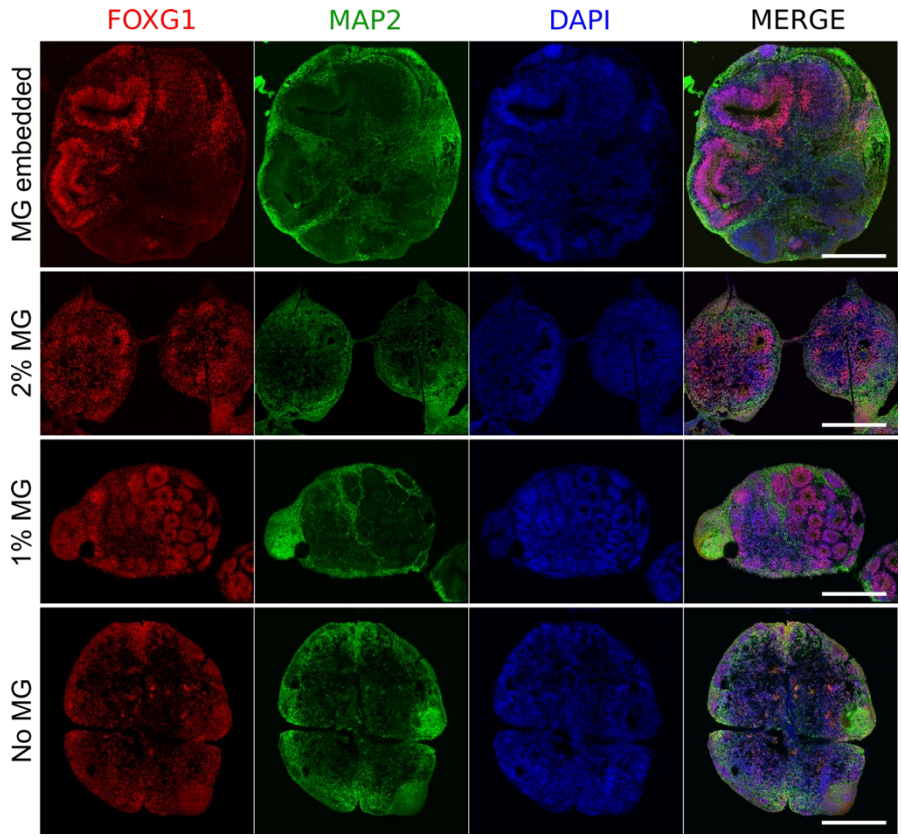


Figure 4.9 Matrigel embedding optimisation. *Image gallery showing histological sections of organoids on scaffolds from different Matrigel embedding conditions immunostained with forebrain marker FOXG1 (red), neuronal marker MAP2 (green) and DAPI (blue). Scale bar corresponds to 200 µm.*

This also avoided the processing steps during the 100% Matrigel embedding stage, further streamlining the protocol for organoid generation. Slightly larger VZ-like regions were observed in the 2% (v/v) rather than 1% (v/v) Matrigel condition, and we therefore proceeded with 2% (v/v) Matrigel supplementation for all long-term culture experiments. Using this method, cerebral organoids were cultured to d 48, with tiled brightfield images revealing a high level of organoid occupancy and homogeneity across the scaffold (**Figure 4.10**).

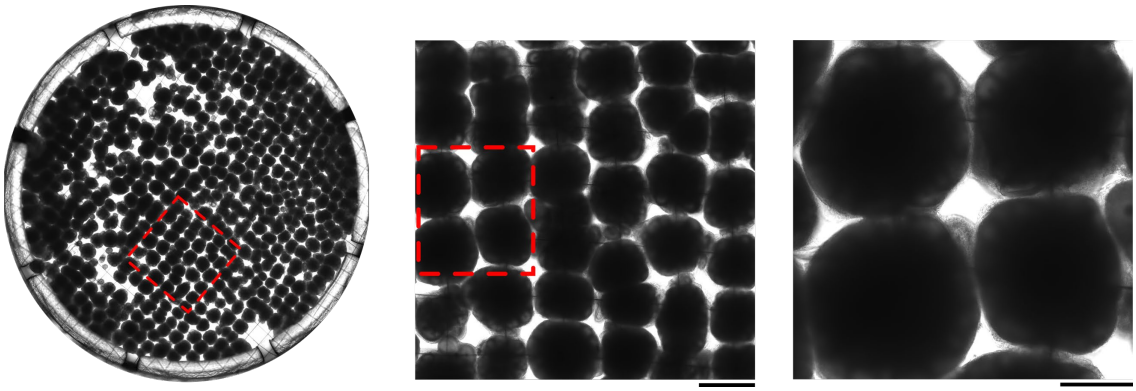


Figure 4.10 Tiled overview image of fixed organoids on 1000 µm spaced scaffolds at d 48. *Magnified regions are marked by a red dashed line. Scale bar corresponds to 1000 µm (middle) and 500 µm (right).*

Further immunostaining characterisation of 2% (v/v) Matrigel treated organoids at d 48 demonstrate co-expression FOXG1 and PAX6 on scaffold organoids, similar to the control organoids (**Figure 4.11a)**. Comparable expression of deep cortical marker CTIP2, and neuronal marker MAP2 was also observed between scaffold and control organoids (**Figure 4.11b)**. To further test the feasibility of long-term organoid cultures, scaffolds with a pore size of 4000 µm were used. It was reasoned that this would provide the spatial separation necessary for organoids to mature further without risking organoid fusion. The 4000 µm spaced scaffolds were assembled onto the CellCrown and cell seeding proceeded as previously described. At d 60, scaffold-cultured organoids showed large VZ-like regions with dorsal forebrain identity, and abundant neurons positive with CTIP2 in the deep cortical layers and MAP2 on the outer cortical layers (**Figure 4.12**).

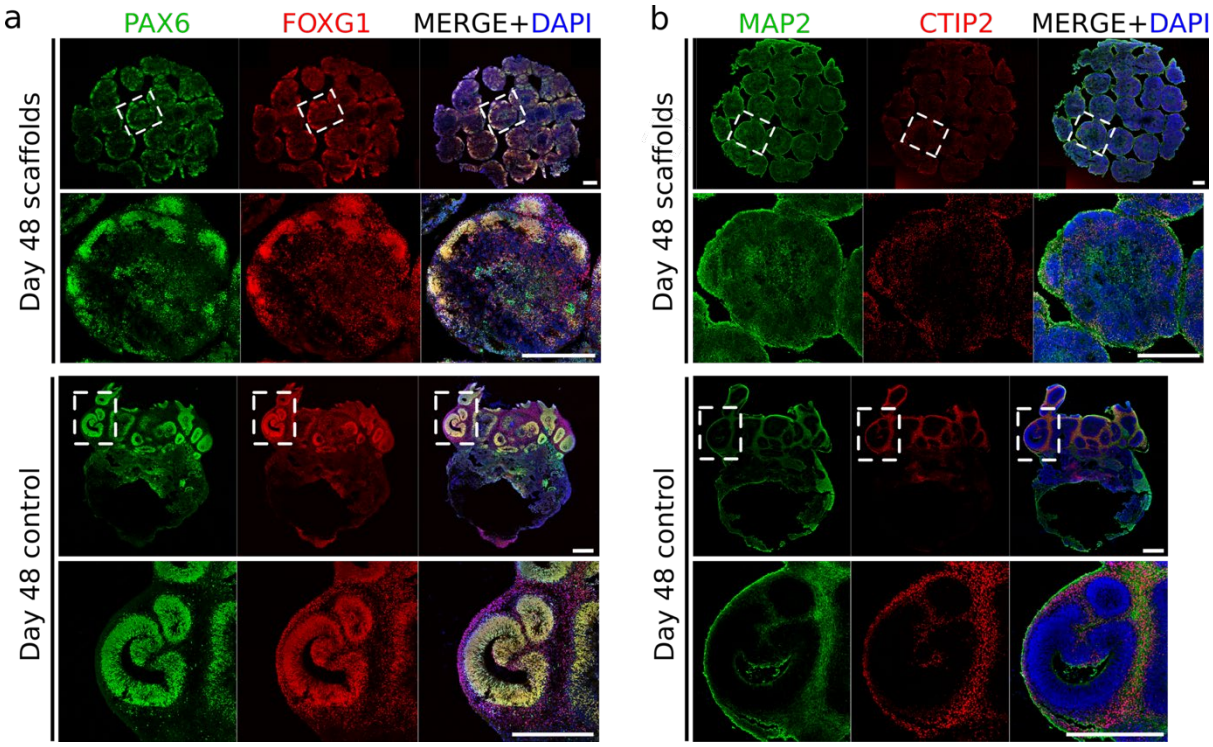


Figure 4.11 Immunostaining characterisation of d 48 organoids on scaffolds. *a) Image gallery of organoid histological sections immunostained with dorsal marker PAX6 (green), forebrain marker FOXG1 (red) and nuclear counterstain DAP (blue)I. Representative images from one independent experiment (N = 1). Scale bar corresponds to 500 µm. b) Image gallery of organoid histological sections immunostained with neuronal marker MAP2 (green), deep cortical marker CTIP2 (red) and nuclear counterstain DAPI (blue). Representative images from one independent experiment (N = 1). Magnified regions are marked with a white dashed line. Scale bar corresponds to 500 µm.*

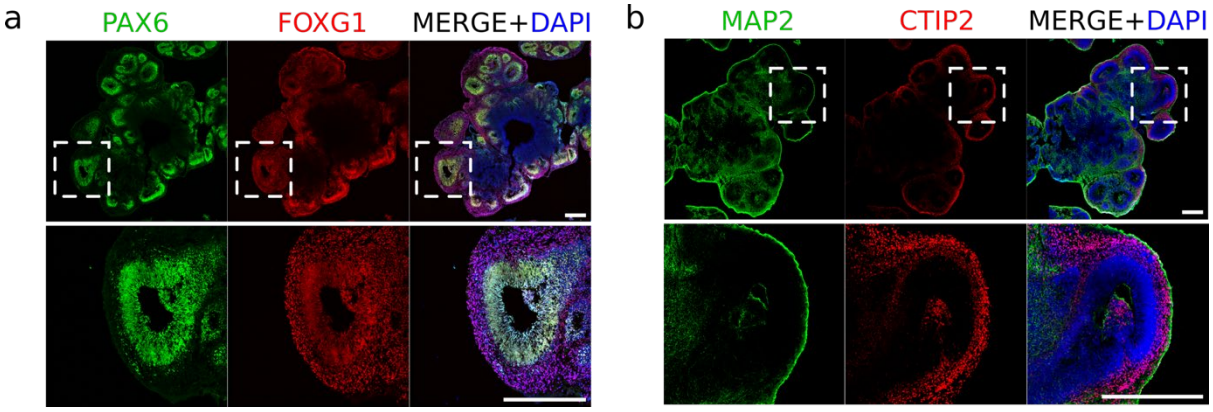


Figure 4.12 Immunostaining characterisation of d 60 organoids on scaffolds*. a) Image gallery of organoid histological sections immunostained with dorsal marker PAX6 (green), forebrain marker FOXG1 (red) and nuclear counterstain DAPI (blue). Scale bar corresponds to*

500 µm. Representative images from one independent experiment (N = 1). b) Image gallery of organoid histological sections immunostained with neuronal marker MAP2 (green), deep cortical marker CTIP2 (red) and nuclear counterstain DAPI (blue). Representative images from one independent experiment (N = 1). Magnified regions are indicated by white dashed line. Scale bar corresponds to 500 µm.

Previous research has shown that cortical organoids exhibit functional network circuity with features similar to that observed in preterm infants from 6 months,[153] and can reliably be cultured for more than 20 months, showing astrocyte formation and maturation that correspond to later embryonic developmental stages *in vivo*.[185] In future work it will be essential to further characterise the scaffold-cultured organoids at later timepoints (>60 d) to assess whether scaffold culture supports further long-term organoid maturation.

It is notable that while the scaffold organoids are smaller in size than the conventionally cultured control organoids, the expression of various markers at different developmental stages are unaffected. One limitation of cerebral organoids is the hypoxia and necrosis associated with long-term organoid cultures, due to the increased size and insufficient surface diffusion of nutrients and oxygen.[186,187] The smaller size of the scaffold-cultured organoids may provide an advantage for long-term culture, by enabling more efficient diffusion-dependent nutrient supply than larger organoids. Indeed, in future studies it will be important to compare differences in the timing and degree of hypoxia and necrosis in scaffold organoids with conventionally grown organoids. Furthermore, it will be interesting to see if there are other specific advantages associated with scaffold-cultured organoids, in terms of tissue development and organisation in more mature (>60 d) organoids, compared to conventionally grown organoids.

4.3.6. Advanced organoid characterisation with Raman spectroscopy

The scaffold-cultured organoid platform was next combined with Raman spectroscopy, with the aim of establishing a basic workflow for non-destructive high-content biochemical analysis. Raman spectroscopy is an optical label-free technique that uses inelastic light

scattering and produces a spectrum of peaks at different wavelengths. These Raman peaks can be mapped to specific chemical bonds and used to identify the biochemical profile of living cells. Importantly, this is usually considered to be a non-invasive technique, and after Raman detection, cells are typically viable for continued culture and growth. Recent studies have used a single cell Raman spectroscopy (SCRM) platform to interrogate the biochemical profile of iPSC-derived neural stem cells (NSCs) and identified glycogen as a key biomarker for neuronal differentiation.[188] Other previous studies have used SCRM to define biochemical signatures for different developmental growth states.[189,190] There is currently an unmet need to introduce such techniques to the field of cerebral organoids, which will be highly desirable for providing quantitative biomolecular information and non-invasive tracking of developmental growth.

To address this, a methodology was sought to facilitate Raman imaging of 3D scaffold-cultured organoids. For optimisation purposes, fixed samples were initially used. For sample preparation, a previously reported protocol was adapted.[191] Briefly, d 20 scaffold-cultured organoid samples were cut from the main scaffold using a 6 mm biopsy punch, and embedded in a 6 cm diameter petri dish in low melting point agarose (type IX), to mitigate movement of the sample during imaging. Once the agarose was sufficiently gelled, PBS was added to completely immerse the sample (**Figure 4.13a**). For future experiments with live organoids, the scaffold structure could alternatively be used to fix the organoids in position in the petri dish, avoiding the necessity to embed the organoids with agarose. As previously described, this sample preparation setup facilitated Raman spectra acquisition with minimal background interference.[191] Raman spectroscopy was performed using a 63x Water immersion objective lens and 532 nm excitation laser. Whilst this wavelength is commonly used for imaging fixed cells and tissues, this can cause intracellular damage in living cells, and a higher wavelength of 785 nm can alternatively be used for live organoid imaging in the future.

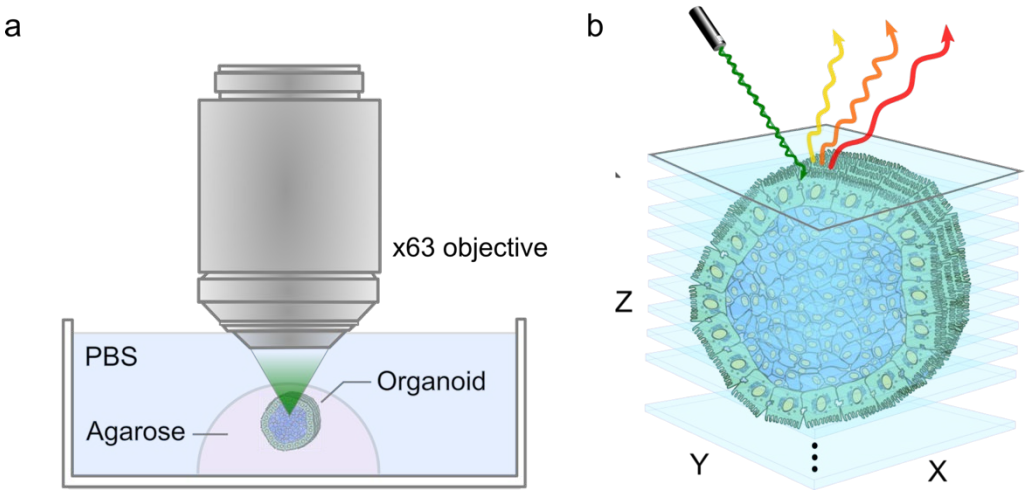


Figure 4.13 Schematic overview of Raman spectroscopic imaging of organoids on scaffolds. *a) Organoids are embedded in agarose to prevent movement during imaging b) 3D z stack images are acquired for quantitative analysis. Image provided by Dr. Vernon Lalone.*

Low resolution Z stack image scans were acquired for qualitative visualisation of an entire organoid on scaffold (**Figure 4.13b, Figure 4.14a,b**). The PCL channel signals were readily distinguishable from the biospecimen due to their unique chemical fingerprint and relatively strong intensity. High resolution scans were obtained to extract high signal-to-noise ratio (SNR) spectral information about the sample composition with subcellular spatial resolution (**Figure 4.14c**). Reference spectra of different biomolecules were generated in-house, and the spectra collected from the organoid samples were compared against these to identify specific biomolecules in the sample. Several spectral signatures were identified, indicative of the most abundant biomolecules in biological specimens: proteins, lipids and nucleic acids. (**Figure 4.14d**)**.** The distribution and cellular morphology of nucleic acid showed a similar distribution to DAPI in conventional fluorescence images. (**Figure 4.14c**).

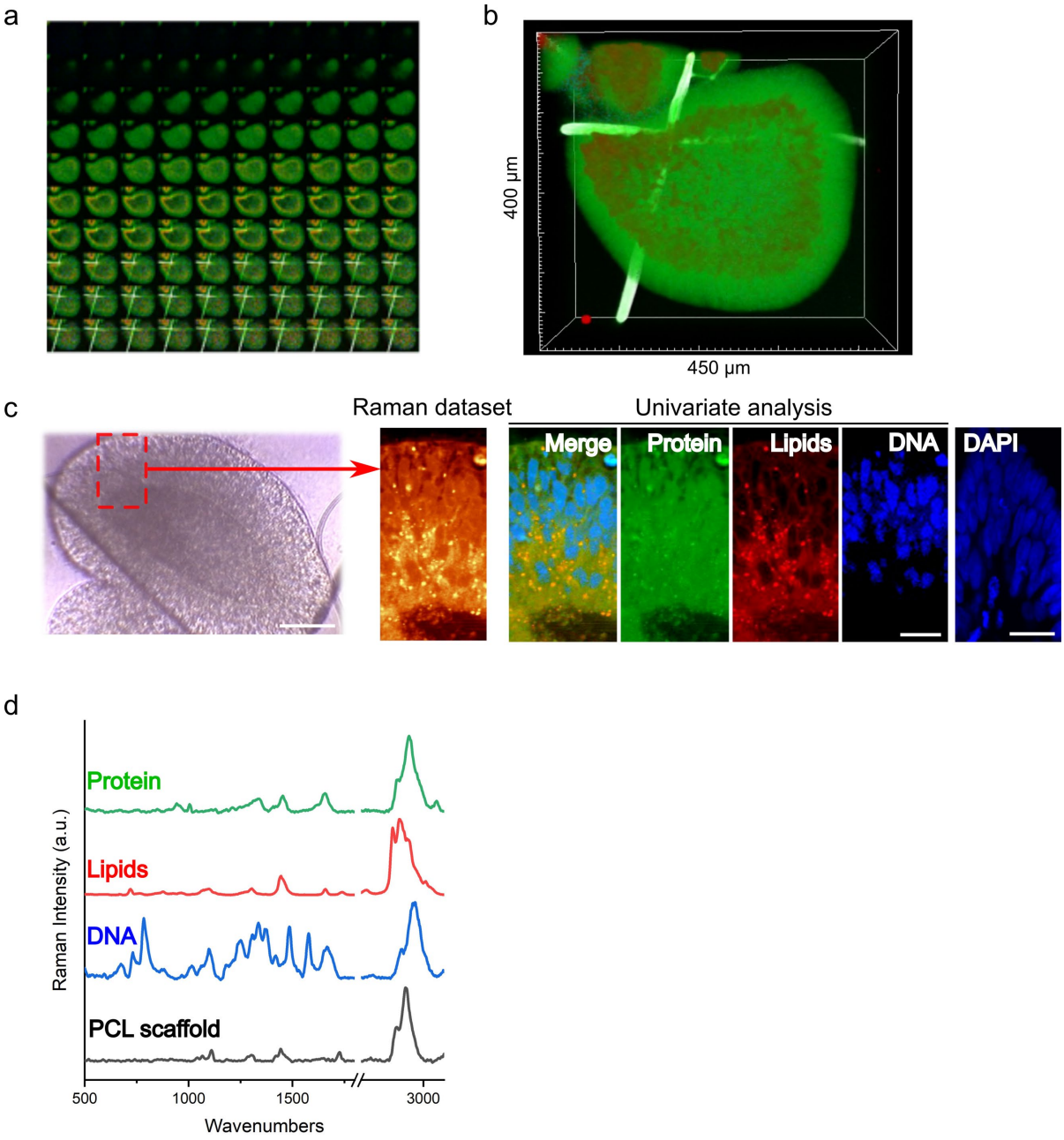


Figure 4.14 Raman spectroscopy imaging of organoids on scaffolds. *Raman spectroscopy was used to image a fixed d 20 brain organoid on scaffold. a) z stack slices of low-resolution imaging demonstrate volumetric imaging of the entire organoid on scaffold b) 3D reconstruction of an organoid showing the PCL scaffold in white c) high-resolution imaging of a smaller ROI of the organoid, as indicated by the red box (left). Single images show relevant biomolecules detected, including proteins (green) lipids (red) and nucleic acids (blue). d) Raman spectra with labelled peaks. Raman imaging and analysis carried out by Dr. Vernon LaLone.*

Here a basic workflow for Raman imaging fixed scaffold-cultured organoids has been demonstrated. In future experiments, the sample preparation and data analysis can be translated to live organoids, as the effects of fixation on sample signals is minimal.[192] For example, this could be applied to live organoid samples to non-invasively track cell differentiation in organoids at different developmental timepoints, similar to previously reported work in 2D neuronal cultures.[188]. A major advantage of the scaffold system is that organoids are physically tethered to the scaffold, which provides a fixed position on a 2D focal plane for experiments requiring positional control of organoids. The coordinated grid structure of the organoid scaffold platform could also facilitate Raman imaging on the same position at different timepoints. This could also be used to detect changes in disease states. For example, recent studies have demonstrated that choroid plexus organoids produce cerebral spinal fluid (CSF).[96] Raman spectroscopy may be used to monitor changes in the contents of CSF fluids in choroid plexus organoids, both to perform comparative analyses between different disease states that affect the CSF, but also to detect the permeability of drugs into the CSF.

4.4. Conclusion

Here, a biomaterial platform for the controlled, high-throughput growth of cerebral organoids has been developed. Previous studies have used microfilaments as floating scaffolds during cerebral organoid culture, demonstrating improved neuroectoderm formation.[143] However, these microfilament-cultured organoids are free floating, without a defined scaffold geometry. Building on this work, a highly defined PCL scaffold, that provides a way to fix multiple organoids in position during culture has been developed. This generates independently growing organoids in a patterned array, guided by the scaffold geometry.

This approach addresses some of the foremost technical challenges in the field, namely the labour-intensive culture methods and lack of reproducibility. The high-throughput and simplified culture method demonstrated in the scaffold-cultured organoid platform provides a promising alternative that addresses these limitations. These results demonstrated that scaffolds can generate hundreds of independently growing organoids on a single scaffold, that can be cultured and treated *en masse*. In future work, this will be highly applicable for drug screening studies, that require large numbers of organoid samples for drawing conclusions with high statistical power.

In addition, the data shows that the scaffold-cultured organoids are significantly smaller than conventionally grown organoids, yet they contain the same key markers as the control organoids at various developmental timepoints. This demonstrates that the scaffold organoid tissue identity is comparable to conventionally grown organoids. In future work it will be essential to explore whether the small size confers an advantage in more mature (>60 d) organoids, by avoiding necrosis and hypoxia.

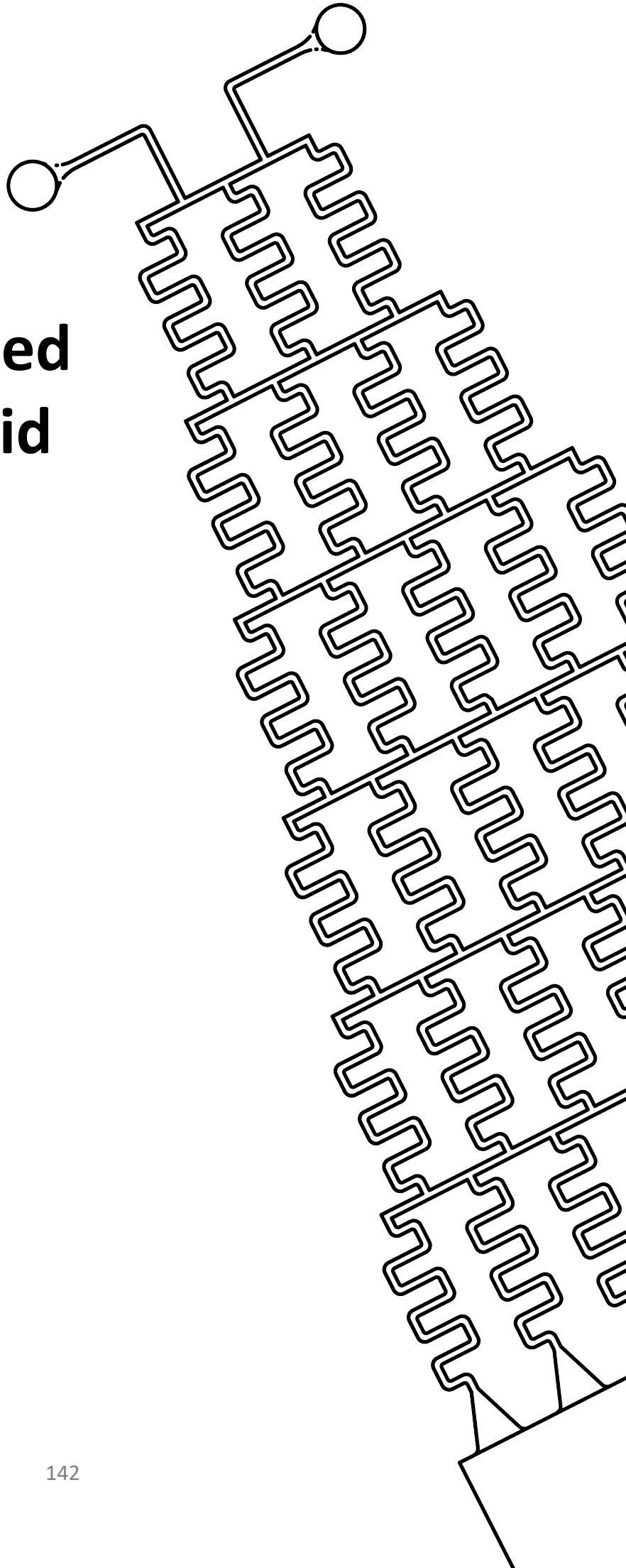
High-content biochemical analysis of organoids using Raman spectroscopy provides an opportunity to non-invasively identify the biochemical profile of organoids. Using fixed samples, a basic workflow for Raman imaging of scaffold-cultured cerebral organoids was established, that can be translated to live organoids in future work. Keeping organoids in a fixed position during live culture is a significant advantage of the scaffold platform, and this

could be further explored as an alternative option to agarose embedding in the future. Furthermore, Raman imaging scaffold-cultured organoids could be paired with other advanced characterisation techniques such as FIB-SEM for ultrastructure visualisation, to combine nanoscale spatial resolution with biochemical imaging. The grid network of the scaffold also provides an ideal framework for controlled manipulation of individual organoids, such as electrophysiology, and these approaches can be explored in future studies. Finally, it will be important to test the adaptability of this platform with other stem-cell based organoid systems, such as liver and intestinal organoids.

Here, it is shown that biomaterials can be used to facilitate high-throughput, reproducible growth of cerebral organoid growth. The next chapter will examine how scaffold geometry can be used to guide elongated organoid growth and how the scaffold can be exploited to direct regional patterning and axis formation of brain organoids.

Chapter 5.

Scaffold guided brain organoid patterning



5. Scaffold guided brain organoid patterning

5.1. General Introduction

Cerebral organoids are typically grown without the complex spatiotemporally controlled morphogen gradients that are present *in vivo,* a situation that leads to uncontrolled morphogenesis and unpredictable anatomies lacking the normal polarised axes (dorso-ventral, antero-posterior). A major approach for generating polarised cerebral organoids is to manually fuse two regionally specified organoids[93,94,106] or an embryoid body with a morphogen-secreting cell aggregate.[107] However, generating and additively assembling separate cellular components does not recapitulate neural morphogenesis, in which complex morphogen gradients establish anatomical brain axes from a single structure. This highlights the current unmet need for a method that enables predictive, programmed development of complex, multi-regional cerebral organoid, which would significantly enhance the current technology and expand its application in modelling neurological development and disease.

Building on work in previous chapters, the scaffold guided organoid platform was applied to direct the regional specification of cerebral organoids. In the first part of this work, a new scaffold geometry was developed to engineer the growth of elongated organoids. Establishing an elongated morphology is essential to facilitate axis formation for organoid polarisation. In the second part of this work, the polymer scaffolds were functionalised with the ventralising morphogen sonic hedgehog (Shh) with the goal to direct differentiation in the elongated organoids. Finally, an alternative methodology was investigated to direct differentiation, by developing a microfluidic gradient generator to establish a dorso-ventral gradient across the elongated organoid. This chapter is subdivided into 3 subchapters, each with its own short introduction.

5.2. Materials and methods

5.2.1. Melt electrospinning writing for scaffold fabrication

Pure PCL (M_w ~ 75 000 g mol^{-1}) was loaded into a 3 cc polypropylene syringe (Nordson #7012074) and heated to 70°C for 30 min. A 23 G needle (Nordson #7018302) was installed, and the syringe was inserted into the spinneret. Scaffolds were printed using a 10 kV accelerating voltage, 10 mm collector distance, axis velocity of 1500 mm/min, feeding air pressure of 1.0 bar, and heating temperatures between 60 and 80°C. Printing was controlled by MACH 3 CNC software (ARTSOFT, Livermore Falls, USA), and dimensions were specified by G-code. Each scaffold consisted of 10 stacked layers, each of about 5 µm height. A 4 × 4 cm scaffold was created by printing fibre lines at 4 mm distance and held in place by orthogonal fibres at either ends, printed at a distance of 500 µm apart, forming a rectangular lattice structure at either ends. Each scaffold consisted of 10 stacked layers. Scaffolds were detached from the collector plate using a drop of ethanol and moved to a petri dish. For cell culture experiments, scaffolds were sterilized by cell culture-grade UV light irradiation for 30 - 45 min.

5.2.2. Fabrication of PDMS substrates for elongated organoid culture

A 3.5 cm diameter mold comprising 2 mm spaced channels was designed in CAD (Solidworks) and processed using PrusaSlicer v2.3.3 (the default 3D printer interface software for the Prusa SL1S 3D printer). Molds were printed using a biocompatible Orange Touch resin. For post-processing, molds were sonicated in absolute isopropyl alcohol (IPA) for 5 - 10 min, then air dried and incubated in the UV post-cure oven for 2 h at 60°C. The molds were then soaked in ethanol or IPA for at least 2 h. The interfacing surface of the 3D printed mold was treated with oxygen plasma at 100 W, 1 mBar O_2 for 5 min, followed by vapour Perfluoroocytyltricholorsilane (PFOS) for 4 h under a desiccator vacuum, and incubated at 60°C overnight. To generate the PDMS channels, PDMS agent (Sylgard 182 Kit, Dow Corning) was prepared using a 10:1 ratio with the curing agent and degassed under vacuum. PDMS was then cured at 60°C for at least 4 h. The PDMS molds were sterilised by

autoclaving for 1 h. Immediately before cell seeding, the PDMS molds were incubated for 1 min in anti-adherence rinsing solution (Stemcell Technologies), then washed three times in PBS.

5.2.3. Scaffold preparation for elongated organoid culture

4 x 4 cm PCL scaffolds were printed using MEW (**section 5.2.1**) and comprised of fibres forming single lines distanced at 4 mm apart, with orthogonal fibres at either end at a distanced at 500 µm apart. The scaffolds were placed in a CellCrown holder, and manually tensioned to ensure that the fibres of the scaffold were taut. The scaffold holder and scaffold assembly were sterilised by UV irradiation for 30 - 45 min. Scaffolds were then placed in a 6-well plate and coated in 1 mL of hESC qualified Matrigel (Corning cat. no. 354277) diluted in DMEM according to the manufacturer's instructions and left to incubate at 37°C for 1 - 2 h. Immediately before cell seeding, scaffolds were rinsed in PBS.

5.2.4. Elongated cerebral organoid culture on scaffolds

*Media formulations are described in **section 2.4**.*

D 0

hESC seeding onto scaffolds

At approximately 60% confluency, hESCs were dissociated from the well-plate by adding 1 mL accutase for 3 min at 37°C. The remaining adherent cells were sprayed off with 1 mL mTESR and cells were centrifuged at 200 g for 3 min. The cell pellet was resuspended in mTESR media, and a cell suspension was prepared in MTESR media containing 50 µM ROCK inhibitor Y27632 (Selleckchem) and 1% Antibiotic-Antimyocytic (ThermoFisher), at a density of 1×10^5, 5×10^5 or 1×10^6 cells per scaffold. After Matrigel incubation, scaffolds were washed once in PBS and placed in low attachment 6-well plates, or plates treated with anti-adherence rinsing solution (Stemcell Technologies) for 1 min, followed by washing three times in PBS. Scaffolds were secured at the bottom of the plate by pushing the CellCrown down using forceps. 3 mL of cell suspension was added per well, and the plate gently rocked in a North-South-East-West direction to evenly distribute the cells across the scaffold.

D 3

The CellCrown and scaffold assembly was lifted by approximately 5 mm in the well plate to prevent the cells from contacting the bottom of the well, while ensuring sufficient media coverage across the scaffold. mTESR media was exchanged without ROCK inhibitor or Antibiotic-Antimyocytic. The cells were left unperturbed on d 4.

D 5 - 20

Media was exchanged with a neural induction media (as described in **section 2.4**). Media was replaced every 2 d until d 10 – 13, when signs of optical clearing on the organoid borders were clearly present. At this stage, 2% (v/v) Matrigel (Corning, cat. no. 356235) was added to the neural induction media, and at every media change until the end of the culture period. 2 – 3 d after the first addition of Matrigel (usually at d 12), media was changed to Improved -A media (as described in **section 2.4**). In non-patterning experiments, 3 µM CHIR 99021 (Tocris) was added for the first 3 d of Improved -A. At approximately d 15, the scaffolds were transferred to a 6 cm petri dish to provide a higher volume of media (10 mL) to support organoid growth. The CellCrown was placed on a sterile plastic ring to prevent the organoids from touching the bottom of the plate. The media was changed every 2 d. At d 18, media was changed to Improved +A media (as described in **section 2.4**).

5.2.5. Generation of ventrally patterned conventionally cultured round organoids with Sonic hedgehog (Shh) morphogen

The protocol for conventionally cultured round organoids is described in **section 2.5**. For ventral patterning, 1 µg/mL recombinant human Shh protein (R&D Systems, 8909-SH) was added to the mTESR cell suspension at d 0. Media was exchanged with fresh mTESR at d 3, without Shh. Organoid culture using the conventional round cerebral organoid protocol was resumed without the addition of 3 µM CHIR 99021 (Tocris).

5.2.6. Layer-by-Layer assembly

To prepare the multilayers, the elongated PCL scaffold was treated with oxygen plasma at 100 W 1 mBar O_2 for 5 min, then attached to a 6 well CellCrown holder. A 2 mg/mL heparin (Sigma-Aldrich H3393) solution was prepared in ultrapure water, and a 2 mg/mL low molecular weight, 85% (w/v) deacetylated chitosan (Sigma-Aldrich 448869) solution was prepared in 0.5% (v/v) acetic acid. 3 mL of chitosan and heparin solutions were added to

separate wells of a 6 well plate, and 3 mL of Ultrapure water was added to the remaining 4 wells. A 3D printer was adapted with a programmable arm, and a custom-made adaptor was used to attach the CellCrown holder to the 3D printer arm. The 3D printer was programmed to immerse the CellCrown and scaffold assembly into the chitosan solution for 10 min, followed by two washes in Ultrapure water for 1 min each, followed by heparin immersion for 10 min, and two washes in Ultrapure water for 1 min each. This cycle was repeated 10, 20 or 40 times, as specified in the results section.

5.2.7. XPS characterisation of Heparin and Chitosan LbL coated scaffolds

XPS experiments were performed on a Thermo-Fisher K Alpha XPS system (Waltham, MA, USA). To acquire the overall elemental composition, a survey of 2 scans was performed with a constant analyser energy of 200 eV, dwell time of 25 ms, 0.5 eV step size and an X-ray spot size of 400 mm. Single element spectra were obtained using a constant analyzer energy of 20 eV, dwell time of 50 milliseconds, 0.1 eV step size, an X-ray spot size of 400 mm, 10 scans for silicon/carbon/oxygen, and 20 scans for nitrogen/sulfur. The carbon peak was used as a reference, with a value of 284 eV for adventitious carbon. Spectra data were analyzed using Avantage software V5.9925 (Thermo Scientific, Waltham, MA, USA). XPS was carried out by Dr Daniel Hachim Diaz

5.2.8. Sonic hedgehog scaffold functionalisation for organoid culture

LbL assembly was carried out as previously described in **section 5.2.6** and scaffolds containing 10, 20 or 40 multilayers of heparin/chitosan were generated. LbL scaffolds and pristine PCL scaffolds were incubated in a Shh solution overnight, at a concentration of 100 ng/ml, 1000 ng/ml or 4000 ng/ml recombinant human Shh protein (R&D Systems, 8909-SH) in PBS, followed by 3 washes for 10 min each, in PBS. Scaffolds were coated in 1 mL of hESC qualified Matrigel (Corning 354277) diluted in DMEM according to the manufacturer's instructions and left to incubate at 37°C for 1 - 2 h and rinsed once in PBS Immediately before cell seeding.

5.2.9. Sonic hedgehog scaffold immunostaining and imaging

The Shh solution was aspirated and the scaffolds were washed twice in PBS for 5 min each. Immunostaining was carried out as described in **section 2.7**. Scaffolds were immunostained using a Shh antibody (DSHB, 5E1) at a 1:15 dilution, from a stock solution of 45 µg/mL. Scaffolds were placed in a glass bottom well plate in PBS for imaging. Widefield imaging was carried out using a Zeiss AxioScope Observer microscope.

5.2.10. Sonic hedgehog release assay

The release profiles of LbL and pristine PCL scaffolds functionalised with Shh were evaluated by ELISA. 800 µm spaced scaffolds were cut into 4 separate 2 x 2 cm squares. LbL scaffolds were prepared as previously described in **section 5.2.6** with the exception that scaffolds were attached to a 24 well CellCrown holder. For Shh functionalisation, 200 µl Shh solution was added to the CellCrown and scaffold assemblies in a 24 well plate at a concentration of 4000 ng/ml Shh and left overnight, followed by 3 washes in PBS for 10 min each. The scaffold and CellCrown assembly were then placed in 24 well plates with 1 mL of hESC qualified Matrigel (Corning Cat. No. 354277) diluted in DMEM according to the manufacturer's instructions and left to incubate at 37 °C for 1 - 2 h and rinsed once in PBS. 500 µl of mTESR media was added to the CellCrown and scaffold assemblies and incubated at 37°C, to mimic the culture conditions of the scaffolds during cell culture. At d 5, the media was exchanged with neural induction media, to mimic the culture conditions of the scaffolds during cell culture. 500 µl of media was exchanged with fresh media at each time point (0 h, 6 h, 12 h, 24 h and then every 24 h for 5 d). Each sample was performed in triplicate and samples were frozen at -20°C until ELISA analysis. Shh release was established by measuring the amount of Shh collected in the cell culture media solutions using an ELISA kit (Quantikine, R&D systems) following the manufacturers instruction. The absorbance was measured at a wavelength of 450 nm using a SpectraMax M5 plate reader. The cumulative release was calculated as the total cumulative amount of Shh at each timepoint.

5.2.11. Microfluidic chip design

The microfluidic chip design was first designed as a negative mold in CAD (Solidworks). Channels were designed with a square cross-section of 200 x 200 µm (width x height) and a minimum inter-channel distance of 200 µm. All corners were filleted to reduce bubble nucleation zones. CAD files were prepared by Dr Richard Wang.

5.2.12. 3D printing resin mold

CAD files were processed using PrusaSlicer v2.3.3 and the following printing parameters were used:

- UltraDetail resolution profile (0.025 mm z resolution).
- Molds were printed with a 'pad' supporting layer.
- Molds were printed flat on the print bed without any supports.

The profile setup for the print was created using Orange Touch resin. On completion of printing, the mold was removed from the printer and sonicated with absolute IPA for 5 - 10 min, before being flipped upside down and sonicated for another 5 - 10 min. The molds were then air dried to remove all visible traces of IPA, and any resin residuals were removed by spritzing with IPA. The molds were then incubated in the UV post-cure oven for 4 h at 60 °C and were flipped at 2 h to ensure full curing across the entire chip. After this, the molds were soaked in ethanol or IPA for at least 2 h. To prepare for fabrication of the positive PDMS mold, the interfacing surfaces of the 3D printed mold was treated with oxygen plasma at 100 W, 1 mBar O_2 for 5 min. The molds were then treated with vapour Perfluorooctylrichlorosilane (PFOS) for 4 h under a desiccator vacuum and incubated at 60°C overnight

5.2.13. PDMS chip fabrication

PDMS was prepared using a 5:1 ratio with the curing agent and degassed under vacuum for 30 min. The PDMS was poured into the 3D printed negative molds and degassed under vacuum for another 30 min. PDMS was then cured at 60°C for at least 4 h. PDMS chips were carefully demolded, taking care to not excessively touch the interfacing surface and excess PDMS was removed from the edges using a blade.

5.2.14. Bonding of chip with glass slide

A glass microscope slide (76 x 36 x 1 mm) was cleaned with IPA and protected with scotch tape. The PDMS interfacing surface was cleaned with scotch tape to remove any particles. The glass microscope slide and PDMS chip were treated with oxygen plasma at 100 W, 1 mBar O_2 for 1 min. The plasma treated PDMS chip was then carefully placed onto the plasma treated glass surface, pressing down on the PDMS to remove air bubbles and to ensure sufficient contact for bonding. To prevent leakage, the PDMS/glass edges were sealed using PDMS from a syringe. The chip was then cured at 60°C for at least 2 h. For organoid culture experiments, the chips were sterilised by autoclaving for 1 h.

5.2.15. Scaffold holder fabrication

Custom holders were designed to suspend the PCL scaffold so as to maintain tension for elongated neuronal organoid growth, whilst also suspending the PCL scaffold within the microfluidic chip such that the organoid was positioned directly in the fluidic flow path of the gradient generator. Scaffold holders were designed as three parts consisting of the scaffold and two separate clips, used to suspend the PCL scaffold and maintain the scaffold in tension. The designs were created in CAD (Solidworks) and processed using PreForm (default slicing software for Formlabs 3D printers). Scaffolds were printed using biocompatible printing resin BioMed Clear V1 (Formlabs). Completed prints were removed from the print platform, washed in IPA, and incubated in the UV post-cure oven for 1 h at 60°C. Scaffolds were sterilised by autoclaving for 1 h prior to use.

5.2.16. Attachment of inlet and outlet valves/tubes

Inlet tubing (outer diameter 1/32" x inner diameter 1/16", Cole-Parmer 06406-60) was directly inserted into the inlet ports and connected to the syringe reservoir via standard luer connectors. Outlet tubing (1/16" ID x 1/8" OD, Cole-Parmer 95802-02) with a barb connector (0.8 mm barb to barb connector, Bio-rad 732-8300) was directly inserted into the outlet port. The syringes were driven via a zero pulsatile motion low flow rate syringe pump (Harvard Apparatus 33DDS) in paired infusion mode where both inlet syringes were driven at equal flow rates.

5.2.17. Glass plate fabrication

Glass plates were custom made (Instrument Glasses, London UK) using 4 mm BK7 optical glass. The plates were designed to be tightened using M3 nuts and bolts, and to clamp down on PDMS microfluidic chip to prevent fluidic leakage, especially from the growth chamber region that houses the organoid and custom scaffold holder.

5.2.18. Widefield Fluorescence microscopy for gradient detection

To verify the ability of the microfludic chips to form a stable gradient prior to biological testing, the chips were first tested using a fluorescent marker. Using the same setup as above, fluorescein sodium salt (2.5 µM in DMEM media) was introduced into the microfludic chip opposite a non-fluorescein DMEM inlet solution. The microfluidic chip was continuously perfused for at least 12 h and the stability of the formed fluorescence gradient was analysed via time-series image acquisition (one image per hour) via fluorescence microscopy (Zeiss AxioScope Observer). For image analysis, data was plotted from time points at 3 h intervals, starting from 0 h to the final time point (12 h). A line was drawn on the image along the gradient direction and the 'plot profile' function in Fiji was used to analyse the fluorescence intensity along the line. To show the temporal stability of the fluorescence gradient, the slope of the linear regression of each replicate (N = 3) at each timepoint was taken. The raw data was normalised against the min/max, which was determined by manually selecting an ROI based on the expected region of the highest and lowest fluorescence. The min/max values were averaged across the dataset to account for imaging artefacts. The slope values were then normalised against the final time point (12 h) and plotted against time. Gradient detection and data analysis was performed by Dr Richard Wang and Dr Ruoxiao Xie.

5.2.19. Computation fluid dynamics (CFD) simulation

Geometry Preparation:

An assembly was created in Solidworks to include the main flow chamber, the placement of clips and a cylindrical approximation of the organoid. The cavity operation was performed to

create a single isolated fluid region and was saved as an independent part. The part file was exported as a Parasolid .xt file.

Preprocessing:

The Parasolid file was imported as a surface mesh into a multiphysics computational fluid dynamics (CFD) simulation software- STAR-CCM+, version 2021.3.1, Siemens 2021. Surfaces were split by Angle (89.0 deg) to define the Organoid Wall. The remaining surfaces were recombined and split by Patch to define the Inlets and outlets.

Physics Assumptions:

A passive scalar modelling approach was appropriate for this analysis to observe mixing from multiple inlets with the same fluid properties. By definition a passive scalar is assumed to have no mass or volume and therefore does not affect the physical properties of the simulation

The transport equation for the passive scalar component ϕ_i is:

$$\frac{\partial}{\partial t}\int_{\bar{V}} \rho\phi_i \, dV + \oint_A \rho\phi_i \boldsymbol{v} \cdot d\boldsymbol{a} = \oint_A \boldsymbol{j}_i \cdot d\boldsymbol{a} + \int_{\boldsymbol{V}} \boldsymbol{S}_{\boldsymbol{\phi_i}} \, \boldsymbol{dV}$$

$i \; is \; the \; component \; index$

$\boldsymbol{V} \; is \; the \; volume$

$\boldsymbol{j}_i \; is \; the \; diffusion \; flux$

$\boldsymbol{a} \; is \; the \; area \; vector$

$. \boldsymbol{S}_{\boldsymbol{\phi_i}} \; is \; a \; source \; term \; for \; the \; passive \; scalar \; component \; i$

$\phi_i \; is \; assumed \; to \; be \; positive - definite$

A new continua was defined as the part mesh.

Mesh Refinement:

The following meshers were selected- Surface Remesher, Automatic Surface Repair, Polyhedral Mesher and Prism Layer Mesher. Mesh refinement was performed using a coarse, medium and fine mesh with the number of elements increasing by a factor of at least 1.5 each time. Both Wall Shear Stress and Fluid Velocity are quantities of interest so the percent differences between meshes were calculated for both the maximum wall shear

stress on the organoid and the maximum velocity in the fluid. The medium mesh of 786665 elements was selected as the next refinement resulted in less than a 5% difference for both of our quantities of interest. All solutions were run to a convergence of 1e-6 for residuals of continuity, passive scalar and momentum. Computational fluid dynamics was performed by Lorna Barron.

5.2.20. Generation of ventrally patterned conventionally cultured round organoids with Smoothened agonist (SAG) and iWP2

The protocol for conventionally cultured round organoids is described in **section 2.5**.
For ventral patterning, 100 nM Smoothened agonist (SAG) (Millipore, cat. no. 566660) from a stock solution of 100 µM in sterile Ultrapure water and 2.5 µM Wnt inhibitor (iWP2) (Sigma, cat. no. I0536) from a stock solution of 2.5 µM in dimethyl sulfoxide (DMSO) were added to neural induction media at d 5, then every 2 d until d 11, or d 20. CHIR 99021 (Tocris) was not added unless specified in the results section.

5.2.21. Scaffold preparation for microfluidic organoid culture

A single PCL scaffold linear fibre was cut from a 4 x 4 cm scaffold. Using forceps, the scaffold was attached to the custom designed scaffold holder described in **section 5.2.15**, and secured in place using the scaffold holder clips. The scaffold holder and scaffold assembly were sterilised by UV irradiation for 30 - 45 min. Scaffolds were then placed in a 6-well plate and coated in 1 mL of hESC qualified Matrigel (Corning Cat. No. 354277) diluted in DMEM according to the manufacturer's instructions and left to incubate at 37°C for 1 - 2 h. Immediately before cell seeding, scaffolds were washed once in PBS.

5.2.22. Microfluidic organoid culture

*Media formulations are described in **section 2.4**.*

D 0-5

hESCs were prepared as a 1 x 10^6 cell suspension in mTESR media, as described in **section 5.2.4.** After Matrigel incubation, scaffolds in the custom designed scaffold holder were

washed once in PBS and placed in low attachment 6-well plates, or plates treated with 1 mL anti-adherence rinsing solution (Stemcell Technologies) for 1 min, followed by washing three times in PBS. 3 mL of cell suspension was added per well, and the plate gently rocked in a North-South-East-West direction to evenly distribute the cells across the scaffold.

D 3

Scaffold holder and scaffold assembly was gently lifted from the well using forceps and placed into a new well containing 3 mL mTESR media (without ROCK inhibitor or Antibiotic-Antimyocytic). The scaffold holder was flipped around so that the scaffold would face upwards, preventing cell-material interactions on the plate surface and ensuring sufficient media coverage across the scaffold. The cells were left unperturbed on d 4.

D 5

For microfluidic chip assembly preparation, the PDMS chip, glass plates, nuts, bolts, washers, and forceps were sterilised by autoclaving. For patterning experiments, one syringe was filled with 15 mL neural induction medium with 200 nM SAG (Millipore, cat. no. 566660) and 2.5 µM iWP2 (Sigma, cat. no. I0536), and the other syringe was filled with 15 mL neural induction media only. The scaffold holder and organoid assembly was gently lifted from the 6 well plate using sterile forceps and placed inside the microfluidic culture chamber, with the scaffold facing downwards such that the organoid was suspended in the middle of the fluidic flow path. The microfluidic device was assembled by clamping the PDMS chip between the sterile glass plates, and secured with M3 nuts, bolts and washers. Once assembled, the inlet and outlet tubing were inserted into the chip. The assembled chip was then first manually perfused with sterile PBS to fill the channels and growth chamber with fluid whilst removing all bubbles, and subsequently filed with pre-warmed media. The assembled microfluidic chip was moved to the incubator, and syringes secured onto the syringe pump. The flow rate reduction program was initiated using the syringe pump (Harvard Apparatus 33DDS):

- Use the syringe pump purge function to remove any excess air bubbles
- Run the pump at 100 µL/min flow rate for 2 min.
- Run the pump at 50 µL/min flow rate for 2 min.
- Run the pump at 30 µL/min flow rate for 2 min.
- Run the pump at 10 µL/min flow rate for 2 min.

- Run the pump at 5 µL/min flow rate for 10 min.
- Set the pump at 1.33 µL/min flow rate for remainder of run.

Culture was performed under a continuous flow (1.33 µL/min) of neural induction medium.

D 7

Syringes were replaced with 15 mL fresh medium.

D 10 – 20

The microfluidic device was disassembled, and the scaffold holder was gently removed from the microfluidic chip and placed in a new 6 well plate with 4 mL neural induction media (as described in **section 2.4**) supplemented with 2% (v/v) Matrigel (Corning, cat. no. 356235). The scaffold holder was placed with the scaffold and organoid facing upwards, to prevent cell-material interactions on the bottom of the plate and facilitate 3D growth of the organoid. At d 12, media was exchanged with Improved -A medium (as described in **section 2.4**). At d 18, media was exchanged with Improved +A medium (as described in **section 2.4**). At d 20, organoids were fixed with 4% (v/v) PFA in PBS for 1 h at room temperature or overnight at 4°C and washed three times in PBS.

5.2.23. Widefield microscopy

Brightfield images were acquired using the EVOS XL Core imaging system. Tiled images were fused manually in inkscape (version 0.92). 2D projected organoid area was calculated by generating a binary image of the entire tiled organoid region using open-source image analysis software Fiji ImageJ (version: 2.3.0) and using the 'Analyze Particles' plugin to measure area. Organoid thickness was measured by allocating 7 random regions of interest (ROIs) across the length of the organoid and measuring the width at each ROI. This is shown in **Appendix C**.

Microfluidic generated organoids: Brightfield images were acquired every day from d 10-20 to track the development and morphological changes of the polarised ends of the organoid

5.2.24. Cryosectioning and immunostaining d 20 organoid samples

D 20 organoids on scaffolds were fixed in 4% (v/v) PFA in PBS overnight at 4°C and washed three times PBS. Single elongated organoids were cut from the main scaffold using micro-dissecting scissors. Cryosectioning is described in **section 2.6**. Immunofluorescence staining is described in **section 2.7**. Antibodies are listed in **Table 5**.

Table 5 Antibodies used in Chapter 5.

Antigen	Host species	Supplier	Cat number	Dilution
SOX2	Rabbit	Abcam	ab97959	1:600
FOXG1	Rabbit	Abcam	ab18259	1:200
PAX6	Sheep	R&D Systems	AF8150	1:200
aPKCzeta	Mouse	Santa Cruz	SC-17781	1:200
NKX2.1	Rabbit	Epitomics	6594-1	1:1000
FOXA2	Goat	R&D systems	AF2400-SP	1:300

5.2.25. Optical clearing organoid samples

For optical clearing, a previously published protocol was adapted.[158] D 20 and d 40 organoids were fixed in 4% (v/v) PFA in PBS overnight at 4°C and washed three times in PBS. Elongated organoid samples were cut from the scaffold using micro-dissecting scissors. Optical clearing is described in **section 2.9**. Primary antibodies SOX2 (Abcam) and aPKCzeta (Santa Cruz) were used at a dilution of 1:200 and 1:100, respectively.

5.3. Results and discussion I: Directing elongated organoid growth on scaffolds

5.3.1. Introduction

The generation of organoids with a physiological axis remains a major challenge within the organoid field. Axis formation is essential for the development of spatially organised structures in the developing embryo, and is initiated by symmetry breaking, which occurs due to the complex choreography of morphogen gradients and signalling molecules.

In conventional cerebral organoid culture, organoids typically develop from spherical embryoid bodies that do not morphologically provide the opportunity to develop polarised axes to mimic the *in vivo* brain anatomy. The isotropic presentation of patterning factors in the media also contribute to the lack of polarisation. This seriously limits the progress of brain organoid research, particularly for neurological development and disease, such as holoprosencephaly, a development defect in the forebrain in which impaired signalling impedes dorsoventral polarisation, causing midline facial defects.[193]

Previous research has shown that geometrically confined culture of hPSCs can orchestrate symmetry breaking and initiate a gradient distribution of signalling molecules for regionalised cell differentiation.[75,194,195] Micropatterning technologies have also been employed for studies showing early human neural tube development and dorso-ventral organisation in spinal cord-like organoids.[196] These studies demonstrate that autonomous self-patterning may be guided by external cues, by engineering the shape of the stem cell microenvironment.

However, these guidance-based technologies have so far been employed in early developmental models and have not yet been shown in the application of more mature 3D cerebral organoid cultures. Here, the scaffold platform has been adapted to guide organoids into an elongated morphology. Furthermore, this platform provides the opportunity to reproducibly form multiple elongated organoids on a single scaffold array, providing a controlled and high-throughput system for elongated cerebral organoid generation. Crucially, the incorporation of the scaffold also provides additional advantages, including the opportunity to bind and release growth factors. This will be explored further in Subchapter 5.4 and 5.5.

5.3.2. Elongated scaffold design optimisation

In previous chapters it was demonstrated that scaffold geometry can be used to guide the organisation and morphology of stem cell and organoid growth. Here, an adapted PCL scaffold was designed using MEW, comprised of fibres forming single lines distanced at 4 mm apart, with the goal to form continuous elongated organoids. The scaffold was held in place by orthogonal fibres at either end and printed at a distance of 500 µm apart to form a rectangular lattice structure at either end. This created a 4 x 4 cm scaffold (**Figure 5.1**). Similar to the scaffold preparation procedure described in Chapter 3 and 4, the scaffolds were placed in a CellCrown holder. The lattice structure at either end of the scaffold facilitated placement in the CellCrown holder. The scaffold was manually tensioned in the direction of the linear fibres during placement, to ensure that the scaffold was taut. This resulted in approximately 4 or 5 linear fibre structures in the region of the CellCrown that was exposed to cells, with the potential to generate the same number of elongated organoids.

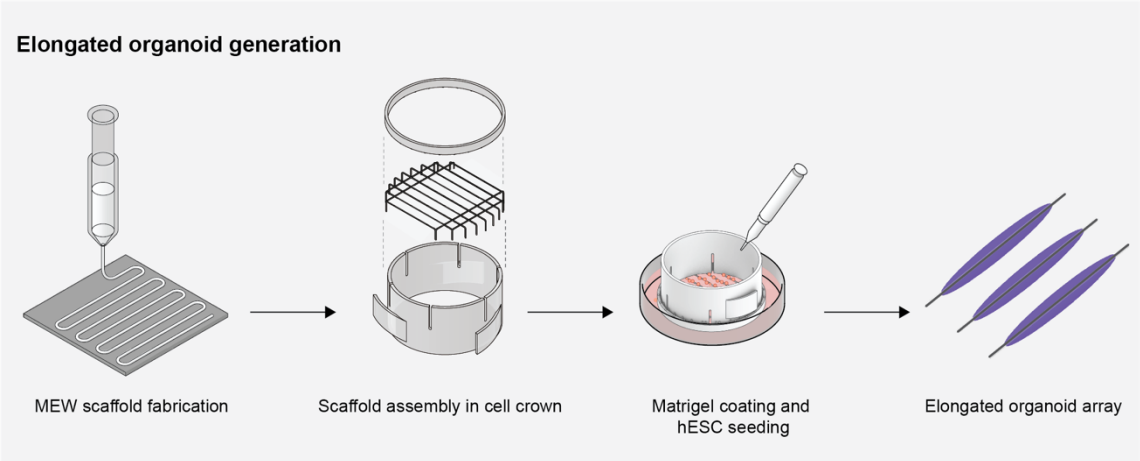


Figure 5.1. Elongated organoid generation schematic. *PCL scaffolds are fabricated by MEW. For cell culture, scaffolds are assembled in a CellCrown, then sterilised by UV irradiation. Prior to cell seeding, scaffolds are coated in Matrigel, then incubated for 1 h and washed in PBS. 1 x 10^6 hESCs are seeded on scaffolds in stem cell media. Cells aggregate on the fibres and grow into elongated organoids.*

In Chapter 3, it was demonstrated that adding Matrigel to the scaffold increased cell adhesion, forming interconnected cerebral organoids on square scaffolds. Furthermore, hESCs were shown to behave in a curvature dependent manner on the scaffolds, showing an increased number of cells in higher curvature regions of triangle and rhombus shaped scaffolds. In the adapted design for elongated organoid culture, the curvature of the linear fibres remains zero. It was therefore reasoned that Matrigel coating the scaffolds was required to promote cell adhesion.

Preliminary studies using the same cell seeding density (1×10^5 cells) as previously reported in Chapter 3 and 4 resulted in sparse cell attachment on the Matrigel coated fibres (**Figure 5.2a**). The cell seeding density was therefore optimised to uniformly coat the scaffold fibres. Three different hESC seeding densities were compared, including 1 x10^5, 1 x 50^5 and 1 x 10^6 hESCs in mTESR stem cell medium (**Figure 5.2a**). Cells were found to attach in all conditions, yet the higher seeding density of 1×10^6 cells resulted in more homogenous cell attachment across the entire fibre. At the lower seeding densities, there was a greater tendency for the cells to attach in clusters, forming non-continuous tissue growth in random regions of the fibre. Using a cell seeding density of 1×10^6 hESCs, the aggregated cells on scaffolds were differentiated to cerebral organoids using the previously optimised protocol in Chapters 3 and 4. Briefly, mTESR stem cell medium was replaced with a neural induction medium at d 5, and 2% (v/v) Matrigel was added at d 10, leading to the formation of VZ-like structures at d 16 (**Figure 5.2b**). To calculate 2D projected organoid surface area, a workflow was established to first tile the brightfield images to show the entire elongated structure of each individual organoid. Fiji was then used to threshold and quantify the 2D area of the organoid as shown in brightfield at three different timepoints (see materials and methods). The results showed that the scaffold-cultured organoids progressively grew between timepoints and reached a mean area of 6.75 mm^2 ± 0.95 at d 16 (**Figure 5.2c**). Tissue thickness was measured by allocating representative ROIs at 7 random locations along the length of the organoids (**Appendix C**). The results showed a significant increase in tissue thickness with increased age, corresponding to ~60% increase in thickness every 5 d, between d 6 and 16 (**Figure 5.2d**). Amorphism and heterogeneity at the organoid surface is well known due to

the nature of the ongoing tissue growth,[80] which was observed on elongated organoids grown on scaffolds at d 20 and 40 (**Figure 5.2d**).

To test if the overall uniformity of the elongated organoid growth could be improved, narrow PDMS channels were designed to align with the scaffold to concentrate the cells around the fibres and promote more uniform cell attachment fibres (see materials and methods). However, results showed that there was minimal difference in the surface homogeneity between the elongated scaffold organoids grown with or without PDMS channels after 20 d of culture (**Appendix D**). As such, to minimise any additional or ongoing effects from using PDMS channels (such as geometric confinement or altered mechanical effects), the PDMS channels were not used in any further experiments.

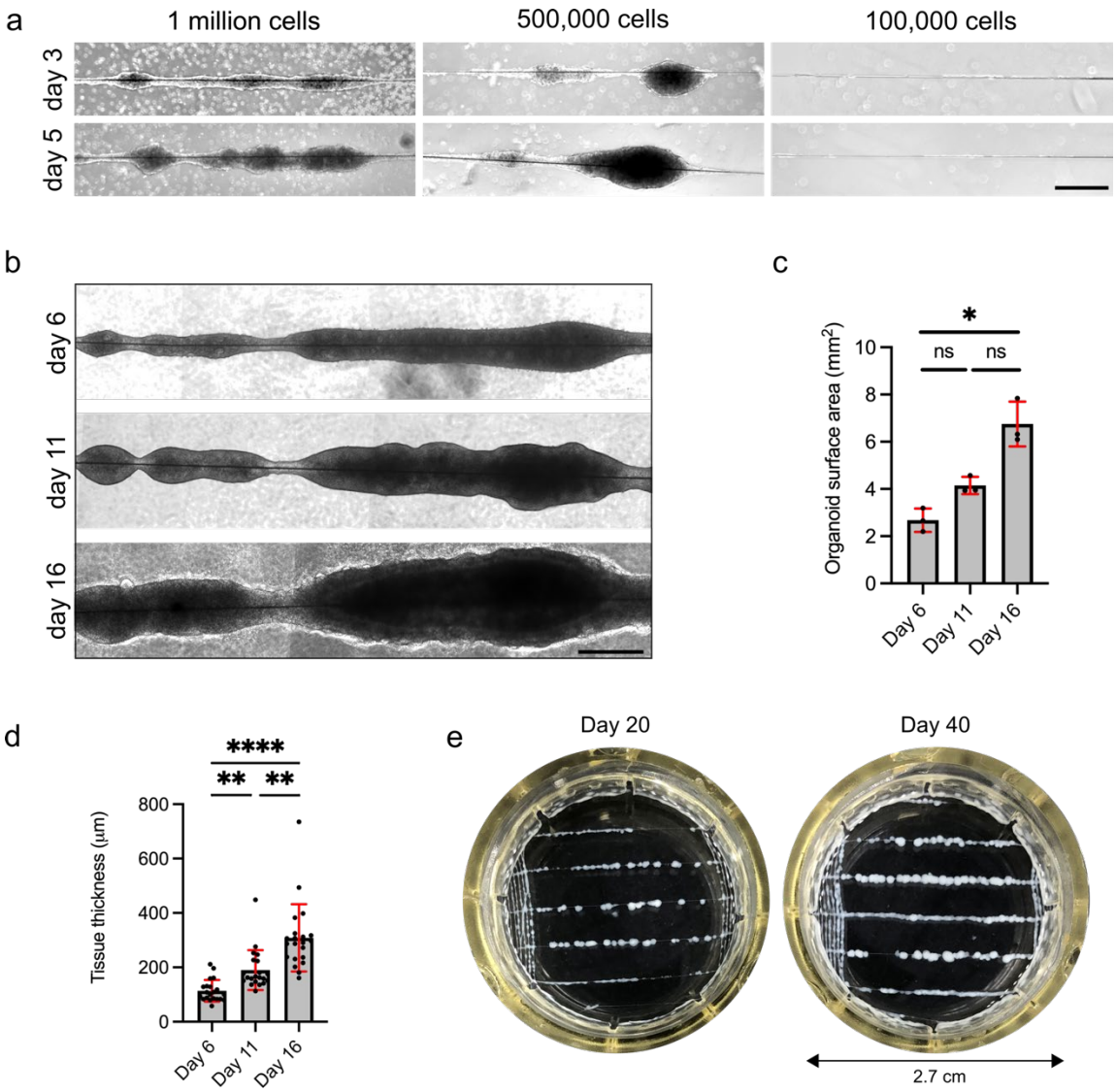


Figure 5.2 Characterisation of elongated cerebral organoid growth on scaffolds. *a) Brightfield images show elongated organoids grown on scaffolds with different seeding densities of 1 × 10^5, 1 × 50^5 and 1 × 10^6 at d 3 and 5. Scale bars correspond to 500 µm. b) Tiled brightfield images show elongated organoids grown at a seeding density of 1 x 10^6 at d 6, 11 and 16. Scale bars correspond to 500 µm. c) 2D surface area of elongated organoids at d 6, 11 and 16. Analysis was performed using 3 independent organoids from the same batch (N = 1, n = 3). P value: (*) <0.0219 determined by Kruskal-Wallis with Dunn's post-test. Data represent mean ± SD. d) Mean tissue thickness of elongated organoid. Tissue thickness was measured at 7 random ROIs for each independent organoid. The ROIs used to measure tissue thickness are shown in Appendix C. Analysis was performed using 3 independent organoids from the same batch (N = 1, n = 3). P values: (**) <0.0048, (****) < 0.0001 determined by Kruskal-Wallis with Dunn's post-test. Data represent mean ± SD. e) Photograph of fixed elongated organoids on scaffolds in CellCrown holder at d 20 and d 40.*

5.3.3. Elongated organoid characterisation

Next, histological sectioning and immunostaining of the elongated organoids was performed to establish if they show a comparable expression of key markers to conventionally grown cerebral organoids. Tiled confocal images show a ~1 cm portion of the elongated organoid at d 40, stained with neuronal marker MAP2 and counterstained with DAPI (**Figure 5.3a**). MAP2 marker was expressed on the outer layers of the organoid, as typically seen in conventional organoids. Additionally, FOXG1 marker, which is typically expressed in the forebrain, and PAX6 marker, which is typically expressed in the dorsal forebrain, showed co-expression in several of the VZ-like lumen areas of the organoid. This expression pattern is typical of a conventionally grown 'unguided' cerebral organoid.

To further characterise the elongated scaffold organoids, tissue clearing and immunostaining were used to visualise the organoid morphology around the scaffold. As reported in Chapter 3 and 4, a previously published protocol was adapted for tissue clearing. Here, fixed elongated organoids were individually cut from the CellCrown and scaffold using micro-dissecting scissors, before proceeding with tissue clearing (materials and methods). During the final step in the protocol, it was found that elongated organoids deformed by becoming rigid and curling up, as an effect of immersion in the organic solvent, ethyl cinnamate (ECi). This prevented imaging of the entire elongated organoid, however high-resolution confocal imaging of SOX2 immunostained organoids at d 20 allowed us to image a segment of the organoid surrounding the fibre. Using the Fiji plugin segmentation editor, the fibre structure was segmented from confocal z stacks to clearly visualise its position in relation to the organoid. 3D reconstruction and cross section of the segmented images indicated that the fibre was located in the center of the organoid tissue (**Figure 5.3b**). 3D reconstruction of z stack confocal images of organoids at d 40 immunostained with SOX2 and apical marker aPKCzeta show the appearance of large VZ-like lumens throughout the entire volume of the imaged organoid region (**Figure 5.3c**). VZ-like regions are essential structures in brain organoids that mimic cellular processes and tissue organisation of the VZ in the human developing brain. These results demonstrate that elongated scaffold organoid culture supports the expansion of large, reproducible VZ-like regions.

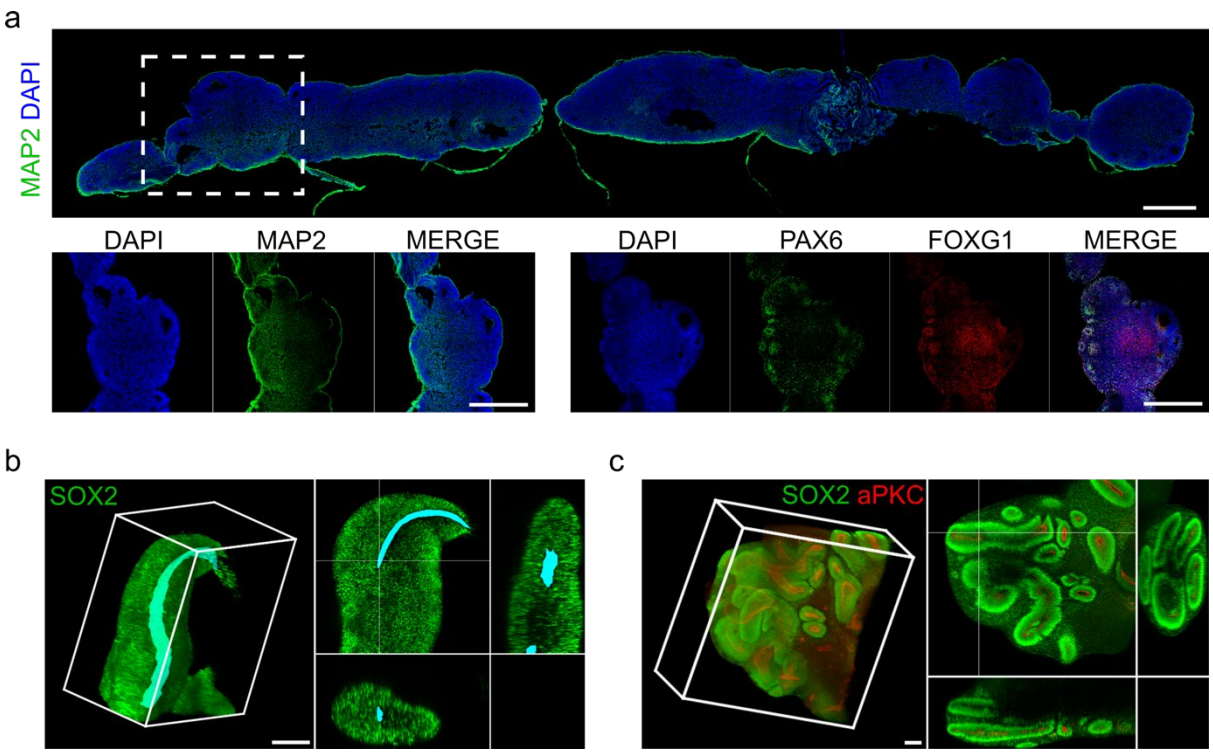


Figure 5.3 Characterisation of elongated scaffold organoids. *a) Histological sections of elongated organoid immunostained with MAP2 (green) and nuclear counterstain DAPI (blue). Dashed box indicates region for image panel below, showing single and merged channels of MAP2 and DAPI (left). A separate histological slice at the same region was immunostained with PAX6 (green), FOXG1 (red) and DAPI (right). Fluorescent images are representative of organoids from 2 biological experiments (N = 2). Scale bars correspond to 500 µm. b) Image gallery at d 20 showing a z stack of an elongated organoid on scaffold cleared and immunostained with SOX2 (green). The scaffold region has been pseudo coloured in cyan to visualise the position of the scaffold in the organoid. Cross-sectional view shown on the right. Scale bar corresponds to 100 µm. c) Image gallery at d 40 showing a z stack of an elongated organoid on scaffold cleared and immunostained with SOX2 (green) and aPKCzeta (red). Cross-sectional view shown on the right. Scale bar corresponds to 100 µm.*

Previous reports have demonstrated that generating brain organoids with elongated or flat morphologies can increase the surface area to volume ratio, leading to enhanced neuroectoderm formation and decreased tissue necrosis.[143,144] The previous results in Chapter 3 demonstrated that culturing round organoids on scaffolds enhanced the formation of VZ-like regions. In future work it will be interesting to decouple the relative contributions of the elongated morphology and the presence of the scaffold fibre, to determine whether organoid elongation further enhances the formation of VZ-like regions,

or if this is purely due to the presence of the fibre scaffold. This could be analysed by quantifiably comparing the size of VZ-like regions and levels of necrosis in round and elongated scaffold organoids, compared to conventionally cultured round organoids. In addition, it will be important to test an alternative tissue clearing method to facilitate high resolution 3D imaging of the entire elongated organoid structure. Tissue rigidity and deformation due to ECi immersion has previously been reported in human brain tissue.[197] An alternative tissue clearing method, such as CLARITY may be used to prevent tissue rigidity of the organoid in the future.

5.3.4. Conclusion

Overall, these results showed that the organoid scaffold platform can be used to generate elongated organoid arrays. Immunostaining demonstrated cerebral organoid viability, showing expression of key developmental markers at d 20. Similar to the scaffold organoids demonstrated in Chapters 3 and 4, the scaffold assembly provided the opportunity to easily move and manipulate organoid position, which is typically not possible in conventional organoids cultured in free floating media. A key advantage to this system is the elongated morphology, which provides an ideal platform for further organoid polarisation strategies. This will be further explored in the next Subchapters 5.4 and 5.5.

5.4. Results and discussion II: Bioactive scaffolds to direct elongated organoid regionalisation

5.4.1. Introduction

In Subchapter 5.3, scaffold geometry was optimised to facilitate the growth of elongated organoids. The scaffold polymer PCL can also be engineered to deliver growth factors to guide cell differentiation. In this subchapter, scaffold functionalisation is explored, with the aim to generate an *in-situ* scaffold reservoir for releasing growth factors to the growing cerebral organoids.

Huge efforts have previously been made to discover strategies for generating growth-factor binding scaffolds for tissue engineering applications. Different approaches have been extensively explored, including physical and covalent immobilization strategies.[198] In the past decade, electrospun scaffolds have gained particular popularity in this field, owing to their thin fibre diameter and subsequent high surface area to volume ratio, which enhances growth factor binding on the polymer surface.[199] Non-covalent immobilization strategies are generally preferred for tissue engineering applications, as growth factors can be structurally denatured by covalent attachment, affecting their functional activity.[200] In our own group, incorporation of spatially organised binding peptides on electrospun PCL fibres was previously achieved by sequentially electrospinning PCL with different biomolecule-binding peptide-polymer conjugates. [200] This strategy supported the non-covalent binding of naturally occurring biomolecules in the ECM, to generate dynamic gradient scaffolds to guide cell growth and differentiation. Layer-by-layer (LbL) assembly represents another non-covalent functionalisation strategy, whereby multiple functional coatings are sequentially layered on a surface by electrostatic interactions.[201]

Scaffold functionalisation to regulate the regional development of cerebral organoids has not currently been reported in the literature, and represents an exciting advancement for the development of more complex organoid systems. Here, the hypothesis that growth factor-releasing scaffolds can be used to guide the regional specification of elongated

organoids is investigated. As a proof-of-principle, scaffolds were functionalised using LbL assembly, with the goal to induce a ventral organoid identity by the sequestration and release of the sonic hedgehog (Shh) growth factor from the scaffold to the growing organoid.

5.4.2. Shh induced ventralisation of conventionally cultured round organoids

Due to the batch-to-batch variabilities that can occur in recombinant proteins, Shh was first tested by culturing conventional round organoids with 1000 ng/ml Shh in media. It was reasoned that using a high concentration would most clearly reveal activation of the Shh signalling pathway and ventralisation of the organoid tissue. Immunostaining at d 20 showed substantially increased expression of the ventral marker NKX2.1 in Shh treated organoids, compared to untreated organoids. The floor plate marker, FOXA2, which is a downstream target of Shh, showed expression in 2 of the 3 Shh-treated organoids. Positive FOXA2 staining was also observed in 1 of the 3 non treated organoids. This is likely because ‘unguided’ cerebral organoids are typically variable and contain a diverse mixture of subregional brain tissue. Whilst further experiments should be carried out to confirm a reduction of dorsal regions in the Shh treated organoids to fully confirm this, these results indicate that Shh treatment induces ventral subregional identity in the organoid tissue, as demonstrated by increased NKX2.1 expression.

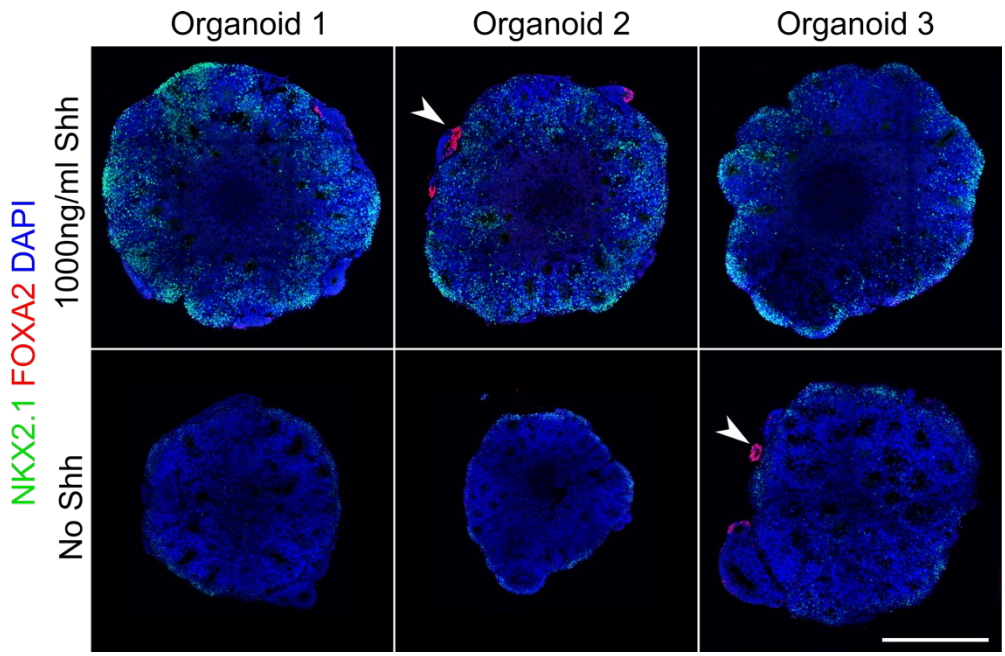


Figure 5.4 Conventionally cultured round organoids show ventral tissue identity at d 20 with Shh morphogen treatment. *Organoids were treated with 1000 ng/ml Shh at d 0 - 3 and negative controls were not exposed to Shh. Histological sections were immunostained for ventral marker NKX2.1 (green), floor plate marker FOXA2 (red) and nuclear counterstain DAPI (blue). Shh treated organoids show increased expression of NKX2.1 compared to negative control. White arrowheads show FOXA2 positive regions. At least 3 organoids were analysed in each condition, from 1 biological experiment (N = 1, n = 3). Scale bar corresponds to 500 µm.*

5.4.3. LbL functionalisation of scaffolds

To promote a ventral organoid identity in the elongated scaffold organoids, a suitable delivery method was first established to bind and release Shh from the scaffold. Glycosaminoglycans (GAGs) represent a class of biologically derived materials that can sequester and release large quantities of protein cargoes in a controlled manner.[202] GAG based coatings have also previously been used for LbL deposition, such as the polyanion heparin. Shh contains a heparin binding domain, as Hedgehog (Hh) proteins require heparan sulfate proteoglycans (HSPGs) for normal distribution and signalling.[203] Heparin therefore represents an ideal candidate to use for LbL assembly on the scaffolds, to facilitate sequestration and Shh release during organoid growth.

For LbL assembly of oppositely charged polyelectrolytes, Shh-binding heparin was used as the polyanion, and chitosan as the polycation to generate electrostatically bound multilayers containing Shh on the scaffold surface. As another GAG, chitosan has been widely used in biomedical applications owing to its biodegradability and biocompatibility.[204] To generate the chitosan/heparin multilayer coating, elongated scaffolds were first treated with oxygen plasma, to increase the hydrophilicity and surface charge of the scaffold surface. This assists the LbL assembly by forming negative ions to enhance electrostatic interaction with the polycation chitosan. Scaffolds were then assembled in the CellCrown holder. A 6 well plate was prepared with solutions of chitosan, heparin and Ultrapure water. To facilitate the successive dipping and washing steps for LbL assembly, a 3D printer was modified and programmed to successively move the scaffold between the different wells, including washing steps between the chitosan and heparin solutions. These steps are shown schematically in **Figure 5.5.** The CellCrown holder was fitted with a custom-made adaptor to attach to the moving arm of the 3D printer. Following the LbL assembly, scaffolds were soaked in Shh solution overnight at 4°C.

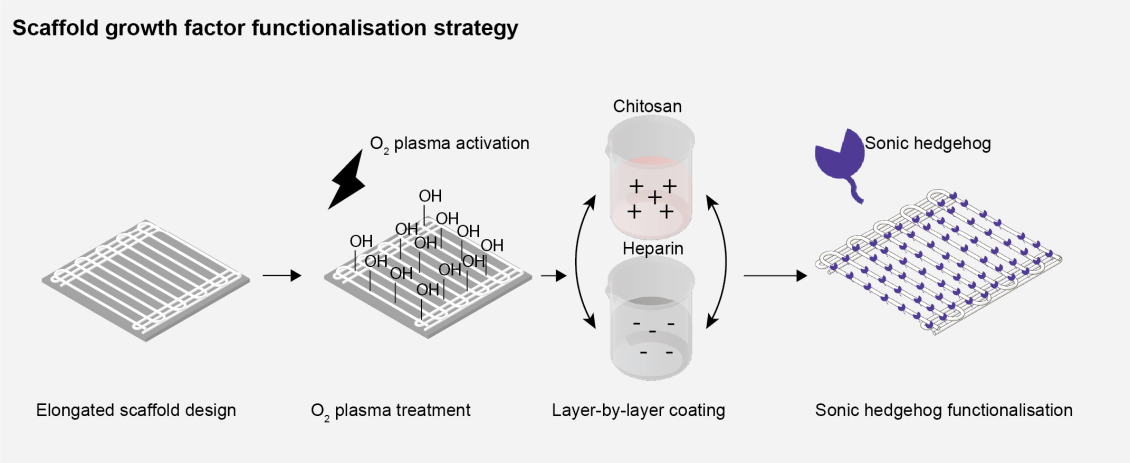


Figure 5.5 Scaffold growth factor functionalisation with LbL assembly. *PCL scaffolds are fabricated by MEW and treated with oxygen plasma to enhance LbL assembly. Using an adapted 3D printer, scaffolds are successively dipped in solutions of chitosan and heparin and washed in Ultrapure water between coatings. After LbL assembly, scaffolds are soaked in Shh solution overnight at 4°C and prepared for cell culture experiments.*

LbL-coated scaffolds (without Shh) were generated with 10 multilayers and analysed using X-ray photoelectron spectroscopy (XPS). **Figure 5.6** shows the elemental spectra of pristine

PCL and chitosan/heparin LbL coated PCL, respectively. In the S2p spectra of the LbL-coated PCL, a peak was observed at 169 eV, associated with sulfate groups from the heparin. In the N1s spectra, the presence of chitosan was indicated by the amino groups. The peak at 402 eV corresponded with protonated amine, and the peak at 401 eV with a neutral amino group. This likely contained contributions from deprotonated amine, amide and a protonated amine interacting with sulfonate. In the C1S spectra of pristine PCL, three peaks were observed at 284 (-C-C-), 286 (-C-O-) and 288 eV (-O-C=O). Heparin and chitosan are both polysaccharides, which are rich in -C-O-. Accordingly, this shifted the peak ratios in the LbL coated sample. Carboxylic acid groups at 288 eV are likely a contribution from heparin. The O1s spectra in pristine PCL showed a peak at 532 eV and 533 eV, corresponding to C-O and C=O bonds respectively. A shift in peak ratio was also noted in the LbL coated spectra, which is likely due to the different functional groups present in heparin and chitosan, such as increased hydroxyl groups. Overall, these results confirmed the presence of heparin and chitosan on the scaffold surface.

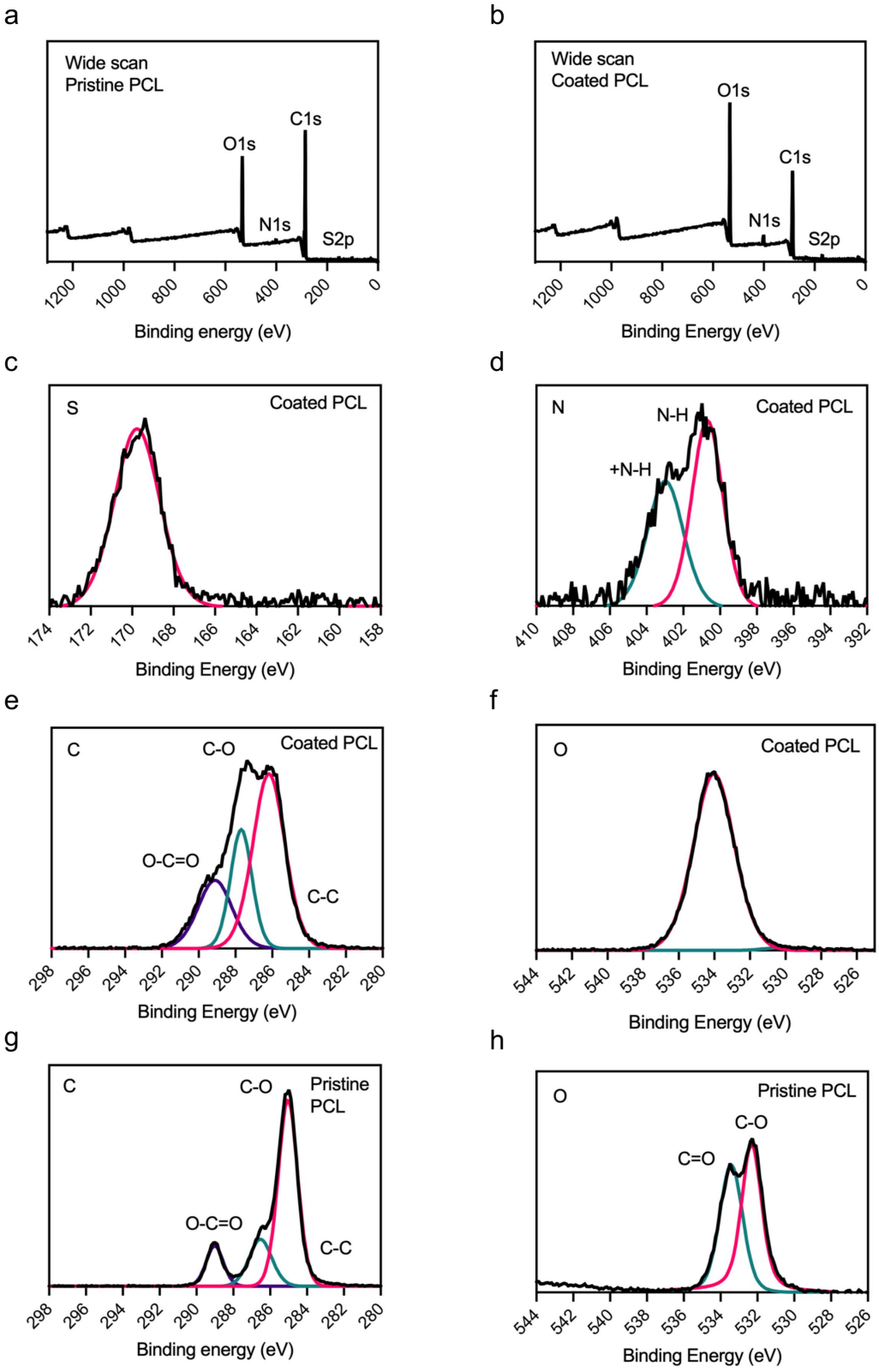


Figure 5.6. XPS spectra shows presence of heparin and chitosan on scaffolds after LbL assembly with 10 layers. *Elemental composition of coated PCL and pristine PCL via XPS showing a) Survey scan of pristine PCL. b) Survey scan of LbL coated PCL. c) S2p core-level fitted spectra of coated PCL. d) N1s core-level fitted spectra of coated PCL e) C1s core-level*

fitted spectra of coated PCL. f) O1s core-level fitted spectra of coated PCL. g) C1s core-level fitted spectra of pristine PCL. h) O1s core-level spectra of pristine PCL. Samples are represented in black and fitted curves shown in pink, green and purple. XPS and analysis carried out by Dr. Daniel Hachim Diaz.

5.4.4. Material characterisation

The Shh growth factor was next immobilized on the LbL scaffolds by soaking the scaffolds in a Shh solution at 4°C overnight. A high Shh concentration of 4000 ng/ml was used to ensure high surface loading of the growth factor. To characterise Shh immobilization, immunostaining of the scaffolds using a Shh marker was performed. The scaffolds were removed from the CellCrown holder to assist imaging a high density of fibres without the need for tiling during imaging. Three different experimental conditions were prepared, including LbL scaffolds with Shh, pristine PCL with Shh, and pristine PCL without Shh as a negative control. The results demonstrated that Shh was expressed in LbL and pristine PCL scaffolds, and no expression was observed in the negative control condition (**Figure 5.7a**). These results showed that Shh protein was immobilised to pristine PCL in the absence of heparin, which likely occurred due to physisorption. Whilst physisorption has previously been used in other studies to bind growth factor molecules to the surface of a biomaterial, this is typically associated with poor control over growth factor release.[205]

To test the hypothesis that the LbL strategy confers an advantage for more sustained and controlled Shh release compared to pristine PCL, Shh was immobilized to the scaffold by soaking the CellCrown and scaffold assembly in a 4000 ng/ml Shh solution. Shh release from the scaffold was monitored using an enzyme-linked immunosorbent assay (ELISA) over a 7-d time course, using cell culture conditions. To assess whether the number of LbL multilayers affected Shh sequestration, scaffold samples with 10, 20 and 40 LbL multilayers of chitosan and heparin were analysed. ELISA results demonstrated that Shh was released from the LbL and pristine PCL scaffold over approximately 4 d (**Figure 5.7b**). Minimal differences were observed in the Shh release profile between the LbL conditions and pristine PCL. The results also showed that Shh release did not exceed 7 ng/ml in any of the conditions, equating to only 0.9% of the total Shh in solution (800 ng) that was initially added to the CellCrown and

scaffold assembly. These concentrations are significantly lower than those reported in the literature for organoid ventralisation. One possible explanation for this is that Shh remains bound to the scaffold. In future experiments, heparinase treatment could be used to induce release of the heparin-bound Shh growth factor, for quantification of scaffold-bound Shh. Low growth factor binding to the scaffold is another possible explanation, which could be measured by analysing the Shh content of the Shh solution after soaking the scaffold. It should also be noted that there was minimal difference observed in the release profile between 10, 20 and 40 LbL conditions. In future work it may be useful to extend the time of the release study, to see if there is any continued or sustained release for the higher LbL conditions.

Despite the low Shh concentration observed in the release assay, the conventional patterning protocols involve adding Shh to the media, and the scaffold functionalisation approach cannot easily be compared in the same manner due to differences in presentation and delivery of Shh from the scaffold. Whilst this stage represented an optimisation point to enhance growth factor loading, it was reasoned that carrying out organoid growth experiments at this stage would provide an alternative, and more immediately relevant readout of whether this functionalisation strategy would be effective for organoid ventralisation.

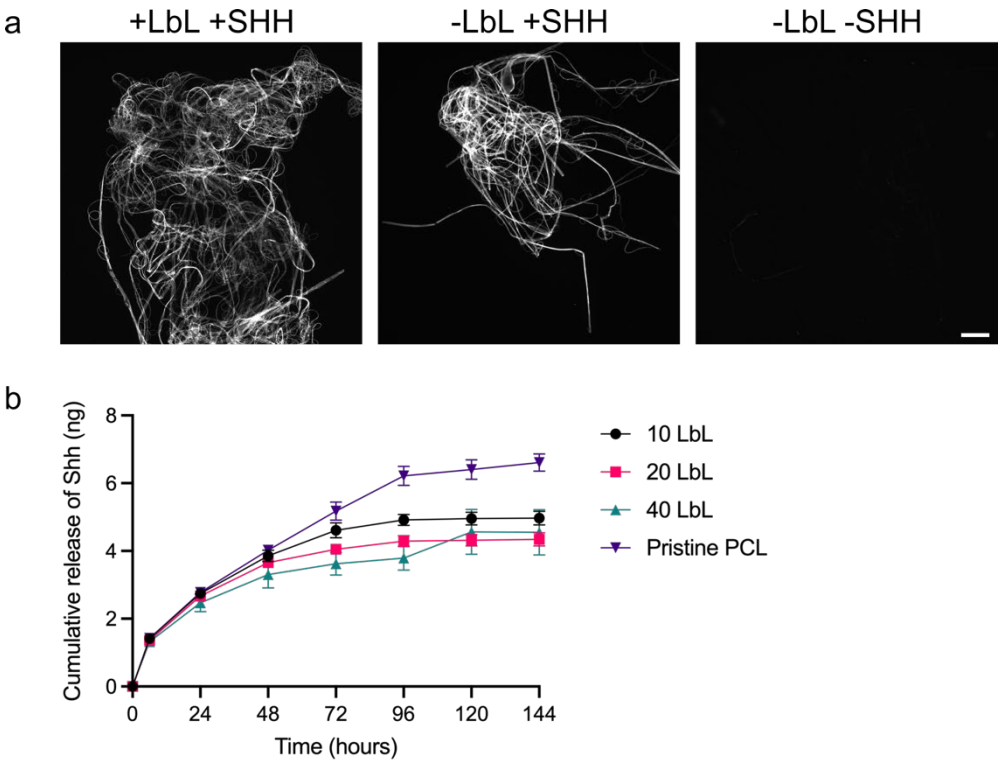


Figure 5.7 Shh functionalisation on scaffolds. *a) Immunostaining of Shh functionalised scaffolds on LbL scaffolds (left), no LbL scaffolds (middle) and negative control scaffolds with no LbL and no Shh (right). Positive Shh expression was observed on the LbL and no LbL Shh functionalised scaffolds. Scale bar corresponds to 500 µm. b) an ELISA was used to detect release of Shh from 10 LbL, 20 LbL, 40 LbL and no LbL scaffolds into cell culture media over a period of 144 h (6 d). N = 3. Data represent mean ± SD.*

5.4.5. Organoid characterisation on Shh functionalised scaffolds

To assess the effectiveness of the LbL strategy for organoid ventral patterning, elongated organoids were grown on the Shh bound scaffolds. Due to the intensive steps involved in scaffold preparation and organoid culture, experiments were performed using LbL and Shh functionalised scaffolds, rather than pristine PCL scaffolds functionalised with Shh by physisorption. ELISA results in **section 5.4.4** showed no significant difference in the release profile between the LbL and Shh, and pristine PCL and Shh scaffolds. However, the LbL approach has previously been shown to improve spatial distribution of growth factors,[205] and was therefore considered more likely to facilitate a controlled biological effect.

In a previous study, a range of Shh concentrations (0, 100, 200, 500 and 1,000 ng/ml) was tested to induce ventral lateral ganglionic eminence- (LGE)-like progenitors from a 2D

culture of hESCs, which was shown by immunostaining to increase the level of ventral markers in a dose-dependent manner.[206] In the LbL and Shh functionalised scaffolds, a range of Shh concentrations (0, 100, 1000, 4000 ng/ml) was similarly tested for organoid culture. After overnight soaking at 4°C, scaffolds were washed three times in PBS for 10 min per wash, to remove any unbound Shh.

To prepare the scaffolds for cell seeding and organoid culture, the optimised protocol for elongated organoid generation was utilised, as described in Subchapter 5.3. In brief, following incubation in Shh and washing steps, the scaffolds were coated with hESC qualified Matrigel for 1 h at 37°C, followed by a washing step in PBS**.** Next, 1 x 10^6 wild-type H9 hESCs suspended in culture media were seeded onto the scaffold in a single cell suspension, gently rocking the well plate to ensure an even distribution of cells across the scaffold. A higher proportion of contaminated samples were observed, compared to culturing the elongated organoids without the LbL and Shh coating. This was attributed to the LbL coating procedure, which occurred in a nonsterile environment. To address this, efforts should be made to carry out the LbL assembly within a sterile environment for future experiments, such as a HEPA-filtered enclosed space.

Brightfield images at d 9 revealed low cell attachment and organoid formation on all LbL scaffolds, compared to the pristine PCL scaffold control. Independent round organoids appeared to form at the edges of the scaffold at the lattice intersections, and minimal attachment occurred on the main fibre strands (**Figure 5.8**). This organoid morphology was highly reminiscent of the independent organoid arrays optimised in Chapter 4, where organoids formed at lattice intersections on pristine PCL scaffolds, without Matrigel coating. In the LbL scaffolds, it is plausible that the negative charge of heparin can exert an anti-adhesion effect on the scaffold, preventing cell attachment. It is also possible that the negative charge inhibits the absorption of key Matrigel components. Furthermore, it is apparent from these results that the anti-adhesion effect was not overcome by the addition of Matrigel coating. For future optimisation experiments, one approach could be to end the LbL assembly in the polycationic chitosan, to increase the number of positively charged sites on the scaffold surface. This could increase cell adhesion by enhancing the electrostatic

interactions with the negatively charged ions in the cell membrane. However, this could also limit the surface binding of Shh to heparin. To address this, Shh could be added to heparin at each assembly step to ensure high surface loading on the scaffold.

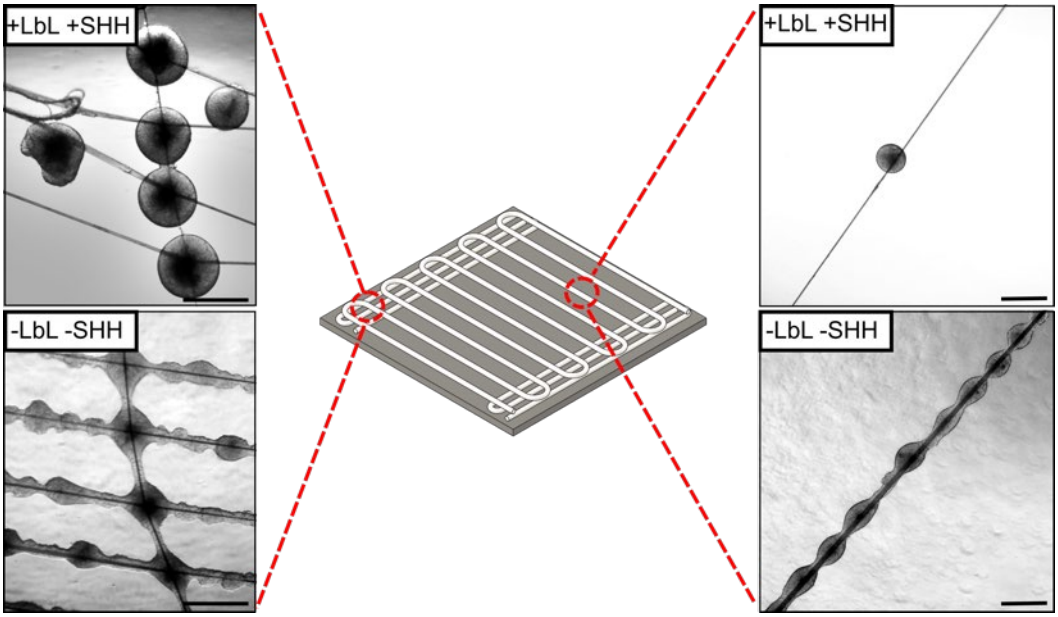


Figure 5.8 Elongated organoid growth on Shh functionalised scaffolds. *Brightfield images show organoids on LbL + 4000 ng/ml Shh coated scaffolds, and negative control pristine PCL (-LBL) without Shh. Red dashed line indicates the region of the scaffold that the brightfield images were taken. N = 3. Scale bar corresponds to 500 µm.*

Before further optimising the LbL coating procedure to enhance cell attachment, the successfully cultured organoids on the scaffold edges were characterised by immunostaining, to establish if ventral patterning could be achieved by LbL Shh sequestration on the scaffold surface. Forebrain marker FOXG1 showed heterogenous expression in the VZ-like regions of the organoids, which was similar in all conditions. In the scaffolds functionalised with higher Shh concentrations (4000 ng/ml and 1000 ng/ml), multiple regions of FOXA2 expression were identified on one side of the organoid (**Figure 5.9**) indicating floor plate identity. This was not observed in the lower Shh concentration, or the negative controls.

Surprisingly, NKX2.1 marker expression was not observed in the higher Shh concentration scaffolds. Previous studies have shown that the floor plate marker FOXA2 is induced by Shh, and FOXA2 positive neuroepithelial cells in the floor plate reciprocally modulate endogenous Shh expression, and act as a signalling center within the developing CNS.[207] Furthermore, Shh mediates the expression of NKX2.1 in the medial ganglionic eminence (MGE) of the ventral forebrain during neurogenesis.[208] It was therefore surprising not to see NKX2.1 marker expression, unlike the previously reported results in Shh treated conventional organoids in this Chapter (**Figure 5.4**). It is plausible that this was a consequence of the differences in timing and presentation of Shh exposure in the scaffold organoids compared to the conventionally cultured organoids. In future experiments it would be valuable to characterise Shh scaffold organoids at earlier and later timepoints to further assess this.

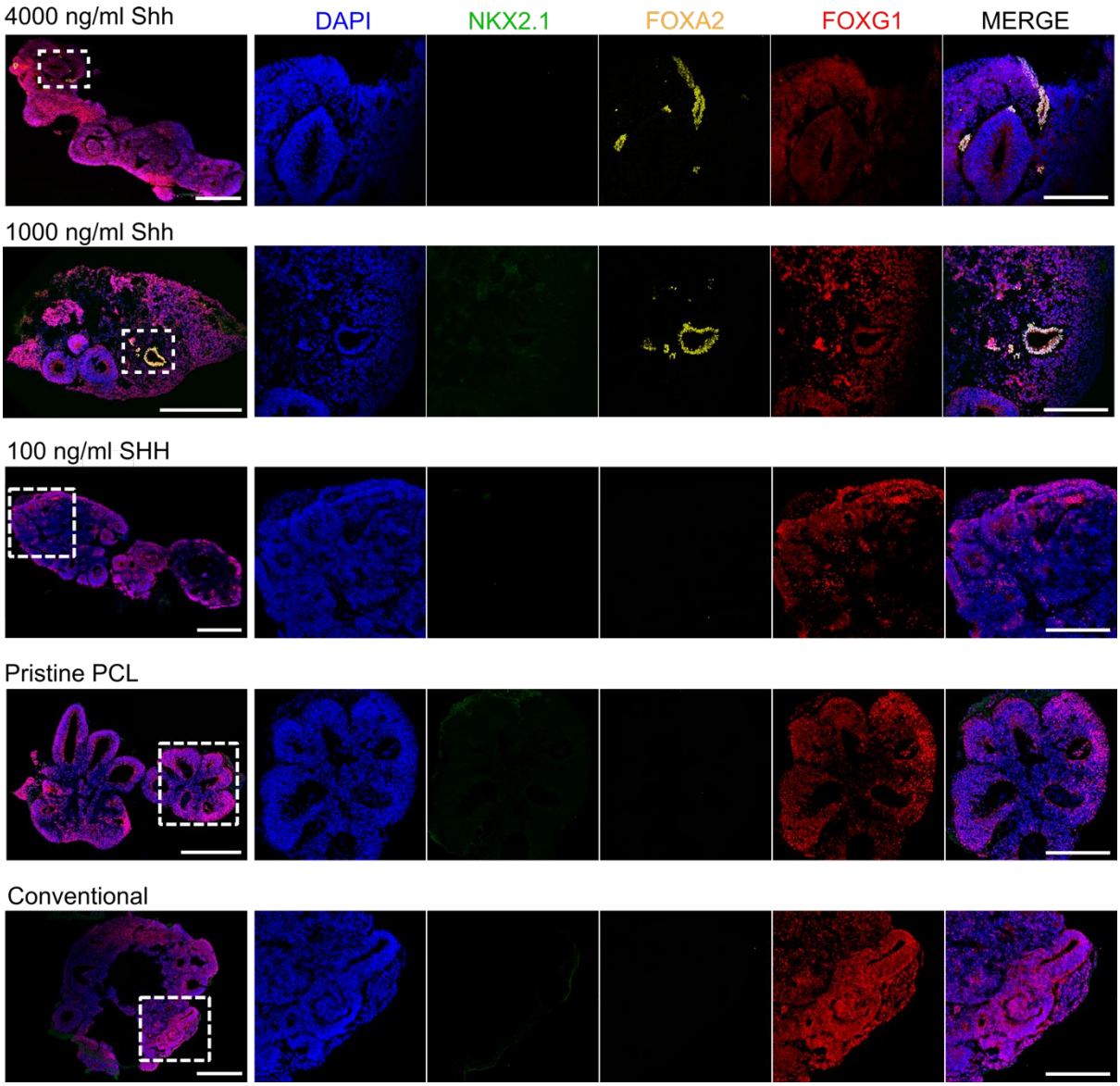


Figure 5.9 Characterisation of d 20 elongated organoids grown on Shh functionalised scaffolds. *Histological section of elongated organoids grown on PCL scaffolds functionalised with: 4000 ng/ml, 1000 ng/ml, 100 ng/ml Shh, and negative controls: pristine PCL without Shh, and conventionally cultured round organoids without Shh. Organoids are immunostained with ventral marker NKX2.1 (green), floor plate marker FOXA2 (yellow), forebrain marker FOXG1 (red) and nuclear counterstain DAPI (blue). White dashed boxes indicate the regions shown in the magnified image gallery on the right. Fluorescent images are representative of organoids from 2 biological experiments (N = 2). Scale bar corresponds to 500 µm (left) and 250 µm (right, magnified view).*

Next, to identify if FOXA2 expression in the high Shh concentration organoids coincided with low PAX6 marker expression, which is typically expressed in the dorsal subdivision of the forebrain, the scaffolds were immunostained with FOXA2 and PAX6. PAX6 marker showed

heterogenous expression throughout the organoid in all conditions (**Figure 5.10a,b** solid white arrowhead). FOXA2 positive regions in the high Shh concentrations were negative for PAX6, as expected. TBR1, a marker for deep cortical neurons that is typically present in the dorsal forebrain, showed heterogenous expression in some VZ like structures, which was similar in all conditions (**Figure 5.10b**). Overall, the immunostaining results provide preliminary evidence that high concentration Shh treated scaffolds induced a floor plate identity in organoids. However, no specific organising strategy showing subregional patterning of ventral and dorsal markers was observed, which is most likely due to the low Shh release from the scaffold, as previously shown in the ELISA results.

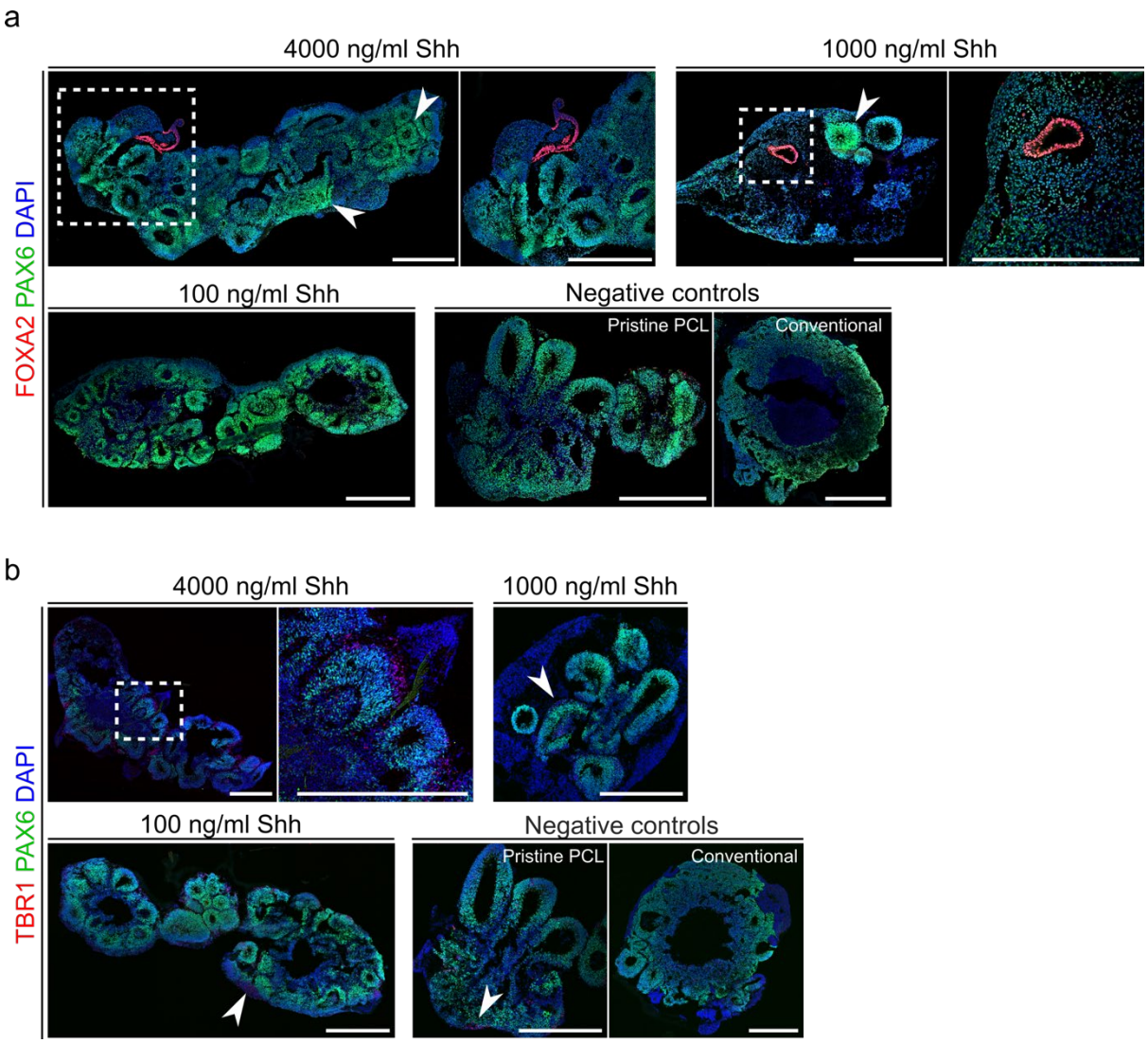


Figure 5.10 Characterisation of d 20 elongated organoids grown on Shh functionalised scaffolds. *Histological section of elongated organoids grown on PCL scaffolds functionalised*

with 4000 ng/ml, 1000 ng/ml, and negative controls: pristine PCL without Shh, and conventionally cultured round organoids without Shh. a) Organoids are immunostained with dorsal marker PAX6 (green), floor plate marker FOXA2 (yellow) and nuclear counterstain DAPI (blue). Solid white arrowheads indicate examples of PAX6 positive regions in the organoid. Scale bar corresponds to 500 µm. b) Organoids are immunostained with dorsal markers PAX6 (green) and TBR1 (red) and nuclear counterstain DAPI (blue). Solid white arrowheads indicate regions with expression of TBR1 marker. White dashed boxes indicate the regions shown in magnified view. Fluorescent images are representative of organoids from 1 biological experiment (N = 1). Scale bar corresponds to 500 µm.

5.4.6. Conclusion

A significant advantage of this system is that growth factors can be delivered in a highly specific and direct way during organoid development. However, specific subregional patterning that corresponded to the location of the Shh loaded fibres in the organoid was not observed. This indicated that further optimisation may be required for Shh loading on the scaffold. It will also be useful to gain more understanding about the spatial presentation of growth factors on the scaffold, and the Shh release dynamics in the context of cell culture.

Whilst LbL functionalisation represents a highly promising technique for organoid patterning, several obstacles were identified during these experiments, including the anti-adhesion effect of heparin, and sterility issues associated with the LbL assembly procedure. Furthermore, the current system is limited to using heparin binding growth factors, which does not apply to all growth factors.

As an alternative option, using a microfluidic approach could address these challenges by providing a more controlled platform to generate gradients of growth factors and small molecules. Microfluidics also represents a more transferable approach for other patterning protocols and organoid systems. This strategy will be explored in the next Subchapter 5.5.

5.5. Results and discussion III: Microfluidic guided organoid polarisation

5.5.1. Introduction

As an alternative approach to physically tethering growth factors to biomaterials to guide lineage specification during cell culture, microfluidic systems have increasingly been used to generate controlled temporal and spatial flow to establish discrete gradients of biochemical signalling molecules.[209–211] Due to the micro-scale structure of microfluidic devices, the fluid flow is usually laminar, with neighbouring fluid streams moving as separate layers. Generating gradients is therefore accomplished by diffusive mixing of the fluid flow streams. This is key to the application of microfluidics in a biological setting, allowing for the possibility to generate highly controlled orthogonal morphogen gradients for cell and organoid culture. Manipulation of input parameters, such as flow rate, channel dimensions and fluid properties make this a highly adaptable technology. Controlling features such as fluid flow and tissue position can also help to deduce their contribution to tissue growth and function.[212]

Microfluidics have previously been used to create complex morphogen gradients on 2D hPSC cultures. In one study, artificial signalling centres were generated by microfluidics to promote the growth of different cell lineage domains in an axially orientated manner. The authors used counteracting sources of bone morphogenetic protein 4 (BMP4) and NOGGIN to break the intrinsic radial symmetry of the hPSC colonies, resulting in precise spatial patterning in an arrangement resembling the mouse epiblast.[213] More recently, a microfluidic device was used to model neural tube development by exposing hESCs to an orthogonal Wnt gradient, to generate a rostro-caudal axis, mimicking neural axis specification in the early embryo.[214] The authors showed that a single Wnt gradient was sufficient for complex regionalisation of early neural tissue in a 2D culture. In another study looking at the dorso-ventral axis, overlapping gradients of retinoic acid and purmorphamine (PM) were used sequentially or simultaneously to generate more complex gradients to mimic in vivo neural tube patterning.[127] The generation of multiple gradients in this study

represents an exciting opportunity to develop spatial patterning along multiple axes to mimic the highly complex choreography of morphogen gradients during early development.

Despite these exciting advances, there is still limited research into the application and adaptation of microfluidics for 3D organoid models. This may be due to the complex culture conditions often involved in organoid culture, and the challenges associated with creating compatible microfluidic systems, such as bubble formation and susceptibility to contamination.[212] One recent study used a micro-chip perfusion system for the generation of mini-intestinal organoids. When connected to an external pump to remove dead cells the organoids were found to have a prolonged lifespan, and an improved capacity to regenerate and develop specialized cell types.[178] This study demonstrated the potential advantage of a microfluidic system on organoid growth, facilitating the removal of waste in a controlled and dynamic culture platform. Similarly, organ-on-chip (OoC) models have employed microfluidic systems to integrate key organ components together to resemble *in vivo* conditions, such as the delivery of oxygen and nutrients, and waste removal. These systems are also amendable to live high-resolution imaging and analyses. For the application of brain organoid growth, one recent study used a microfluidic device for periodic perfusion of the organoids, demonstrating improved survival and reproducibility of the organoid tissue.[215]

Together, these studies demonstrate that with careful design, microfluidics may be applied for 3D macro-scale organoid cultures. Additionally, the fluid flow intrinsic to generating morphogen gradients may provide a further advantage to organoid culture by removing waste and providing a dynamic culture system in a highly controlled setting. As demonstrated in studies using 2D cell cultures, microfluidic systems with multiple overlapping gradients can be generated. Adapting these systems for 3D organoid cultures will undoubtedly accelerate organoid technology, by directing complex subregional domains for the generation of more anatomically accurate and relevant organoid models.

5.5.2. Design principle

A microfluidic chip was designed to establish a controlled morphogen gradient for organoid culture. To achieve this, the previously established microfluidic pyramidal network model was used, where mixing channels facilitate controlled diffusion to generate spatially controlled gradients. Implementation of the microfluidic device as a 3D system is key to our application with a 3D organoid model. In order to fabricate the parts at a large enough scale to support 3D organoid culture, a 3D printing approach was used, based on stereolithography (SLA). This allowed us to rapidly prototype and optimise the microfluidic device, avoiding the need to use traditional soft lithography methods, which are time consuming, error prone and require specialized clean room access.[216] To integrate the organoid in the microfluidic chip, an open-well design was used, where the culture chamber was open and accessible, allowing for addition and removal of the organoid at a specified timepoint. This is in contrast to most microfluidic platforms, where the culture chamber is sealed.[217] Utilising this approach, the organoid culture chamber was designed to contain and culture the elongated organoid perpendicular to the concentration gradient. A custom-made scaffold holder was designed to suspend the scaffold and organoid at a precise position inside the chamber. The scaffold-guided organoid platform provided an ideal opportunity for implementation inside a microfluidic chip for organoid polarisation, whereby the elongated organoid morphology promoted axis formation and polarisation. Additionally, the scaffold platform provided the unique opportunity to easily manipulate and fix the organoid position. The overall design schematic is shown in **Figure 5.11.**

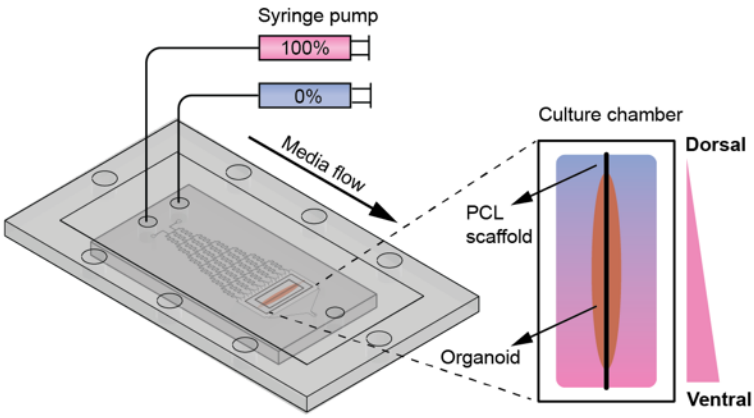


Figure 5.11 Design schematic of microfluidic gradient generator for elongated organoid culture. *The microfluidic chip is fabricated by 3D printing and assembled between two glass plates. The in vivo dorso-ventral gradient of Shh in early embryonic brain development is mimicked by the sequential mixing of two media inlets containing 0% and 100% morphogen. The media flow is controlled by syringe pumps. The elongated organoid on scaffold is fixed in position inside the culture chamber using a custom-made holder, positioning the organoid orthogonal to the gradient. Microfluidic chip design by Dr. Richard Wang.*

5.5.3. Microfluidic chip fabrication

A microfluidic gradient was generated by using a pyramidal network model. The morphogen gradient was formed as two solutions (A) and (B) were repeatedly split, mixed, and recombined in a series of generations of microchannel systems. This formed a highly stable and linear concentration gradient, owing to the laminar flow conditions. To ensure proper diffusive mixing of the solutions in the channels, a serpentine channel design was used to increase the length of the channels which, in turn, prolonged the time allowed for diffusive mixing during flow (**Figure 5.12a**). In this way, the length of serpentine channels was designed relative to the expected steady state flow rate so as to maximise the mixing time.[218]

A channel width of 200 µm was selected for the mixer channels as a compromise between minimising the channel size to support laminar flow, and 3D printing resolution. To incorporate the elongated organoids on scaffolds, a custom scaffold holder was designed to affix a single linear scaffold fibre, cut from the larger 4 x 4 cm scaffold previously described

in this chapter. The custom scaffold holder comprised of a raised rectangular structure that fitted into the growth chamber, with two clips to secure the scaffold in place across the rectangular base (**Figure 5.12b**). This was 3D printed using stereolithographic (SLA) 3D printer with a proprietary biocompatible resin. The organoid culture chamber was designed with chamfered sides at a height of 4 mm, such that the scaffold holder would be suspended inside the chamber and positioned in the middle of the flow stream (**Figure 5.12c**). To reduce the effects of turbulent flow, the serpentine channels were flared out into the culture chamber to ease the fluidic flow transitioning from a thin narrow channel into a large open volume. In this way, the width of the channels was flared from 200 µm to 1.6 mm, whilst the height of the channels was flared from 200 µm to 1 mm. In particular, maintaining the height of the flared region to at least one quarter of the overall chamber height was essential to minimising turbulence in this region. Bubble formation is one of the primary issues reported in microfluidic systems. To help remove bubbles from the culture chamber, a single large outlet channel was designed rather than multiple channels, to reduce the number of features that could trap bubbles.

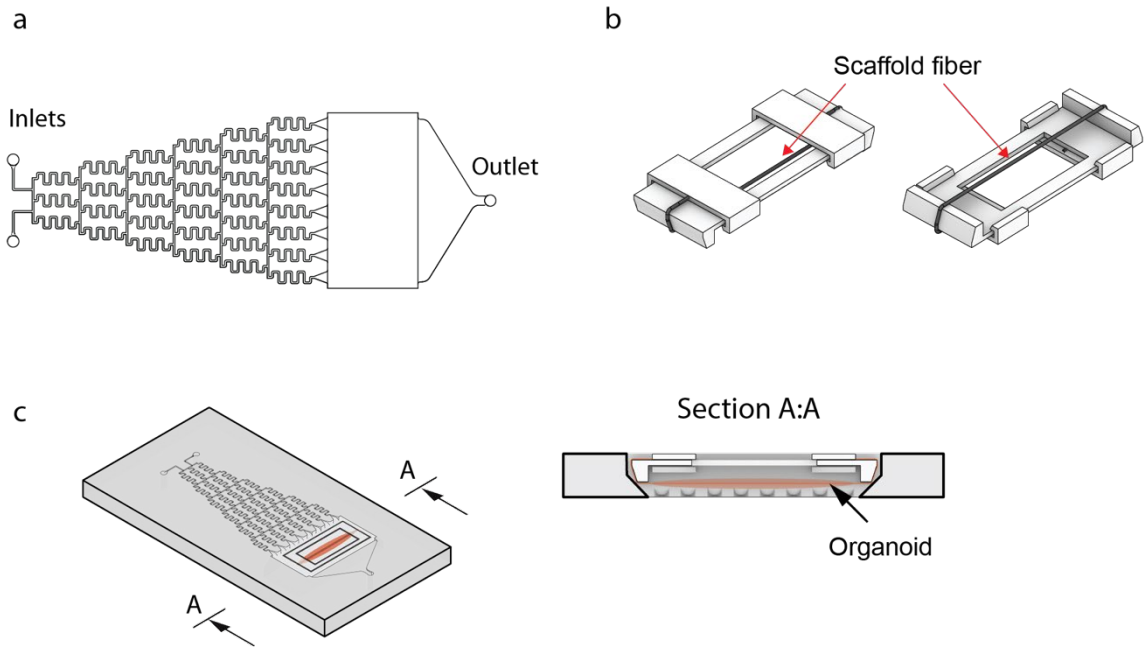


Figure 5.12 Microfluidic chip design. *a) Serpentine channel design shown in 2D. The channels are flared out into the culture chamber to transition fluid flow from a narrow channel to open volume. b) Two clips secure the scaffold across the rectangular base of a custom designed scaffold holder. The scaffold holder and organoid assembly are placed inside the culture chamber of the microfluidic chip, positioning the organoid in the middle of*

the flow stream. c) 3D view of the microfluidic chip showing the organoid on scaffold in orange in the culture chamber. Section A:A shows the organoid inside the culture chamber. The scaffold holder is positioned by the chamfered edges of the culture chamber.

3D printing represents a low-cost fabrication technique that is easily accessible and does not require cleanroom access.[219] High resolution SLA 3D printing was therefore used to fabricate the master mold of the microfluidic chip (**Figure 5.13a**). The molds were then postprocessed and prepared for molding the microfluidic chips via PDMS casting (see materials and methods). PDMS molds were cast from the masters and bonded onto a microscopic glass slide after plasma treating both the glass and PDMS. To further ensure that the chip was fully bonded, the edges were sealed with PDMS using a syringe. Brightfield microscopy revealed a smooth surface and consistent channel width (**Figure 5.13b**).

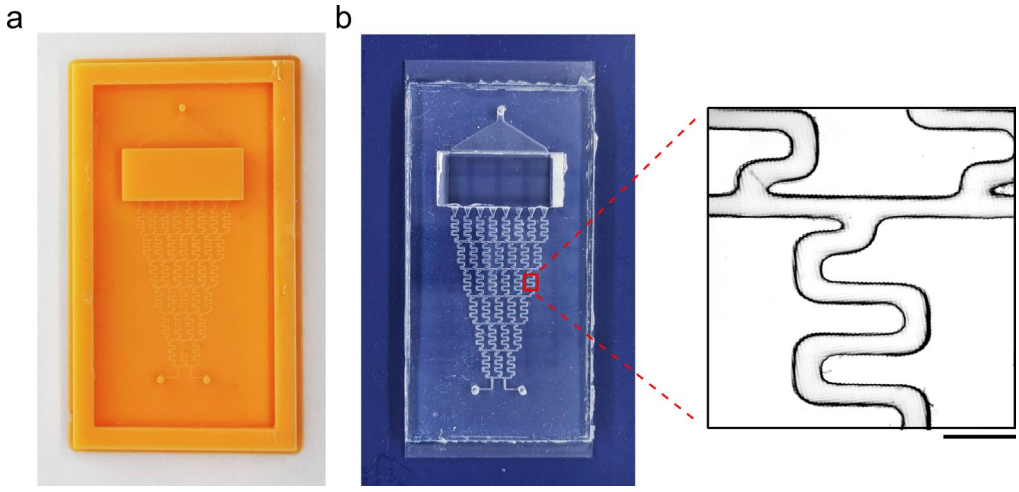


Figure 5.13 Microfluidic chip fabrication. *Master mold (left) is 3D printed in resin using an SLA printer and used as a negative mold to cast the PDMS chip (right). Magnified view shows a brightfield image of the channels, showing a smooth surface. Scale bar corresponds to 200 µm.*

To assemble the microfluidic device, the PCL scaffold holder with the attached organoid was first mounted within the growth chamber of the PDMS microfluidic chip, before being sealed by clamping between two glass plates in a water-tight manner (**Figure 5.14**). Inlet and outlet tubing with a barb connector were then connected to the inlet and outlet ports respectively. The outlet tubing was selected to be larger in diameter than the inlet tubing to

ensure conservation of mass transport was not impeded across the microfluidic device. Finally, the chips were manually purged with PBS, then media was introduced into the microfluidic device via a zero pulsatile motion low flow rate syringe pump (see materials and methods for details about the ramp down protocol).

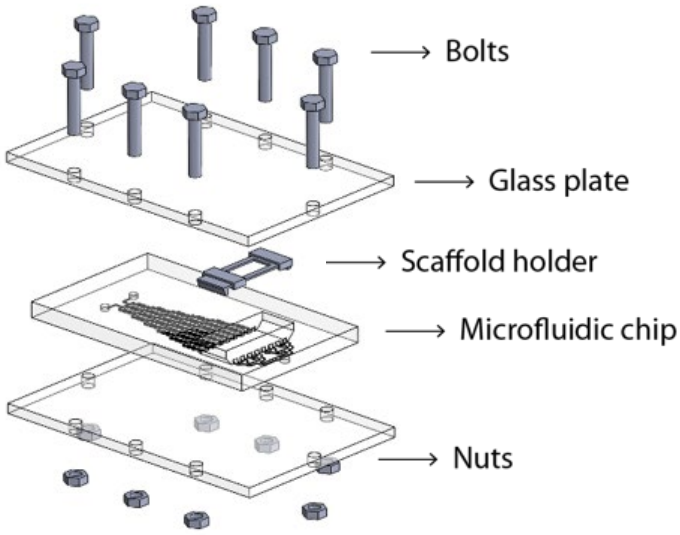


Figure 5.14 Exploded view of the fully assembled microfluidic gradient generator device. *The scaffold holder and organoid assembly is mounted inside the culture chamber. The chip is sealed by clamping between two glass plates. Diagram provided by Dr. Richard Wang.*

5.5.4. CFD modelling and Gradient optimisation

To assess the flow characteristic and gradient generation in the culture chamber of microfluidic chip, CFD simulations were performed using a passive scalar model of diffusive fluorescent additives. This was an appropriate model that assumed negligible physical effects from the additives, such as mass or buoyancy. After optimising mesh refinement through convergence of wall shear stress and fluid velocity residuals, a stable linear gradient was observed to form inside the culture chamber containing the scaffold holder and organoid (**Figure 5.15a**). CFD modelling confirmed a low Reynolds number (0.0023) confirming that the flow was dominated by a laminar flow regime, rather than turbulent flow. Furthermore, a Peclet number >1 (2.19) was calculated for the fluorescent additives, confirming their mode of transfer in the chip design was predominantly advection rather

than diffusion. Simulations of the velocity magnitude in the culture chamber showed higher velocity in the central portion, with diminishing flow towards the boundary edges of the culture chamber (**Figure 5.15b**). However, this variation did not impede stable gradient formation, as shown in (**Figure 5.15a)**. In future work, it will be interesting to assess whether higher velocity corresponds to any effects of shear stress on organoid growth.

To empirically verify the ability of the microfluidic chips to form a stable gradient prior to biological testing, microfluidic chips were fabricated and tested using a fluorescent marker. Fluorescein sodium salt was introduced into the microfluidic chip opposite a non-fluorescein DMEM inlet solution. The microfluidic chip was continuously perfused for at least 12 h and the stability of the formed fluorescence gradient was analysed via time-series image acquisition. Similar to CFD simulations, the results confirmed that a stable chemical gradient could be established across the culture chamber upon reaching equilibrium flow conditions **Figure 5.15c,d**), and that the gradient was temporally stable over the course of at least 12 h (**Figure 5.15e**).

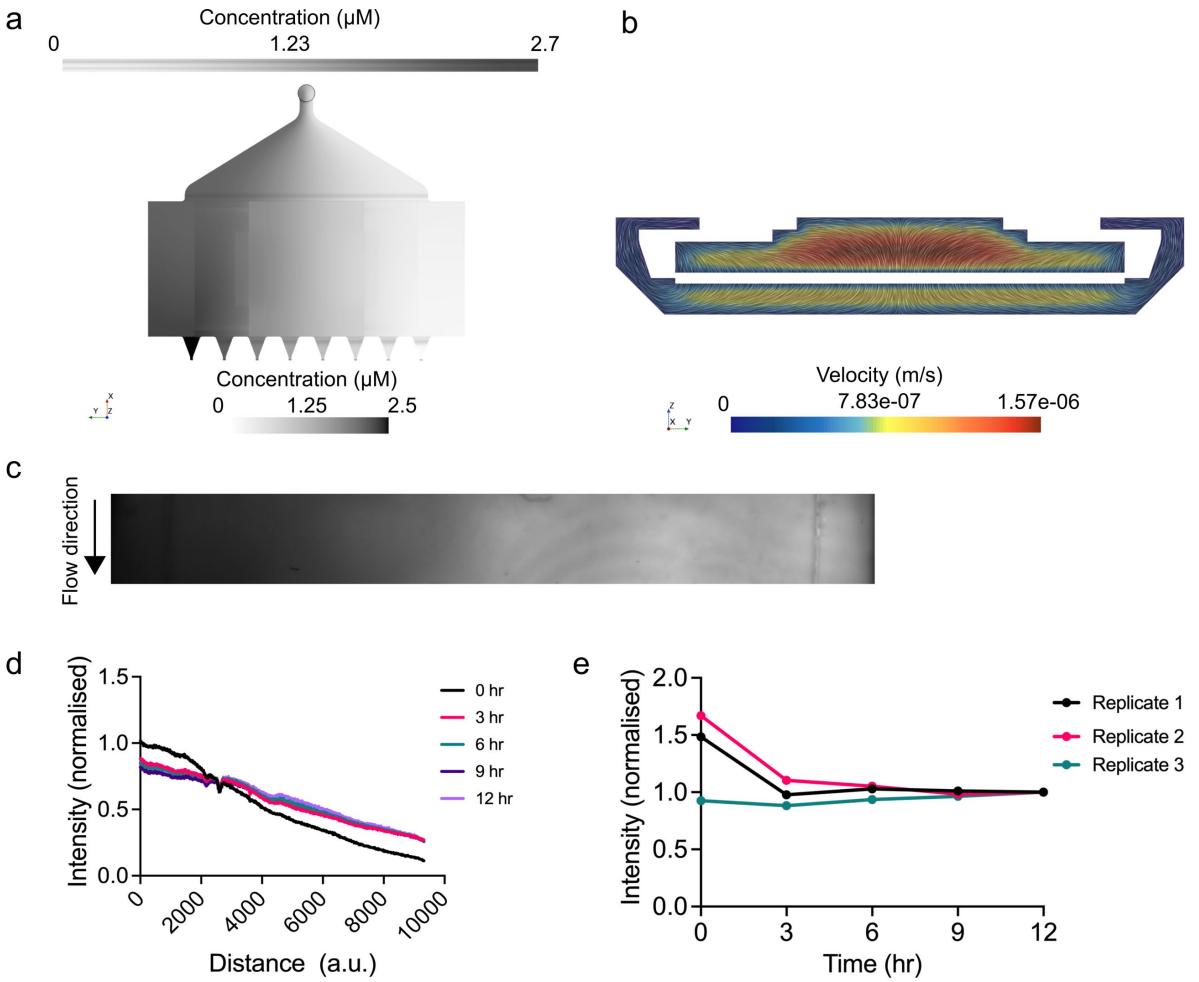


Figure 5.15 CFD modelling and gradient optimisation. *a) Passive scalar model of microfluidic generated gradient as visualised on the elongated organoid (top) and within the microfluidic chip chamber (bottom). b) 2D surface plot of the velocity magnitude in the culture chamber. c) Fluorescein gradient in the culture chamber, imaged by fluorescence microscopy. d) Fluorescein gradient measured across the length of the culture chamber at 0 h, 6 h and 12 h at a flow rate of 1.33 µL/min. Graph shows representative plot from 4 individual samples (n = 4). e) Graph showing stabilisation of formed gradients over time. The slope of the linear regression of each replicate was taken at each 3 h timepoint. These slope values were normalised against the final time point (12 h) and plotted against time. CFD modelling and analysis was carried out by Lorna Barron and gradient optimisation was carried out by Dr Richard Wang and Dr Ruoxiao Xie.*

5.5.5. Organoid growth and characterisation on custom scaffold holder

Next, the compatibility of the custom scaffold holder with elongated organoid culture was tested. Elongated 4 x 4 cm scaffolds were cut with a scalpel to create individual, single line

scaffolds**.** These were attached to the sterile scaffold holder, using the clips to lock the scaffold in place, resulting in a single, taut fibre across the cell exposed region of the holder (**Figure 5.16**). For cell culture, the scaffold holder and scaffold were sterilized using UV irradiation and incubated in a Matrigel solution. These were then placed in a 6 well low adherence plate and seeded with 1 x 10^6 hESCs in mTESR stem cell medium. At d 3, the scaffold holders were flipped so that the scaffold was on the top side of the holder, to facilitate 3D growth on the fibre and prevent the cells from growing on the bottom of the plate (**Figure 5.16**). Media exchange occurred according to the cerebral organoid culture protocol (see materials and methods). A pulse of Wnt activator (CHIR) was added at d 13 for 3 d to promote more consistent formation of dorsal forebrain identity, as previously described in Chapter 3 and 4.

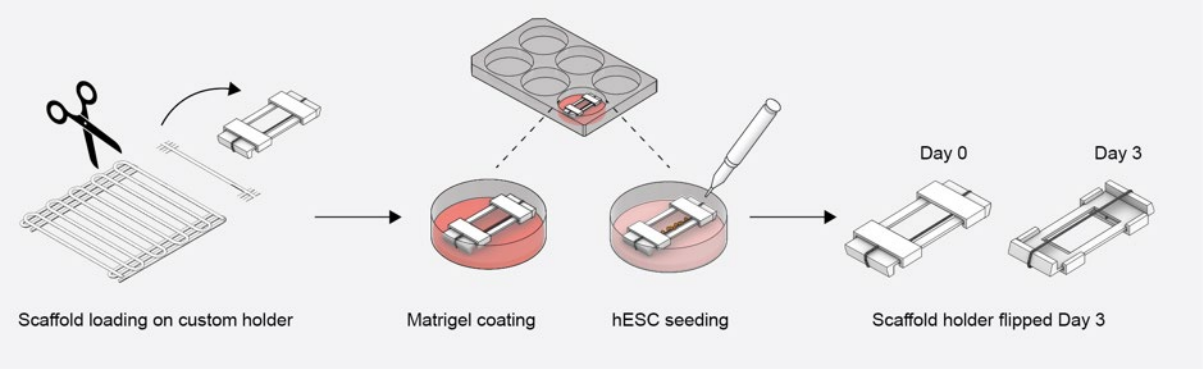


Figure 5.16 Schematic illustration of scaffold preparation and cell seeding on custom-built scaffold holders. *PCL scaffolds are fabricated by melt MEW. A single strand is cut from the scaffold and assembled on the scaffold holder. Prior to cell seeding, scaffolds are coated in Matrigel, then incubated for 1 h and washed in PBS. 1 x 10^6 hESCs are seeded on the scaffolds in a low adhesion 6 well plate. On d 3 the scaffold holder is flipped inside the well to facilitate 3D growth.*

Tiled brightfield images at d 5 demonstrated a similar tissue morphology and growth trajectory to the elongated organoids described in **section 5.3.** At d 21, the organoids displayed lumen budding, indicative of developing VZ-like regions (**Figure 5.17a**). To characterise the elongated organoid tissue, immunostaining was performed. Expression of the apical marker aPKCzeta showed large lumen regions surrounding the outer portion of the tissue. Broad expression of the FOXG1 marker showed a predominantly forebrain organoid identity (**Figure 5.17b**). Extensive regions of co-expression of FOXG1 and the dorsal

marker PAX6 indicated a dorsal forebrain identity. This is consistent with CHIR treatment, which promotes a dorsal identity, as previously described in Chapter 3 and 4. Overall, these results demonstrate that elongated organoids can be successfully cultured using the adapted scaffold holder.

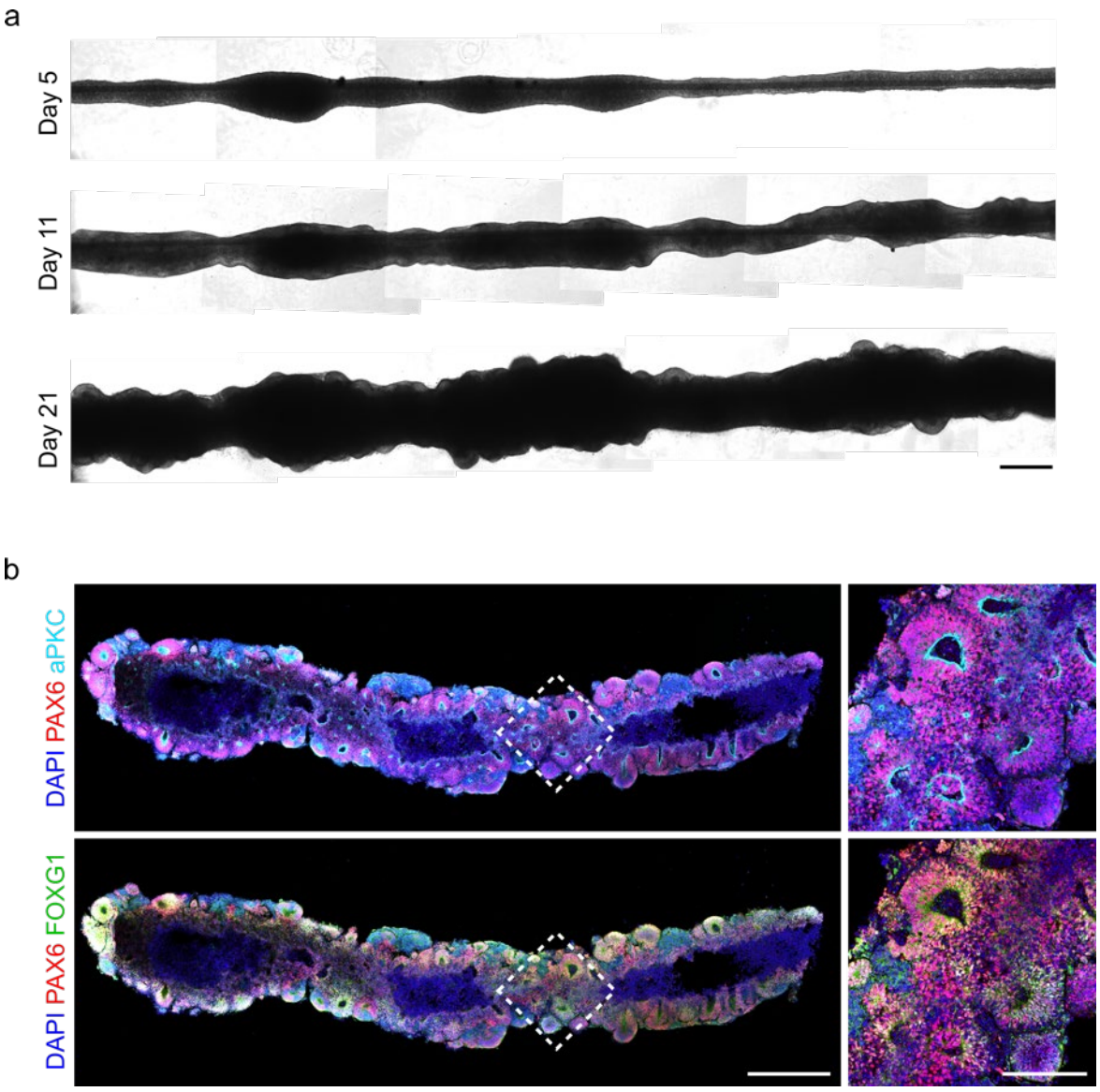


Figure 5.17 Characterisation of elongated scaffold organoids cultured using custom-built scaffold holders. *a) Tiled brightfield images of elongated scaffold organoid at d 5, 11 and 21. Scale bar corresponds to 1 mm. b) Histological sections of elongated organoids immunostained with: dorsal marker PAX6 (red), apical marker aPKCzeta (cyan) and nuclear counterstain DAPI (blue). Bottom panel: PAX6, forebrain marker FOXG1 and DAPI. 2 organoids were analysed from a single biological repeat (N = 1, n = 2). Right side shows magnified view. Scale bar corresponds to 500 µm (left), 200 µm (right).*

5.5.6. Ventral patterning optimisation

Next, a suitable ventral patterning protocol was established. In **section 5.4** the sonic hedgehog (Shh) recombinant protein was used, which formed a complex with heparin on the surface of the scaffolds. The small molecule Smoothened agonist (SAG) has alternatively been used as a Shh agonist, owing to its longer shelf life and minimal batch-to-batch variability compared to Shh.[220] SAG is also considerably less expensive than Shh, reducing the experimental costs. Inhibition of Wnt signalling has previously been shown to induce a forebrain identity during neural plate formation. Similar to previously published protocols for ventralisation of organoids, a Wnt inhibitor (iWP2) in combination with SAG was used.[221,222] A range of timelines has previously been described in the literature, including the addition of SAG (100 nM) and iWP2 (2.5 µM) from d 5-11,[94] d 15-21,[223] and d 12-24,[93] with iWP2 being applied from d 4 in the latter study. In the proposed patterning platform, organoids would be transferred to the microfluidic chip for the duration of the ventralisation timeframe, before being transferred back to a 6 well plate for continued culture. A range of timelines was therefore tested to establish the minimum timeframe required for ventralisation.

Using conventional round organoids, exposure times of SAG (100 nM) and iWP2 (2.5 µM) were tested from d 5 - 20 and d 5 - 11, alongside no exposure, and CHIR exposure at d 13 - 15 as the negative controls (**Figure 5.18**). Immunostaining for the ventral marker NKX2.1 was used to characterise ventral specification of the organoids. These results demonstrated a similar pattern of positive NKX2.1 expression in the d 5 - 20 and d 5 - 11 conditions. The organoids also appeared smaller than the negative control conditions. Organoids without patterning factors also showed some NKX2.1 expression. This is in accordance with 'unguided' cerebral organoids that typically contain different subregional brain tissues. As previously described in this chapter, organoids exposed to the Wnt activator, CHIR, adopted a dorsal identity. Accordingly, no NKX2.1 expression was observed in these organoids. Based on these results the shorter patterning timeframe of d 5 - 11 was selected for organoid polarisation experiments in the microfluidic chip.

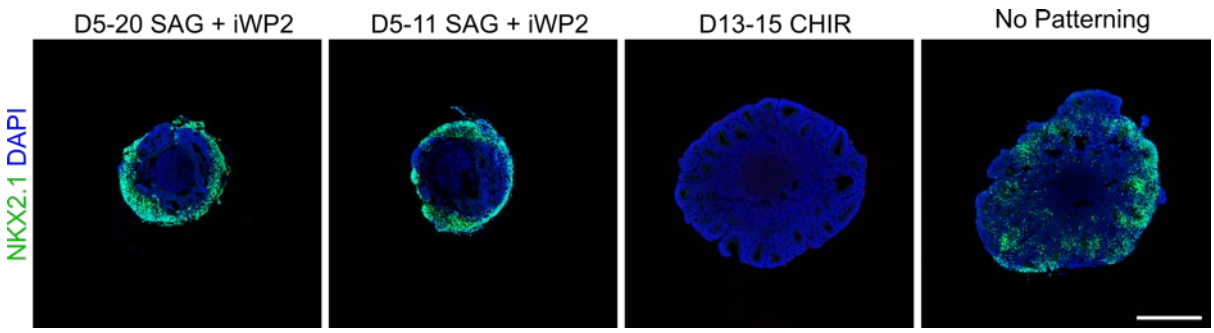


Figure 5.18 Conventionally cultured round organoids show ventral tissue identity with morphogen treatment. *Organoids treated with 100 nM SAG and 2.5 µM iWP2 at d 5-20 and d 5-11 show expression of ventral marker NKX2.1 (green). Organoids treated with CHIR from d 13-15 show no expression of NKX2.1. Untreated organoids show some expression of NKX2.1. DAPI (blue) was used as a nuclear counterstain. At least 6 organoids were analysed in each condition, from 2 biological experiments (N = 2, n = 6)). Scale bar corresponds to 500 µm.*

5.5.7. Organoids perfused on microfluidic chip without a morphogen gradient

Before proceeding with organoid polarisation experiments, the compatibility of elongated organoid culture inside the microfluidic chip was first evaluated (**Figure 5.19**). Under sterile conditions, two syringes were filled with 15 mL of neural induction media, connected to the two inlets on the chip. The scaffold holder was gently inserted into the culture chamber region of the microfluidic chip, with the scaffold and organoid facing downwards, positioned at the level of the incoming flow from the mixer channels. This was then assembled between the glass plates, and the chip was manually primed by perfusing with PBS followed by neural induction media to flood the growth chamber and ensure no bubbles remained in the growth chamber. This assembly was moved into an incubator and connected to a syringe pump and outlet tube. The syringe pump was used to purge the chip of bubbles using a flow rate ramp down protocol (see materials and methods for more details). Once the flow rate was steady, the organoid was cultured under dynamic flow conditions. This was tested for 2 d and 5 d in 2 separate experiments. For organoids perfused for 5 d, media was exchanged at d 2, by replacing the syringes with fresh neural induction medium. After 2 or 5 d, the organoids were transferred from the chip to a 6 well plate, proceeding with cerebral organoid culture protocol until d 20, when the organoids were fixed.

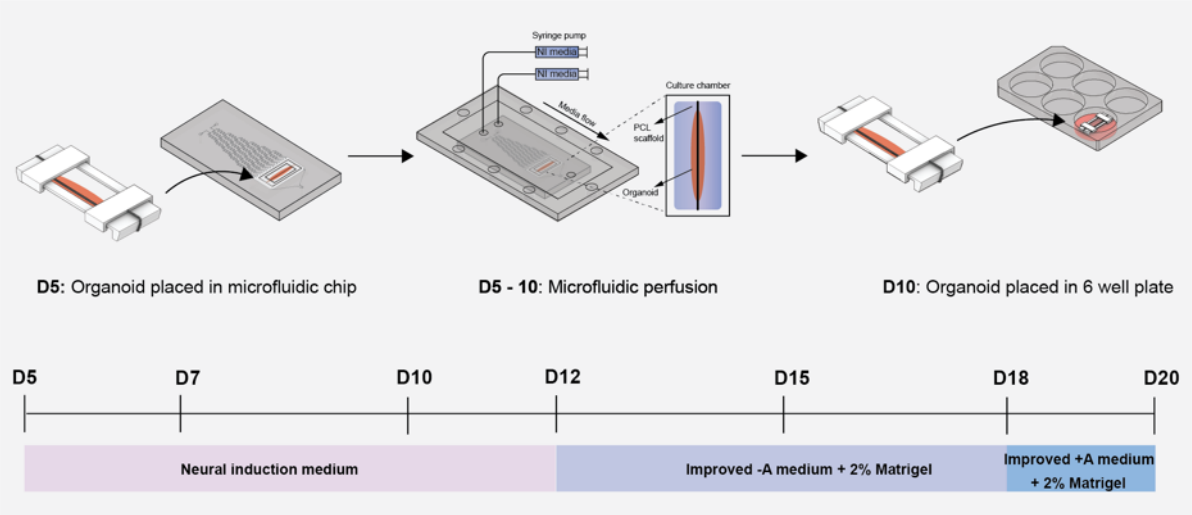


Figure 5.19 Schematic illustration and timeline of elongated organoid perfusion in microfluidic chip without a morphogen gradient. *The scaffold and organoid holder are placed inside the sterile culture chamber at d 5. The microfluidic chip is secured inside the glass plates which are clamped together, and the organoid is perfused with neural induction media for 5 d. At d 10, the glass plates are unscrewed, and the scaffold and organoid holder is placed inside a 6 well plate containing neural induction media. At d 12, media is exchanged to improved -A media, supplemented with 2% (v/v) Matrigel. At d 18 the media is exchanged to improved +A media, supplemented with 2% (v/v) Matrigel.*

Immunostaining was performed to characterise the organoid tissue. Organoids perfused for 2 d showed large lumen structures with expanded neuroepithelia demarcated by expression of the apical marker aPKCzeta (**Figure 5.20a**). High expression levels of the ventral marker FOXG1 and dorsal marker PAX6 were observed in the organoid tissue. However, in contrast to the previously reported non-perfused elongated organoid samples (**section 5.3.3**), these markers did not appear to co-express, and showed more discrete expression patterns. Positional domains of PAX6 positive and FOXG1 negative tissue were observed in the organoid tissue, raising the possibility that media perfusion may promote some form of self-patterning. As stem cells and neuronal stem cells endogenously produce signalling molecules, including basal levels of Wnt and Shh, the concentration of these factors can build up in the media, changing the micropatterning of the organoid. It is plausible that by perfusing the media, this phenomenon may be reduced, causing less heterogeneity, and encouraging the development of more discrete brain regions within the organoid. Whilst

the tissue in organoids perfused for 5 d was damaged during cryosectioning, similar expression levels were also observed in the intact tissue (**Figure 5.20b**). Further biological repeats and immunostaining will be required to confirm this hypothesis. The VZ-like lumen regions also appeared throughout the organoid tissue perfused for 2 d. A previous study showed that brain organoids grown under perfused culture exhibit enhanced expression of key cortical markers, compared to those grown under static cultures.[224] Organoid necrosis typically occurs due to oxygen and nutrient depletion, and it is likely that the perfusion of fresh media may avert this. To further investigate this in future work, it will be essential to quantifiably assess changes in organoid growth and health, such as cell proliferation and cell death.

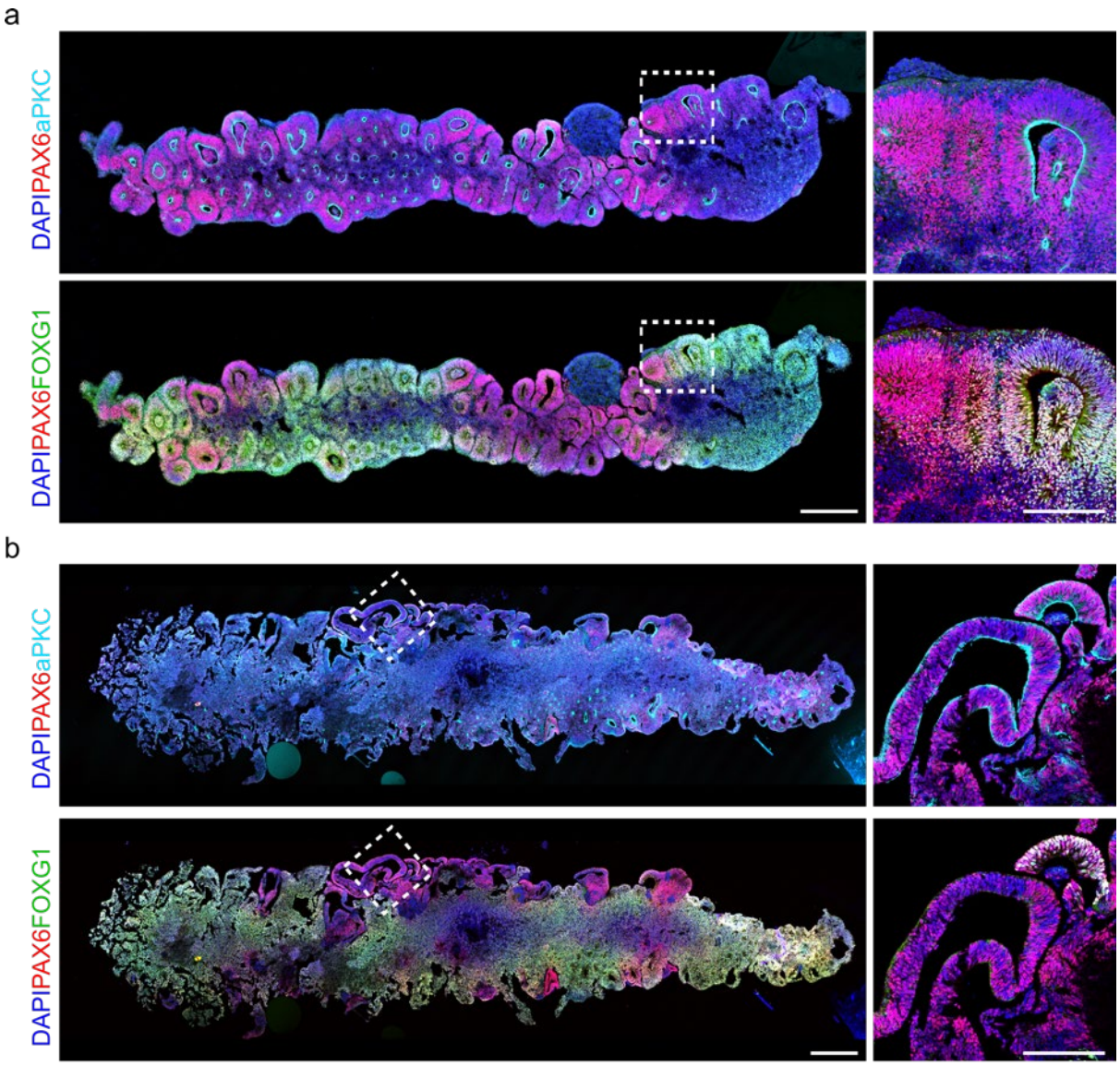


Figure 5.20 Characterisation of elongated scaffold organoids perfused in the microfluidic chip without a morphogen gradient. *a) Histological sections of elongated organoids cultured under perfusion for 2 d in the microfluidic chip. Organoids are immunostained on the top panel with: dorsal marker PAX6 (red), apical marker aPKCzeta (cyan) and nuclear counterstain DAPI (blue). Bottom panel: PAX6, forebrain marker FOXG1 and DAPI. Right side shows magnified view. b) Histological sections of elongated organoids cultured under perfusion for 5 d in the microfluidic chip. Immunostaining as indicated for (a). Magnified view shown on the right. 1 organoid was analysed in each condition from a single biological repeat (N = 1). Scale bar corresponds to 500 µm (left) and 200 µm (right).*

5.5.8. Organoids perfused on microfluidic chip with a morphogen gradient

Finally, the organoids were exposed to a controlled gradient of ventral patterning factors in the microfluidic chip. The previous results in this chapter demonstrated organoid ventralisation using 100 nM SAG and 2.5 µM iWP2 for 5 d. Although the CFD modelling confirmed a concentration gradient was generated across the entire width of the microfluidic chamber, the organoid itself did not span the entire width of the chamber. As such, the extremities of the organoid were not exposed to the theoretical maximum concentrations. It was therefore reasoned that increasing the SAG concentration would ensure that a morphogen gradient was generated with a sufficiently high enough concentration to generate a biological effect. A gradient was therefore generated by adding SAG (200 nM) and iWP2 (2.5 µM) to the neural induction media in one syringe and leaving the second syringe with neural induction media only (**Figure 5.21**). The procedure for microfluidic perfusion of organoids was carried out as described in **section** Error! Reference source not found. with media exchange occurring at d 7, and organoid removal from the microfluidic chip at d 10. From this point, organoids were cultured in 6 well plates, and fixed at d 20 for characterisation by immunostaining.

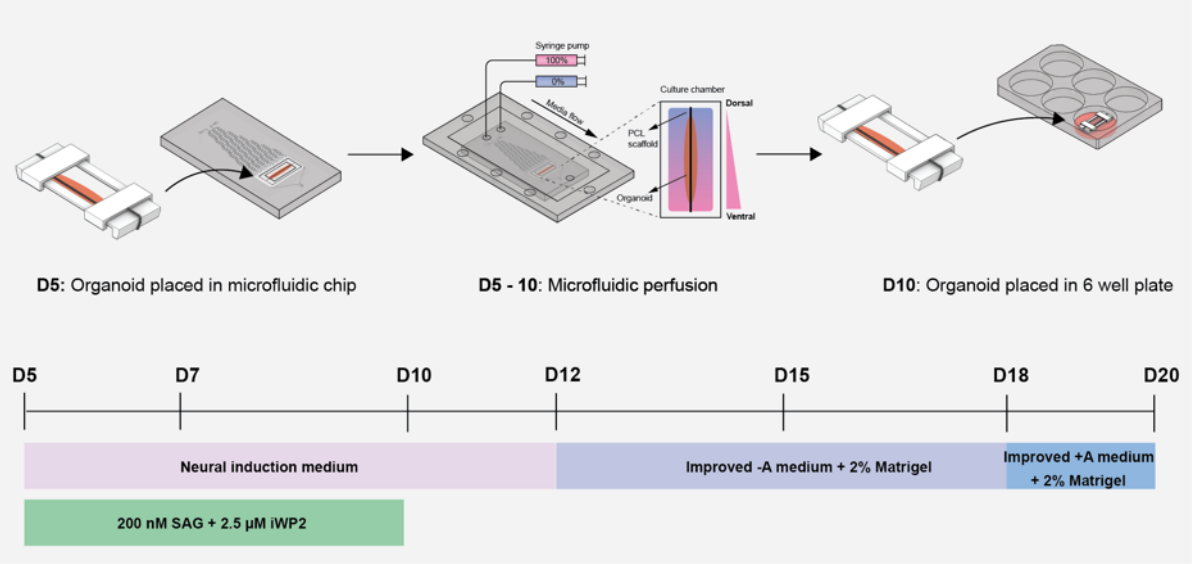


Figure 5.21 Schematic illustration and timeline of elongated organoid perfusion in microfluidic chip with a morphogen gradient. *The scaffold and organoid holder are placed inside the sterile culture chamber at d 5. The microfluidic chip is secured between the glass plates which are clamped together, and the organoid is perfused with neural induction*

media in one syringe (0%) and neural induction supplemented with 200 nM SAG and 2.5 µM iWP2 (100%) in the other syringe, for 5 d. At d 10, the glass plates are unscrewed, and the scaffold and organoid holder is placed inside a 6 well plate containing neural induction media. At d 12, media is exchanged to improved -A media, supplemented with 2% (v/v) Matrigel. At d 18 the media is exchanged to improved +A media, supplemented with 2% (v/v) Matrigel.

Under these conditions, the organoids formed a distinct ventral domain on one side of the elongated organoid, marked by the expression of FOXA2 and NKX2.1, indicating that the SAG gradient is translated into a Shh signalling gradient (**Figure 5.22a**). A NKX2.1 and FOXA2 positive domain was also observed on the tip of the organoid, at the negative SAG side (as shown in magnified view, organoid region D). This may be due to stagnating flow towards the edges of the culture chamber, where the flow velocity is approaching zero. This was further confirmed by the CFD modelling in the previous section (**Figure 5.15**). It is likely that the growth factors initially accumulated at the negative growth factor side during the purging or ramp down process, which may be more turbulent than the final equilibrium flow condition. In current optimisation experiments, new techniques are being explored to prevent cell and organoid attachment at the fibre ends to prevent this artefact, including the application of an anti-adhesion substrate to the fibre ends. An orthogonal ventral gradient was also observed on one edge, in the direction of the fluid flow. Neural rosettes positive for the floor plate marker FOXA2 were present on one edge of the organoid. (**Figure 5.22a**, as shown in magnified view organoid region B). Whilst it was not possible to retrospectively confirm the precise rotational organoid orientation in the microfluidic chip, it was assumed that FOXA2 positive edge was directly facing the inlets and fluid flow. FOXA2 is a target gene of Shh and typically forms a signalling centre that regulates endogenous Shh signalling.[207] NKX2.1 marker was similarly positioned on the exposed organoid edge. No co-expression of these markers was observed, indicating a ventral medial ganglionic eminence (MGE) identity in the NKX2.1 positive tissue. In ongoing work, a double positive SAG/iWP2 control experiment is being cultured under perfusion to confirm that the flow stably forms an orthogonal Shh gradient in the organoid. As a positive control, elongated organoids were supplemented with 200 nM SAG and 2.5 µM iWP2 for 5 d, and cultured in a 6 well plate**.** Characterisation by immunostaining demonstrated widespread expression of NKX2.1

throughout the organoid tissue and FOXA2 expression on the outside edges of the organoid (**Figure 5.22b**). Furthermore, no gradient of expression in any axes of the organoid was observed. A smaller region with no expression of these markers was also observed within the middle section of the organoid. This may be attributed to uneven OCT embedding; however it is currently unclear why this occurred, and further biological repeats are required to establish if this is a random artefact. Negative control organoids were also cultured in 6 well plates with neural induction media, in the absence of any morphogens. Similar to previous results in this chapter (**section 5.5.6**), low expression levels of NKX2.1 and FOXA2 markers were observed (**Figure 5.22c)**.

In future work, immunostaining of the forebrain maker FOXG1 will be important to confirm the presence of forebrain tissue. Further immunostaining will reveal more about the observed gradient and biological phenotype. It is expected that an LGE domain will be adjacent to the MGE, and positive GSX2 staining will confirm this. Furthermore, immunostaining of dorsal cortical markers such as PAX6 will show dorsal regionalization of the tissue, which will be important to confirm a dorsoventral organoid polarity.

These preliminary results indicate that using a microfluidic platform, it is possible to generate gradients on multiple axes. In ongoing work, experiments are being carried out to apply a gradient of Shh antagonist, Cyclopamine A, in the opposing direction to SAG and iWP2 to enhance the dorsoventral phenotype.

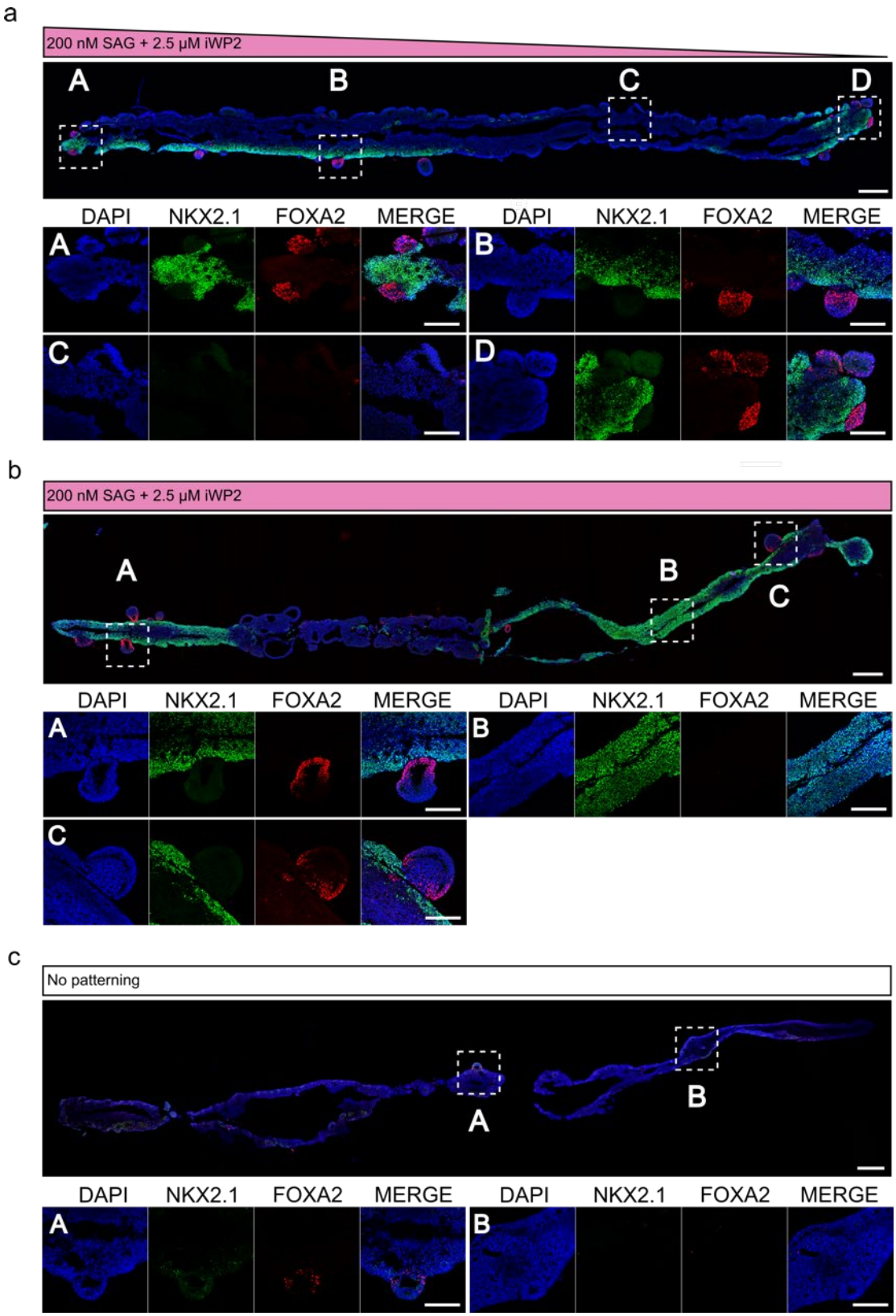


Figure 5.22 Characterisation of elongated scaffold organoids perfused in the microfluidic chip with a morphogen gradient. *a) Histological section of elongated organoids perfused with neural induction media in one syringe (0%) and neural induction supplemented with 200 nM SAG and 2.5 µM iWP2 (100%) in the other syringe, for 5 d. Organoids are*

immunostained with ventral marker NKX2.1 (red), floor plate marker FOXA2 (green) and (red) and nuclear counterstain DAPI (blue). White dashed boxes indicate the regions shown in the magnified image gallery below. b) Histological section of positive control elongated organoids cultured in a 6 well plate, with neural induction media supplemented with 200 nM SAG and 2.5 µM iWP2 for 5 d. Magnified view shown in image gallery below. Immunostaining as indicated in (a). c) Histological section of negative control elongated organoid cultured in a 6 well plate, with neural induction media for 5 d. Magnified view shown in image gallery below. Immunostaining as indicated in (a). Experiments were carried out with 2 biological repeats (N = 2). Scale bar: 500 µm (top), 200 µm (magnified view, bottom).

5.6. Conclusion

Here, preliminary findings for a microfluidic gradient generator are reported for the 3D culture and regional specification of elongated organoids. Previous research has demonstrated neural tube-like anteroposterior (AP) or dorsoventral (DV) polarisation of 2D hiPSCs using a microfluidic based gradient generator.[126,127] However, 2D cell monolayers lack the tissue complexity and maturation potential of organoid systems. Building on previous work with scaffold guided organoid generation, a scaffold-based approach to integrate elongated organoids with a microfluidic gradient generator has been developed. The elongated organoid morphology is ideal for axes formation in organoids, and the scaffold enables easy manipulation and positioning of the organoid.

Using a 3D printing approach, it was possible to rapidly prototype and optimise the microfluidic chip. Advantageously, this avoided time-consuming traditional soft lithography approaches that also require clean-room access. The custom designed microfludic chip allowed us to add and remove the organoid from the chip at required timepoints, whilst an additionally custom-built scaffold holder was designed to easily move the organoid in and out of the chip, and carefully position it in the fluid stream.

Organoid fusion has previously been used to engineer interregional brain organoid interactions; whereby pre-patterned organoids are fused together in a drop of Matrigel. However, this modular approach does not accurately mimic neural morphogenesis *in vivo*, where complex morphogen gradients establish the neural tube axis from a single structure. Using the microfluidic approach discussed in this chapter, a single elongated organoid can be exposed to a specified morphogen gradient for a pre-determined time. In agreement with the CFD modelling data, preliminary biological results show that by applying the Shh agonist SAG and Wnt inhibitor iWP2 in the gradient generator, a signalling gradient is established, forming dorso-ventral organoid polarisation. However, further optimisation will be required to avoid organoid growth in the zero-velocity region of the chamber, to prevent growth factor accumulation at the extreme ends of the culture chamber. Preliminary results also indicate that a gradient can be formed orthogonal to the organoid, in the direction of

the fluid flow. This highlights the possibility to further develop the complexity of this system in the future, by generating gradients at different axes and at different timepoints.

In future work, it will be essential to confirm these preliminary results by completing more biological repeats. It will also be necessary to expand the repertoire of markers used in the immunostaining characterisation to gain a more complete understanding of the biological effect caused by the morphogen gradient. Finally, it will be interesting to test this platform with other organoid systems.

Chapter 6.

Conclusions and Future work

6. Conclusions and future work

6.1. Motivation

In recent years, brain organoids have emerged as an effective 3D *in vitro* model system, capable of recapitulating features of the developing embryonic human brain. This nascent technology holds enormous promise to investigate human brain development and disease, and is increasingly being used to model neurological disorders, such as microcephaly,[45] and glioblastoma.[46] However, major challenges remain, including lack of brain organoid reproducibility, lack of regional organisation and shape heterogeneity. Brain organoids are also highly labour- and time-intensive to culture in the lab. The principal goal of this thesis was to address these limitations, by developing a biomaterial scaffold to guide 3D stem cell and brain organoid growth and organisation. This was achieved through the design and fabrication of a fibrous PCL scaffold, using MEW, and developing a culture platform for stem cell growth. Scaffold geometry was shown to be a key determinant of collective tissue growth and organisation during stem cell culture. The scaffold platform was further used to generate a new protocol for controlled and high-throughput cerebral organoid growth. This research provided a platform to direct organoid morphogenesis, both to improve the scalability and reduce labour- and time-intensive costs during culture, but also to exploit the scaffold to direct cell differentiation and organoid patterning. It is hoped that this will open new opportunities for modelling neurological disease and development in the future.

6.2. Conclusions

6.2.1. Scaffold guided self-organisation of stem cells

In the first part of this thesis, in Chapter 3, a macroscale PCL scaffold was designed to facilitate 3D stem cell culture. The scaffolds were fabricated using MEW, resulting in stacked microscale fibres with a predetermined geometry. A variety of scaffold geometries were fabricated, demonstrating the versatility of the process, and mechanical testing showed that the tensile properties were tuneable according to geometry. The main aim of Chapter 3 was to develop a scaffold-based platform to culture and guide stem cells. A simple protocol was developed by sterilising the scaffolds and attaching to a CellCrown device. This approach was used for the rest of the work presented in this thesis and the CellCrown devices provided a support structure to fix the scaffolds in place, and easily move the assembly to a new culture well or dish without disrupting the layout of the scaffold. Immediately before cell culture, scaffolds were coated in Matrigel. This was a key feature of the protocol and facilitated uniform cell attachment across the entire scaffold. hESCs were seeded directly on the CellCrown and scaffold assembly, and brightfield imaging demonstrated a high level of reproducibility in tissue growth across the scaffold. A key characteristic of stem cells is their ability to self-organise and form lumen structures. Immunostaining characterisation showed that primary, large lumens typically formed in the scaffold corners, with smaller lumens developing on the scaffold walls. Further investigation showed that tissue preferentially grew in the scaffold corners, leading to the hypothesis that lumenogenesis occurs in a curvature dependent manner on the scaffold. To further investigate this hypothesis of curvature-driven tissue growth, lumen formation was compared across scaffolds with different geometries, including square-, rhombus-, and triangle-shaped scaffolds. As expected, a clear correlation was found between lumen size and the underlying scaffold geometry, as scaffold angles with higher curvature corresponded to increased cell density and larger lumen size. This confirmed the hypothesis that scaffold geometry and the underlying curvature guides lumen formation. Furthermore, this curvature-controlled growth evolution was accurately modelled using a 2D curvature driven growth law, based on the mathematical concept of curve shortening flow theory. Organoids are typically derived from stem cells, and the scaffold-cultured stem cell system in Chapter 3 provided an

ideal platform to differentiate the cells and generate scaffold-cultured cerebral organoids. This resulted in an interconnected array of cerebral organoids. 3D characterisation of the developing organoids demonstrated that the scaffold guided lumen formation directed organoid formation, resulting in the development of VZ-like regions in the high curvature scaffold corner regions. Furthermore, the organoids showed expression of antibody markers typically present in cerebral organoids at d 20.

Taken together, the scaffold platform developed in Chapter 3 demonstrated a high level of versatility to guide 3D stem cell growth and cerebral organoid culture. In future work, electrophysiological characterisation techniques could be used to evaluate functional connectivity of the interconnected scaffold-cultured cerebral organoids. For example, the co-ordinated grid structure of the scaffold could facilitate controlled placement on multi electrode arrays (MEAs) to allow spatial mapping of the functionally active neurons on a larger network scale. As previously discussed in Chapter 1, 3D MEAs have recently been developed for 3D tissue culture, by incorporating electrodes inside the tissue or organoid.[145] In previously reported work in the Stevens group, MEW electroactive PCL scaffolds were developed for neural tissue engineering.[225] In future work, this could be combined with scaffold-cultured cerebral organoids to electrically stimulate or probe the functional activity of organoids in 3D.

6.2.2. Scaffold guided cerebral organoid generation

In Chapter 4, the scaffold platform was tailored to develop a system for the high-throughput growth of spatially separated, independently growing cerebral organoids. To enable this, the scaffold Matrigel coating step described in Chapter 3 was removed from the protocol. Using this adapted protocol, cells were found to preferentially aggregate at the scaffold intersections, forming spherical embryoid bodies that were differentiated to cerebral organoids. Whilst the number of organoids generated per scaffold was high (an average of 402 organoids) the overall percentage of scaffold occupancy could be further optimised in future work. Characterisation of scaffold-cultured organoids showed that the organoids were smaller than conventionally cultured round organoids, but looked morphologically similar, showing characteristic neuroepithelial budding after neural differentiation. To

support longer-term culture, scaffold geometry was tuned to accommodate larger organoid sizes and prevent fusion. At d 20 and 60, scaffold-cultured organoids showed expression of key developmental markers, similar to conventionally cultured organoids, demonstrating that the scaffold platform can be adapted to short- or long- term organoid culture. Taken together, these results show that high-throughput cerebral organoids can be cultured using the PCL scaffold platform. As previously discussed, conventional organoid culture is labour- and time- intensive, and typically involves manually pipetting and treating each individual organoid. This platform provides a strategy to culture hundreds of organoids per scaffold, where the entire scaffold array can be removed from the well plate to simultaneously embed the organoids with Matrigel, or move to a new culture dish. In future work, it will be important to investigate whether the smaller size of the scaffold-cultured organoids is advantageous for longer-term organoid maturation by enabling more efficient diffusion-dependent nutrient and oxygen supply to the organoid tissue, compared to conventionally cultured larger organoids.

In the final section of this Chapter, scaffold-cultured organoids were used to develop a basic workflow for high content Raman imaging, which could be translated to live organoids in future work. The scaffold structure could also provide a way to fix the organoids in place during imaging, as an alternative to agarose embedding, which does not support long-term culture or survival of the organoid. Furthermore, the coordinated grid structure of the scaffold could be particularly advantageous during live imaging experiments over a time course, by creating a positional co-ordinate of a specific organoid that could be identified and tracked at different timepoints. This positional information could also be utilised in parallel with other advanced characterisation techniques post-fixation, such as FIB-SEM to combine biochemical imaging with nanoscale spatial resolution.

6.2.3. Scaffold guided brain organoid patterning

In the final Chapter, the scaffold platform was harnessed to guide cell differentiation and regional organoid growth, with the aim to generate a polarised dorso-ventral axis.

In the first part of this work, the scaffold geometry was designed to guide organoid elongation, to more closely mimic the morphology of the *in vivo* neural tube and facilitate the formation of a polarised axis. By designing a scaffold comprising single linear fibres and utilising the Matrigel coating platform developed in Chapter 3, cells adhered to the scaffold surface, forming scaffold-cultured elongated organoids. In the second part of this study, growth factor immobilization on the scaffold surface was explored. Using a LbL strategy, multilayers of chitosan and heparin were generated on the PCL scaffold surface. The goal here was to immobilize the heparin binding growth factor Sonic hedgehog (Shh) on the scaffold for slow release to the scaffcortfold adhered cells, to induce a ventral organoid fate. An ELISA was performed to determine Shh release from the scaffold and results showed a low cumulative concentration of Shh release over a 7-d timespan. This suggests that either a low concentration of Shh was bound to the scaffold during the functionalisation step, or that Shh remained bound to the scaffold surface, without being released. In future experiments, heparinase treatment to induce Shh release of the functionalised scaffolds could potentially be used to determine the total Shh-heparin binding efficiency. Furthermore, scaffold-cultured organoids on Shh functionalised scaffolds revealed sparse organoid attachment to the scaffold, which was attributed to the negative charge of heparin, causing an anti-adhesion effect. This represented a key optimisation stage, and ending the multilayers with chitosan, which is positively charged, could be considered for future work. Alternative coatings to Matrigel could also be considered at this step. Despite low adherence to the scaffolds, organoids were characterised to assess whether Shh functionalised scaffolds induced a biological effect in the developing organoid. Intriguingly, the organoids showed enhanced expression of the floor plate marker FOXA2, which is a downstream target of the Shh signalling molecule. However, the organoids were negative for the ventral marker NKX2.1, which is typically expressed in Shh treated organoids.

Whilst LbL growth factor functionalisation of scaffolds has significant potential to direct regional organoid growth, further optimisation will be required to enhance Shh immobilization and release for controlled subregional organoid patterning. Other challenges, including sterility issues with LbL coating, and low organoid attachment to the LbL scaffolds suggested that alternative options to guide organoid regional growth should

also be considered. Therefore, in the final part of this Chapter, microfluidics was explored as a strategy to direct organoid patterning, with the goal to establish a dorso-ventral gradient. Utilising the scaffold-cultured elongated organoids, a microfluidic chip gradient generator was designed and optimised. An open well design was used, to easily incorporate and remove the organoid and scaffold assembly at specific timepoints. A custom-built scaffold holder was also fabricated to secure the elongated organoid at a specified position in the microfluidic culture chamber. To verify gradient formation, a fluorescein salt was used as a surrogate for the small molecules smoothened agonist (SAG) and iWP2, and showed stable gradient formation across the culture chamber. This was further supported by CFD simulations. To test organoid viability in the microfluidic chip, elongated organoids were first perfused without a small molecule gradient. Intriguingly, the perfused samples appeared to show a different expression pattern of key cortical markers, compared to non-perfused organoids, indicating that perfusion alters endogenous organoid patterning. A previous study reported that organoid perfusion led to enhanced expression of cortical markers in brain organoids.[224] Whilst further biological repeats will be required to confirm these phenomena, this represents a key area for further exploration in future work. Organoids perfused in the SAG and iWP2 gradient showed a distinct ventral domain on one side of the elongated organoid. An orthogonal gradient in the direction of the fluid flow was also observed. This highlights an important finding, and opens the possibility of incorporating other patterning factors to generate multiple axes in future work, for example, an antero-posterior axis.

To verify the validity of the preliminary results reported here, it will be important to complete more biological replicates. Additionally, there are several points of optimisation, such as avoiding the stagnating flow at the ends of the culture chamber. Furthermore, a rigorous investigation into the patterning effect of the gradient will be required, including more extensive immunostaining of ventral and dorsal markers. Single cell RNA-sequencing could also provide a powerful technique to investigate the cell types in the polarised tissue.

6.3. Perspectives

This thesis has explored geometry guided self-organisation of stem cells and cerebral organoids. Dissociated hPSCs show intrinsic properties of self-organisation, but these structures are usually heterogenous and non-reproducible, which limits their use. Recent studies have used micropatterning approaches to modulate stem cell growth.[52,75,76] However, these micropatterns are typically created in 2D, which can create unfavourable interactions with the bottom of the cell culture plate. In contrast to these studies, the scaffold-based system presented in this thesis provides mechanical guidance to guide stem cell growth in a controlled and reproducible way, whilst simultaneously facilitating 3D growth. In Chapter 3 and 4, interconnected and spatially separated cerebral organoids were cultured on the scaffolds, demonstrating the utility of this system as an organoid platform. Organoid irreproducibility, shape heterogeneity and labour-intensive culture methods are some of the current challenges associated with brain organoid generation.[109] This platform provides a 'one-pot' system to simultaneously generate hundreds of organoids in a highly controlled and reproducible way. Another advantage of this system is the tuneable scaffold geometry, which can be tailored according to the application or organoid type. For example, VZ-like cavities in cerebral organoids specifically grew in the scaffold corners, as shown in Chapter 3. This was further explored in the final Chapter 5, where the scaffold geometry was adapted to generate elongated organoids, which are more reminiscent of *in vivo* neural tube morphology.

Regional patterning of brain organoid models represents another major challenge in the field. Current approaches have used additive assembly of individual brain region specific organoids,[106] as well as genetic engineering approaches.[107] However, these do not recapitulate *in vivo* human brain development. Scaffold functionalisation has been extensively explored for tissue engineering applications, by immobilising growth factors to biomaterials for controlled spatiotemporal release to encourage tissue generation or repair.[198] This approach shows promise for brain organoid patterning, as a strategy to release relevant growth factors to specific regions of the developing organoid. As demonstrated in Chapter 5, the PCL scaffold material was exploited for growth factor functionalisation. Whilst several challenges emerged in this study, including sterility issues

and anti-adhesion effects on the scaffold surface, this represents a promising approach to guide regional organoid patterning in the future. Microfluidics was explored as an alternative strategy to direct brain organoid regionalisation. Microfluidic gradient generators have recently been used to direct regional patterning in 2D culture.[126,127] However, this has not yet been reported for the application of 3D brain organoid models. In Chapter 5, the elongated scaffold platform was incorporated with a microfluidic gradient generator to expose the organoid to a growth factor gradient. In this study, a small molecule agonist of the growth factor Shh was used to generate a dorso-ventral gradient in the organoid. A major advantage of this system is the versatility, where a multitude of different growth factors can be incorporated into the microfluidic system as single or dual gradients, and the timing can be tuned accordingly. Combined with the scaffold-guided elongated morphology, this approach provides an opportunity to generate organoids that are more morphologically reminiscent of the developing human brain, with the potential to generate multiple physiological axes in future work.

6.4. Concluding remarks

Bioengineering organoids requires a fine balance between guiding the tissue growth using external cues and simultaneously facilitating the stochastic nature of self-organisation that is key to organogenesis. It is hoped that the scaffold-based stem cell- and organoid-cultured scaffold platform presented in this thesis provides a universal system that can be adapted for other organoid systems in the future.

References

1. Silbereis, J. C., Pochareddy, S., Zhu, Y., Li, M. & Sestan, N. The Cellular and Molecular Landscapes of the Developing Human Central Nervous System. *Neuron* **89**, 248–268 (2016).
2. Kriegstein, A., Noctor, S. & Martínez-Cerdeño, V. Patterns of neural stem and progenitor cell division may underlie evolutionary cortical expansion. *Nat. Rev. Neurosci.* **7**, 883–890 (2006).
3. Bear, M. F., Connors, B. W. & Paradiso, M. A. *Neuroscience: Exploring the brain*. *Neuroscience: Exploring the Brain: Fourth Edition* (Wolters Kluwer, 2015).
4. Kiecker, C. & Lumsden, A. The role of organizers in patterning the nervous system. *Annu. Rev. Neurosci.* **35**, 347–367 (2012).
5. Dre, G. Le & Martı, E. Dorsal – Ventral Patterning of the Neural Tube : A Tale of Three Signals. **1**, 1471–1481 (2012).
6. Gammill, L. S. & Bronner-Fraser, M. Neural crest specification: migrating into genomics. *Nat. Rev. Neurosci.* **4**, 795–805 (2003).
7. Brady, M. V. & Vaccarino, F. M. Role of shh in patterning human pluripotent cells towards ventral forebrain fates. *Cells* **10**, 914 (2021).
8. Howard, B. M. *et al.* Radial glia cells in the developing human brain. *Neuroscientist* **14**, 459–473 (2008).
9. Taverna, E. & Huttner, W. B. Neural progenitor nuclei IN motion. *Neuron* **67**, 906–914 (2010).
10. Miyata, T. *et al.* Asymmetric production of surface-dividing and non-surface-dividing cortical progenitor cells. *Development* **131**, 3133–3145 (2004).
11. Lancaster, M. A. & Knoblich, J. A. Spindle orientation in mammalian cerebral cortical development. *Curr. Opin. Neurobiol.* **22**, 737–746 (2012).
12. Smart, I. H. M., Dehay, C., Giroud, P., Berland, M. & Kennedy, H. Unique morphological features of the proliferative zones and postmitotic compartments of the neural epithelium giving rise to striate and extrastriate cortex in the monkey. *Cereb. Cortex* **12**, 37–53 (2002).
13. Lewitus, E., Kelava, I., Kalinka, A. T., Tomancak, P. & Huttner, W. B. An Adaptive

Threshold in Mammalian Neocortical Evolution. *PLOS Biol.* **12**, e1002000 (2013).

14. Alvarez-Buylla, A. & Nottebohm, F. Migration of young neurons in adult avian brain. *Nature* **335**, 353–354 (1988).
15. Beattie, R. & Hippenmeyer, S. Mechanisms of radial glia progenitor cell lineage progression. *FEBS Letters* **591**, 3993–4008 (2017).
16. Harrison, R. G. Observations on the living developing nerve fiber. *Proc. Soc. Exp. Biol. Med.* **4**, 140–143 (1907).
17. C.H., W. & Cohen, A. Experiments on the Development of the Head of the Chick Embryo. *J. Exp. Biol.* **13**, 219–236 (1936).
18. Crain, S. M. Development of 'Organotypic' Bioelectric Activities in Central Nervous Tissues During Maturation in Culture. *Int. Rev. Neurobiol.* **9**, 1–43 (1966).
19. Wolf, M. K. Anatomy of cultured mouse cerebellum. II. Organotypic migration of granule cells demonstrated by silver impregnation of normal and mutant cultures. *J. Comp. Neurol.* **140**, 281–297 (1970).
20. Croft, C. L., Futch, H. S., Moore, B. D. & Golde, T. E. Organotypic brain slice cultures to model neurodegenerative proteinopathies. *Molecular Neurodegeneration* **14**, 45 (2019).
21. Giandomenico, S. L. *et al.* Cerebral organoids at the air–liquid interface generate diverse nerve tracts with functional output. *Nat. Neurosci.* **22**, 669–679 (2019).
22. Lingor, P., Unsicker, K. & Krieglstein, K. Midbrain dopaminergic neurons are protected from radical induced damage by GDF-5 application. *J. Neural Transm.* **106**, 139–144 (1999).
23. Brewer, G. J. Serum-free B27/neurobasal medium supports differentiated growth of neurons from the striatum, substantia nigra, septum, cerebral cortex, cerebellum, and dentate gyrus. *J. Neurosci. Res.* **42**, 674–683 (1995).
24. Dotti, C. G., Sullivan, C. A. & Banker, G. A. The establishment of polarity by hippocampal neurons in culture. *J. Neurosci.* **8**, 1454–1468 (1988).
25. Gordon, J., Amini, S. & White, M. K. General overview of neuronal cell culture. *Methods in Molecular Biology* **1078**, 1–8 (2013).
26. Biedler, J. L. & Schachner, M. Multiple Neurotransmitter Synthesis by Human Neuroblastoma Cell Lines and Clones. *Cancer Res.* **38**, 3751–3757 (1978).

27. Kovalevich, J. & Langford, D. Considerations for the use of SH-SY5Y neuroblastoma cells in neurobiology. *Methods Mol. Biol.* **1078**, 9–21 (2013).
28. Temple, S. Division and differentiation of isolated CNS blast cells in microculture. *Nature* **340**, 471–473 (1989).
29. Kelava, I. & Lancaster, M. A. Stem Cell Models of Human Brain Development. *Cell Stem Cell* **18**, 736–748 (2016).
30. Conti, L. & Cattaneo, E. Neural stem cell systems: Physiological players or in vitro entities? *Nature Reviews Neuroscience* **11**, 176–187 (2010).
31. JA, T. *et al.* Embryonic stem cell lines derived from human blastocysts. *Science* **282**, 1145–1147 (1998).
32. Takahashi, K. & Yamanaka, S. Induction of Pluripotent Stem Cells from Mouse Embryonic and Adult Fibroblast Cultures by Defined Factors. *Cell* **126**, 663–676 (2006).
33. Kirkeby, A. *et al.* Generation of Regionally Specified Neural Progenitors and Functional Neurons from Human Embryonic Stem Cells under Defined Conditions. *Cell Rep.* **1**, 703–714 (2012).
34. Chambers, S. M. *et al.* Highly efficient neural conversion of human ES and iPS cells by dual inhibition of SMAD signaling. *Nat. Biotechnol.* **27**, 275–280 (2009).
35. World Health Organization. WHO | What are neurological disorders? *World Health Organization* (2016).
36. Pfeuffer, S., Ruck, T., Kleinschnitz, C., Wiendl, H. & Meuth, S. G. Failed, interrupted and inconclusive trials on relapsing multiple sclerosis treatment: update 2010–2015. *Expert Review of Neurotherapeutics* **16**, 689–700 (2016).
37. Anderson, R. M., Hadjichrysanthou, C., Evans, S. & Wong, M. M. Why do so many clinical trials of therapies for Alzheimer's disease fail? *The Lancet* **390**, 2327–2329 (2017).
38. Slanzi, A., Iannoto, G., Rossi, B., Zenaro, E. & Constantin, G. In vitro Models of Neurodegenerative Diseases. *Frontiers in Cell and Developmental Biology* **8**, 328 (2020).
39. Gratten, J., Wray, N. R., Keller, M. C. & Visscher, P. M. Large-scale genomics unveils the genetic architecture of psychiatric disorders. *Nature Neuroscience* **17**, 782–790

(2014).

40. Quadrato, G., Brown, J. & Arlotta, P. The promises and challenges of human brain organoids as models of neuropsychiatric disease. *Nat. Med.* **22**, 1220–1228 (2016).
41. Soliman, M. A., Aboharb, F., Zeltner, N. & Studer, L. Pluripotent stem cells in neuropsychiatric disorders. *Molecular Psychiatry* **22**, 1241–1249 (2017).
42. Brennand, K. J. *et al.* Modelling schizophrenia using human induced pluripotent stem cells. *Nature* **473**, 221–225 (2011).
43. Pacitti, D., Privolizzi, R. & Bax, B. E. Organs to Cells and Cells to Organoids: The Evolution of in vitro Central Nervous System Modelling. *Front. Cell. Neurosci.* **13**, 1–22 (2019).
44. Hanzlik, E. & Gigante, J. Microcephaly. *Children* **4**, 47 (2017).
45. Lancaster, M. A. *et al.* Cerebral organoids model human brain development and microcephaly. *Nature* **29**, 185–185 (2014).
46. Bian, S. *et al.* Genetically engineered cerebral organoids model brain tumor formation. *Nat. Methods* **15**, 631–639 (2018).
47. Schweisguth, F. & Corson, F. Self-Organization in Pattern Formation. *Dev. Cell* **49**, 659–677 (2019).
48. Chen, Q., Shi, J., Tao, Y. & Zernicka-Goetz, M. Tracing the origin of heterogeneity and symmetry breaking in the early mammalian embryo. *Nat. Commun.* **9**, 1–11 (2018).
49. Ishihara, K. & Tanaka, E. M. Spontaneous symmetry breaking and pattern formation of organoids. *Curr. Opin. Syst. Biol.* **11**, 123–128 (2018).
50. Turing, A. M. The chemical basis of morphogenesis. *Bull. Math. Biol.* **52**, 153–197 (1990).
51. Shao, Y. *et al.* Self-organized amniogenesis by human pluripotent stem cells in a biomimetic implantation-like niche. *Nature Materials* **16**, 419–427 (2017).
52. Taniguchi, K. *et al.* Lumen Formation Is an Intrinsic Property of Isolated Human Pluripotent Stem Cells. *Stem Cell Reports* **5**, 954–962 (2015).
53. Shahbazi, marta N. *et al.* Pluripotent state transitions coordinate morphogenesis in mouse and human embryos. *Nature* **552**, 239–243 (2017).
54. Deglincerti, A. *et al.* Self-organization of the in vitro attached human embryo. *Nature* **533**, 251–254 (2016).

55. Shahbazi, M. N. *et al.* Self-organization of the human embryo in the absence of maternal tissues. *Nat. Cell Biol.* **18**, 700–708 (2016).
56. Taniguchi, K. *et al.* An apicosome initiates self-organizing morphogenesis of human pluripotent stem cells. *J. Cell Biol.* **216**, 3981–3990 (2017).
57. Eiraku, M. *et al.* Self-organizing optic-cup morphogenesis in three-dimensional culture. *Nature* **472**, 51–58 (2011).
58. McCracken, K. W. *et al.* Modelling human development and disease in pluripotent stem-cell-derived gastric organoids. *Nature* **516**, 400–404 (2014).
59. Takebe, T. *et al.* Vascularized and functional human liver from an iPSC-derived organ bud transplant. *Nature* **499**, 481–484 (2013).
60. Wong, A. P. *et al.* Directed differentiation of human pluripotent stem cells into mature airway epithelia expressing functional CFTR protein. *Nat. Biotechnol.* **30**, 876–882 (2012).
61. Takasato, M. *et al.* Directing human embryonic stem cell differentiation towards a renal lineage generates a self-organizing kidney. *Nat. Cell Biol.* **16**, 118–126 (2014).
62. Mackinlay, K. M. L. *et al.* An in vitro stem cell model of human epiblast and yolk sac interaction. *Elife* **10**, (2021).
63. Moris, N. *et al.* An in vitro model of early anteroposterior organization during human development. *Nature* **582**, 410–415 (2020).
64. Vining, K. H. & Mooney, D. J. Mechanical forces direct stem cell behaviour in development and regeneration. *Nature Reviews Molecular Cell Biology* **18**, 728–742 (2017).
65. Ladoux, B. & Mège, R. M. Mechanobiology of collective cell behaviours. *Nat. Rev. Mol. Cell Biol.* **18**, 743–757 (2017).
66. Martino, F., Perestrelo, A. R., Vinarský, V., Pagliari, S. & Forte, G. Cellular Mechanotransduction: From Tension to Function. *Front. Physiol.* **9**, 824 (2018).
67. Ingber, D. E. Tensegrity and Mechanotransduction. *J. Bodyw. Mov. Ther.* **12**, 198 (2008).
68. Callens, S. J. P., Uyttendaele, R. J. C., Fratila-Apachitei, L. E. & Zadpoor, A. A. Substrate curvature as a cue to guide spatiotemporal cell and tissue organization. *Biomaterials* **232**, 119739 (2020).

69. Rumpler, M., Woesz, A., Dunlop, J. W. C., Van Dongen, J. T. & Fratzl, P. The effect of geometry on three-dimensional tissue growth. *J. R. Soc. Interface* **5**, 1173–1180 (2008).
70. Lanaro, M. *et al.* A quantitative analysis of cell bridging kinetics on a scaffold using computer vision algorithms. *Acta Biomater.* **136**, 429–440 (2021).
71. Buenzli, P. R. *et al.* Cell proliferation and migration explain pore bridging dynamics in 3D printed scaffolds of different pore size. *Acta Biomater.* **114**, 285–295 (2020).
72. Werner, M. *et al.* Surface Curvature Differentially Regulates Stem Cell Migration and Differentiation via Altered Attachment Morphology and Nuclear Deformation. *Adv. Sci.* **4**, 1600347 (2017).
73. Von Erlach, T. C. *et al.* Cell-geometry-dependent changes in plasma membrane order direct stem cell signalling and fate. *Nat. Mater.* **17**, 237–242 (2018).
74. Warmflash, A., Sorre, B., Etoc, F., Siggia, E. D. & Brivanlou, A. H. A method to recapitulate early embryonic spatial patterning in human embryonic stem cells. *Nat. Methods* **11**, 847–854 (2014).
75. Deglincerti, A. *et al.* Self-organization of human embryonic stem cells on micropatterns. *Nat. Protoc.* **11**, 2223–2232 (2016).
76. Karzbrun, E. *et al.* Human neural tube morphogenesis in vitro by geometric constraints. *Nature* **599**, 268–272 (2021).
77. Abdel Fattah, A. R. *et al.* Actuation enhances patterning in human neural tube organoids. *Nat. Commun.* **12**, 3192 (2021).
78. Sato, T. *et al.* Single Lgr5 stem cells build crypt-villus structures in vitro without a mesenchymal niche. *Nature* **459**, 262–265 (2009).
79. Watanabe, K. *et al.* Directed differentiation of telencephalic precursors from embryonic stem cells. *Nat. Neurosci.* **8**, 288–296 (2005).
80. Lancaster, M. A. & Knoblich, J. A. Generation of cerebral organoids from human pluripotent stem cells. *Nat. Protoc.* **9**, 2329–2340 (2014).
81. Renner, M. *et al.* Self-organized developmental patterning and differentiation in cerebral organoids. *EMBO J.* **36**, 1316–1329 (2017).
82. Qian, X. *et al.* Brain-Region-Specific Organoids Using Mini-bioreactors for Modeling ZIKV Exposure. *Cell* **165**, 1238–1254 (2016).

83. Sidhaye, J. & Knoblich, J. A. Brain organoids: an ensemble of bioassays to investigate human neurodevelopment and disease. *Cell Death and Differentiation* **28**, 52–67 (2021).
84. Quadrato, G. *et al.* Cell diversity and network dynamics in photosensitive human brain organoids. *Nature* **545**, 48–53 (2017).
85. Klaus, J. *et al.* Altered neuronal migratory trajectories in human cerebral organoids derived from individuals with neuronal heterotopia. *Nat. Med.* **25**, 561–568 (2019).
86. Di Lullo, E. & Kriegstein, A. R. The use of brain organoids to investigate neural development and disease. *Nature Reviews Neuroscience* **18**, 573–584 (2017).
87. Eiraku, M. *et al.* Self-Organized Formation of Polarized Cortical Tissues from ESCs and Its Active Manipulation by Extrinsic Signals. *Cell Stem Cell* **3**, 519–532 (2008).
88. Muguruma, K., Nishiyama, A., Kawakami, H., Hashimoto, K. & Sasai, Y. Self-organization of polarized cerebellar tissue in 3D culture of human pluripotent stem cells. *Cell Rep.* **10**, 537–550 (2015).
89. Sakaguchi, H. *et al.* Generation of functional hippocampal neurons from self-organizing human embryonic stem cell-derived dorsomedial telencephalic tissue. *Nat. Commun.* **6**, 8896 (2015).
90. Kadoshima, T. *et al.* Self-organization of axial polarity, inside-out layer pattern, and species-specific progenitor dynamics in human ES cell-derived neocortex. *Proc. Natl. Acad. Sci. U. S. A.* **110**, 20284–20289 (2013).
91. Xiang, Y. *et al.* hESC-Derived Thalamic Organoids Form Reciprocal Projections When Fused with Cortical Organoids. *Cell Stem Cell* **24**, 487–497 (2019).
92. Jo, J. *et al.* Midbrain-like Organoids from Human Pluripotent Stem Cells Contain Functional Dopaminergic and Neuromelanin-Producing Neurons. *Cell Stem Cell* **19**, 248–257 (2016).
93. Birey, F. *et al.* Assembly of functionally integrated human forebrain spheroids. *Nature* **545**, 54–59 (2017).
94. Bagley, J. A., Reumann, D., Bian, S., Lévi-Strauss, J. & Knoblich, J. A. Fused cerebral organoids model interactions between brain regions. *Nat. Methods* **14**, 743–751 (2017).
95. Lee, J.-H. *et al.* Production of human spinal-cord organoids recapitulating neural-tube

morphogenesis. *Nat. Biomed. Eng.* **6**, 435–448 (2022).

96. Pellegrini, L. *et al.* Human CNS barrier-forming organoids with cerebrospinal fluid production. *Science (80-.).* **369**, eaaz5626 (2020).
97. Moore, D. J., West, A. B., Dawson, V. L. & Dawson, T. M. Molecular pathophysiology of Parkinson's disease. *Annu. Rev. Neurosci.* **28**, 57–87 (2005).
98. Kim, H. *et al.* Modeling G2019S-LRRK2 Sporadic Parkinson's Disease in 3D Midbrain Organoids. *Stem Cell Reports* **12**, 518–531 (2019).
99. Smits, L. M. *et al.* Modeling Parkinson's disease in midbrain-like organoids. *npj Park. Dis.* **5**, 1–8 (2019).
100. Pellegrini, L. *et al.* SARS-CoV-2 Infects the Brain Choroid Plexus and Disrupts the Blood-CSF Barrier in Human Brain Organoids. *Cell Stem Cell* **27**, 951–961 (2020).
101. Xiang, Y. *et al.* Fusion of Regionally Specified hPSC-Derived Organoids Models Human Brain Development and Interneuron Migration. *Cell Stem Cell* **21**, 383-398.e7 (2017).
102. Birey, F. *et al.* Dissecting the molecular basis of human interneuron migration in forebrain assembloids from Timothy syndrome. *Cell Stem Cell* **29**, 248–264 (2022).
103. Miura, Y. *et al.* Generation of human striatal organoids and cortico-striatal assembloids from human pluripotent stem cells. *Nat. Biotechnol.* **38**, 1421–1430 (2020).
104. Ao, Z. *et al.* Controllable fusion of human brain organoids using acoustofluidics. *Lab Chip* **21**, 688–699 (2021).
105. Pasca, S. P. Assembling human brain organoids. *Science* **363**, 126–127 (2019).
106. Andersen, J. *et al.* Generation of Functional Human 3D Cortico-Motor Assembloids. *Cell* **183**, 1913–1929 (2020).
107. Cederquist, G. Y. *et al.* Specification of positional identity in forebrain organoids. *Nat. Biotechnol.* **37**, 436–444 (2019).
108. Miura, Y. & Pașca, S. P. Polarizing brain organoids. *Nat. Biotechnol.* **37**, 377–378 (2019).
109. Qian, X., Song, H. & Ming, G. L. Brain organoids: Advances, applications and challenges. *Development* **146**, 166074 (2019).
110. Karakatsani, A., Shah, B. & Ruiz de Almodovar, C. Blood vessels as regulators of neural stem cell properties. *Frontiers in Molecular Neuroscience* **12**, 85 (2019).

111. Matsui, T. K., Tsuru, Y., Hasegawa, K. & Kuwako, K. ichiro. Vascularization of human brain organoids. *Stem Cells* **39**, 1017–1024 (2021).
112. Mansour, A. A. *et al.* An in vivo model of functional and vascularized human brain organoids. *Nat. Biotechnol.* **36**, 432–441 (2018).
113. Cakir, B. *et al.* Engineering of human brain organoids with a functional vascular-like system. **16**, 1169–1175 (2019).
114. Shi, Y. *et al.* Vascularized human cortical organoids (vOrganoids) model cortical development in vivo. *PLoS Biol.* **18**, e3000705 (2020).
115. Bhatia, S. N. & Ingber, D. E. Microfluidic organs-on-chips. *Nat. Biotechnol.* **32**, 760–772 (2014).
116. Wu, Q. *et al.* Organ-on-a-chip: Recent breakthroughs and future prospects. *BioMedical Engineering Online* **19**, 1–19 (2020).
117. Ingber, D. E. Human organs-on-chips for disease modelling, drug development and personalized medicine. *Nat. Rev. Genet.* 1–25 (2022).
118. Maoz, B. M. Brain-on-a-Chip: Characterizing the next generation of advanced in vitro platforms for modeling the central nervous system. *APL Bioeng.* **5**, 030902 (2021).
119. Bang, S., Jeong, S., Choi, N. & Kim, H. N. Brain-on-a-chip: A history of development and future perspective. *Biomicrofluidics* **13**, 51301 (2019).
120. Booth, R. & Kim, H. Characterization of a microfluidic in vitro model of the blood-brain barrier (μBBB). *Lab Chip* **12**, 1784–1792 (2012).
121. Velasco, V., Shariati, S. A. & Esfandyarpour, R. Microtechnology-based methods for organoid models. *Microsystems Nanoeng.* **6**, 1–13 (2020).
122. Park, S. E., Georgescu, A. & Huh, D. Organoids-on-a-chip. *Science* **364**, 960–965 (2019).
123. Wang, Y., Wang, L., Zhu, Y. & Qin, J. Human brain organoid-on-a-chip to model prenatal nicotine exposure. *Lab Chip* **18**, 851–860 (2018).
124. Cho, A. N. *et al.* Microfluidic device with brain extracellular matrix promotes structural and functional maturation of human brain organoids. *Nat. Commun.* **12**, 1–23 (2021).
125. Ao, Z. *et al.* One-Stop Microfluidic Assembly of Human Brain Organoids to Model Prenatal Cannabis Exposure. *Anal. Chem.* **92**, 4630–4638 (2020).

126. Rifes, P. *et al.* Modeling neural tube development by differentiation of human embryonic stem cells in a microfluidic WNT gradient. *Nat. Biotechnol.* **38**, 1265–1273 (2020).
127. Demers, C. J. *et al.* Development-on-chip: *in vitro* neural tube patterning with a microfluidic device. *Development* **143**, 1884–1892 (2016).
128. Magno, V. *et al.* Polymer Hydrogels to Guide Organotypic and Organoid Cultures. *Adv. Funct. Mater.* **30**, 2000097 (2020).
129. Caliari, S. R. & Burdick, J. A. A practical guide to hydrogels for cell culture. *Nature Methods* **13**, 405–414 (2016).
130. Hughes, C. S., Postovit, L. M. & Lajoie, G. A. Matrigel: a complex protein mixture required for optimal growth of cell culture. *Proteomics* **10**, 1886–1890 (2010).
131. Kozlowski, M. T., Crook, C. J. & Ku, H. T. Towards organoid culture without Matrigel. *Commun. Biol. 2021 41* **4**, 1–15 (2021).
132. Kratochvil, M. J. *et al.* Engineered materials for organoid systems. *Nat. Rev. Mater.* **4**, 606–622 (2019).
133. Murphy, A. R., Haynes, J. M., Laslett, A. L., Cameron, N. R. & O'Brien, C. M. Three-dimensional differentiation of human pluripotent stem cell-derived neural precursor cells using tailored porous polymer scaffolds. *Acta Biomater.* **101**, 102–116 (2020).
134. Lam, D. *et al.* Optimizing cell encapsulation condition in ECM-Collagen I hydrogels to support 3D neuronal cultures. *J. Neurosci. Methods* **329**, 108460 (2020).
135. Karumbaiah, L. *et al.* Chondroitin Sulfate Glycosaminoglycan Hydrogels Create Endogenous Niches for Neural Stem Cells. *Bioconjug. Chem.* **26**, 2336–2349 (2015).
136. Zhu, J. Bioactive modification of poly(ethylene glycol) hydrogels for tissue engineering. *Biomaterials* **31**, 4639–4656 (2010).
137. Enemchukwu, N. O. *et al.* Synthetic matrices reveal contributions of ECM biophysical and biochemical properties to epithelial morphogenesis. *J. Cell Biol.* **212**, 113–124 (2016).
138. Lutolf, M. P. & Hubbell, J. A. Synthesis and Physicochemical Characterization of End-Linked Poly(ethylene glycol)-co-peptide Hydrogels Formed by Michael-Type Addition. *Biomacromolecules* **4**, 713–722 (2003).
139. Ranga, A. *et al.* Neural tube morphogenesis in synthetic 3D microenvironments. *Proc.*

Natl. Acad. Sci. U. S. A. **113**, E6831–E6839 (2016).

140. Brown, J. W. & Mills, J. C. Implantable synthetic organoid matrices for intestinal regeneration. *Nat. Cell Biol.* **19**, 1307–1308 (2017).
141. Below, C. R. *et al.* A microenvironment-inspired synthetic three-dimensional model for pancreatic ductal adenocarcinoma organoids. *Nat. Mater.* **21**, 110–119 (2022).
142. Heo, J. H., Kang, D., Seo, S. J. & Jin, Y. Engineering the Extracellular Matrix for Organoid Culture. *Int. J. Stem Cells* **15**, 60–69 (2022).
143. Lancaster, M. A. *et al.* Guided self-organization and cortical plate formation in human brain organoids. *Nat. Biotechnol.* **35**, 659–666 (2017).
144. Rothenbücher, T. S. P. *et al.* Next generation human brain models: Engineered flat brain organoids featuring gyrification. *Biofabrication* **13**, 011001 (2021).
145. Tasnim, K. & Liu, J. Emerging Bioelectronics for Brain Organoid Electrophysiology. *J. Mol. Biol.* **434**, 167165 (2022).
146. Fair, S. R. *et al.* Electrophysiological Maturation of Cerebral Organoids Correlates with Dynamic Morphological and Cellular Development. *Stem Cell Reports* **15**, 855–868 (2020).
147. Park, Y. *et al.* Three-dimensional, multifunctional neural interfaces for cortical spheroids and engineered assembloids. *Sci. Adv.* **7**, 9153–9170 (2021).
148. Li, Q. *et al.* Cyborg Organoids: Implantation of Nanoelectronics via Organogenesis for Tissue-Wide Electrophysiology. *Nano Lett.* **19**, 5781–5789 (2019).
149. Gjorevski, N. *et al.* Tissue geometry drives deterministic organoid patterning. *Science (80-.).* **375**, (2022).
150. Brassard, J. A., Nikolaev, M., Hübscher, T., Hofer, M. & Lutolf, M. P. Recapitulating macro-scale tissue self-organization through organoid bioprinting. *Nat. Mater.* **20**, 22–29 (2021).
151. Salaris, F. & Rosa, A. Construction of 3D in vitro models by bioprinting human pluripotent stem cells: Challenges and opportunities. *Brain Res.* **1723**, 146393 (2019).
152. Abdel Fattah, A. R. *et al.* Actuation enhances patterning in human neural tube organoids. *Nat. Commun.* **12**, 3192 (2021).
153. Trujillo, C. A. *et al.* Complex Oscillatory Waves Emerging from Cortical Organoids Model Early Human Brain Network Development. *Cell Stem Cell* **25**, 558–569 (2019).

154. Lavazza, A. & Lavazza, A. Human cerebral organoids and consciousness: a double-edged sword. *Monash Bioeth. Rev.* **38**, 105–128 (2020).
155. Reardon, S. Can lab-grown brains become conscious? *Nature* **586**, 658–661 (2020).
156. Farahany, N. A. *et al.* The ethics of experimenting with human brain tissue. *Nat. 2021 5567702* **556**, 429–432 (2018).
157. Koplin, J. J. & Savulescu, J. Moral Limits of Brain Organoid Research. *J. Law, Med. Ethics* **47**, 760–767 (2019).
158. Masselink, W. *et al.* Broad applicability of a streamlined ethyl cinnamate-based clearing procedure. *Dev.* **146**, 166884 (2019).
159. Shahbazi, M. N., Siggia, E. D. & Zernicka-Goetz, M. Self-organization of stem cells into embryos: A window on early mammalian development. *Science (80-.).* **364**, 948–951 (2019).
160. Bagnat, M. & Navis, A. Apicobasal polarity and lumen formation during development. in *Cell Polarity 2: Role in Development and Disease* 67–93 (Springer International Publishing, 2015).
161. Sigurbjörnsdóttir, S., Mathew, R. & Leptin, M. Molecular mechanisms of de novo lumen formation. *Nat. Rev. Mol. Cell Biol. 2014 1510* **15**, 665–676 (2014).
162. Bedzhov, I. & Zernicka-Goetz, M. Self-Organizing Properties of Mouse Pluripotent Cells Initiate Morphogenesis upon Implantation. *Cell* **156**, 1032–1042 (2014).
163. Xiang, L. *et al.* A developmental landscape of 3D-cultured human pre-gastrulation embryos. *Nature* **577**, 537–542 (2020).
164. Hofer, M. & Lutolf, M. P. Engineering organoids. *Nature Reviews Materials* **6**, 402–420 (2021).
165. Petridou, N. I., Spiró, Z. & Heisenberg, C. P. Multiscale force sensing in development. *Nature Cell Biology* **19**, 581–588 (2017).
166. Stevens, M. M. & George, J. H. Exploring and engineering the cell surface interface. *Science (80-.).* **310**, 1135–1138 (2005).
167. Hoang, P. & Ma, Z. Biomaterial-guided stem cell organoid engineering for modeling development and diseases. *Acta Biomaterialia* **132**, 23–36 (2021).
168. Bidan, C. M. *et al.* Geometry as a Factor for Tissue Growth: Towards Shape Optimization of Tissue Engineering Scaffolds. *Adv. Healthc. Mater.* **2**, 186–194 (2013).

169. Ehrig, S. *et al.* Surface tension determines tissue shape and growth kinetics. *Sci. Adv.* **5**, 9394 (2019).
170. Mondal, D., Griffith, M. & Venkatraman, S. S. Polycaprolactone-based biomaterials for tissue engineering and drug delivery: Current scenario and challenges. *International Journal of Polymeric Materials and Polymeric Biomaterials* **65**, 255–265 (2016).
171. Wunner, F. M. *et al.* Melt electrospinning writing of three-dimensional poly(ε-caprolactone) scaffolds with controllable morphologies for tissue engineering applications. *J. Vis. Exp.* **2017**, 56289 (2017).
172. Brown, T. D., Dalton, P. D. & Hutmacher, D. W. Direct writing by way of melt electrospinning. *Adv. Mater.* **23**, 5651–5657 (2011).
173. Sozen, B. *et al.* Reconstructing aspects of human embryogenesis with pluripotent stem cells. *Nat. Commun.* **12**, 1–13 (2021).
174. Epstein, C. L. & Gage, M. The Curve Shortening Flow. in 15–59 (Springer, New York, NY, 1987).
175. Martin-Belmonte, F. & Mostov, K. Regulation of cell polarity during epithelial morphogenesis. *Current Opinion in Cell Biology* **20**, 227–234 (2008).
176. Yu, W. *et al.* β1-integrin orients epithelial polarity via Rac1 and laminin. *Mol. Biol. Cell* **16**, 433–445 (2005).
177. O'Brien, L. E. *et al.* Rac1 orientates epithelial apical polarity through effects on basolateral laminin assembly. *Nat. Cell Biol.* **3**, 831–838 (2001).
178. Nikolaev, M. *et al.* Homeostatic mini-intestines through scaffold-guided organoid morphogenesis. *Nature* **585**, 574–578 (2020).
179. Meinhardt, A. *et al.* 3D reconstitution of the patterned neural tube from embryonic stem cells. *Stem cell reports* **3**, 987–99 (2014).
180. Karzbrun, E., Kshirsagar, A., Cohen, S. R., Hanna, J. H. & Reiner, O. Human brain organoids on a chip reveal the physics of folding. *Nat. Phys.* **14**, 515–522 (2018).
181. Knight, G. T. *et al.* Engineering induction of singular neural rosette emergence within hPSC-derived tissues. *Elife* **7**, 1–23 (2018).
182. Jakobsson, A. *et al.* Three-dimensional functional human neuronal networks in uncompressed low-density electrospun fiber scaffolds. *Nanomedicine Nanotechnology, Biol. Med.* **13**, 1563–1573 (2017).

183. Schnell, E. *et al.* Guidance of glial cell migration and axonal growth on electrospun nanofibers of poly-ε-caprolactone and a collagen/poly-ε-caprolactone blend. *Biomaterials* **28**, 3012–3025 (2007).
184. Delepine, C., Pham, V. A., Tsang, H. W. S. & Sur, M. GSK3ß inhibitor CHIR 99021 modulates cerebral organoid development through dose-dependent regulation of apoptosis, proliferation, differentiation and migration. *PLoS One* **16**, e0251173 (2021).
185. Paşca, A. M. *et al.* Functional cortical neurons and astrocytes from human pluripotent stem cells in 3D culture. *Nat. Methods* **12**, 671–678 (2015).
186. Kelava, I. & Lancaster, M. A. Dishing out mini-brains: Current progress and future prospects in brain organoid research. *Dev. Biol.* **420**, 199–209 (2016).
187. Brassard, J. A. & Lutolf, M. P. Engineering Stem Cell Self-organization to Build Better Organoids. *Cell Stem Cell* **24**, 860–876 (2019).
188. Hsu, C. C. *et al.* A single-cell Raman-based platform to identify developmental stages of human pluripotent stem cell-derived neurons. *Proc. Natl. Acad. Sci. U. S. A.* **117**, 18412–18423 (2020).
189. Ghita, A., Pascut, F. C., Mather, M., Sottile, V. & Notingher, I. Cytoplasmic RNA in undifferentiated neural stem cells: A potential label-free raman spectral marker for assessing the undifferentiated status. *Anal. Chem.* **84**, 3155–3162 (2012).
190. Hashimoto, K., Kudoh, S. N. & Sato, H. Analysis of the developing neural system using an in vitro model by Raman spectroscopy. *Analyst* **140**, 2344–2349 (2015).
191. Høgset, H. *et al.* In vivo biomolecular imaging of zebrafish embryos using confocal Raman spectroscopy. *Nat. Commun.* **11**, 6172 (2020).
192. Hobro, A. J. & Smith, N. I. An evaluation of fixation methods: Spatial and compositional cellular changes observed by Raman imaging. *Vib. Spectrosc.* **91**, 31–45 (2017).
193. Cohen, M. M. Holoprosencephaly: Clinical, anatomic, and molecular dimensions. *Birth Defects Res. Part A - Clin. Mol. Teratol.* **76**, 658–673 (2006).
194. Blin, G. *et al.* Geometrical confinement controls the asymmetric patterning of brachyury in cultures of pluripotent cells. *Dev.* **145**, (2018).
195. Morgani, S. M., Metzger, J. J., Nichols, J., Siggia, E. D. & Hadjantonakis, A. K.

Micropattern differentiation of mouse pluripotent stem cells recapitulates embryo regionalized cell fate patterning. *Elife* **7**, (2018).

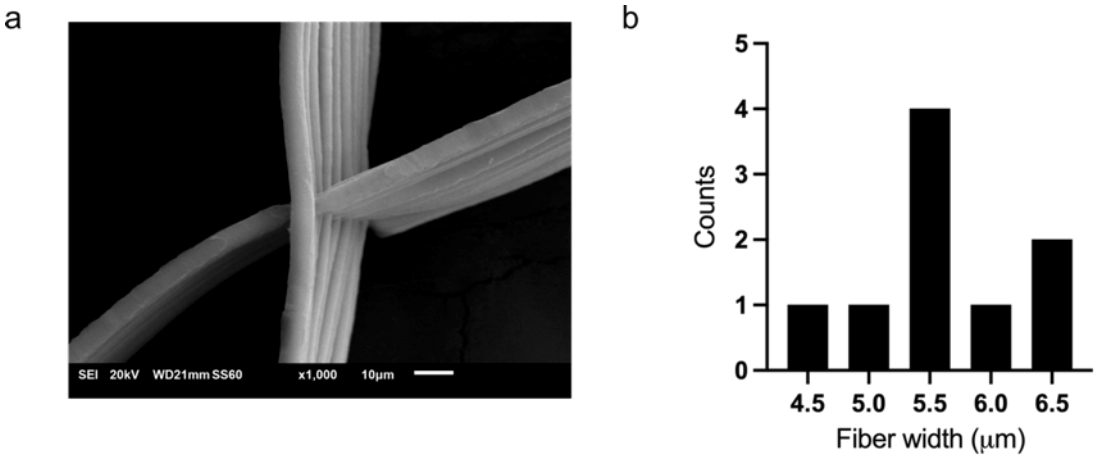
196. Seo, K. *et al.* Symmetry breaking of hPSCs in micropattern generates a polarized spinal cord-like organoid (pSCO) with dorsoventral organization. *bioRxiv* (2021).
197. Rusch, H. *et al.* Finding the best clearing approach - Towards 3D wide-scale multimodal imaging of aged human brain tissue. *Neuroimage* **247**, 118832 (2022).
198. Wang, Z. *et al.* Novel biomaterial strategies for controlled growth factor delivery for biomedical applications. *NPG Asia Materials* **9**, 435 (2017).
199. Ji, W. *et al.* Bioactive electrospun scaffolds delivering growth factors and genes for tissue engineering applications. *Pharm. Res.* **28**, 1259–1272 (2011).
200. Chow, L. W. *et al.* Peptide-directed spatial organization of biomolecules in dynamic gradient scaffolds. *Adv. Healthc. Mater.* **3**, 1381–1386 (2014).
201. Campbell, J. & Vikulina, A. S. Layer-By-Layer Assemblies of Biopolymers: Build-Up, Mechanical Stability and Molecular Dynamics. *Polymers (Basel).* **12**, 1–30 (2020).
202. Hachim, D., Whittaker, T. E., Kim, H. & Stevens, M. M. Glycosaminoglycan-based biomaterials for growth factor and cytokine delivery: Making the right choices. *J. Control. Release* **313**, 131–147 (2019).
203. Chang, S. C., Mulloy, B., Magee, A. I. & Couchman, J. R. Two distinct sites in sonic Hedgehog combine for heparan sulfate interactions and cell signaling functions. *J. Biol. Chem.* **286**, 44391–44402 (2011).
204. Shi, C. *et al.* Therapeutic Potential of Chitosan and Its Derivatives in Regenerative Medicine. *J. Surg. Res.* **133**, 185–192 (2006).
205. Enriquez-Ochoa, D., Robles-Ovalle, P., Mayolo-Deloisa, K. & Brunck, M. E. G. Immobilization of Growth Factors for Cell Therapy Manufacturing. *Front. Bioeng. Biotechnol.* **8**, 620 (2020).
206. Ma, L. *et al.* Human embryonic stem cell-derived GABA neurons correct locomotion deficits in quinolinic acid-lesioned mice. *Cell Stem Cell* **10**, 455–464 (2012).
207. Cho, G., Lim, Y., Cho, I. T., Simonet, J. C. & Golden, J. A. Arx together with FoxA2, regulates Shh floor plate expression. *Dev. Biol.* **393**, 137 (2014).
208. Gulacsi, A. & Anderson, S. A. Shh maintains Nkx2.1 in the MGE by a Gli3-independent mechanism. *Cereb. Cortex* **16**, 89–95 (2006).

209. Duncombe, T. A., Tentori, A. M. & Herr, A. E. Microfluidics: reframing biological enquiry. *Nat. Rev. Mol. Cell Biol. 2015 169* **16**, 554–567 (2015).
210. Sonnen, K. F. & Merten, C. A. Microfluidics as an Emerging Precision Tool in Developmental Biology. *Dev. Cell* **48**, 293–311 (2019).
211. Tehrani-Rokh, M., Kouzani, A. Z. & Kanwar, J. R. Gradient Generating Microfluidic Devices for Cell Cultivation. *Procedia Eng.* **29**, 1740–1744 (2012).
212. Yin, X. *et al.* Cell Stem Cell Engineering Stem Cell Organoids. *Cell Stem Cell* **18**, 25–38 (2016).
213. Manfrin, A. *et al.* Engineered signaling centers for the spatially controlled patterning of human pluripotent stem cells. *Nat. Methods* **16**, 640–648 (2019).
214. Rifes, P. *et al.* Modeling neural tube development by differentiation of human embryonic stem cells in a microfluidic WNT gradient. *Nat. Biotechnol.* **38**, 1265–1273 (2020).
215. Cho, A.-N. *et al.* Microfluidic device with brain extracellular matrix promotes structural and functional maturation of human brain organoids. *Nat. Commun.* **12**, 1–23 (2021).
216. Yazdi, A. A. *et al.* 3D printing: an emerging tool for novel microfluidics and lab-on-a-chip applications. *Microfluid. Nanofluidics 2016 203* **20**, 1–18 (2016).
217. Byrne, M. B., Leslie, M. T., Patel, H. S., Gaskins, H. R. & Kenis, P. J. A. Design considerations for open-well microfluidic platforms for hypoxic cell studies. *Biomicrofluidics* **11**, 054116 (2017).
218. Jeon, N. L. *et al.* Generation of solution and surface gradients using microfluidic systems. *Langmuir* **16**, 8311–8316 (2000).
219. Tiwari, S. K., Bhat, S. & Mahato, K. K. Design and Fabrication of Low-cost Microfluidic Channel for Biomedical Application. *Sci. Rep.* **10**, 1–14 (2020).
220. Mak, S. K. *et al.* Small molecules greatly improve conversion of human-induced pluripotent stem cells to the neuronal lineage. *Stem Cells Int.* **2012**, 140427 (2012).
221. Houart, C. *et al.* Establishment of the Telencephalon during Gastrulation by Local Antagonism of Wnt Signaling. *Neuron* **35**, 255–265 (2002).
222. Kim, T. G. *et al.* Efficient specification of interneurons from human Pluripotent stem cells by dorsoventral and rostrocaudal modulation. *Stem Cells* **32**, 1789 (2014).

223. Watanabe, M. *et al.* Self-Organized Cerebral Organoids with Human-Specific Features Predict Effective Drugs to Combat Zika Virus Infection. *Cell Rep.* **21**, 517–532 (2017).
224. Wang, Y., Wang, L., Guo, Y., Zhu, Y. & Qin, J. Engineering stem cell-derived 3D brain organoids in a perfusable organ-on-a-chip system. *RSC Adv.* **8**, 1677–1685 (2018).
225. Ritzau-Reid, K. I. *et al.* An Electroactive Oligo-EDOT Platform for Neural Tissue Engineering. *Adv. Funct. Mater.* **30**, 2003710 (2020).

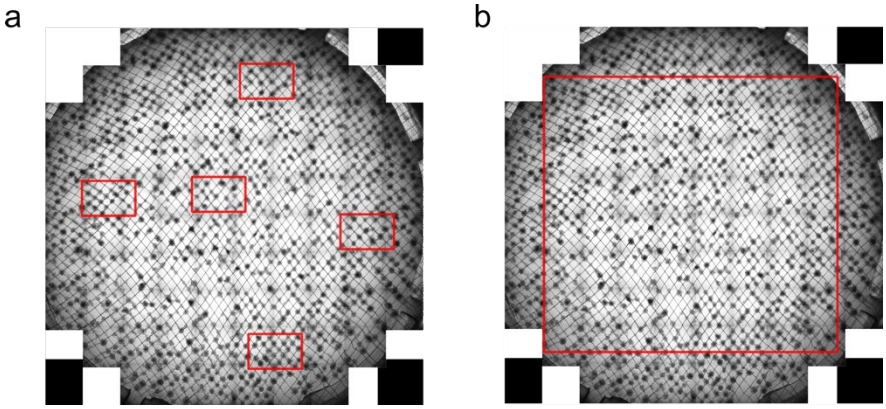
Appendix

Appendix A



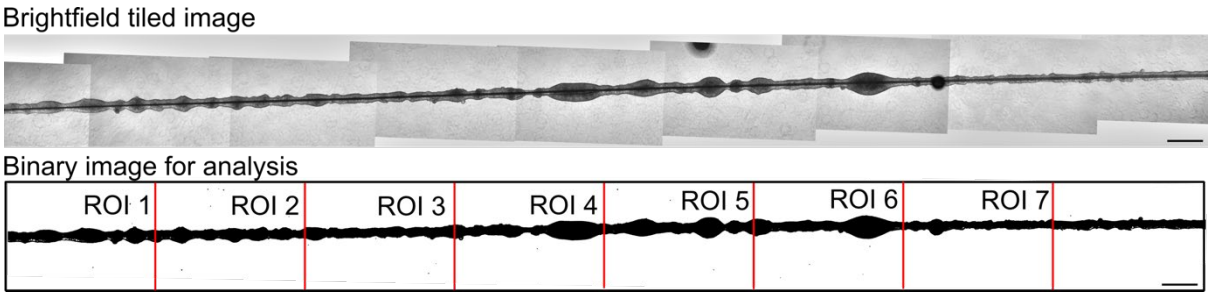
Chapter 3. SEM micrographs show consistent fibre width. *a) Representative SEM image of 1000 µm pore size square scaffold b) histogram to indicate the fibre width distribution of uncoated PCL fibres (N = 1, n = 9).*

Appendix B



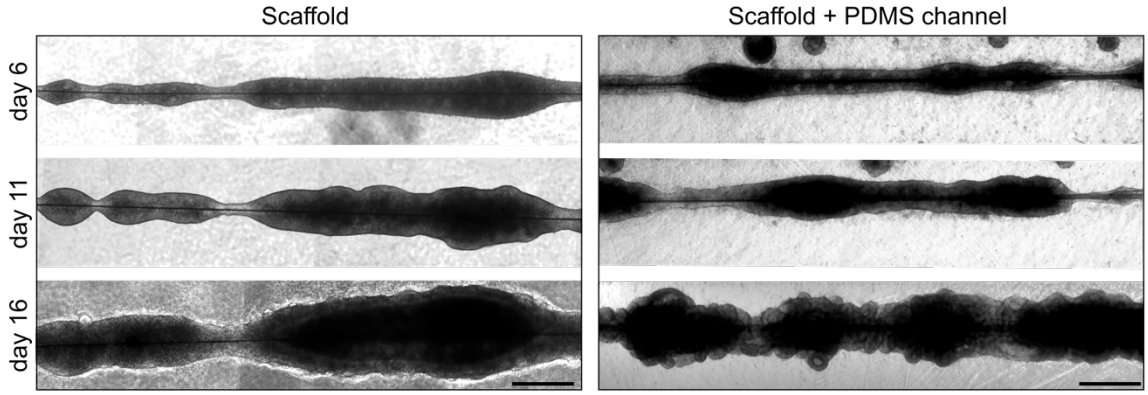
Chapter 4. Tiled overview image of scaffold-cultured organoids at d 20 showing ROIs used for analysis. *a) 5 ROIs selected to assess organoid circularity and maximum diameter over 3 independent experiments. b) ROI selected to assess organoid occupancy over 3 independent experiments.*

Appendix C



Chapter 5. Brightfield images of elongated organoids for analysis. *Tiled brightfield image of entire elongated organoid (top). Binarized image for measurement of 2D projected organoid area and organoid thickness (bottom). Organoid thickness is measured at the ROIs indicated. Image analysis carried out using Fiji ImageJ. Scale bar corresponds to 500 µm.*

Appendix D



Chapter 5. Brightfield images show elongated organoids grown on scaffolds (left) and grown on scaffolds in PDMS channels (right). *Organoids grown at a seeding density of 1 x 10^6 at d 6, 11 and 16. Scale bar corresponds to 500 µm.*

Appendix E: Authorisations

SPRINGER NATURE LICENSE
TERMS AND CONDITIONS

May 25, 2022

This Agreement between Ms. Kaja Ritzau-Reid ("You") and Springer Nature ("Springer Nature") consists of your license details and the terms and conditions provided by Springer Nature and Copyright Clearance Center.

License Number	5314850524337
License date	May 23, 2022
Licensed Content Publisher	Springer Nature
Licensed Content Publication	Nature Reviews Neuroscience
Licensed Content Title	The use of brain organoids to investigate neural development and disease
Licensed Content Author	Elizabeth Di Lullo et al
Licensed Content Date	Sep 7, 2017
Type of Use	Thesis/Dissertation
Requestor type	academic/university or research institute
Format	electronic
Portion	figures/tables/illustrations
Number of figures/tables/illustrations	2

SPRINGER NATURE LICENSE
TERMS AND CONDITIONS

May 25, 2022

This Agreement between Ms. Kaja Ritzau-Reid ("You") and Springer Nature ("Springer Nature") consists of your license details and the terms and conditions provided by Springer Nature and Copyright Clearance Center.

License Number	5314851435076
License date	May 23, 2022
Licensed Content Publisher	Springer Nature
Licensed Content Publication	Nature Biotechnology
Licensed Content Title	Polarizing brain organoids
Licensed Content Author	Yuki Miura et al
Licensed Content Date	Apr 1, 2019
Type of Use	Thesis/Dissertation
Requestor type	academic/university or research institute
Format	electronic
Portion	figures/tables/illustrations
Number of figures/tables/illustrations	1

SPRINGER NATURE LICENSE
TERMS AND CONDITIONS

May 25, 2022

This Agreement between Ms. Kaja Ritzau-Reid ("You") and Springer Nature ("Springer Nature") consists of your license details and the terms and conditions provided by Springer Nature and Copyright Clearance Center.

License Number	5315961177119
License date	May 25, 2022
Licensed Content Publisher	Springer Nature
Licensed Content Publication	Nature Biotechnology
Licensed Content Title	Modeling neural tube development by differentiation of human embryonic stem cells in a microfluidic WNT gradient
Licensed Content Author	Pedro Rifes et al
Licensed Content Date	May 25, 2020
Type of Use	Thesis/Dissertation
Requestor type	academic/university or research institute
Format	electronic
Portion	figures/tables/illustrations
Number of figures/tables/illustrations	1

Order Number: 1224267
Order Date: 23 May 2022

Payment Information

Kaja Ritzau-Reid
k.ritzau-reid16@ic.ac.uk
Payment method: Invoice

Billing Address:
Ms. Kaja Ritzau-Reid
Imperial College London
South Kensington campus
London, SW72AZ
United Kingdom

+44 7717343928
k.ritzau-reid16@ic.ac.uk

Customer Location:
Ms. Kaja Ritzau-Reid
Imperial College London
South Kensington campus
London, SW72AZ
United Kingdom

Order Details

1. Cell

Billing Status: Open

Article: Generation of Functional Human 3D Cortico-Motor Assembloids

Order License ID	1224267-1	**Type of use**	Republish in a thesis/dissertation
Order detail status	Completed	**Publisher**	Cell Press,M I T PRESS
ISSN	1097-4172	**Portion**	Image/photo/illustration

0.00 GBP
Republication Permission

LICENSED CONTENT

Publication Title	Cell	**Publication Type**	e-Journal
Article Title	Generation of Functional Human 3D Cortico-Motor Assembloids	**Start Page**	1913
		End Page	1929.e26
		Issue	7
Date	01/01/1974	**Volume**	183
Language	English	**URL**	http://www.elsevier.com/journals/cell/0092-8674
Country	United States of America		
Rightsholder	Elsevier Science & Technology Journals		

REQUEST DETAILS

Portion Type	Image/photo/illustration	**Distribution**	Worldwide

SPRINGER NATURE LICENSE
TERMS AND CONDITIONS

May 25, 2022

This Agreement between Ms. Kaja Ritzau-Reid ("You") and Springer Nature ("Springer Nature") consists of your license details and the terms and conditions provided by Springer Nature and Copyright Clearance Center.

License Number	5314761309321
License date	May 23, 2022
Licensed Content Publisher	Springer Nature
Licensed Content Publication	Nature Reviews Neuroscience
Licensed Content Title	Neural crest specification: migrating into genomics
Licensed Content Author	Laura S. Gammill et al
Licensed Content Date	Oct 1, 2003
Type of Use	Thesis/Dissertation
Requestor type	academic/university or research institute
Format	electronic
Portion	figures/tables/illustrations
Number of figures/tables/illustrations	1

SPRINGER NATURE LICENSE
TERMS AND CONDITIONS

May 25, 2022

This Agreement between Ms. Kaja Ritzau-Reid ("You") and Springer Nature ("Springer Nature") consists of your license details and the terms and conditions provided by Springer Nature and Copyright Clearance Center.

License Number	5314841227153
License date	May 23, 2022
Licensed Content Publisher	Springer Nature
Licensed Content Publication	Nature Cell Biology
Licensed Content Title	Self-organization of the human embryo in the absence of maternal tissues
Licensed Content Author	Marta N. Shahbazi et al
Licensed Content Date	May 4, 2016
Type of Use	Thesis/Dissertation
Requestor type	academic/university or research institute
Format	print
Portion	figures/tables/illustrations
Number of figures/tables/illustrations	1

SPRINGER NATURE LICENSE
TERMS AND CONDITIONS

May 25, 2022

This Agreement between Ms. Kaja Ritzau-Reid ("You") and Springer Nature ("Springer Nature") consists of your license details and the terms and conditions provided by Springer Nature and Copyright Clearance Center.

License Number	5314850140397
License date	May 23, 2022
Licensed Content Publisher	Springer Nature
Licensed Content Publication	Nature
Licensed Content Title	Human neural tube morphogenesis in vitro by geometric constraints
Licensed Content Author	Eyal Karzbrun et al
Licensed Content Date	Oct 27, 2021
Type of Use	Thesis/Dissertation
Requestor type	academic/university or research institute
Format	electronic
Portion	figures/tables/illustrations
Number of figures/tables/illustrations	1

SPRINGER NATURE LICENSE
TERMS AND CONDITIONS

May 25, 2022

This Agreement between Ms. Kaja Ritzau-Reid ("You") and Springer Nature ("Springer Nature") consists of your license details and the terms and conditions provided by Springer Nature and Copyright Clearance Center.

License Number	5314850372980
License date	May 23, 2022
Licensed Content Publisher	Springer Nature
Licensed Content Publication	Cell Death & Differentiation
Licensed Content Title	Brain organoids: an ensemble of bioassays to investigate human neurodevelopment and disease
Licensed Content Author	Jaydeep Sidhaye et al
Licensed Content Date	Jun 1, 2020
Type of Use	Thesis/Dissertation
Requestor type	academic/university or research institute
Format	electronic
Portion	figures/tables/illustrations
Number of figures/tables/illustrations	1